Length Dependence of the Raman Spectra of Carbon Nanotubes

by

Aurea Tucay Zare

B.S. Applied Physics
Columbia University, 2001

M.S. Electrical Engineering
Columbia University, 2001

SUBMITTED TO THE DEPARTMENT OF ELECTRICAL ENGINEERING AND COMPUTER SCIENCE IN PARTIAL FULFILLMENT OF THE REQUIREMENTS FOR THE DEGREE OF

DOCTOR OF PHILOSOPHY IN ELECTRICAL ENGINEERING AND COMPUTER SCIENCE
AT THE
MASSACHUSETTS INSTITUTE OF TECHNOLOGY

FEBRUARY 2009

Signature of Author: _____
Department of Electrical Engineering and Computer Science
September 15, 2008

Certified by: _____
Mildred S. Dresselhaus
Institute Professor of Electrical Engineering and Physics
Thesis Supervisor

Accepted by: _____
Terry P. Orlando
Professor of Electrical Engineering
Chairman, Department Committee on Graduate Students

Abstract

DNA-wrapping technology, combined with size-exclusion chromatography, have made possible the sorting of carbon nanotubes according to length. In particular, length sorted nanotube samples, with finite lengths approaching the exciton size, are now available. Hence, experiments that explore the finite size effects, in addition to length dependence, are now possible. Although there are many experimental and theoretical studies of the diameter dependence of carbon nanotubes, only a few studies of length-dependent effects exist. Raman spectroscopy is a powerful tool for the characterization of carbon nanotubes. Although Raman spectroscopy nominally probes the phonon scattering processes in carbon nanotubes, the technique provides information on a wide variety of phenomena and properties, including diameter and chirality, defects, and electron-phonon coupling.

This thesis presents the measurement and analysis of Raman spectra in length sorted, DNA-wrapped carbon nanotubes. Three different samples of short nanotubes having lengths of 100 nm, 70 nm, and 50 nm, where the 100 nm tubes behave quite similarly to long nanotubes, were studied using several different values of laser excitation energy. We study the length and excitation energy dependence of various features, each reflecting different physical processes, in the Raman spectra of the length sorted nanotubes. Specifically, the G-band (which includes the G^+ and G^- peaks), D-band, G', G*, and RBM Raman features were examined. We have found that the spectra fall into two categories: spectra with a narrow G^- peak, and spectra with a broad and asymmetric G^- peak which is commonly observed in metallic nanotubes. Although a mixture of semiconducting and metallic nanotubes are resonant for each laser excitation energy, we tentatively assign the spectra with a narrow G^- peak as being from semiconducting tubes, and spectra exhibiting a broad, asymmetric G^- peak to metallic tubes. When the spectra are divided in this way, we have found that the properties of the various Raman peaks differ significantly between the two groups.

We have found that the Raman spectra, especially for metallic nanotubes, varies for different spots on the same sample. This results in noisier data, for which the trends are not clear. We describe the use of the linear correlation analysis method, which allows correlations to be identified despite noisy data. For several of the Raman features, we have found that metallic nanotubes appear to be more sensitive to length than semiconducting tubes. From our analysis of the G-band, electron-phonon coupling seems to decrease for shorter nanotubes. The correlations between the different G-band parameters (frequency, linewidth, normalized intensity, and asymmetry) were identified. The D-band, which arises from a breakdown in selection rules brought about by finite size effects, was found to have a normalized intensity (relative to the G^+ peak) that is inversely proportional to the nanotube length. We observe that the G' feature is comprised of two peaks, which is a result of two energy levels being simultaneously excited. Although the G* peak was weak and noisy, a few length dependent effects above the noise level were observed. Finally, we also observed some length dependence in the RBM peak.

Acknowledgements

Finishing this thesis would not have been possible without the aid of many people.

First of all, I wish to express my sincere gratitude to my academic advisor, Prof. Mildred Dresselhaus, not just for her guidance and help in writing this thesis, but also for her support in my pre-thesis graduate career.

Many thanks also to the other members of my thesis committee, Profs. Jing Kong and Terry Orlando, for their helpful advice and input, and their kindness and understanding. Thanks to Prof. Gene Dresselhaus for his helpful input.

The research team of Dr. Ming Zheng at Dupont provided the length-sorted DNA-wrapped carbon nanotubes which is the basis for this thesis. Many thanks to Prof. Riichiro Saito and Dr. Gustavo Cançado for their valuable expertise and helpful discussions on carbon nanotube physics and Raman spectroscopy. Thank you to Dr. Angela R. Hight Walker and Dr. Jeffrey Simpson of NIST for sharing their knowledge on the length dependence of carbon nanotubes, and for providing additional samples.

Thanks to Dr. Shin Grace Chou for helpful discussions, sample preparation, and her earlier work in this area of research. I am grateful to my fellow graduate students, Alfonso Reina Cecco, Mario Hofmann, Hyungbin Son and Hootan Farhat, for stimulating discussions. Many thanks also to Hyungbin Son, Hootan Farhat for giving tremendous assistance with the Raman spectroscopy setup.

I am very grateful for Laura Doughty for her help and support behind the scenes. Finally, thanks to Dr. Douglas Zare for mathematics assistance, particularly on the correlation analysis, and also for his moral support.

Contents

Chapter 1 – Introduction

1.1 Motivation

Recent advances in post-growth processing have allowed the sorting of carbon nanotubes by length [1]. In particular, length sorted nanotube samples, having finite lengths that are less than the wavelength of light, are now available. Hence, it is now possible to perform experiments that explore finite size effects, as well as the length dependence, of various carbon nanotube properties.

This thesis explores the length dependence of the Raman spectra in carbon nanotubes. In particular, the properties of short nanotubes, with lengths approaching the exciton size, will be studied. Geometrically, the two main parameters of a carbon nanotube are its diameter and length, and the chirality is an additional structural parameter. Although there are many experimental and theoretical studies of the diameter dependence of carbon nanotubes, only a few studies of length dependent effects in carbon nanotubes exist. In addition, studying the properties of short nanotubes would add to our understanding of the transition from 1D to 0D systems.

Raman spectroscopy has emerged as an important characterization technique for carbon nanotubes [2]. Although Raman spectroscopy nominally probes the phonon scattering processes in carbon nanotubes, the technique reveals a wide variety of properties and phenomena related to carbon nanotubes more generally. For example, information about defects, the diameter and chirality, and the degree of electron-phonon coupling can be extracted from the Raman spectra of carbon nanotubes [2, 3]. In order to better utilize Raman spectroscopy for nanotube characterization, it is important to understand how length affects the Raman spectra of carbon nanotubes. For example, in nanographite, Raman spectroscopy is used to estimate the crystallite size [4]; an analogous application may exist for carbon nanotubes.

1.2 Background Information

Introduction to Carbon Nanotubes

A carbon nanotube can be thought of as a rolled-up graphene sheet [5]. Figure 1-1 shows how a carbon nanotube can be constructed from a 2D graphite sheet. Connecting point A to A' and B to B' results in a cylinder, its circumference being the length of the vector C_h. There are different ways to roll up this graphene sheet such that the hexagons (which are comprised of carbon atoms at the vertices) can have different orientations with respect to the nanotube axis. The orientation of a hexagon is specified by the chiral vector C_h. It can be written in terms of the unit vectors a_1 and a_2:

$$C_h = na_1 + ma_2$$

The orientations of a_1 and a_2 are shown in figure 1; n and m are integers. A carbon nanotube is specified by the values of n and m, and by convention, a particular nanotube is referred to as an *(n, m)* nanotube. The nanotube diameter is given by

$$d_t = \frac{|C_h|}{\pi} = a\sqrt{n^2 + m^2 + nm}$$

where a is the lattice constant, 2.49 angstroms. The chiral angle θ is the angle between C_h and a vector parallel to a_1. It is given by

$$\cos\theta = \frac{C_h \bullet a_1}{|C_h||a_1|} = \frac{2n + m}{2\sqrt{n^2 + m^2 + nm}},$$

where $0 \le \theta \le 30^\circ$. Nanotubes with indices (n, 0) have $\theta = 0^\circ$ and are called zigzag tubes (since a circumferential cross section exhibits a zigzag pattern). Nanotubes with (n, n) type indices have $\theta = 30^\circ$ and are called armchair tubes. Nanotubes at all other θ are called chiral tubes. These three types of nanotubes are shown in Figure 1-2.

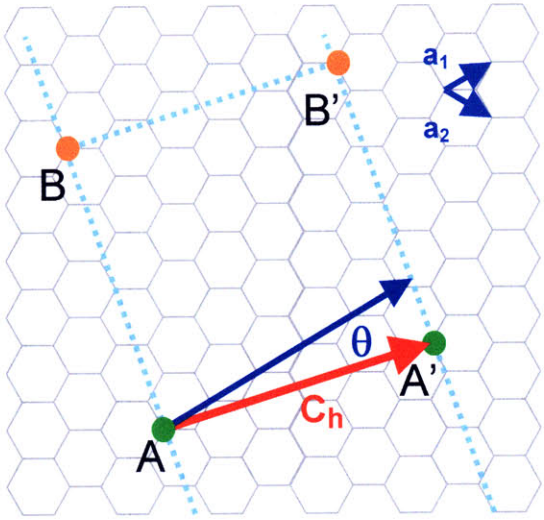

Figure 1-1. Construction of a carbon nanotube from a graphene sheet. The length of the chiral vector C_h is the circumference of the nanotube.

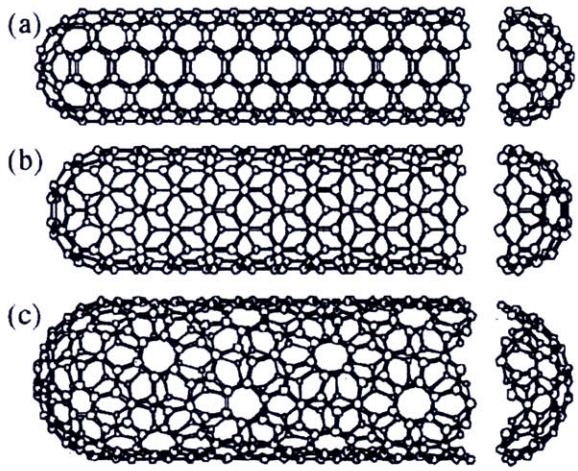

Figure 1-2. The three main types of carbon nanotubes: (a) armchair, (b) zigzag, and (c) chiral nanotubes. This figure is taken from Ref. [5].

The electronic structure of carbon nanotubes can be extracted from that of 2D graphene. Periodic boundary conditions along the circumference of the tube lead to quantization of the wave vector in the C_h direction. Therefore the energy bands for carbon nanotubes are cross sections of the dispersion relations for graphene. Figure 1-3(a) shows the electronic dispersion for the valence and conduction bands of graphene in the first Brillouin zone. The valence and conduction bands touch each other at the K

points, which correspond to the corners of the hexagonal Brillouin zone. Superimposed on the figure are solid curves which show the cross sections, or "cutting lines," that result from periodic boundary conditions for a (4, 2) nanotube. Single walled carbon nanotubes (SWNTs) can be metallic or semiconducting, depending on the values of n and m. If MOD($2n + m$, 3) = 1 or 2 then the SWNT is semiconducting; if MOD($2n + m$, 3) = 0, then the SWNT is metallic. This is because a cutting line crosses the K point for MOD($2n + m$, 3) = 0 nanotubes. Figure 1-3(b) shows the electronic energy band diagram for the (4, 2) nanotube which results from the graphene cross sections of Figure 1-3(a).

The density of states for the (4, 2) tube is shown in Figure 3(c) [6]. The sharp spikes seen in the density of states are the van Hove singularities (vHSs), which are typical of 1D systems. Figure 1-4 shows a schematic of the density of states for a semiconducting nanotube, where two possible optical transitions are highlighted. The lowest energy transition involves the first van Hove singularity and is from v_1 to c_1 and has transition energy E_{11}; the second-lowest transition is from v_2 to c_2 with energy E_{22}. The transition energies of carbon nanotubes depend on their chirality. Bachilo et. al., using a combination of spectrofluorimetric measurements and Raman spectroscopy, have experimentally determined the transition energies of different (n, m) carbon nanotube species [7]. A partial list of their results is shown in Table 1-1.

Excitons have been predicted to exist in carbon nanotubes [8, 9], and recently it has been experimentally demonstrated that the optical resonances in carbon nanotubes are due to excitons [10]. For a semiconducting single-walled nanotube with 0.8 nm diameter, the exciton binding energy was estimated to be about 400 meV. This is a substantial fraction of the nanotube band gap, which is around 1-2 eV. In contrast, in bulk semiconductors the exciton binding energy is a few meV, which is less than the room temperature thermal energy of 26 meV. Hence unlike excitons in bulk semiconductors, excitons in carbon nanotubes are not just perturbations but instead play a major role in the optical properties of carbon nanotubes [10].

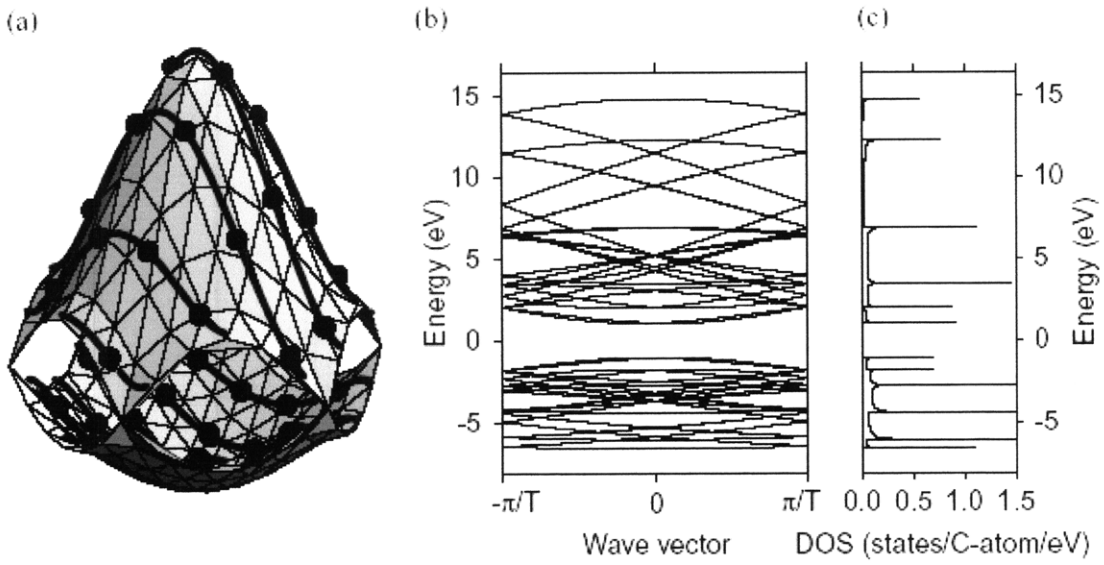

Figure 1-3. (a) The electronic dispersion for the π (valence) and π^* (conduction) bands of graphene in the first Brillouin zone. The solid curves show the cross sections, or "cutting lines," that result from periodic boundary conditions for a (4, 2) nanotube. (b) The electronic energy band diagram for the (4, 2) nanotube which was extracted from (a). (c) The density of states for the (4, 2) nanotube. Image taken from Ref. [6].

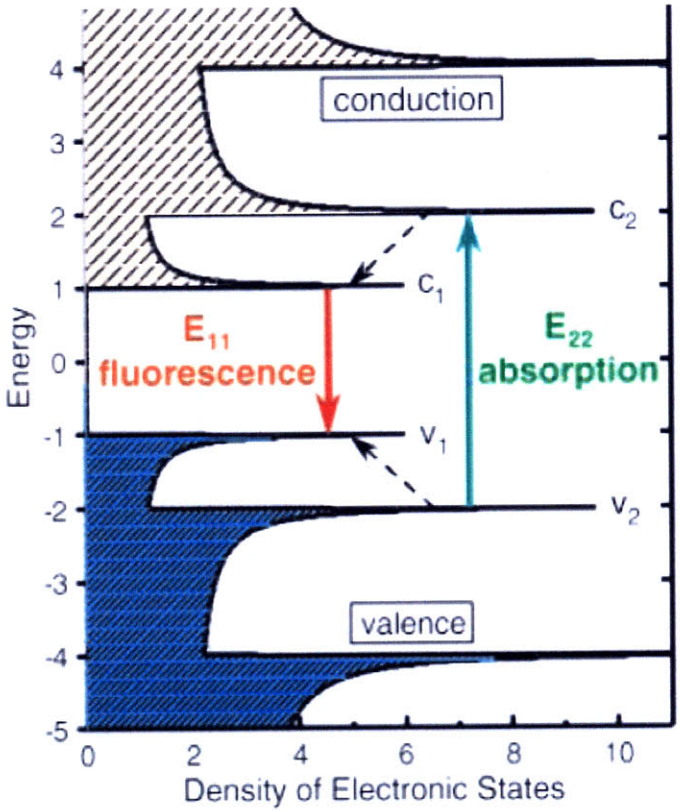

Figure 1-4. Schematic of the density of states for a carbon nanotube, with possible transitions. Image taken from Ref. [7].

λ_{11} (nm)	λ_{22} (nm)	E_{11} (eV)	E_{22} (eV)	Assignment
833	483	1.488	2.567	(5, 4)
873	581	1.420	2.134	(6, 4)
912	693	1.359	1.789	(9, 1)
952	663	1.302	1.870	(8, 3)
975	567	1.272	2.187	(6, 5)
1023	644	1.212	1.925	(7, 5)

Table 1-1. Partial list of transition energies E_{ii} and assignments to (*n*, *m*) nanotubes, as determined in [7]. The λ_{ii} are the corresponding wavelengths.

Raman Spectroscopy

Raman scattering is an inelastic light scattering process. In carbon nanotubes, the Raman process begins when a photon excites an electron from the valence to the conduction band. The excited electron is inelastically scattered by phonons, then eventually relaxes to the valence band by emitting a photon. Raman spectra plot the

intensity of the scattered light as a function of the frequency difference between the incident and scattered light. Thus the phonon frequencies of the nanotube can be measured.

Resonance raman scattering occurs when the incident or scattered photon energy coincides with an electronic transition. The resulting signal is much larger in intensity than in the non-resonant case. In carbon nanotubes, the high density of states along the van Hove singularities further enhances the Raman signal. When a van Hove singularity is resonant with the incident or scattered photon, the Raman intensity becomes strong enough that even an isolated nanotube can give a detectable signal [6].

Additional scattering events can occur along with the inelastic Raman scattering, such as elastic scattering from defects. The *order* of a scattering event is its number in a sequence of total scattering events (including elastic events). Figure 1-5 shows a schematic of the Raman scattering processes in carbon nanotubes. Second-order processes can involve one or two phonons. In the one-phonon, second-order process, the additional scattering event is elastic scattering (shown as dashed lines in Figure 1-5). In the figure, k denotes the initial electron momentum, $\pm q$ is the phonon momentum, and solid circles represent resonance points.

The Raman spectra of very small samples can be measured by the Raman microscopy technique, which combines Raman spectroscopy and optical microscopy. Figure 1-6 shows a typical Raman microscopy setup [11]. The laser output is focused by a microscope objective (M.O.) onto the sample. The backscattered light is then spectrally separated by a spectrometer (which can be a monochromator or a spectrograph) before reaching the detector.

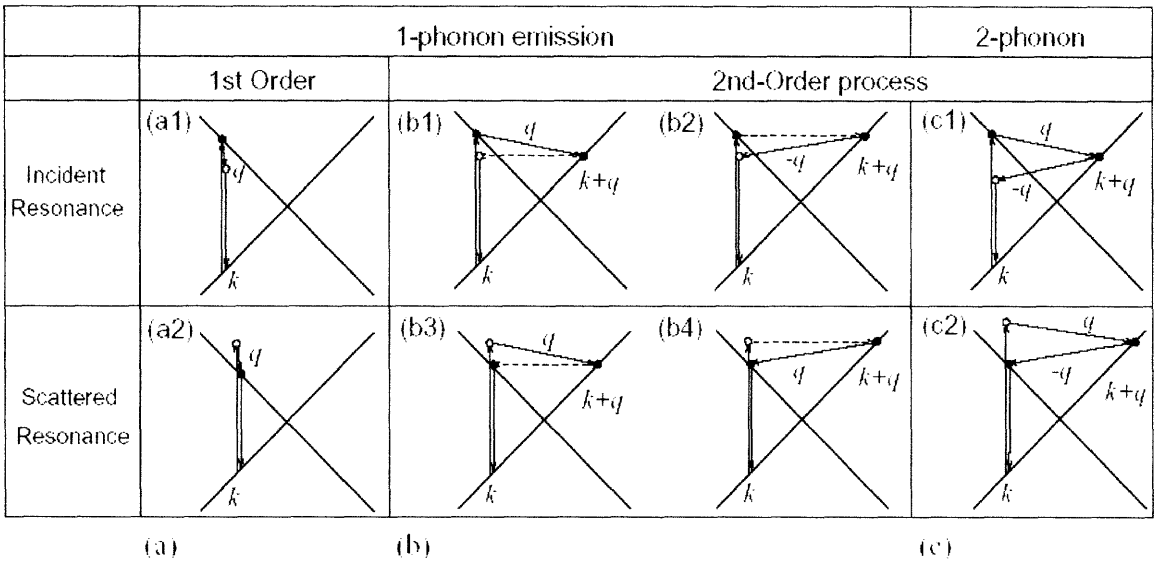

Figure 1-5. Schematic diagrams of (a) first-order and (b) second-order, one-phonon emission Raman scattering processes, and (c) second-order, two-phonon emission processes. In the one-phonon, second-order process, the additional scattering event is elastic scattering, which is denoted by a dashed line. In the figure, k denotes the initial electron momentum, $\pm q$ is the phonon momentum, and solid circles represent resonance points. This image is taken from Ref. [6].

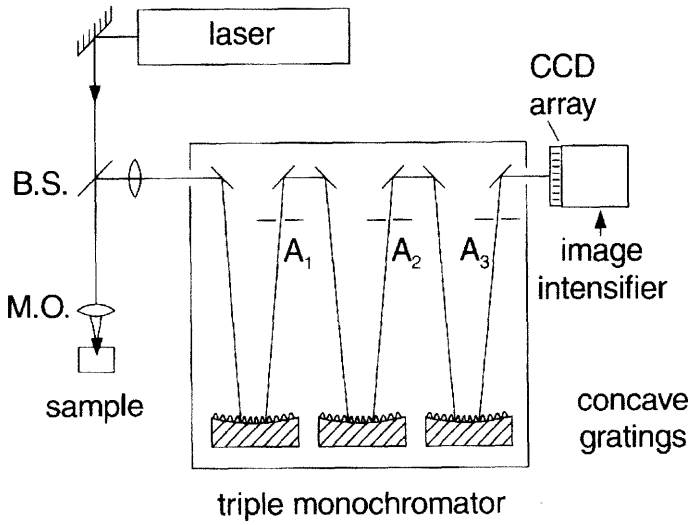

Figure 1-6. A typical Raman microscopy setup. The laser output is focused by a microscope objective (M.O.) onto the sample. The backscattered light is then spectrally separated by a spectrometer (which can be a monochromator or a spectrograph) before reaching the detector. This figure is taken from Ref. [11].

1.3 Overview of Previous Work

This section provides a summary of previous studies on the length-dependent and finite size effects of carbon nanotubes. Recently, a general study on the length dependence of the optical properties of carbon nanotubes was performed [12]. In the series of experiments performed in Ref. [12], the absorption, fluorescence, and Raman spectra of length-sorted carbon nanotubes were examined. A wide variety of nanotube lengths (10 – 700 nm) were available for the experiments of Ref. [12]. The absorbance for the first and second electronic transitions for semiconducting nanotubes, E_{11}^{S} and E_{22}^{S}, were found to decrease approximately linearly with decreasing nanotube length. The trends were less clear for the E_{11}^{M} and E_{33}^{S} transitions. For the (6, 5) semiconducting nanotube, the fluorescence peak intensities were found to decrease linearly as the nanotube length gets shorter. In addition, various features in the Raman spectra were found to decrease in intensity as the nanotube length decreases. Hence the intrinsic optical response of carbon nanotubes was found to get weaker as the nanotube length decreases, at least for semiconducting nanotubes.

More specific studies which focus on the length dependence in the Raman spectra of carbon nanotubes also exist [13, 14]. In Raman spectroscopy of carbon nanotubes, the multiple peaks comprising the G-band at about 1500 – 1600 cm^{-1} corresponds to carbon atom vibrations along the nanotube axis (LO phonon mode) and along the circumference (TO phonon mode) [2]. The D-band centered at about 1350 cm^{-1} (for laser excitation energy E_{laser} = 2.47 eV) results from lattice defects or finite size effects [15]. The intensity ratio I_D/I_G between the D- and G-bands can be used to gauge the relative defect concentration in carbon nanotubes. In a previous work, Raman spectroscopy of short (having lengths of about 50 – 100 nm), length-sorted carbon nanotubes confirmed that the intensity ratio I_D/I_G increases as the nanotube length decreases [13]. In Ref. [13], I_D/I_G was also found to increase as E_{laser} was tuned from resonance with semiconducting nanotubes to resonance with metallic tubes. Finally, for metallic nanotubes excited with the particular laser line E_{laser} = 2.33 eV, the dependence of I_D/I_G on nanotube length and E_{laser} was found to be similar to the behavior of nanographite [4, 13]. In this thesis, we shall examine the length dependence of I_D/I_G for higher values of E_{laser} that were not used

in Ref. [13]. This thesis will give us a more complete understanding of the length dependence of I_D/I_G, and in particular, the different behaviors between semiconducting and metallic nanotubes.

When the carbon nanotube length becomes short enough, peaks associated with finite size effects are expected to appear in the Raman spectra [16 – 18]. Of particular interest are the relatively weak intermediate frequency modes (IFM) that can appear in Raman spectra in the 500 – 1000 cm^{-1} frequency range. These IFM modes correspond to vibrations along the length of the carbon nanotube. Because of symmetry, an infinite length nanotube does not support polarization in the axial direction, and the IFM modes do not appear in the Raman spectra. The Raman spectrum for a finite-length nanotube, however, is expected to exhibit IFM peaks [16]. These IFM peaks were indeed observed in samples of short nanotubes having lengths of about 50 – 100 nm [14]. As the nanotube length decreases, more IFM peaks, and greater relative intensities I_{IFM}/I_G of the IFM peaks, were observed in the Raman spectra. In addition, the length dependent behavior of the various IFM features were found to differ from each other depending on the physical process associated with each IFM peak. For example, peaks at 1189 cm^{-1}, 1402 cm^{-1} and 1462 cm^{-1} are vibrational modes activated by translational symmetry breaking, and have also been observed in C_{60} and C_{70} fullerenes. These same modes were found to have a large intensity increase as the nanotube length decreases. This length sensitivity is attributed to symmetry breaking from the finite size, and also to contributions from the nanotube end caps, which become more important as the tube length decreases. By contrast, IFM peaks found at 838 – 842 cm^{-1} were found to have little length dependence. These peaks are attributed to out-of-plane transverse optical phonon modes, which are not expected to depend on length [14].

1.4 Overview of the Thesis

The following chapter describes the length sorting process, sample preparation, and experimental details of the Raman measurements. In addition, the (*n, m*) indices of resonant nanotubes and whether the tubes are semiconducting or metallic are identified in Chapter 2. The rest of the thesis examines the length and excitation energy dependence of

the various peaks that comprise the Raman spectra of carbon nanotubes. Each of these peaks reflects different physical processes. Chapter 3 examines the length dependence of the G-band in terms of its two major components: the sharp G^+ peak at 1590 cm^{-1}, and the lower frequency G^- peak around 1540 cm^{-1}. Chapter 3 will also introduce the statistical analysis method, which allows us to identify correlations from noisy data, that we will use throughout this thesis. Chapter 4 is a continuation of the G-band studies, and will examine the correlations between the different G-band parameters (frequency, linewidth, relative intensity, and asymmetry) for carbon nanotubes in general, regardless of length. In Chapter 5 we will examine the length dependence of the Raman D-band, which is activated by finite size or lattice defects. Chapter 6 focuses on the G' peak, which is the second harmonic of the D-band, and provides additional insight to the electronic structure of carbon nanotubes. Chapter 7 examines the G* peak at 2417 cm^{-1} (for laser excitation energy E_{laser} = 2.66 eV), of which little is known. In Chapter 8, we will examine the length dependence of the radial breathing mode (RBM) peaks, which fall between 120 – 350 cm^{-1} and correspond to vibrations along the radial direction of the nanotube. We will conclude with Chapter 9, which gives a summary of our findings and a discussion on future work.

References

[1] X. Y. Huang et al., "High-resolution length sorting and purification of DNA-wrapped carbon nanotubes by size-exclusion chromatography." *Anal. Chem,* **77** (2005) 6225-6228.

[2] M. S. Dresselhaus et al., "Raman spectroscopy of carbon nanotubes," *Physics Reports,* **409** (2005) 47.

[3] M. Lazzeri et al., "Phonon linewidths and electron-phonon coupling in graphite and nanotubes," *Physical Review B,* **73** (2006) 155426.

[4] L. G. Cancado et al., "General equation for the determination of the crystallite size L_a of nanographite by Raman spectroscopy," *Applied Physics Letters,* **88** (2006) 163106.

[5] R. Saito, G. Dresselhaus, M. S. Dresselhaus, *Physical Properties of Carbon Nanotubes.* London: Imperial College Press (1998).

[6] M. S. Dresselhaus et al., "Raman spectroscopy of carbon nanotubes," *Physics Reports,* **409** (2005) 47.

[7] S. M. Bachilo, M. S. Strano et. al., "Structure-Assigned Optical Spectra of Single-Walled Carbon Nanotubes," *Science* **298** 2361 (2002).

[8] T. Ando, "Excitons in Carbon Nanotubes," *Journal of the Physical Society of Japan* **66** 1066 (1997).

[9] C. L. Kane and E. J. Mele, "Ratio Problem in Single Carbon Nanotube Fluorescence Spectroscopy," *Physical Review Letters* **90** 207401 (2003).

[10] F. Wang, G. Dukovic et. al., "The Optical Resonances in Carbon Nanotubes Arise from Excitons," *Science* **308** 838 (2005).

[11] W. Demtroder, *Laser Spectroscopy*. Berlin: Springer-Verlag (2003).

[12] J. A. Fagan et al., "Length-Dependent Optical Effects in Single-Wall Carbon Nanotubes." *J. A. Chem. Soc*, **129** (2007) 10607-10612.

[13] S. G. Chou et al., "Length characterization of DNA-wrapped carbon nanotubes using Raman spectroscopy." *Applied Physics Letters*, **90** (2007) 131109.

[14] S. G. Chou et al., "Finite length effects in DNA-wrapped carbon nanotubes," *Chemical Physics Letters,* **90** (2007) 328.

[15] M. A. Pimenta et al., "Diameter dependence of the Raman *D*-band in isolated single-wall carbon nanotubes," *Physical Review B,* **64** (2001) 041401.

[16] R. Saito, T. Takeya, et. al, "Finite-size effect on the Raman spectra of carbon nanotubes," *Physical Review B,* **59** (1999) 2388.

[17] A. Rochefort, D. R. Salahub, et al., "Effects of Finite Length on the Electronic Structure of Carbon Nanotubes," *Journal of Physical Chemistry B,* **103** (1999) 641.

[18] A. Rahmani, J.-L. Sauvajol, et al., "Nonresonant Raman spectrum in infinite and finite single-wall carbon nanotubes," *Physical Review B,* **66** (2002) 125404.

Chapter 2 – Experimental Details

2.1 Length Sorting of Carbon Nanotubes

This chapter provides an overview of the length sorting process, sample preparation, and experimental details of the Raman measurements. In addition, the (*n, m*) indices of resonant nanotubes and whether the tubes are semiconducting or metallic are identified, for each value of laser excitation energy E_{laser}.

Length sorting of carbon nanotubes into fractions having 10% or less nanotube length variation was recently achieved by our collaborators at DuPont [1]. Sorting was performed using size-exclusion chromatography (SEC), a commonly used method for sorting macromolecules according to size. Figure 2-1 is a simplified diagram showing the SEC process. In SEC, the macromolecules are passed through a column containing beads having a certain pore size. Larger molecules cannot enter the pores and pass through the column quickly. The choice of pore size is important, since SEC becomes less sensitive if the molecules are too large or too small in relation to the pores. If the molecules have a broad size distribution, then better results can be obtained by using multiple columns, each having a different pore size.

A carbon nanotube's physical dimensions are dominated by its length. Therefore, it was expected that SEC would sort the nanotubes according to length but not diameter. Our collaborators used specially designed SEC columns that do not allow DNA-wrapped carbon nanotubes to become adsorbed into the column material. The SEC columns consist of silica beads whose surfaces contain negatively charged functional groups. These functional groups prevent adsorption of the negatively charged DNA-wrapped carbon nanotubes. Three columns, having pore sizes of 2000, 1000, and 300 Angstroms, were used in series. The carbon nanotubes were CoMoCAT (synthesized using Cobalt-Molybdenum catalyst) nanotubes [2, 3] purchased from Southwest Nanotechnologies. DNA wrapping of these nanotubes was performed by our collaborators.

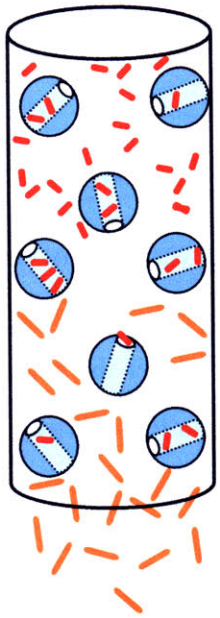

Figure 2-1. A simplified schematic diagram showing the principle behind the size-exclusion chromatography (SEC) process. The longer nanotubes cannot fit into the pores and thus they pass through the column faster than the shorter nanotubes.

The lengths of the sorted nanotubes were measured by our collaborators using AFM (atomic force microscopy) imaging. The AFM images of the sorted nanotubes are shown in Figure 2-2. The SEC procedure was found to be effective in separating the DNA-wrapped carbon nanotubes into fractions, each containing nanotubes of a certain length. The average length of the nanotubes in the earlier fractions was greater than 500 nm; later fractions contained nanotubes with lengths of less than 100 nm. Each fraction had a narrow length distribution of 10% or less. The heights of the sorted nanotubes were found to be about the same in the different fractions, measuring 1.2 – 1.4 nm, and confirmed that the tubes were individual single walled carbon nanotubes (SWNTs) [1]. Thus, according to the AFM images, SEC resulted in length, but not diameter, sorting of carbon nanotubes. In Chapter 8 of this thesis we will use Raman spectroscopy to further investigate whether the SEC procedure inadvertently leads to diameter sorting.

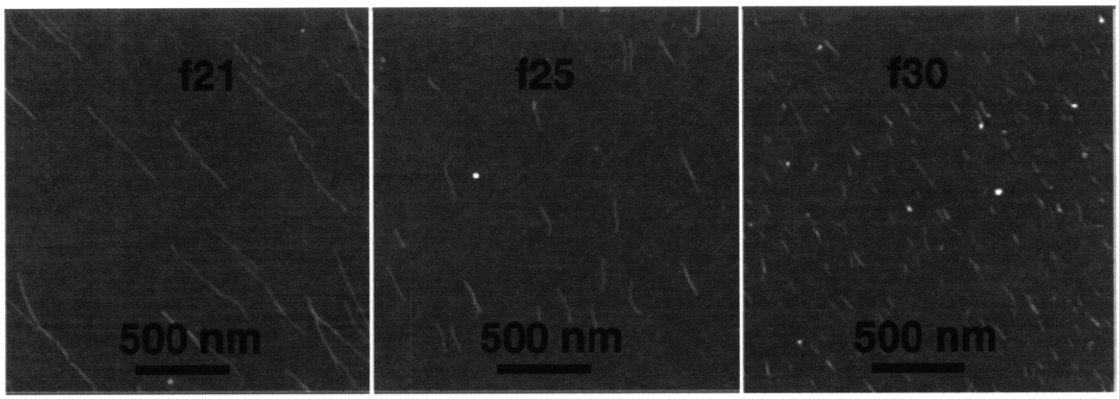

Figure 2-2. AFM images of three different samples after sorting by SEC. The samples shown in these images consisted of individual DNA-wrapped SWNTs that were deposited onto a SiO_2 substrate. The nanotube lengths are 527 nm (f21), 192 nm (f25), and 75 nm (f30), where fxx denotes the fraction number [1].

2.2 Sample Preparation and Raman Spectroscopy

DNA-wrapped CoMoCAT single walled nanotubes were sorted by length using size exclusion chromatography [1]. For the Raman experiments discussed in this chapter, three sorted samples, with average nanotube lengths L_{tube} of 50, 70 and 100 nm, were used. The length variation that results from the SEC procedure was found to be 10% [1]. Dried samples for Raman characterization were prepared from the fractionated liquid samples by dropping 15 uL of solution onto a sapphire substrate, 1 μL at a time.

Raman measurements were taken using a home built micro-Raman system in the backscattering geometry [4]. Raman spectra were taken with Kr^+ ion and Ar^+ ion lasers over a wide range of laser excitation energies. A 50x microscope objective was used, and the laser power at the sample was kept below 2 mW to avoid overheating the sample. Spectra were recorded using a thermoelectrically cooled Si CCD detector. Data were recorded for different spots on each sample to account for sample inhomogeneities. The sample inhomogeneities became more serious with decreasing L_{tube}.

Examples of Raman spectra for the three available L_{tube} are shown in Figure 2-3 for E_{laser} = 488 nm (2.54 eV). The spectra were normalized to the sharp G^+ peak at around 1592 cm^{-1}. The reason for the need for a normalization is that the signal in general is

proportional to the fraction of the laser spot intercepted by nanotubes. From Figure 2-3 it is evident that certain Raman features change with L_{tube}, such as the G and D bands. The changes go beyond the differences in light beam interception that may occur for different length tubes. The length dependence of the various Raman bands will be covered in subsequent chapters. In addition, there are peaks at about 420 cm^{-1}, 577 cm^{-1}, and 750 cm^{-1} that appear to increase in intensity (relative to the intensity of the G^+ feature) as L_{tube} decreases. However, these are likely sapphire peaks, since they appear in Raman measurements of the sapphire substrate, as shown in Figure 2-4. The reason these peaks appear to increase in intensity as L_{tube} decreases is because the Raman spectra have been normalized to the G^+ peak. In the previous study on length-dependent optical effects in SWNTs [5], the absolute intensity of a number of Raman peaks, including the G-band, were found to increase with increasing nanotube length. In the current study, we have found that in general, a longer acquisition time was required to collect a good Raman signal from the shortest nanotubes; therefore the substrate signal would be greater. Therefore when the Raman spectra are normalized to the G-band, the substrate peaks, which should not change with L_{tube}, would appear to increase with decreasing L_{tube}.

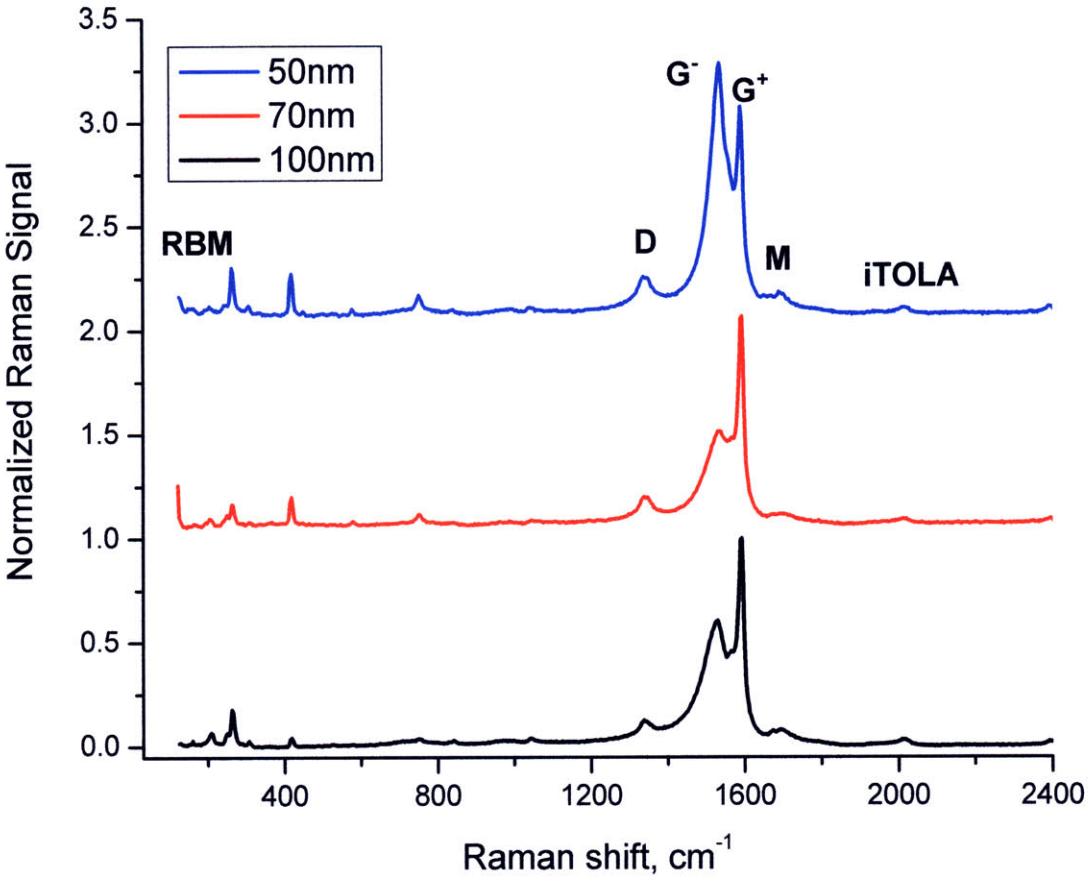

Figure 2-3. Representative Raman spectra for nanotubes excited with E_{laser} = 488 nm = 2.54 eV. Spectra for nanotubes with average lengths of 50, 70, and 100 nm are shown. Baselines were subtracted, and then the spectra were normalized to the G^+ peak at 1592 cm^{-1} and offset from one another for readability. The major Raman features are labeled.

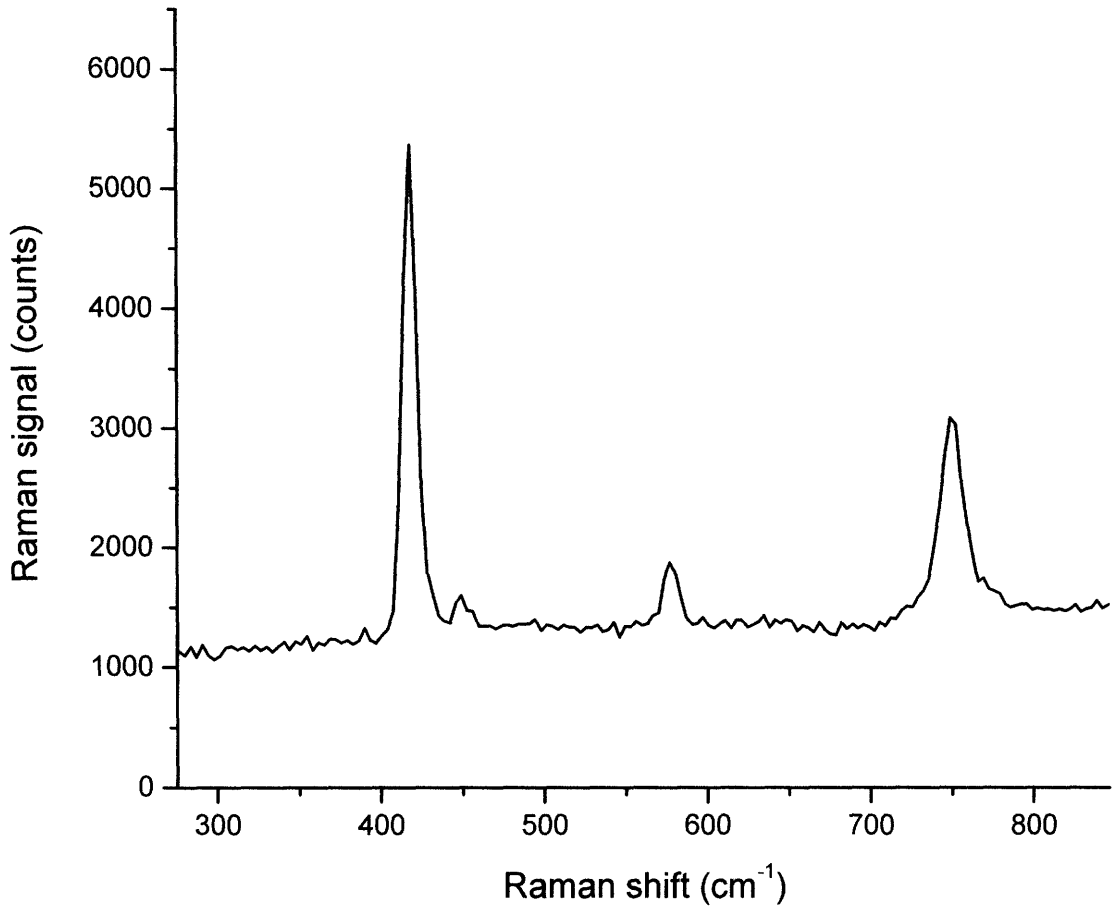

Figure 2-4. Raman spectrum of the sapphire substrate. E_{laser} = 488 nm (2.54 eV) and the acquisition time is 60 s.

2.3 Identification of Nanotubes in Length Sorted Samples

In this section we will use the measured radial breathing mode (RBM) frequencies to identify which (*n, m*) tubes are excited in the samples. The RBM peaks, which appear in the Raman spectra of carbon nanotubes at frequencies between 120 – 350 cm^{-1}, correspond to phonon vibrations in the radial direction. The RBM frequency varies inversely with nanotube diameter, since for larger diameters, there are more carbon atoms which result in a lower vibrational frequency. In order to identify the (*n, m*) tubes resonant with each E_{laser}, we use a Kataura plot (Figure 2-5), which plots the excitation energy of each (*n, m*) nanotube against the RBM frequency [6]. In Table 2-1, the observed RBM frequencies, the corresponding nanotube diameter, the resonant (*n, m*) nanotubes, and whether the nanotubes are metallic or semiconducting, are listed for each

E_{laser} used in the Raman measurements. As can be seen from Table 2-1, a mixture of semiconducting and metallic nanotubes is excited by each E_{laser}.

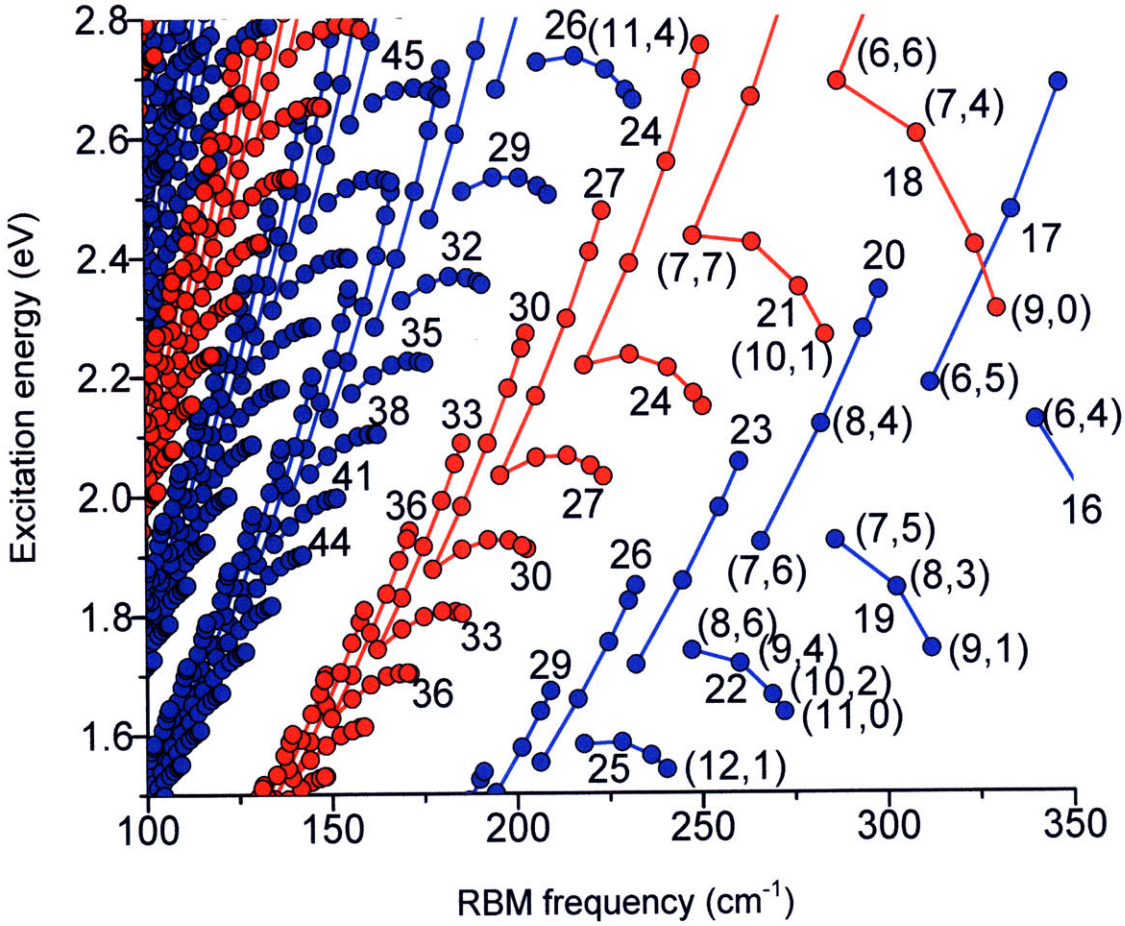

Figure 2-5. Kataura plot, which shows the excitation energy vs. RBM frequency, for each (*n, m*) tube. The blue dots represent semiconducting nanotubes and the red dots represent metallic nanotubes.

E_{laser} (eV)	Observed RBM frequencies (cm^{-1})	Nanotube diameter (nm)	Resonant nanotubes (n, m) and S or M
2.71	227	1.04	(11, 4)S
	286	0.82	(6, 6)M
	302	0.77	(7, 4)M
2.66	180	1.33	(22, 1)S
	230	1.03	(13, 0)S
	291	0.80	(6, 6)M
	310	0.75	(7, 4)M
2.62	206	1.16	(9, 8)S
	228	1.04	(13, 0)S
	262	0.90	(8, 5)M
	287	0.81	(6, 6)M
	306	0.76	(7, 4)M
2.60	206	1.16	(13, 3)S
	224	1.06	(11, 4)S
	264	0.89	(8, 5)M
	286	0.82	(6, 6)M
	307	0.76	(7, 4)M
2.54	160	1.52	(21, 6)S
	209	1.14	(14, 1)S
	250	0.94	(7, 7)M
	264	0.89	(8, 5)M
	307	0.76	(7, 4)M
2.50	212	1.12	(14, 1)S
	253	0.93	(7, 7)M
	267	0.88	(8, 5)M
	309	0.75	(7, 4)M
2.47	227	1.04	(13, 1)M
	267	0.88	(8, 5)M
	281	0.83	(9, 3)M
	328	0.71	(8, 2)M
2.41	153	1.59	(25, 1)S
	188	1.27	(15, 2)S
	250	0.94	(7, 7)M
	264	0.89	(8, 5)M
	272	0.86	(9, 3)M
2.07	218	1.09	(12, 3)M
	256	0.92	(11, 1)S
	281	0.83	(8, 4)S
2.03	199	1.20	(9, 9)M
	218	1.09	(12, 3)M
	259	0.91	(11, 1)S
	285	0.82	(7, 5)S
1.92	197	1.21	(13, 4)M
	267	0.88	(7, 6)S
	286	0.82	(7, 5)S

Table 2-1. The observed RBM frequencies (ω_{RBM}), corresponding nanotube diameters, the (n, m) indices, and whether the tube is metallic (M) or semiconducting (S), for each E_{laser} used in the experiment. The formula for calculating nanotube diameter d_t is $\omega_{RBM} = 223.5/d_t + 12.5$ (Ref. [7]). The most prominent ω_{RBM} observed for each E_{laser} are underlined.

References

[1] X. Y. Huang et al., "High-resolution length sorting and purification of DNA-wrapped carbon nanotubes by size-exclusion chromatography." *Anal. Chem,* **77** (2005) 6225-6228.

[2] Kitiyanan et al., "Controlled production of single-wall carbon nanotubes by catalytic decomposition of CO on bimetallic Co-Mo catalysts." *Chemical Physics Letters*, **317** (2000) 497.

[3] Alvarez et al., "Synergism of Co and Mo in the catalytic production of single-wall carbon nanotubes by decomposition of CO." *Carbon*, **39** (2001) 547.

[4] H. B. Son et al., "Characterizing the chirality distribution of single-walled carbon nanotube materials with tunable Raman spectroscopy," *Phys. Stat. Sol. (b),* **243** (2006) 3161.

[5] J. A. Fagan et al., "Length-Dependent Optical Effects in Single-Wall Carbon Nanotubes." *J. A. Chem. Soc*, **129** (2007) 10607-10612.

[6] Ge. G. Samsonidze et al., "Family behavior of the optical transition energies in single-wall carbon nanotubes of smaller diameters," *Applied Physics Letters,* **85** (2004) 5703.

[7] S. M. Bachilo et al., "Structure-Assigned Optical Spectra of Single-Walled Carbon Nanotubes," *Science,* **298** (2002) 2361.

Chapter 3 – Length Dependence of the Raman G-band

3.1 Overview

In Raman spectroscopy of carbon nanotubes, the multiple peaks comprising the G-band at about 1500 – 1600 cm^{-1} correspond to carbon atom vibrations along the nanotube axis (LO phonon mode) and along the circumference (TO phonon mode) [1]. In this chapter we examine the length dependence of the Raman G-band feature of carbon nanotubes. We refer to background material in Chapter 2 relevant to the samples, the laser lines available for this study, and the Kataura plot used to design the experiments discussed in this chapter. The relative intensities, lineshapes, linewidths and frequencies of the two major peaks comprising the G-band will be discussed. First we will present the length-dependent trends observed for the G-band of semiconducting nanotubes. The G-band length-dependent behavior of semiconducting nanotubes will then be compared to that of metallic nanotubes. We will study the length dependence of metallic nanotubes in greater detail, since the G-band for metallic nanotubes is more complicated than for semiconducting tubes. We find that metallic nanotubes tend to show significant spot-to-spot variation between individual Raman spectra taken for the same sample and with the same laser line, which introduces noise that obscures the length-dependent trends. Therefore we focus on a specific laser line (E_{laser} = 2.71 eV) for which low spot-to-spot variation in the Raman spectra was observed. In addition, we also examine the Raman data for several laser lines to see if general trends for metallic nanotubes, which corroborate the E_{laser} = 2.71 eV data, can be identified. To address the problem of noise introduced by the spot-to-spot variation in the Raman spectra, we present a statistical analysis method that allows us to quantify the correlation between nanotube length and the G-band parameters. We then use this correlation analysis to draw general conclusions about the G-band length dependence, despite having noisy data. This chapter ends with a summary of the G-band length dependence results. Further discussion of the correlation between G-band parameters that were identified through the length-dependent studies will be continued in Chapter 4.

3.2 Semiconducting Nanotubes

To get an idea of the general length dependent behavior of semiconducting nanotubes, we first examine the Raman spectra for E_{laser} = 647 nm = 1.92 eV. At this excitation energy, there is a dominant RBM peak at 286 cm^{-1}, which corresponds to the (7, 5) semiconducting nanotube. Figure 3-1 shows representative Raman spectra at this E_{laser} for different lengths (L_{tube}) of nanotubes. From Figure 3-1, we see that for semiconducting nanotubes, the RBM and G-band show little length dependence. The length dependence of the RBM and the G' peaks will be discussed in later chapters of this thesis. Spectra were taken for different spots on each sample to account for sample inhomogeneities. Figures 3-2(a) – (c) show the Raman spectra for different spots on each sample. Not much spot-to-spot variation was found for this E_{laser} (1.92 eV).

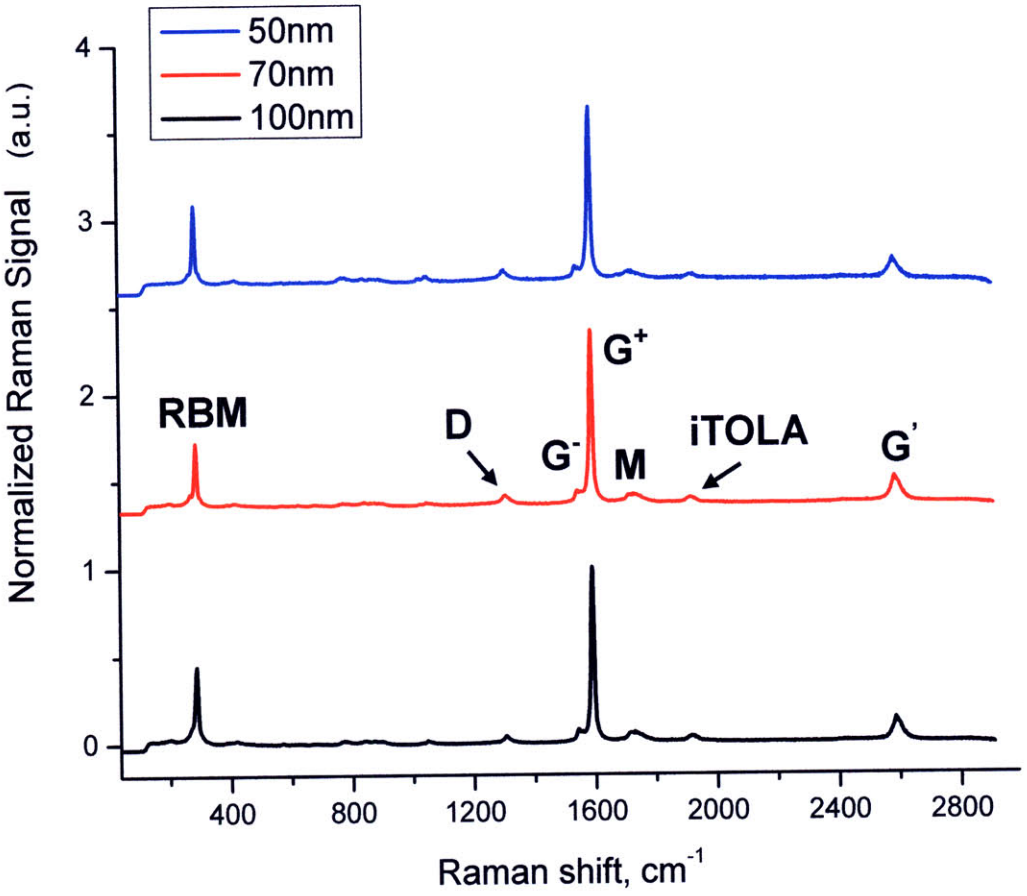

Figure 3-1. Representative Raman spectra for semiconducting nanotubes excited with E_{laser} = 647 nm = 1.92 eV. Spectra for nanotubes with average lengths of 50, 70, and 100 nm are shown. The spectra were normalized to the G^+ peak at 1590 cm^{-1}, and the spectra were then offset for readability. The individual Raman features are labeled.

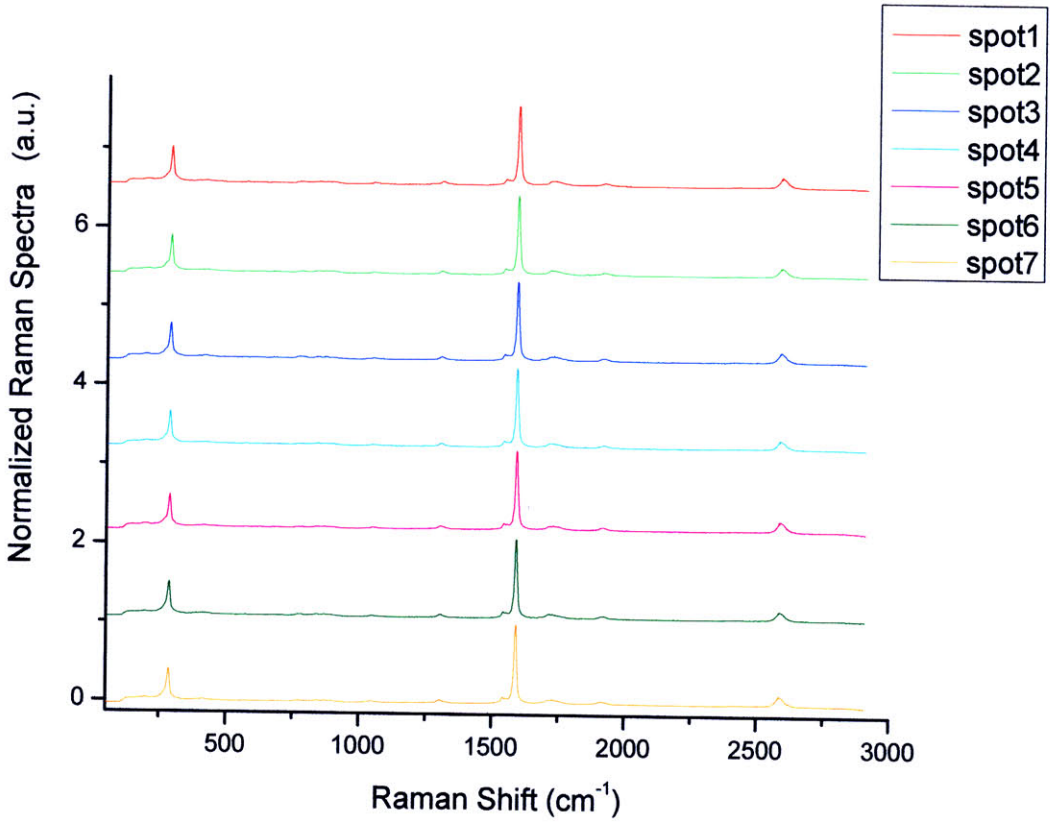

Figure 3-2(a). Raman spectra for semiconducting nanotubes, for different spots on a sample. The laser excitation energy is 647 nm (1.92 eV) and the average nanotube length is 100 nm. The spectra have been normalized to the G^+ peak and offset from each other.

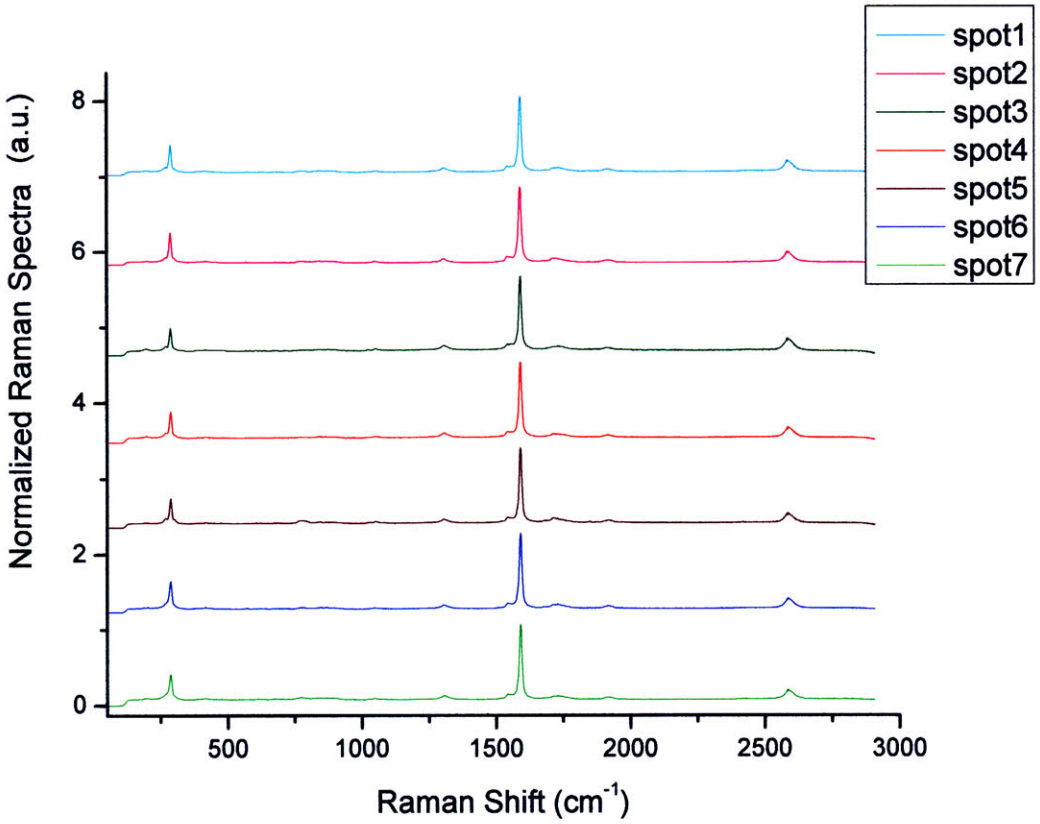

Figure 3-2(b). Same as Figure 3-2(a), but for 70 nm long nanotubes.

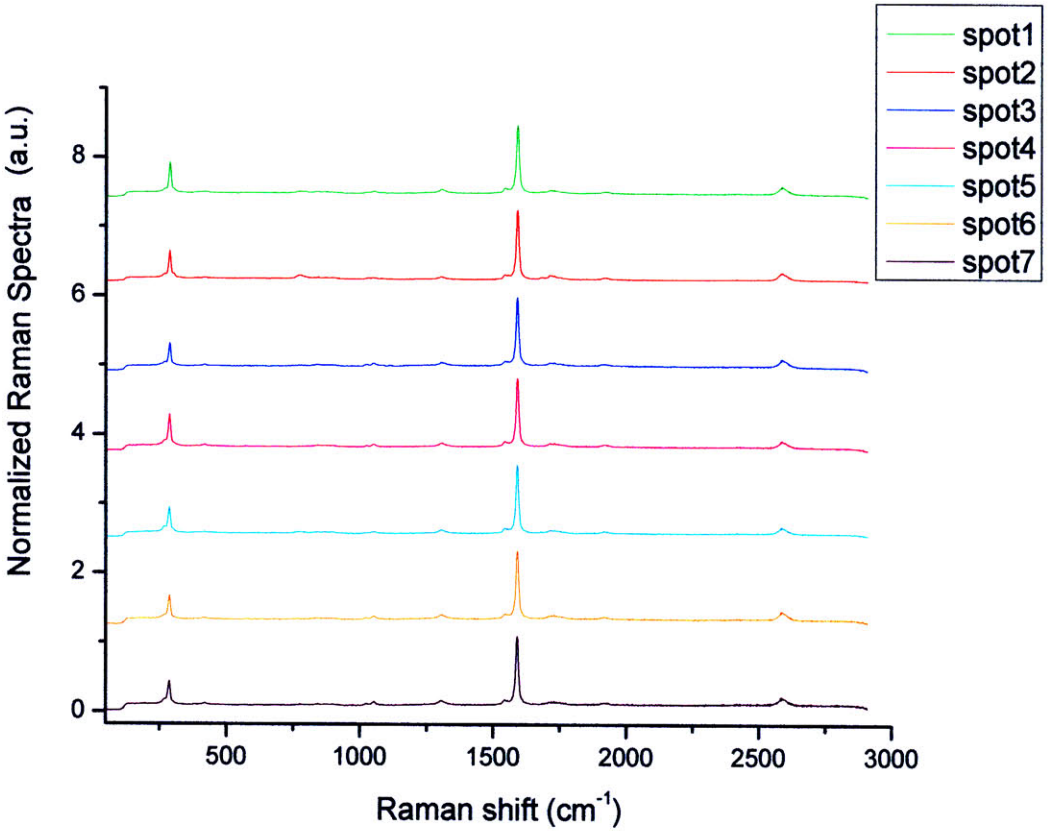

Figure 3-2(c). Same as Figure 3-2(a), but for 50 nm long nanotubes.

For these values of E_{laser}, peak fitting was performed on the raw data to extract the individual G-band components. The peaks in the vicinity of the G-band were fitted with Lorentzians. We find that the G-band is dominated by a sharp peak at 1590 cm^{-1}. Two smaller peaks were resolved at 1543 cm^{-1} and 1555 cm^{-1}. Henceforth we refer to the highest frequency peak at 1590 cm^{-1} as the "G^+" peak. The two lower frequency peaks around 1540 cm^{-1} and 1555 cm^{-1} are identified as the "G^-" peak [1]. In addition to the G-band peaks, we also include the D-band at 1305 cm^{-1} and M-band at 1730 cm^{-1} because of these peaks' proximity to the G-band. The D-band and M-band will be discussed in later chapters of the thesis. Figure 3-3 shows a sample Raman trace with curves resulting from peak fitting superimposed.

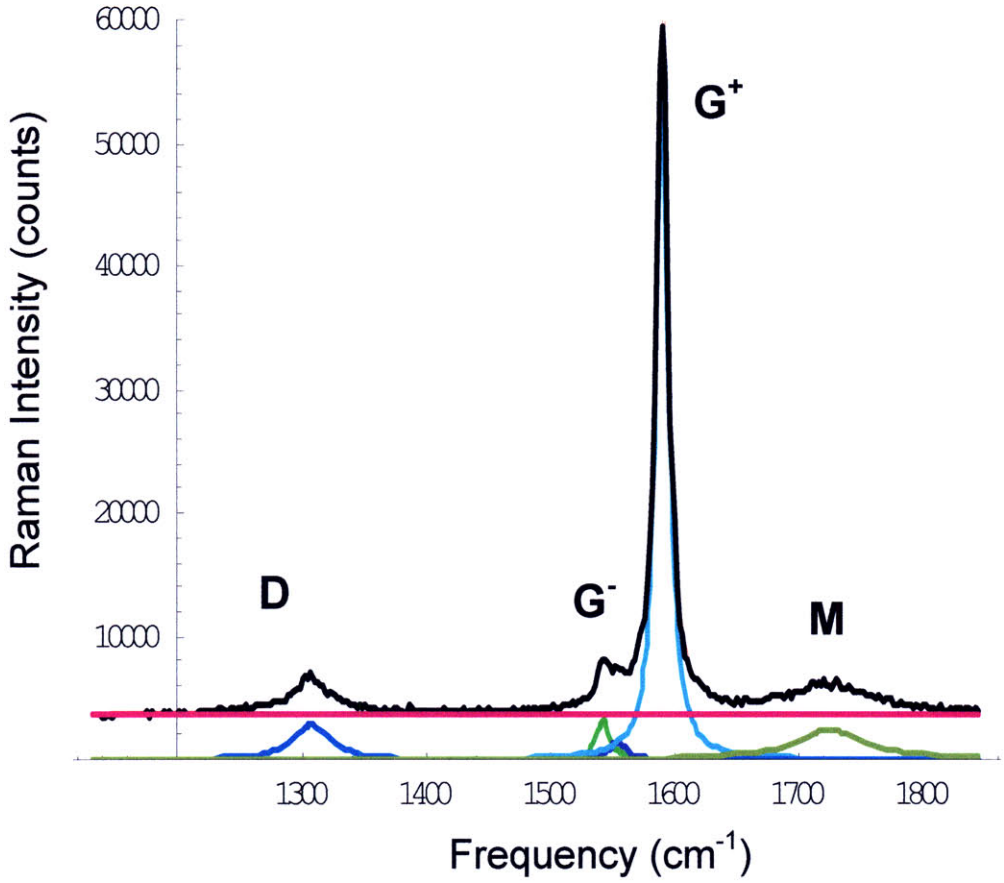

Figure 3-3. Sample peak fitting results showing the individual peaks in the vicinity of the Raman G-band. This Raman spectrum corresponds to semiconducting nanotubes probed with the 647 nm (1.92 eV) laser line. The black curve is the raw data. The individual peaks are shown, as well as a baseline that was determined by the peak fitting procedure. The red curve is the sum of the baseline and the five Lorentzian peaks that comprise the peak fitting model. The average nanotube length in this sample is 50 nm.

In this section (3.2) we provide an overview of the data analysis for the G-band Raman spectra. We extract the parameters of the G-band components from the peak fitting as shown in Fig. 3-3. The parameters for the G^- component are composite parameters, which were calculated from the two peaks (at 1540 cm^{-1} and 1555 cm^{-1}) that comprise the G^- band. Figure 3-4(a) and (b) show the frequency and the full-width half-maximum (FWHM) linewidth of the G^+ and G^- peaks. As mentioned earlier, several spectra were taken on different spots for each sample. The Raman spectra for each of these spots were analyzed, and then the median value over all spots was extracted. Thus,

each data point on these graphs represents the median value over several (about 7) spots on a sample.

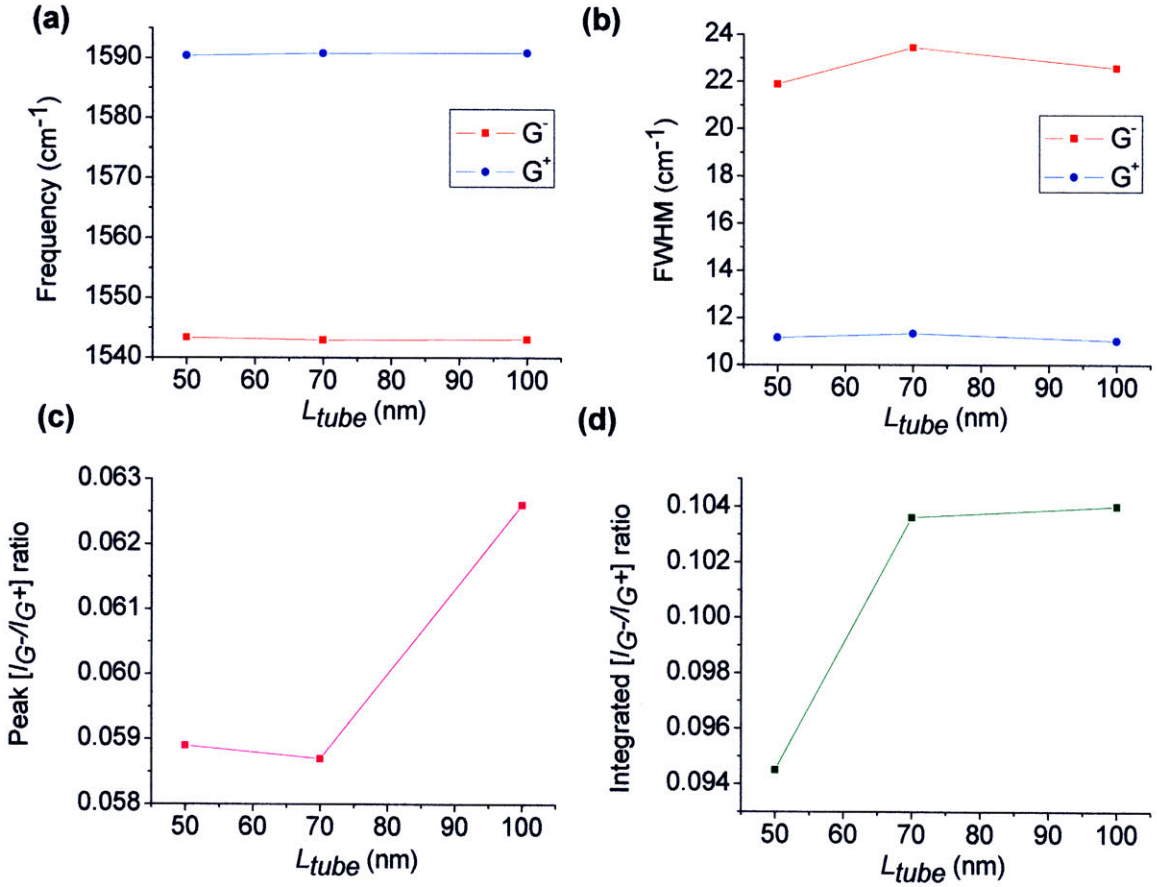

Figure 3-4. Length dependence of 4 parameters of the G-band components, extracted from the peak fitting (the frequency, FWHM width, peak $[I_{G^-}/I_{G^+}]$ ratio, and integrated $[I_{G^-}/I_{G^+}]$ ratio. The parameters for the G^- component were calculated from the two peaks (at 1540 cm^{-1} and 1555 cm^{-1}) that comprise the G^- band. The laser excitation energy is 647 nm (1.92 eV), which excites the (7, 5) semiconducting nanotube. Each point represents the median value taken over several spots on a sample. Plots are given for: **(a)** frequency, **(b)** the FWHM linewidth, **(c)** the G^-/G^+ peak intensity ratio, and **(d)** the integrated $[I_{G^-}/I_{G^+}]$ ratio are shown vs. average nanotube length L_{tube}.

For both the G^+ and G^- peaks of semiconducting nanotubes, no change in the frequency (ω_{G^+} and ω_{G^-}) or FWHM was observed as a function of nanotube length L_{tube}. However the FWHM width of the G^- peak ($(FWHM)_{G^-}$) is approximately twice the width of the G^+ peak ($(FWHM)_{G^+}$). The peak intensity ratio of the G^- peak to the G^+

peak (peak $[\hat{I}_{G^-}/\hat{I}_{G^+}]$) was also examined and the length dependence is shown in Figure 3-4(c). Note that the $[\hat{I}_{G^-}/\hat{I}_{G^+}]$ shown in Figure 3-4(c) considers the peak height, not the integrated intensity. We find that this intensity ratio decreases by about 7% when L_{tube} decreases from 100 nm to 50 nm.

We also examine the integrated intensity ratio between the G^- and the G^+ features. Figure 3-4(d) shows the integrated $[I_{G^-}/I_{G^+}]$ ratio for E_{laser} = 1.92 eV for the different samples. A 9% decrease in the integrated intensity ratio was found when the L_{tube} decreases from 100 nm to 50 nm.

To verify that these trends hold true for semiconducting nanotubes, we also checked the Raman spectra for E_{laser} = 612 nm (2.03 eV). At this E_{laser}, a mixture of semiconducting and metallic nanotubes were excited (Table 2-1). However, the observed G-band for this E_{laser} (Figure 3-5) has a low intensity G^- component, which is characteristic of semiconducting nanotubes. For E_{laser} = 612 nm (2.03 eV), the G-band frequencies show no appreciable change with length. However, both the peak and integrated $[I_{G^-}/I_{G^+}]$ ratios increase (by ~18% and 122%, respectively) as L_{tube} decreases. These discrepancies with the E_{laser} = 647 nm (1.92 eV) results could be due to metallic nanotubes also being excited at E_{laser} = 612 nm (2.03 eV). The length dependence of the G-band for metallic nanotubes will be discussed in the next section.

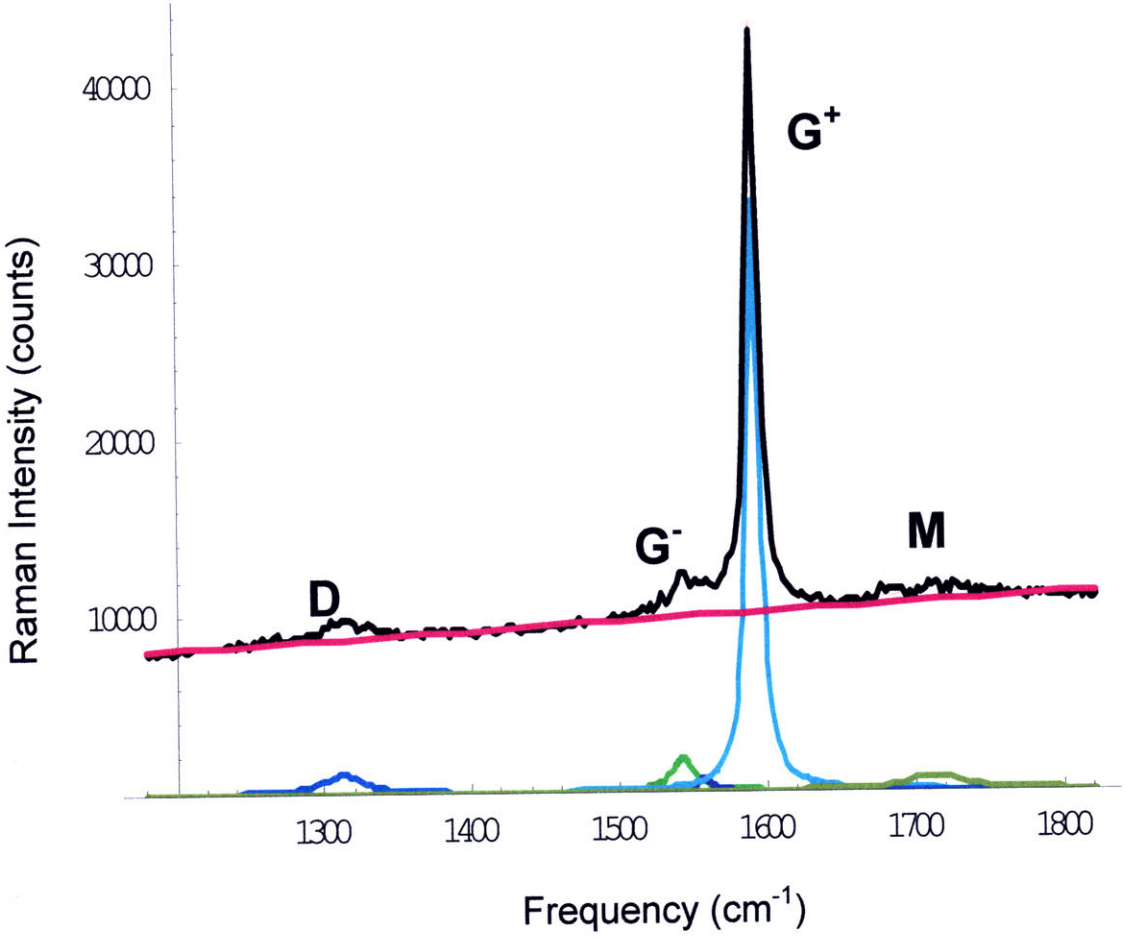

Figure 3-5. A representative G-band Raman spectrum for E_{laser} = 612 nm (2.03 eV). The nanotube length in this case is 100 nm. A small contribution from metallic tubes is expected for this E_{laser}, but the contribution is mainly from nanotubes with a small chiral angle for which the G^- intensity is expected to be weak.

3.3 Metallic Nanotubes

3.3.1 Overview and Comparison to Semiconducting Nanotubes

We examine the length dependence of nanotubes for E_{laser} = 488 nm = 2.54 eV, since this laser line is expected to most likely excite the (8, 5) metallic nanotube (Table 2-1). Figure 3-6 shows representative Raman spectra at this E_{laser} for different lengths of nanotubes. Analysis of the G-band lineshape exhibits a sharp peak around 1592 cm^{-1}, a broad, asymmetric peak around 1530 cm^{-1}, as well as a peak around 1570 cm^{-1} as shown in Figure 2-11. The appearance of a sharp peak at 1592 cm^{-1} and a broad, asymmetric

peak at a lower frequency is consistent with previous measurements on metallic nanotubes [2, 3]. The peak at 1570 cm^{-1} could not be resolved for all of the spectra; therefore we shall restrict our analysis to the asymmetric peak at 1530 cm^{-1} (henceforth referred to simply as G^-) and the sharp peak at 1592 cm^{-1} (the G^+ peak). The intensity and lineshape of the G^- peak was found to vary from spot to spot on a given sample, indicative of different (*n, m*) nanotubes in resonance with a given laser line for different spots on the samples with tubes of different lengths.

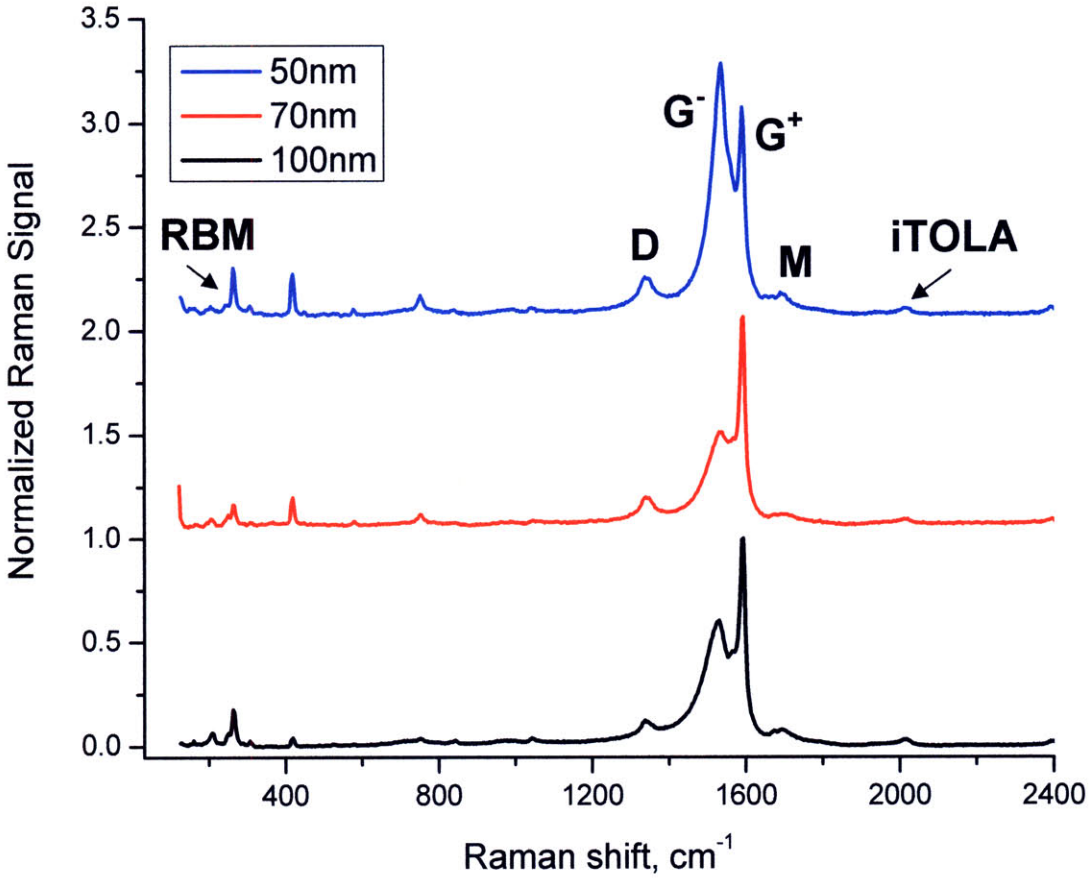

Figure 3-6. Representative Raman spectra for metallic nanotubes excited with E_{laser} = 488 nm = 2.54 eV. Spectra for nanotubes with average lengths of 50, 70, and 100 nm are shown. Baselines were subtracted, and then the spectra were normalized to the G^+ peak at 1592 cm^{-1} and offset from one another for readability. The known Raman features are labeled. Other peaks that are not commonly known will be discussed in a later chapter.

Peak fitting was performed on the raw data, in the vicinity of the G-band. The D-band was included in the fitting procedure in order to separate its effects from any asymmetry inherent to the G-band. All of the peaks were fitted with Lorentzians except for the peak around 1530 cm^{-1}, which was fit with the asymmetric Breit-Wigner-Fano (BWF) lineshape,

$$I(\omega) = I_o \frac{[1+(\omega-\omega_o)/(q\Gamma)]^2}{1+[(\omega-\omega_o)/\Gamma]^2} \qquad (3.1),$$

where I_o is the peak intensity, ω_o is the center frequency, Γ is the full width at half-maximum (FWHM) intensity, and $1/q$ is a parameter that indicates the degree of asymmetry of the lineshape. Figure 3-7 shows example plots of the BWF lineshape. When 1/q is positive, a tail occurs on the higher frequency side of the peak. When 1/q is negative, the tail is on the lower frequency side. When $1/q$ = 0, the BWF lineshape reduces to a Lorentzian. In carbon nanotubes, the $1/q$ parameter is a measure of the coupling between the phonon and the continuum [2].

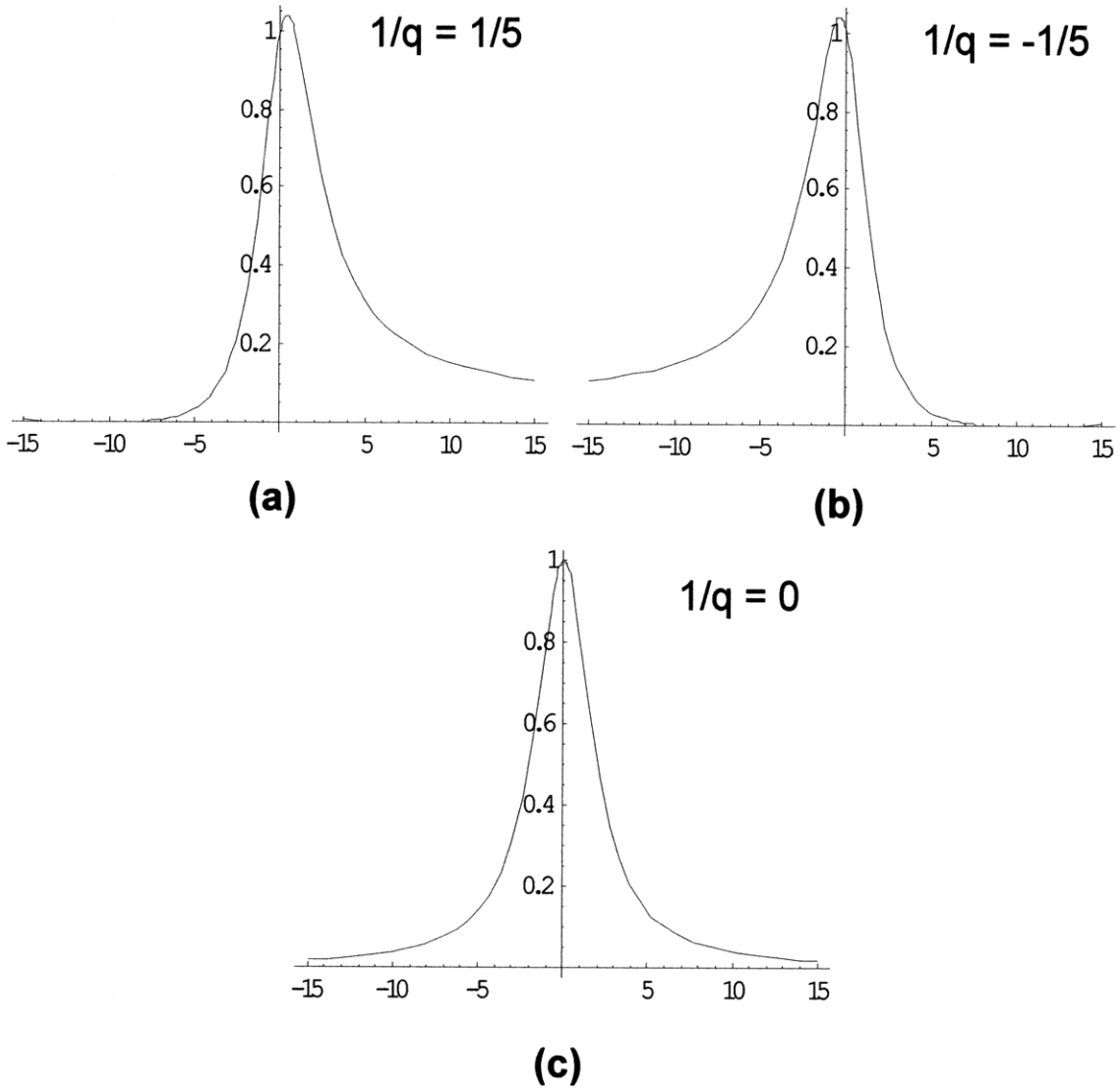

Figure 3-7. Example plots of the Breit-Wigner-Fano lineshape with different values of the asymmetry parameter $1/q$: (a) $1/q$ = 1/5, (b) $1/q$ = -1/5, and (c) $1/q$ = 0. For all three curves, I_o = 1, ω_o = 0, and Γ = 2.

Figure 3-8 shows a sample peak fitting result for a metallic nanotube. From the peak fitting, we extract the intensities, frequencies and linewidths of the G^+ and G^- peaks. For the G^- peak, we also examine the asymmetry parameter $[1/q]_{G^-}$. To account for sample inhomogeneities, we consider the median values among different (about 7) spots on a sample. A synopsis of the length dependence of the G-band parameters for metallic nanotubes is shown in Figure 3-9, alongside the results for semiconducting nanotubes. Since metallic nanotubes have a more complex length dependence than semiconducting

nanotubes, as shown below, we will examine the Raman spectra of metallic nanotubes in more detail.

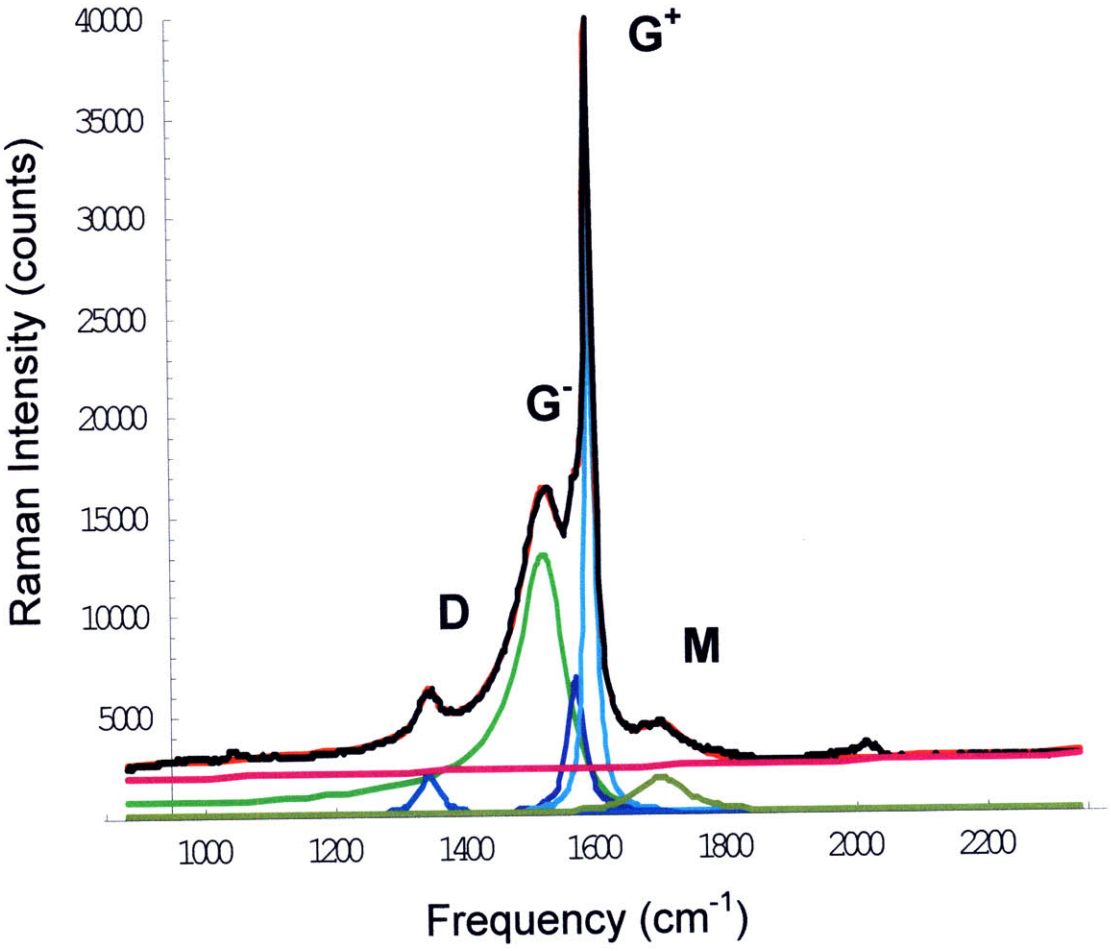

Figure 3-8. Sample peak fitting results showing the individual peaks in the vicinity of the Raman G-band. This Raman spectrum corresponds to metallic nanotubes probed with the 488 nm (2.54 eV) laser line. The black curve is the raw data. The individual peaks are shown, as well as a baseline that was determined by the peak fitting procedure. The red curve is the sum of the baseline and the peaks found from peak fitting. The average nanotube length in this case is 100 nm.

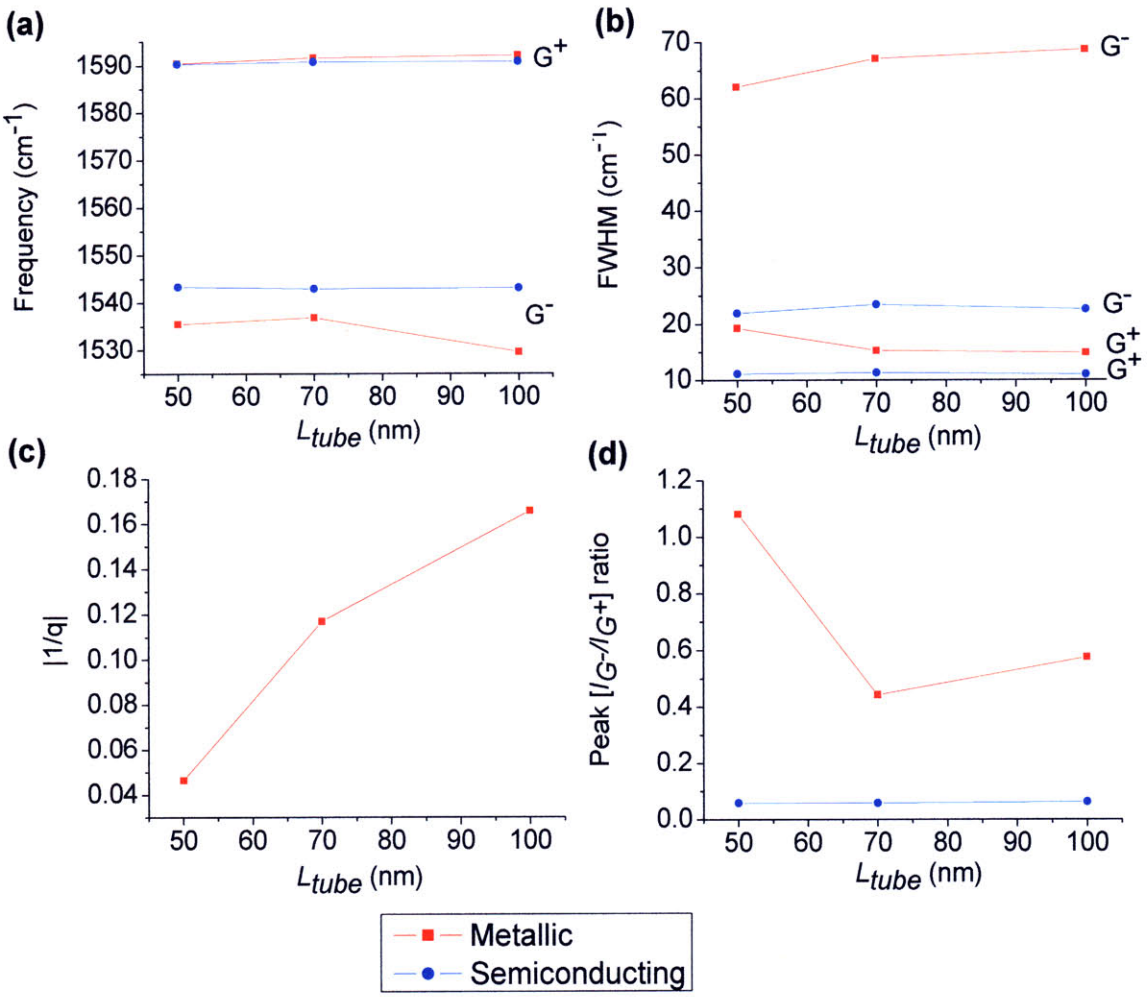

Figure 3-9. Length dependence of the individual G-band components, extracted from the peak fitting. The red curves correspond to metallic nanotubes excited with the 488 nm (2.54 eV) laser line, and the blue curves correspond to semiconducting nanotubes excited at 647 nm (1.92 eV). Each point represents the median value taken over several spots on a sample. The **(a)** frequency, **(b)** the FWHM linewidth, **(c)** the magnitude of the BWF coupling factor $[1/q]_{G^-}$, and **(d)** the peak $[\hat{I}_{G^-}/\hat{I}_{G^+}]$ ratio are shown vs. average nanotube length L_{tube}.

For the G^+ peak, the median frequency (ω_{G^+}) decreases by a small amount overall, from 1592 cm^{-1} to 1590 cm^{-1}, as the nanotube length decreases from 100 nm to 50 nm. The magnitude of the G^+ frequency for metallic tubes resonant at 2.54 eV is similar to that for the semiconducting tubes resonant at 1.92 eV for all tube lengths. The median $(FWHM)_{G^+}$ shows a modest increase from about 15 cm^{-1} to 19 cm^{-1}, as the

nanotube length drops from 100 nm to 50 nm. The magnitude of $(FWHM)_{G^+}$ for the metallic tubes is about 3 times larger than for the semiconducting tubes.

The length dependence of the median G^- frequency (ω_{G^-}) for the metallic tubes is small and unclear, meaning that the dependence on length is comparable to the signal-to-noise. The median ω_{G^-} for the metallic tubes increases from 1530 cm^{-1} (100 nm tube) to 1537 cm^{-1} (70 nm tube), then shows a negligible decrease to 1536 cm^{-1} (50 nm tube). The $(FWHM)_{G^-}$, which was evaluated from Equation 3.1, decreases from about 69 cm^{-1} to 62 cm^{-1}, as L_{tube} decreases from 100 nm to 50 nm, and this effect is well beyond signal-to-noise uncertainties. The very much larger $(FWHM)_{G^-}$ (by a factor of 3) for metallic tubes as compared to semiconducting tubes is also noteworthy. In addition, we find that the lineshape becomes more Lorentzian as the nanotube length decreases. The asymmetry parameter $[1/q]_{G^-}$ is always negative, regardless of the nanotube length. The negative $[1/q]_{G^-}$ indicates that the phonon coupling is to a continuum of lower frequency states [4]. The magnitude of the asymmetry parameter $[1/q]_{G^-}$ is 0.17 for 100 nm nanotubes, 0.12 for 70 nm nanotubes, and 0.05 for 50 nm nanotubes, and the dependence of $[1/q]_{G^-}$ on L_{tube} is a large effect for metallic nanotubes.

For this E_{laser} (2.54 eV), we find that the median peak $[\hat{I}_{G^-}/\hat{I}_{G^+}]$ ratio dips from 0.57 to 0.44 as the nanotube length decreases from 100 nm to 70 nm. However, the peak $[\hat{I}_{G^-}/\hat{I}_{G^+}]$ ratio *increases* as L_{tube} changes from 70 nm to 50 nm, and the 50 nm nanotubes have the highest peak $[\hat{I}_{G^-}/\hat{I}_{G^+}]$ ratio at 1.1. Hence, in some cases, the G^- peak height for the 50 nm long SWNTs can be higher than that of the G^+ peak.

3.3.2 Length Dependence When a Mixture of Semiconducting and Metallic Nanotubes are Present

To check if the above trends hold true for metallic nanotubes in general, we examine the G-band length dependence for E_{laser} = 465.8 nm (2.66 eV). A mixture of metallic and semiconducting nanotubes is resonant at this laser line (Table 2-1). However, the broad and asymmetric G^- peak observed at E_{laser} = 2.66 eV (Figure 3-10) indicates that metallic nanotubes dominantly contribute to the Raman G-band spectra.

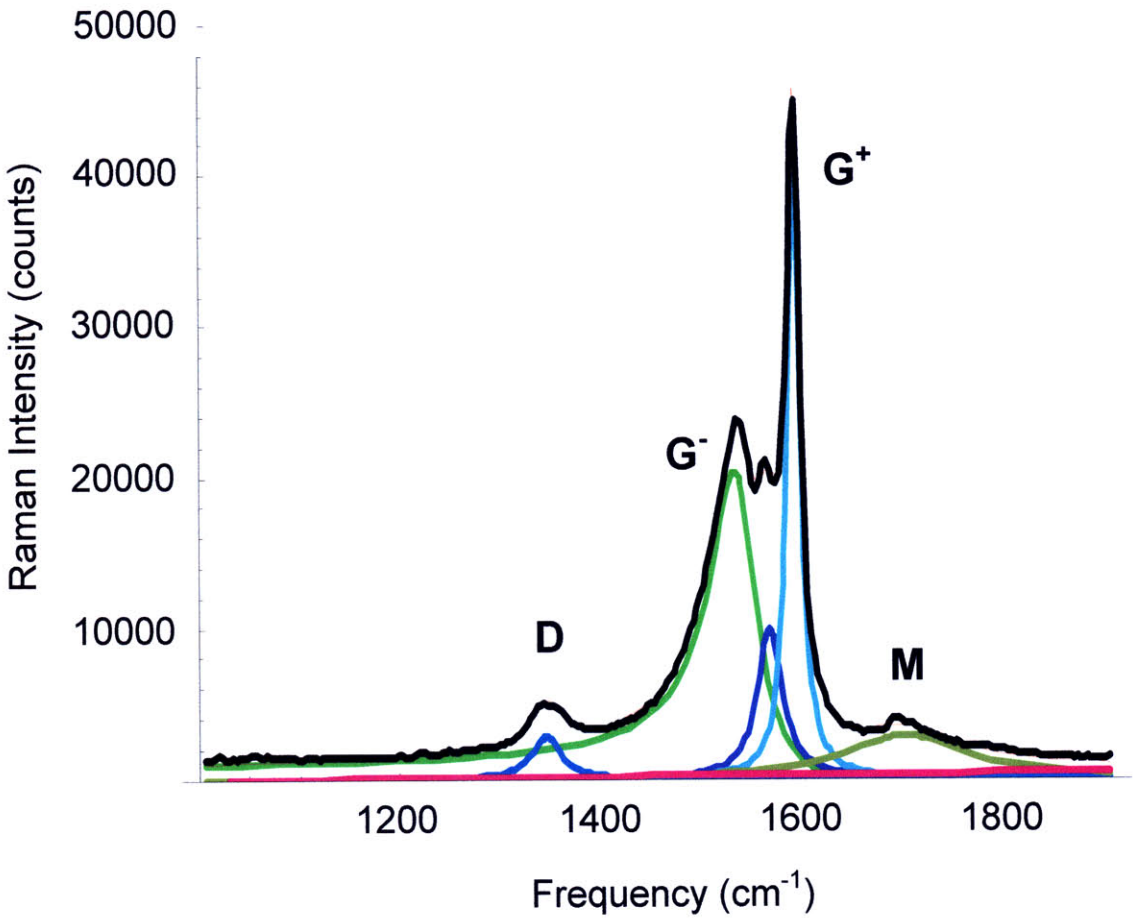

Figure 3-10. Sample peak fitting results showing the individual peaks in the vicinity of the Raman G-band. This Raman spectrum corresponds to metallic nanotubes probed with the 465.8 nm (2.66 eV) laser line. The black curve is the raw data. The individual peaks are shown, as well as a baseline that was determined by the peak fitting procedure. The red curve is the sum of the baseline and the peaks found from peak fitting. The average nanotube length in this case is 100 nm.

The length dependence of the G-band components for E_{laser} = 2.66 eV is shown in Figure 3-11, along with the results for E_{laser} = 2.54 eV. Although the FWHM and peak $[\hat{I}_{G^-} / \hat{I}_{G^+}]$ ratio length-dependent behavior are similar for the two laser lines, the general trends for the G-band frequencies and asymmetry parameter $[1/q]_{G^-}$ are less clear. The discrepancies in the length-dependent behavior for different laser lines may be due to the variation in the Raman spectra observed in different spots within the same sample, and we investigate this effect below in detail.

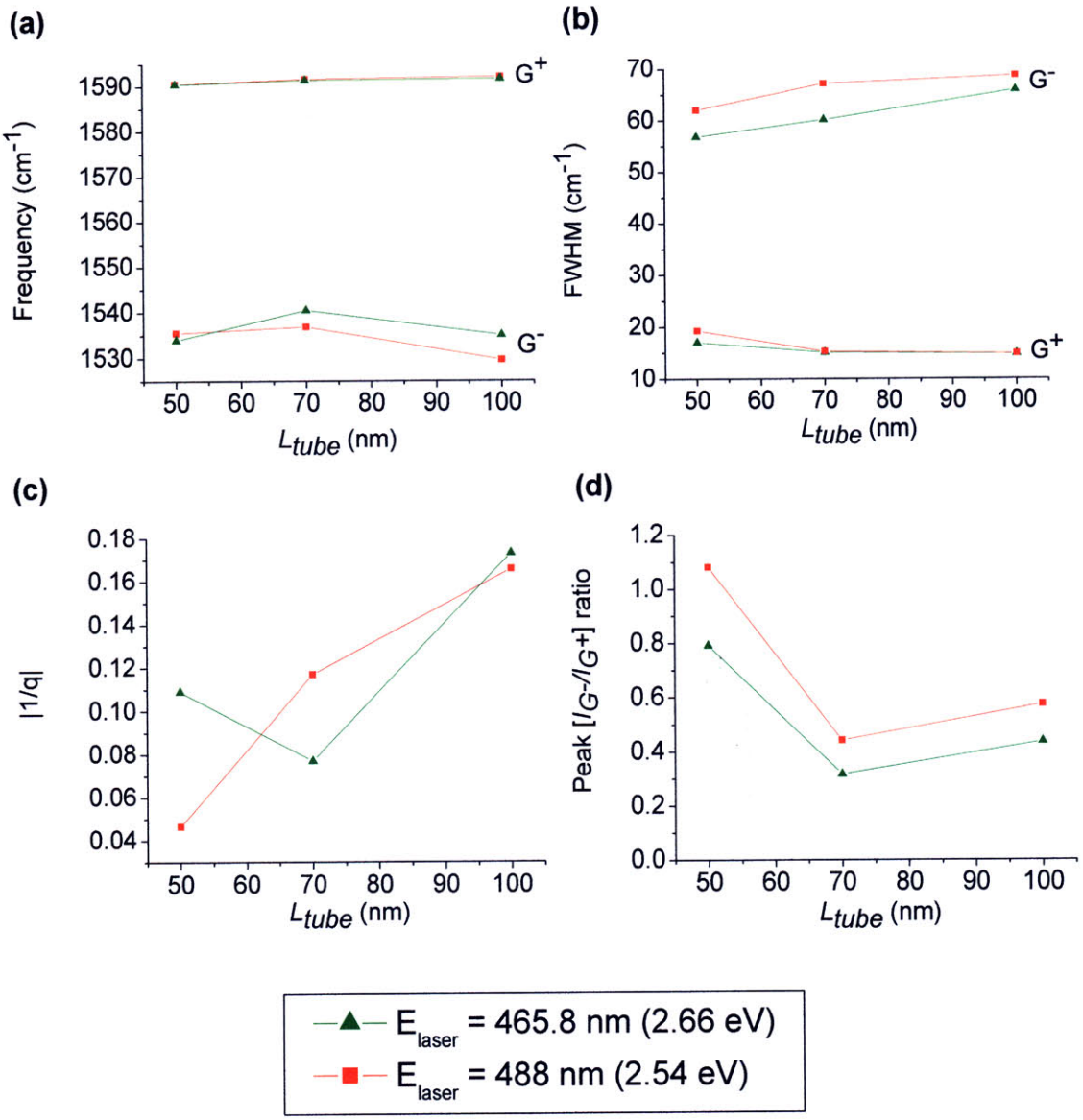

Figure 3-11. The G-band length dependence for two laser lines that excite metallic nanotubes. The red curves correspond to nanotubes excited with the 488 nm (2.54 eV) laser line, and the green curves correspond to nanotubes excited at 465.8 nm (2.66 eV). Each point represents the median value taken over several spots on a sample. The **(a)** frequency, **(b)** the FWHM linewidth, **(c)** the magnitude of the asymmetry parameter $[1/q]_{G^-}$, and **(d)** the peak $[\hat{I}_{G^-}/\hat{I}_{G^+}]$ ratio are shown vs. L_{tube}.

3.3.3 Spot-to-Spot Variation

Thus far we have seen that for metallic nanotubes, certain G-band parameters have a clear length dependence, while others are ambiguous. Figure 3-11(b) shows that for metallic nanotubes, the FWHM of the G^+ and G^- peaks have a clear length dependence. Specifically, the G^- lineshape narrows as the nanotube length decreases, while the G^+ lineshape broadens as the nanotube length decreases. According to Figure 3-11(a), the G^+ frequency ω_{G^+} is constant with nanotube length for metallic nanotubes. The G^- frequency ω_{G^-} likely increases as the length decreases, but the exact length dependence is unclear. Figure 3-11(c) suggests that overall, the magnitude of the $[1/q]_{G^-}$ asymmetry parameter decreases as the nanotube length decreases. Again, this trend is dubious because the 2.66 eV and 2.54 eV curves shown have different length-dependent behaviors. Finally, Figure 2-14(d) suggests that the G^-/G^+ peak intensity ratio increases as the nanotube length decreases. However, the peak $[\hat{I}_{G^-}/\hat{I}_{G^+}]$ ratio does not increase steadily with decreasing length.

The inconsistencies in the G-band length dependence for metallic nanotubes is likely due to the variation in the Raman spectra observed at different spots on the same sample. Figures 3-12(a) – (c) shows the Raman spectra taken at E_{laser} = 476.5 nm (2.60 eV), for different spots on each of the length-sorted samples. It is evident from these figures that the G-band lineshape varies widely from spot to spot on the same sample.

The degree of spot-to-spot variation in the Raman spectra depends on the laser excitation energy. The Raman spectra at different spots for E_{laser} = 457.9 nm (2.71 eV) are shown in Figures 3-13(a) – (c). At this E_{laser}, the spectra appear fairly uniform across the spots probed.

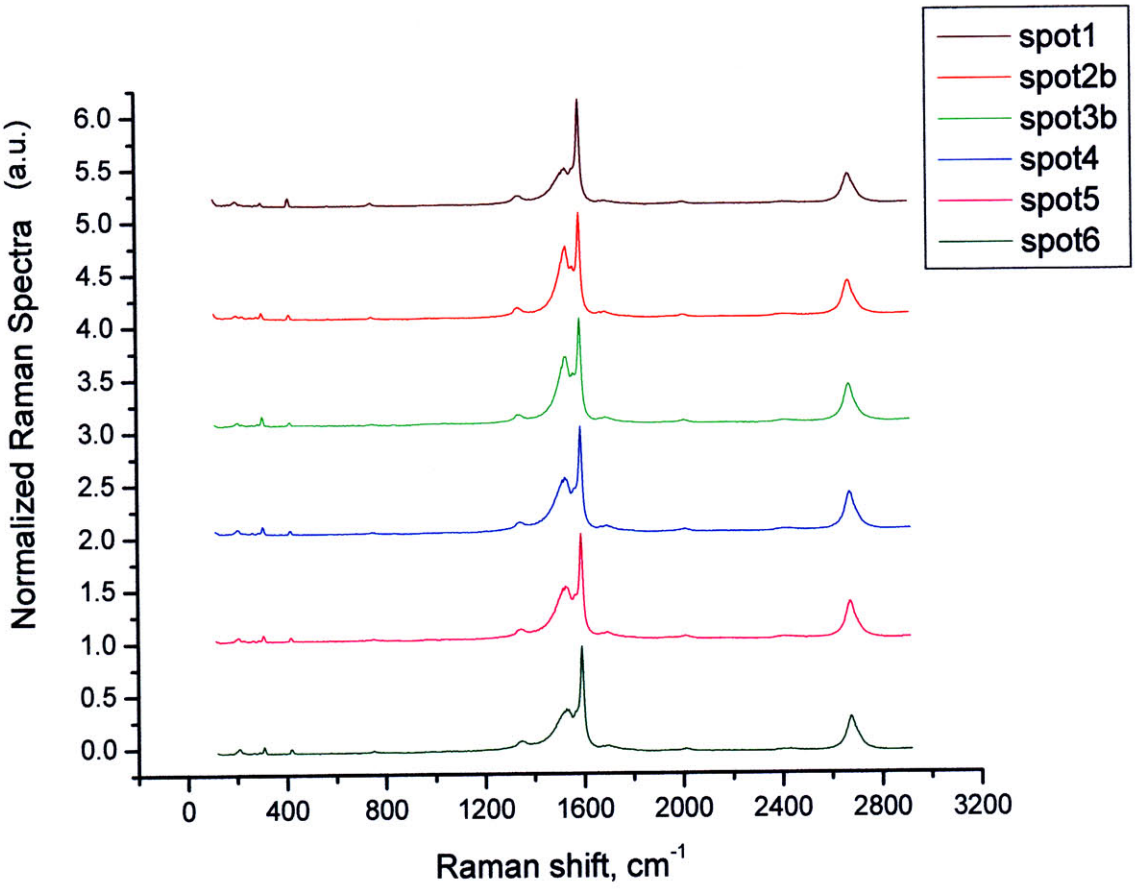

Figure 3-12(a). Raman spectra for metallic nanotubes, for different spots on a sample. The laser excitation energy is 476.5 nm (2.60 eV) and the average nanotube length is 100 nm. After a baseline was subtracted, the spectra were normalized to the G^+ peak and offset from each other.

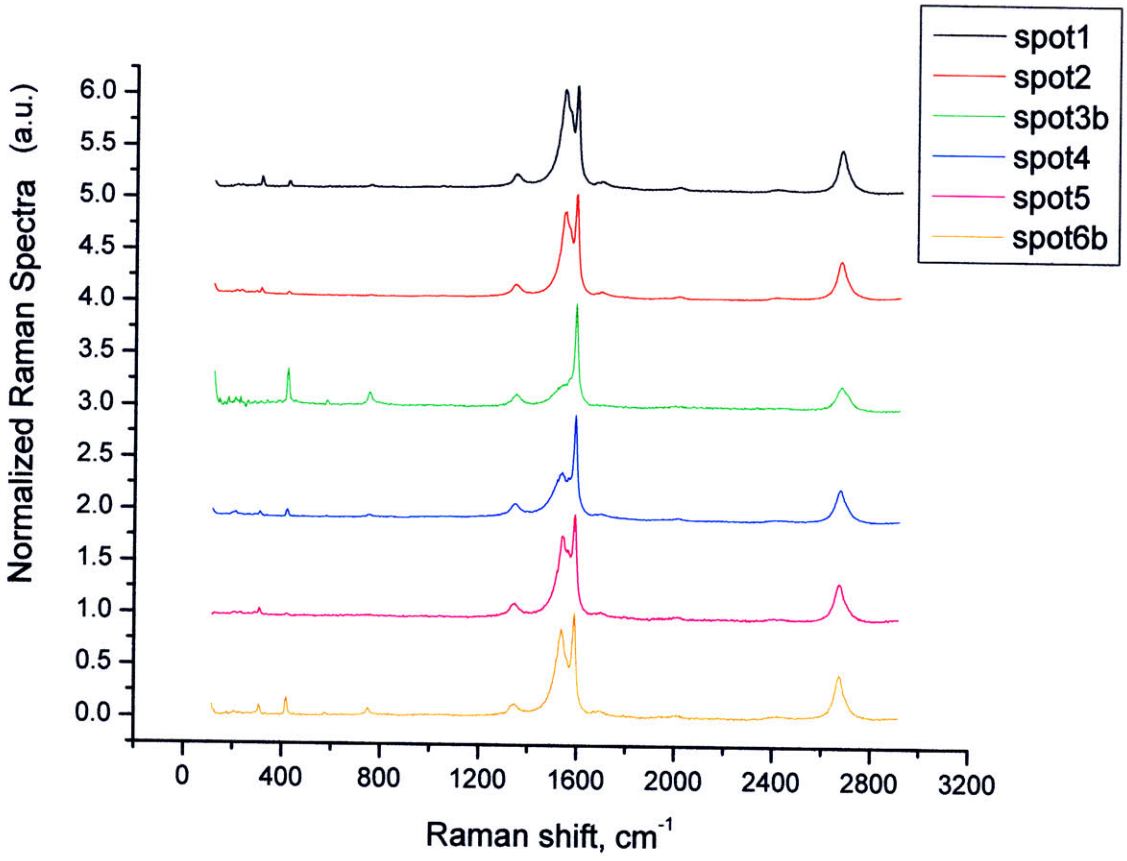

Figure 3-12(b). Same as Figure 3-12(a), but for nanotubes with average length of 70 nm.

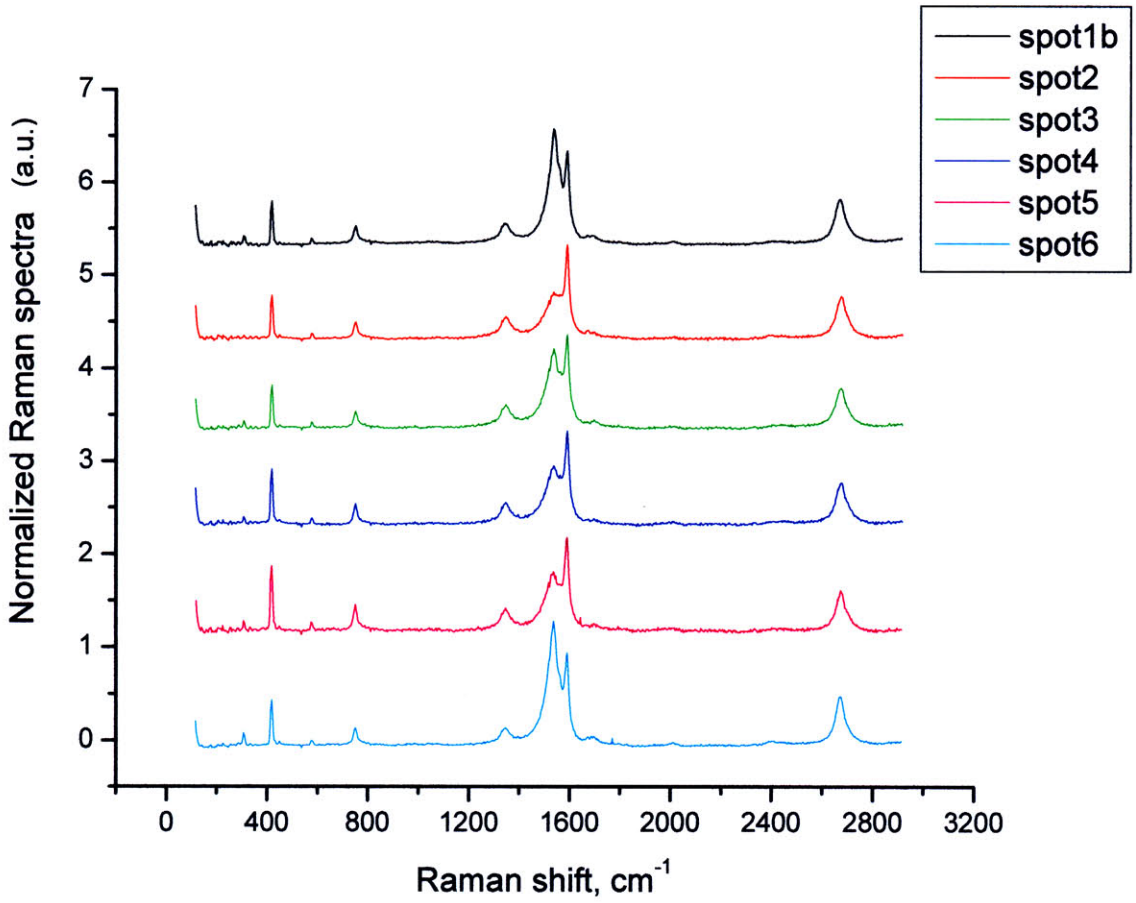

Figure 3-12(c). Same as Figure 3-12(a), but for nanotubes with average length of 50 nm.

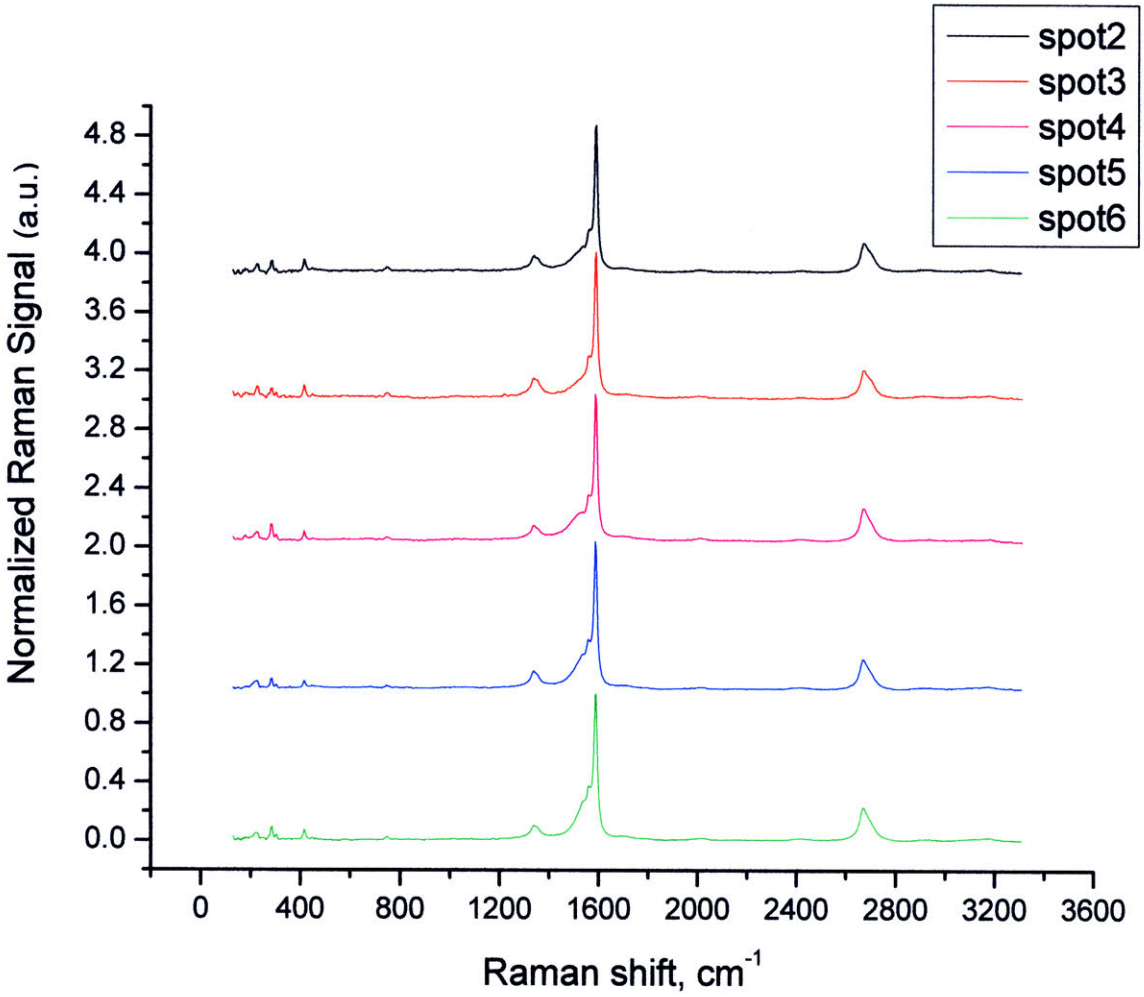

Figure 3-13(a). Raman spectra for metallic nanotubes, for different spots on a sample. The laser excitation energy is 457.9 nm (2.71 eV) and the average nanotube length is 100 nm. After a baseline was subtracted, the spectra were normalized to the G^+ peak and offset from each other.

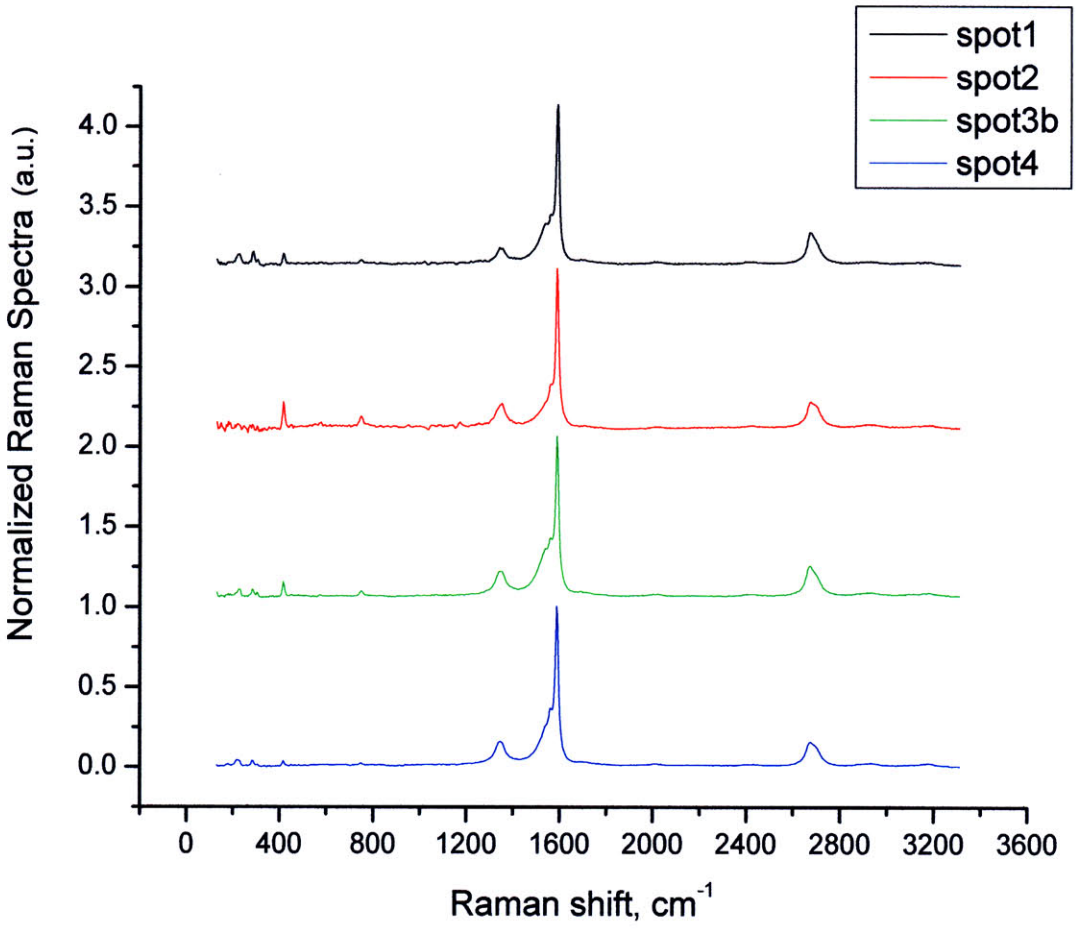

Figure 3-13(b). Same as Figure 3-13(a), but for nanotubes with average length of 70 nm.

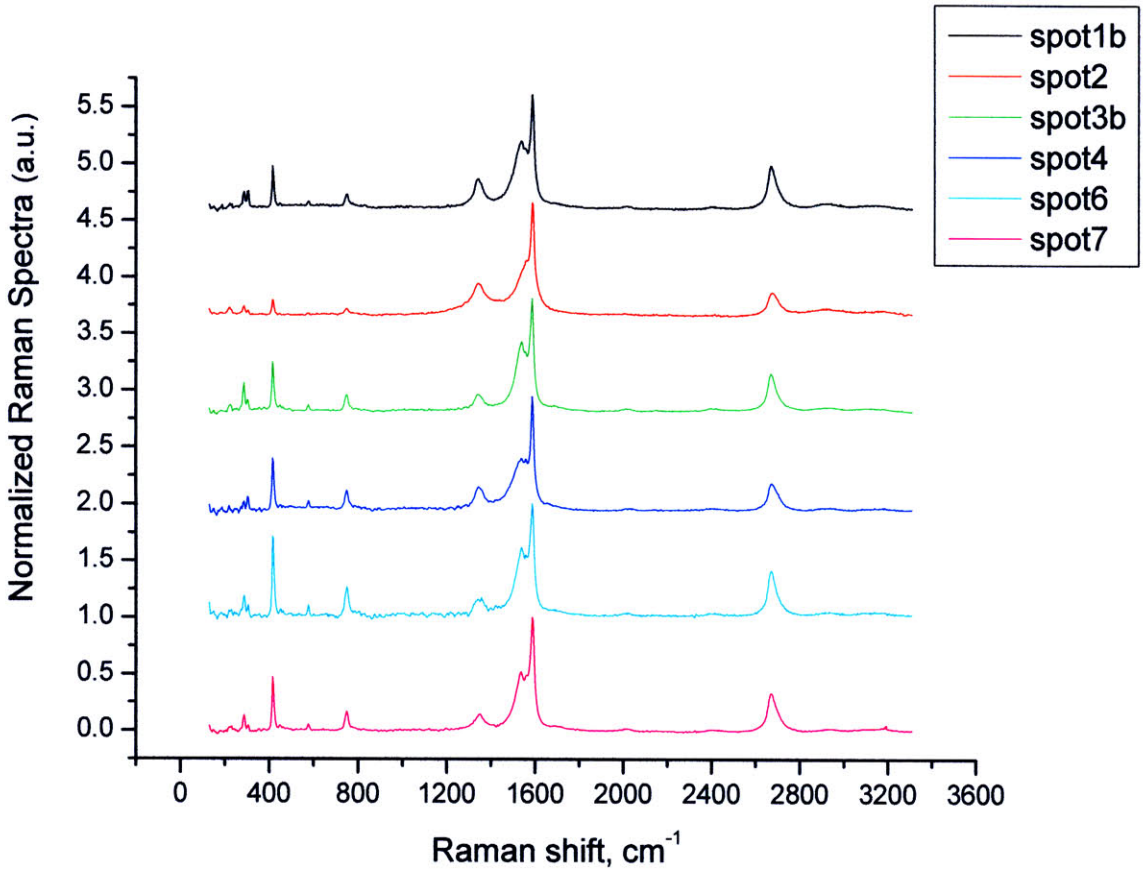

Figure 3-13(c). Same as Figure 3-13(a), but for nanotubes with average length of 50 nm.

It is useful to identify which values of E_{laser} give uniform Raman spectra for different spots on the same sample. We here use the standard deviation of the peak $[\hat{I}_{G^-} / \hat{I}_{G^+}]$ ratio, taken among several spots on a sample, as a measure of the sample inhomogeneity. Figures 3-14(a) and (b) show the peak $[\hat{I}_{G^-} / \hat{I}_{G^+}]$ standard deviation as a function of E_{laser}, for the different lengths of nanotubes. From Figure 3-14(a), we find that semiconducting nanotubes excited at E_{laser} = 1.92 eV show negligible variation in the Raman spectra, for different spots on a sample. The laser excitation energies that excite metallic nanotubes, however, result in greater spot-to-spot variation in the Raman spectra. Figure 3-14(b) shows that in general, the shortest nanotubes (50 nm) show the greatest spot-to-spot variation. Unusually high spot-to-spot variation can be seen for 50 nm long nanotubes excited by E_{laser} = 2.41 eV (514 nm) and 100 nm long nanotubes excited by

E_{laser} = 2.47 eV (501.7 nm). Figure 3-14(b) roughly suggests that the sample inhomogeneity has peaks at E_{laser} = 2.41 eV and E_{laser} = 2.60 eV. For E_{laser} higher than 2.60 eV, the spot-to-spot variation shows a decline, and the most uniform spot-to-spot behavior for metallic nanotubes is seen at 2.71 eV. The inhomogeneity in the Raman spectra could arise because multiple (*n, m*) nanotubes are excited by the same laser line. According to Table 2-1, there are 5 different (*n, m*) nanotubes resonant at either E_{laser} = 2.41 eV or E_{laser} = 2.60 eV. At E_{laser} = 2.71 eV, three (*n, m*) nanotubes are resonant; the minimized spot-to-spot variation in the spectra at this E_{laser} may be due to the fewer number of resonant nanotubes in this case.

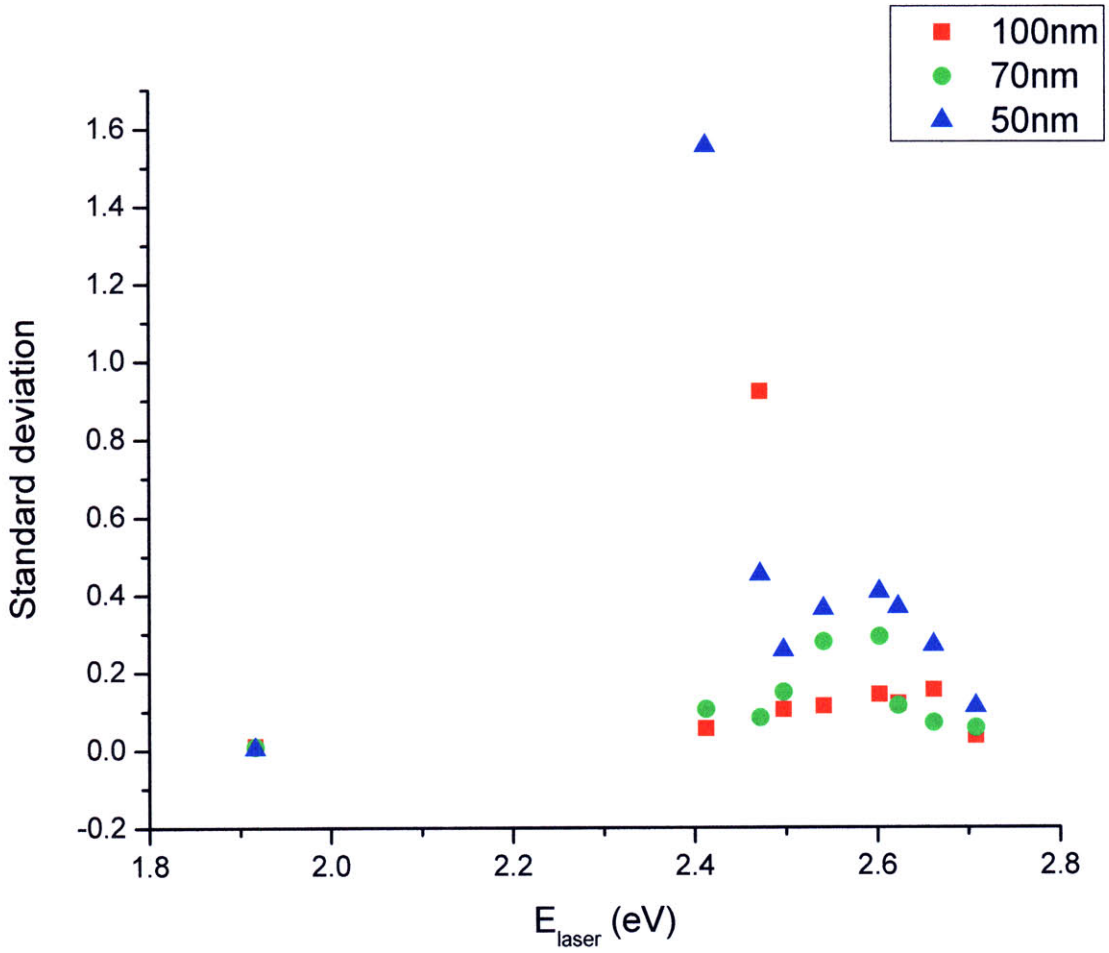

Figure 3-14(a). The standard deviation of the peak $[\hat{I}_{G^-} / \hat{I}_{G^+}]$ ratio across multiple spots on a sample. This is a measure of the spot-to-spot variation in the Raman spectra of a given sample.

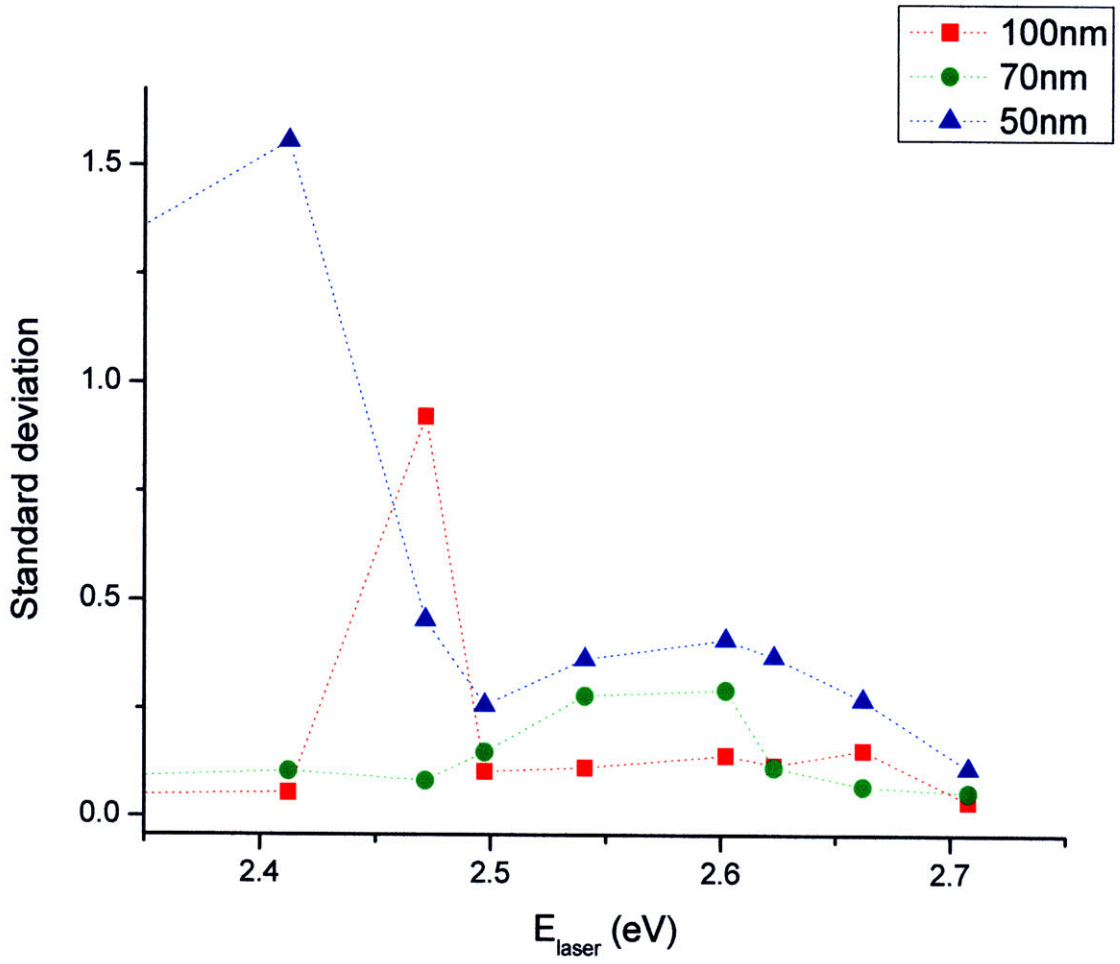

Figure 3-14(b). The standard deviation of the peak $[\hat{I}_{G^-} / \hat{I}_{G^+}]$ ratio across multiple spots on a sample. This figure is the same as Figure 3-14(a), but zoomed in to show the spot-to-spot variation for metallic nanotubes (E_{laser} = 2.41 to 2.71 eV).

3.3.4 Trends for an E_{laser} for Which the Spot-to-Spot Variation is Low

As discussed above, the G-band spot-to-spot variation in the Raman spectra is lowest for spectra taken with E_{laser} = 457.9 nm (2.71 eV). The resonant nanotubes at this excitation energy are the (11, 4) semiconducting tube and the (6, 6) and (7, 4) metallic tubes (Table 2-1). The G-band lineshape for spectra measured with E_{laser} = 2.71 eV shows the broad G^- peak that is typical of metallic nanotubes. Therefore the data for E_{laser} = 2.71 eV is expected to give the most reliable picture of the length dependence of the G-band in metallic nanotubes.

Figure 3-15 summarizes the length dependence of the individual G-band parameters found from the peak fitting, for E_{laser} = 2.71 eV. As before, the median values among several spots on each sample are shown in Figure 3-15.

The $(FWHM)_{G^+}$ linewidth increases from about 14 cm^{-1} to 16 cm^{-1}, and the $(FWHM)_{G^-}$ linewidth decreases from 75 cm^{-1} to 60 cm^{-1}, as the nanotube length decreases from 100 nm to 50 nm (Figure 3-15(a)). The magnitude of the asymmetry parameter $[1/q]_{G^-}$ decreases as the nanotube length decreases, as shown in Figure 3-15(b), indicating a change to a more Lorentzian lineshape. The $[1/q]_{G^-}$ magnitude decreases by a factor of 4 over this length interval. The G^+ frequency ω_{G^+} remains about the same, but the G^- frequency ω_{G^-} increases with decreasing tube length, as shown in Figure 3-15(c), indicating a decrease of ~15% in $(\omega_{G^+} - \omega_{G^-})$ over this range in tube length. Figure 3-15(d) shows $(\omega_{G^+} - \omega_{G^-})$ vs. L_{tube}. As the L_{tube} decreases, $(\omega_{G^+} - \omega_{G^-})$ decreases, and the G^- peak moves closer to the G^+ peak. Figures 3-15(e) and (f) show the peak $[\hat{I}_{G^-} / \hat{I}_{G^+}]$ ratio and the integrated $[I_{G^-} / I_{G^+}]$ ratio, respectively, as a function of L_{tube}. As L_{tube} decreases, both the peak and the integrated $[I_{G^-} / I_{G^+}]$ ratios were found to increase, with the peak intensity increasing by a factor of 3.7 and the integrated intensity by only a factor of 2.5, reflecting the decrease in linewidth with decreasing tube length.

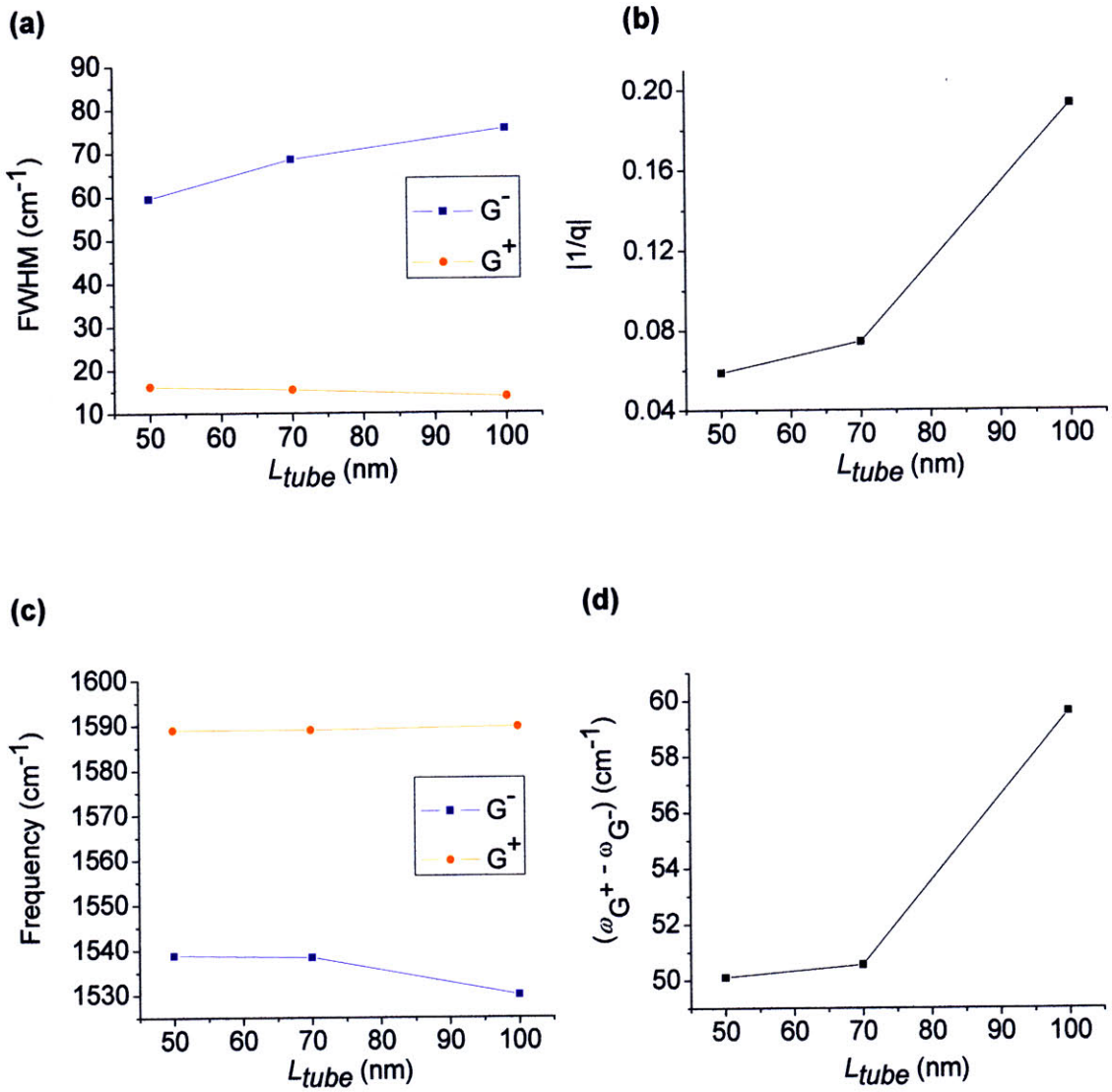

Figures 3-15(a) – (d). Length dependence of the individual G-band parameters for E_{laser} = 457.9 nm (2.71 eV). Each point represents the median value taken over several spots on a sample. The **(a)** FWHM linewidth, **(b)** magnitude of the asymmetry parameter $[1/q]_{G^-}$, **(c)** G-band frequencies ω_{G^+} and ω_{G^-}, **(d)** frequency difference $(\omega_{G^+} - \omega_{G^-})$ are shown.

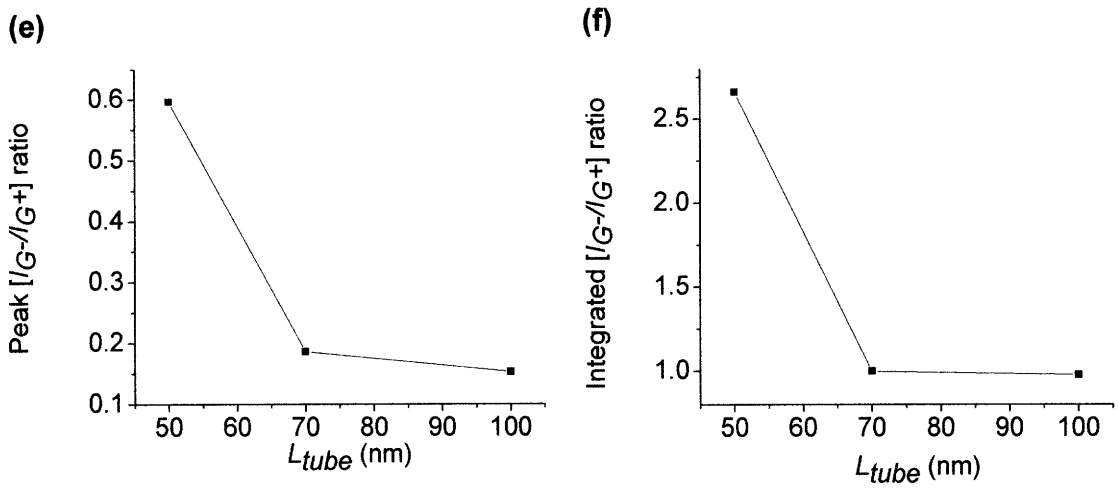

Figures 3-15(e) – (f). Length dependence of the individual G-band parameters for E_{laser} = 457.9 nm (2.71 eV). Each point represents the median value taken over several spots on a sample. The **(e)** peak $[\hat{I}_{G^-}/\hat{I}_{G^+}]$ ratio, and **(f)** integrated $[I_{G^-}/I_{G^+}]$ ratio are shown vs. average nanotube length L_{tube} are shown.

3.3.5 Results for General E_{laser}

In the previous section we examined the length-dependent G-band behavior for metallic nanotubes excited with the E_{laser} = 457.9 nm (2.71 eV) laser line. Because the Raman spectra at E_{laser} = 2.71 eV shows low spot-to-spot variation, studying the Raman spectra for this laser line may give us the clearest picture of the length dependence in the Raman G-band of metallic nanotubes. However, only considering E_{laser} = 2.71 eV may not give the complete story. For example, there may be length-dependent effects that are influenced by nanotube chirality, and restricting our study to one laser line would neglect the probing for any chirality-dependent effects. Therefore it is also important to examine the Raman spectra for other laser lines, despite the noise introduced by the observed spot-to-spot variation.

Thus far we have considered only the median values (among different spots on a sample) of the G-band parameters obtained from peak fitting. Because of the large spot-to-spot variation that is observed, it may be more appropriate to consider each Raman spectrum individually, for each E_{laser}, sample, and for each spot probed.

When every spectrum is considered, an analysis of the results can appear daunting. For example, on Figure 3-16 the linewidth $(FWHM)_{G^-}$ is plotted against nanotube length. Each point on Figure 3-16 represents the peak fitting result from one Raman spectrum, corresponding to a specific E_{laser}, to a specific sample (nanotube length), and to a specific spot on that sample. Note that in this section we only consider the E_{laser} for which a characteristic "metallic" G-band (meaning G^- has an asymmetric BWF lineshape) was observed. There are however many laser lines at which the Raman spectra for metallic tubes can be observed, including E_{laser} = 514 nm (2.41 eV), 501.7 nm (2.47 eV), 496.5 nm (2.50 eV), 488 nm (2.54 eV), 476.5 nm (2.60 eV), 472.7 nm (2.62 eV), 465.8 nm (2.66 eV), and 457.9 nm (2.71 eV). It is evident from Figure 3-16 that, when all the data are considered, there is a large spread in the observed G^- FWHM, which ranges from 40 cm^{-1} to over 90 cm^{-1}. How to draw meaningful conclusions from data that can have a wide variance is the subject of the next section.

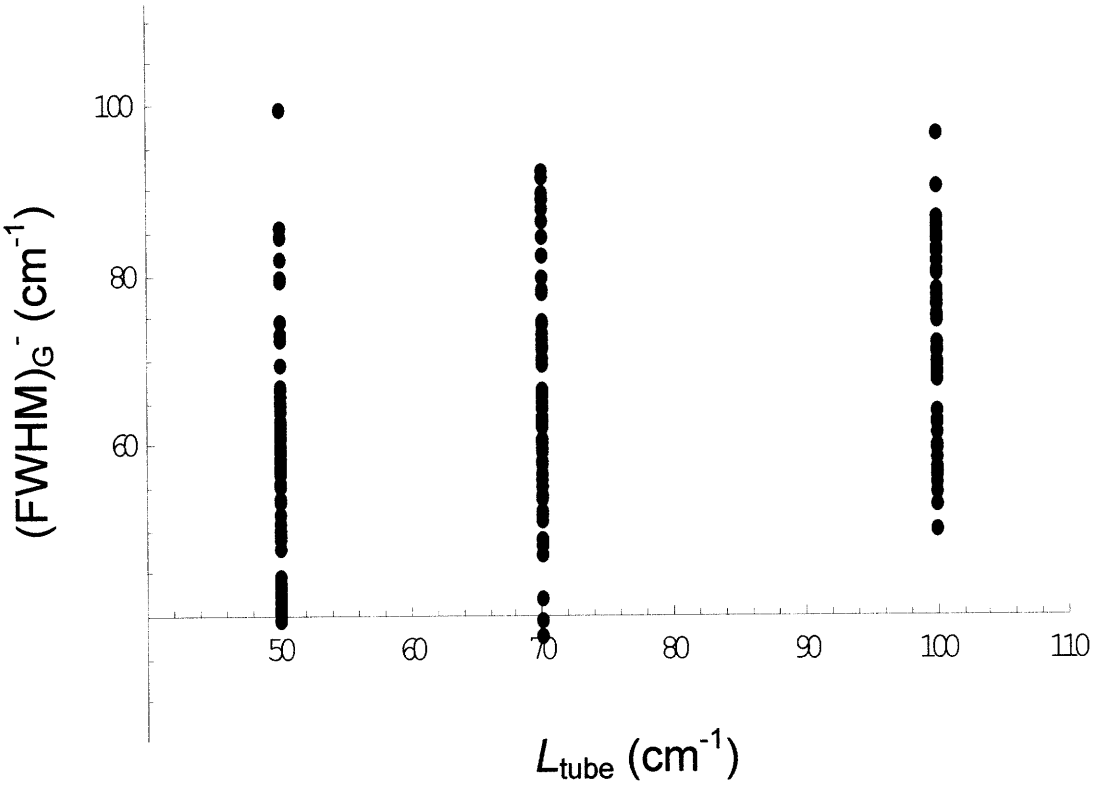

Figure 3-16. The observed $(FWHM)_{G^-}$ linewidth vs. nanotube length L_{tube}. Each point on the plot represents the peak fitting result from one Raman spectrum, corresponding to a specific E_{laser}, a specific sample (nanotube length), and a specific spot on that sample.

3.4 Mathematical Background

Correlation is a way to measure the linear dependence between two variables. Two variables, X and Y, are said to be positively correlated if Y tends to be big when X is big. X and Y are negatively correlated if Y is small when X is big. When a data set is complicated or noisy, numerical analysis may be required to determine the correlation between the variables of interest.

Figures 3-17(a) – (d) shows sample scatter plots, using data from our Raman measurements as examples. In Figure 3-17(a), there is a clear positive correlation between X (integrated $[I_{G^-} / I_{G^+}]$ ratio) and Y (peak $[\hat{I}_{G^-} / \hat{I}_{G^+}]$ ratio), while the exact

relationship between the variables is unclear. In Figure 3-17(b) there is a statistically significant positive correlation between the frequency difference $(\omega_{G^+} - \omega_{G^-})$ and the $(FWHM)_{G^-}$ linewidth, but the correlation is less obvious to the eye. In Figure 3-17(c) it is clear that a negative correlation exists between $[1/q]_{G^-}$ and L_{tube}, but the discrete tube lengths make it hard to identify the length-dependent pattern. In Figure 3-17(d), the integrated $[I_{G^-} / I_{G^+}]$ ratio and L_{tube} are not independent but there is close to zero correlation. That is, a nonlinear or multivariant dependence between the integrated $[I_{G^-} / I_{G^+}]$ ratio and the nanotube length may exist.

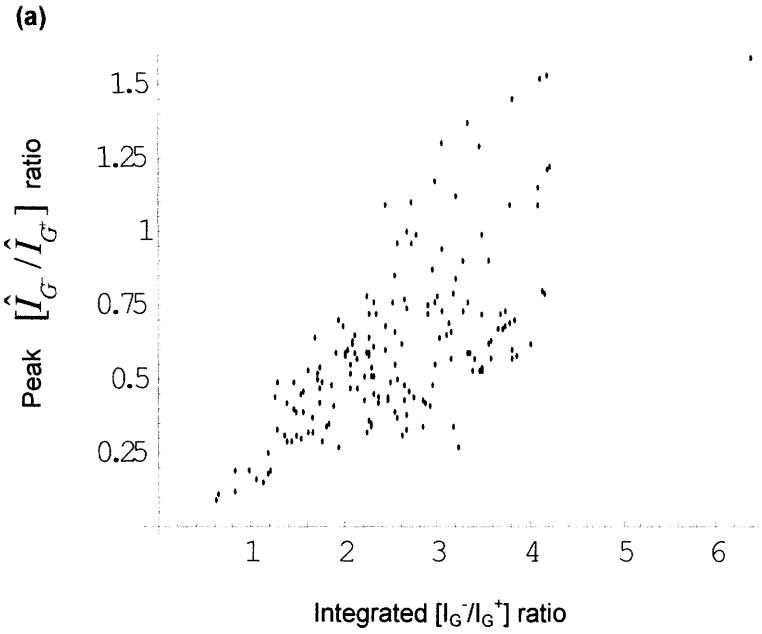

Figure 3-17(a). Scatter plot of the peak $[\hat{I}_{G^-} / \hat{I}_{G^+}]$ ratio vs. integrated $[I_{G^-} / I_{G^+}]$ ratio. Data from the Raman measurements of length-sorted carbon nanotubes were used. Each data point corresponds to a spectrum taken at a specific E_{laser}, a specific sample (nanotube length), and a specific spot on that sample.

(b)

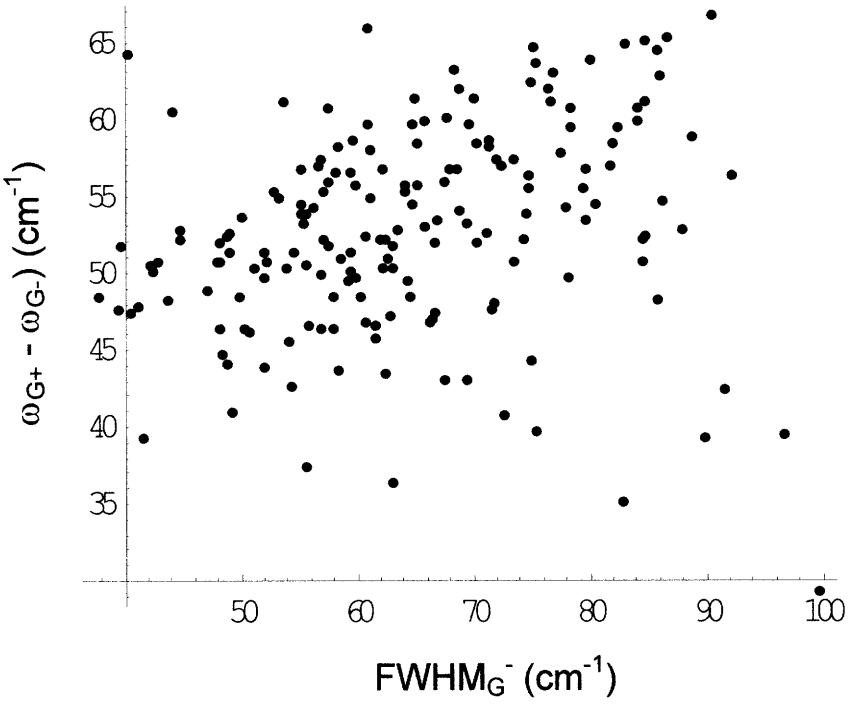

Figure 3-17(b). Scatter plot of $(\omega_{G^+} - \omega_{G^-})$ vs. $(FWHM)_{G^-}$. Data from the Raman measurements of length-sorted carbon nanotubes were used. Each data point corresponds to a spectrum taken at a specific E_{laser}, a specific sample (nanotube length), and a specific spot on that sample.

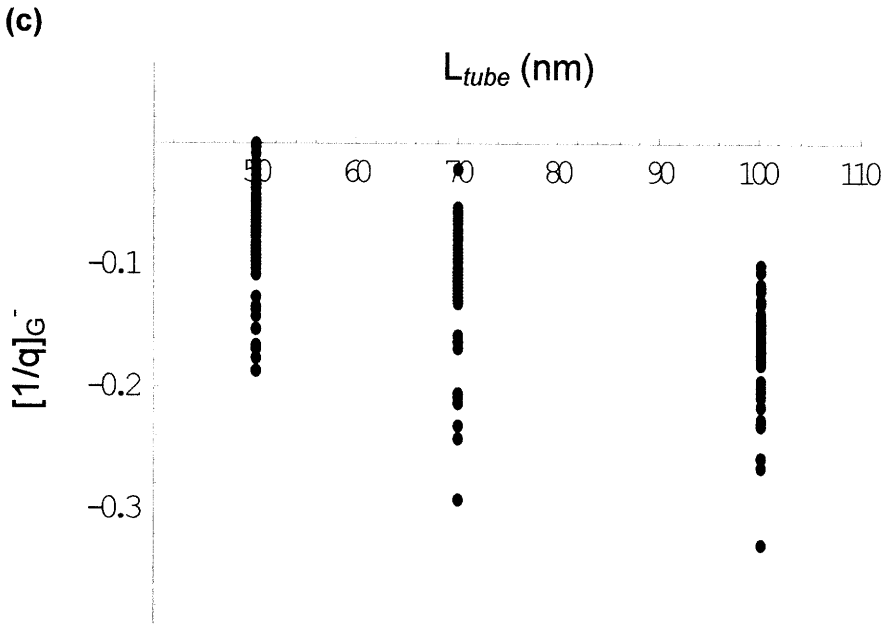

Figure 3-17(c). Scatter plot of the G^- BWF asymmetry parameter $[1/q]_{G^-}$ vs. L_{tube}. Data from the Raman measurements of length-sorted carbon nanotubes were used. Each data point corresponds to a spectrum taken at a specific E_{laser}, a specific sample (nanotube length), and a specific spot on that sample.

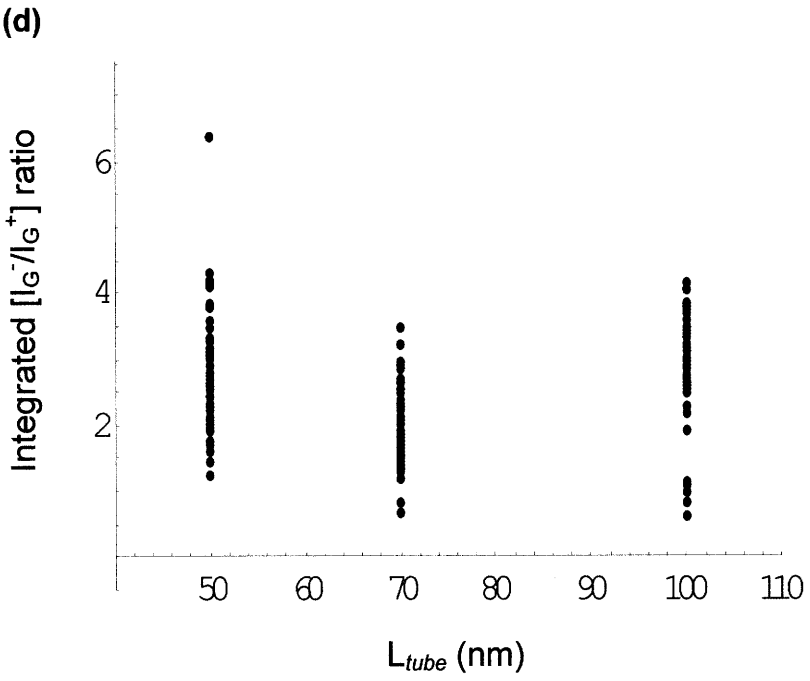

Figure 3-17(d). Scatter plot of the integrated $[I_{G^-} / I_{G^+}]$ intensity ratio vs. L_{tube}. Data from the Raman measurements of length-sorted carbon nanotubes were used. Each data point corresponds to a spectrum taken at a specific E_{laser}, a specific sample (nanotube length), and a specific spot on that sample.

The Pearson product moment correlation coefficient is a natural way to quantify the correlation between two variables X and Y [5]. The Pearson correlation coefficient r is defined as

$$r = \frac{<(X - X_{avg})(Y - Y_{avg})>}{\sigma_X \sigma_Y} \qquad (3.2),$$

where X_{avg}, Y_{avg} are the average values of the variables X and Y; σ_X, σ_Y are the standard deviations of X and Y, and the < > brackets denote the expected value. The Pearson correlation is the cosine of the angle between two vectors, which are comprised of the deviations of X from its average and the deviations of Y from its average.

The Pearson correlation coefficient is a unitless number between -1 (perfectly anticorrelated) and 1 (perfectly correlated). If X and Y are independent from each other, r = 0. However, the converse is not true: it is possible for X and Y to share a nonlinear or multivariant dependence while r = 0. Physically, one effect may cause a positive

correlation while another may cause a negative correlation and the two may nearly cancel one another. The correlation coefficient is scale invariant; that is, each variable can be independently rescaled without changing r. This is because the rescaling of vectors does not change the angle between them. The Pearson correlation coefficient is symmetric: the correlation between X and Y is equal to the correlation between Y and X.

The Pearson correlation coefficient is sensitive to outliers. Changing the value of one point far from (X_{avg}, Y_{avg}) can significantly alter r. Hence, unlike the median, the correlation coefficient is affected by changes in any data point.

A high correlation coefficient (r close to 1 or -1) means that the scatter plot between X and Y is close to a line. However a high r value does not mean the slope is large; that is, Y may depend *consistently* on X, rather than *strongly*.

When is the correlation coefficient considered "high"? The statistical significance of the correlation coefficient depends on its magnitude and on the number of data points. With more data points, it is less likely for a sample to have a high observed correlation if the true correlation is zero. If the true correlation is zero, then for at least N = 6 points, the correlation roughly follows a Student t-distribution with N – 2 degrees of freedom [23]. For example, if N = 6, the threshold for P = 0.10 significance is $|r| > 0.73$. This means that if the true correlation is zero, then for 10 percent of the time, a correlation greater than 0.73 in magnitude will be observed. For N = 6, the threshold for P = 0.05 significance is $|r| > 0.81$. This means that if the true correlation is zero, then for 5 percent of the time, a correlation greater than 0.81 in magnitude will be observed. With 20 data points, the threshold for P = 0.05 significance is $|r| > 0.44$. With 10,000 data points, then there is a strong P = 0.05 significance at $|r| > 0.020$.

3.4.1 Length Dependence Analysis

Now we make use of the mathematical background described above to deduce the length dependence of the various parameters associated with the G-band. We use a weighted correlation to avoid biasing the results by the data collection procedure. Specifically, in the Raman measurements, different numbers of points were taken from different spots at different values of E_{laser}. Hypothetically, if a lot of spectra were taken for the 70 nm length sample at E_{laser} = 488 nm, then the average of all 70 nm data would

be pulled towards the characteristics at that value of E_{laser}. If a lot of data points were available for the 50 nm long tubes at E_{laser} = 457.9 nm, then using an unweighted correlation to compare 70 nm with 50 nm might instead be inadvertently comparing nanotube properties between E_{laser} = 488 nm and E_{laser} = 457.9 nm. Hence, simply adding more data points from a specific (E_{laser}, nanotube length) combination could skew the result. To avoid this bias, we weight the sample points so that each (E_{laser}, nanotube length) combination has the same total weight of 1. For example, if there are seven spots (spectra) for a specific sample at a given E_{laser}, then the weight given to each is 1/7. The weighted Pearson coefficient is still given by

$$r^w = \frac{\left\langle (X - X^w_{avg})(Y - Y^w_{avg}) \right\rangle^w}{\sigma^w_X \sigma^w_Y} \qquad (3.3)$$

but X^w_{avg}, Y^w_{avg} now represent weighted averages and σ^w_X, σ^w_Y are the weighted standard deviations, and $\langle\ \rangle^w$ is a weighted expected value.

3.4.2 Example

Now we present an example to show how the weighted Pearson correlation coefficient r^w is calculated. Specifically, we shall calculate r^w between the nanotube length L_{tube} and $(FWHM)_{G^-}$.

Table 3-1 shows a portion of the tabulated data. This portion corresponds to Raman spectra taken with the E_{laser} = 472.7 nm laser line. Of the measured quantities, only the $(FWHM)_{G^-}$ is shown. Each Raman spectrum is labeled by the sample name (Sample 9, 11, 13 corresponding to 100 nm, 70 nm, and 50 nm tubes, respectively) and the spot on the sample. The last column in Table 3-1 contains the weights used to calculate r^w. The weights are chosen such that each (E_{laser}, nanotube length) combination has the same total weight of 1. For E_{laser} = 472.7 nm, Sample 9, five Raman spectra corresponding to five spots on the sample were available. Therefore, each data point (row on Table 3-1) for E_{laser} = 472.7 nm, Sample 9 has weight 1/5. Similarly, seven spots were examined for E_{laser} = 472.7 nm, Sample 11, so each corresponding row on Table 3-1 has weight 1/7.

E_{laser} (nm)	Sample	Spot	L_{tube} (nm)	$(FWHM)_{G^-}$	Weight
472.7	9	2	100	67.54	1/5
472.7	9	3	100	69.58	1/5
472.7	9	4	100	57.14	1/5
472.7	9	5	100	68.46	1/5
472.7	9	6	100	57.58	1/5
472.7	11	1	70	65.04	1/7
472.7	11	2	70	48.16	1/7
472.7	11	3	70	59.46	1/7
472.7	11	4	70	57.92	1/7
472.7	11	5	70	53.84	1/7
472.7	11	6	70	51.16	1/7
472.7	11	7	70	52.2	1/7
472.7	13	1b	50	39.62	1/6
472.7	13	2	50	51.92	1/6
472.7	13	3	50	57.54	1/6
472.7	13	4	50	55.58	1/6
472.7	13	5	50	47.88	1/6
472.7	13	6	50	42.74	1/6

Table 3-1. A portion of the data extracted from the Raman spectra and associated weights used to calculate r^w.

For illustrative purposes, three data points points and their corresponding weights are shown in Table 3-2. We will use these points as examples in calculating r^w.

L_{tube}	$(FWHM)_{G^-}$	Weight
50	48.8	1/16
70	74.8	1/6
100	71.0	1/9

Table 3-2. Three data points to be used as examples in calculating r^w.

The weighted Pearson coefficient between the variables X and Y is given by Equation (3.3),

$$r^w = \frac{\left\langle (X - X^w_{avg})(Y - Y^w_{avg}) \right\rangle^w}{\sigma^w_X \sigma^w_Y} \qquad (3.3),$$

where X^w_{avg}, Y^w_{avg} are weighted averages and σ^w_X, σ^w_Y are the weighted standard deviations, and < > is a weighted expected value. In this case, X is L_{tube} and Y is $(FWHM)_{G^-}$. We have, for X^w_{avg},

$$X^w_{avg} = L^w_{tube,avg} = \frac{(50)\frac{1}{16}+(70)\frac{1}{6}+(100)\frac{1}{9}+...}{\frac{1}{16}+\frac{1}{6}+\frac{1}{9}+...} = 73.3, \tag{3.4}$$

where the first three terms were taken from Table 3-2, but the quantity $L^w_{tube,avg}$ was calculated from the entire data set of 179 points. For Y^w_{avg},

$$Y^w_{avg} = (FWHM)^w_{G^-,avg} = \frac{(48.8)\frac{1}{16}+(74.8)\frac{1}{6}+(71.0)\frac{1}{9}+...}{\frac{1}{16}+\frac{1}{6}+\frac{1}{9}+...} = 64.6 \tag{3.5}.$$

Again, the average value $(FWHM)^w_{G^-,avg}$ was calculated from all 179 data points. Using equations (3.4), (3.5), and Table 3-2 for the first few terms, the weighted expected value $\left\langle (X - X^w_{avg})(Y - Y^w_{avg}) \right\rangle^w$ is given by

$$\left\langle (L_{tube} - L^w_{tube,avg})((FWHM)_{G^-} - (FWHM)^w_{G^-,avg}) \right\rangle^w$$

$$= \frac{(50-73.3)(48.8-64.6)\frac{1}{16}+(70-73.3)(74.8-64.6)\frac{1}{6}+(100-73.3)(71.0-64.6)\frac{1}{9}+...}{\frac{1}{16}+\frac{1}{6}+\frac{1}{9}+...}$$

$$= 100.4 \tag{3.6}$$

for the entire dataset.

The weighted standard deviation σ_A of a variable A is defined as

$$\sigma^w_A = \sqrt{\left\langle (A - A^w_{avg})^2 \right\rangle^w}$$

$$= \sqrt{\frac{\text{weighted sum of } (A - A^w_{avg})^2}{\text{sum of weights}}}$$

Using equation (3.4) and Table 3-2, σ^w_X is given by

$$\sigma_X^w = \sigma_{L_{tube}}^w = \sqrt{\frac{(50-73.3)^2\frac{1}{16}+(70-73.3)^2\frac{1}{6}+(100-73.3)^2\frac{1}{9}+\ldots}{\frac{1}{16}+\frac{1}{6}+\frac{1}{9}+\ldots}} = 20.5 \tag{3.7}$$

and σ_Y^w is

$$\sigma_Y^w = \sigma_{(FWHM)_{G^-}}^w = \sqrt{\frac{(48.8-64.6)^2\frac{1}{16}+(74.8-64.6)^2\frac{1}{6}+(71.0-64.6)^2\frac{1}{9}+\ldots}{\frac{1}{16}+\frac{1}{6}+\frac{1}{9}+\ldots}} = 13.1 \tag{3.8}$$

when equation (3.5) and Table 3-2 are used. Finally, we use equations (3.6), (3.7) and (3.8) to calculate r^w:

$$r^w = \frac{\left\langle (L_{tube} - L_{tube,avg}^w)((FWHM)_{G^-} - (FWHM)_{G^-,avg}^w)\right\rangle^w}{\sigma_{L_{tube}}^w \sigma_{(FWHM)_{G^-}}^w}$$

$$= \frac{100.4}{(20.5)(13.1)}$$

$$= 0.372$$

(3.9)

3.4.3 Length Dependence Results

Table 3-3 shows the calculated weighted Pearson correlation coefficients between nanotube length and the various G-band parameters. All of the E_{laser} lines that are probing metallic nanotubes and all of the spots on the samples were used in calculating the correlation coefficient. With this number of data points (179), the threshold for P = 0.05 significance is $|r| > 0.15$. Despite the variance in the data, we can see statistically significant length dependence in most of the G-band parameters considered. Specifically, the $(FWHM)_{G^-}$ and the frequency difference $(\omega_{G^+} - \omega_{G^-})$ are correlated with nanotube length. The $[1/q]_{G^-}$, ω_{G^-}, $(FWHM)_{G^+}$ and peak $[\hat{I}_{G^-} / \hat{I}_{G^+}]$ ratio are anticorrelated with nanotube length. The ω_{G^+} and the integrated $[I_{G^-} / I_{G^+}]$ ratio show no statistically significant length dependence.

X	Y	$r^w(X,Y)$
L_{tube}	$(FWHM)_{G^-}$	0.372
L_{tube}	$[1/q]_{G^-}$	-0.632
L_{tube}	ω_{G^-}	-0.166
L_{tube}	$(FWHM)_{G^+}$	-0.613
L_{tube}	ω_{G^+}	0.0774
L_{tube}	$(\omega_{G^+} - \omega_{G^-})$	0.255
L_{tube}	Integrated $[I_{G^-} / I_{G^+}]$ ratio	0.0277
L_{tube}	Peak $[\hat{I}_{G^-} / \hat{I}_{G^+}]$ ratio	-0.336

Table 3-3. The calculated weighted Pearson correlation coefficients $r^w(X,Y)$ between nanotube length (X) and the various G-band parameters (Y). All of the E_{laser} lines probing metallic nanotubes and all of the spots on the samples were used in the calculation. With this number of data points (179), the threshold for P = 0.05 significance is $|r| > 0.15$.

Now that we have established which of the G-band parameters are correlated with nanotube length, we can take a weighted least squares linear fit to determine the strength of the length dependence. We use the built-in statistics package in the *Mathematica* software to perform the fitting. Also included with *Mathematica* is the capability to calculate the confidence interval of a linear fit, which is related to the weighted correlation coefficient r^w. The confidence interval ((m_1, m_2) for the slope and (b_1, b_2) for the y-intercept) is a measure of the relative uncertainty of the linear fit. The true value of the slope of the linear fit should be within the confidence interval (between m_1 and m_2) 95% of the time. Similarly, the true value of the y-intercept of the linear fit should be within the confidence interval (between b_1 and b_2) 95% of the time. If the correlation coefficient r^w exceeds the P = 0.05 significance threshold by a greater amount, then the smallest magnitude (the lesser value between $|m_1|$ and $|m_2|$) in the confidence interval is farther from zero relative to the fitted slope. In other words, the greater the $|r^w|$, the more isolated the fitted slope becomes from zero. For example, in the case of the integrated

$[I_{G^-} / I_{G^+}]$ vs. L_{tube}, the zero slope falls within the confidence interval for the fitted slope because $|r^w|$ does not exceed the threshold for statistical significance.

Figures 3-18(a) – (h) show the scatter plots of each of the G-band parameters vs. length. Superimposed on each scatter plot is the linear fit to the data points. Table 3-4 summarizes the linear fits and gives 95% confidence intervals for the slopes and *y*-intercepts of the fits. In Tables 3-3 and 3-4, at least 3 significant figures were kept throughout to avoid round-off errors.

Figure 3-18(a) shows the length dependence of the G^+ frequency ω_{G^+}. From the linear fit, we see that ω_{G^+} downshifts by only 1 cm^{-1} when the tube length L_{tube} decreases from 100 nm to 50 nm. However, the confidence interval for the slope of ω_{G^+} vs. L_{tube} plot contains the zero slope (Table 3-3). Also, the correlation coefficient r^w between ω_{G^+} and L_{tube} is too low to be statistically significant. Therefore we can say that ω_{G^+} does not depend on nanotube length. This result agrees with that found for nanotubes excited with E_{laser} = 457.9 nm (2.71 eV), for which the Raman spectra have low spot-to-spot variation. For E_{laser} = 457.9 nm (2.71 eV), no appreciable change in the ω_{G^+} was observed with length.

Figure 3-18(b) shows the length dependence of the G^- frequency ω_{G^-}. Over a 50 nm length range, ω_{G^-} was found to increase by about 3 cm^{-1} as the nanotube length decreases. However, from Table 3-4, the edge of the confidence interval for the slope was found to be -0.007. Hence, in the "worst" case scenario, over a 50 nm length range, ω_{G^-} only changes by 0.362 cm^{-1}. This is consistent with the calculated correlation coefficient r^w of -0.166, which is not far from the P = 0.05 significance threshold of 0.15. Therefore, the length dependence of the ω_{G^-} is a small one when all E_{laser} are taken into account. By contrast, the E_{laser} = 457.9 nm (2.71 eV) result shows a larger increase of about 9 cm^{-1} when the nanotube length decreases from 100 nm to 50 nm. The observed ω_{G^-} shift with length may be a property of metallic nanotubes, which could be diminished when a mixture of semiconducting and metallic nanotubes are resonant.

Figure 3-18(c) plots the $(\omega_{G^+} - \omega_{G^-})$ frequency difference vs nanotube length. The corresponding correlation coefficient was found to be 0.255, which is greater than those found for either ω_{G^+} or ω_{G^-} vs. tube length. From the fitted slope, the frequency difference $(\omega_{G^+} - \omega_{G^-})$ was found to decrease by about 4 cm^{-1} when the nanotube length decreases by 50 nm. Again, the $(\omega_{G^+} - \omega_{G^-})$ decrease was found to be more significant (about 10 cm^{-1}) in the case of nanotubes excited with E_{laser} = 457.9 nm (2.71 eV).

The $(FWHM)_{G^+}$ vs. nanotube length is shown in Figure 3-18(d). The corresponding r^w is -0.613, which indicates a strong anticorrelation between the $(FWHM)_{G^+}$ and nanotube length. From the fitted slope of $(FWHM)_{G^+}$ vs nanotube length (Table 3-4), we find that when the nanotube length decreases by 50 nm, the $(FWHM)_{G^+}$ increases by about 3 cm^{-1}. This is consistent with the results for E_{laser} = 457.9 nm (2.71 eV), for which $(FWHM)_{G^+}$ shows an increase of about 2 cm^{-1}.

In Figure 3-18(e) the plot of $(FWHM)_{G^-}$ vs. nanotube length is shown. These two parameters are correlated (r^w = 0.372), and as the nanotube length decreases by 50 nm, the $(FWHM)_{G^-}$ narrows by 12 cm^{-1}. This is again consistent with the results for E_{laser} = 457.9 nm (2.71 eV) which shows $(FWHM)_{G^-}$ to narrow by 15 cm^{-1}.

Figures 3-18(f) and (g) plot the peak $[\hat{I}_{G^-} / \hat{I}_{G^+}]$ ratio vs. L_{tube} and the integrated $[I_{G^-} / I_{G^+}]$ ratio vs. L_{tube}, respectively. While the peak $[\hat{I}_{G^-} / \hat{I}_{G^+}]$ ratio increases with decreasing nanotube length, the integrated $[I_{G^-} / I_{G^+}]$ ratio remains constant. In terms of the correlation coefficient, r^w = -0.336 for the peak $[\hat{I}_{G^-} / \hat{I}_{G^+}]$ ratio vs. L_{tube}, which is statistically significant. However, r^w = 0.0277 for the integrated $[I_{G^-} / I_{G^+}]$ ratio vs. L_{tube}, which is below the P = 0.05 significance threshold. The constant integrated $[I_{G^-} / I_{G^+}]$ ratio with L_{tube} can be explained by considering the length dependence of the $(FWHM)_{G^-}$ and the peak $[\hat{I}_{G^-} / \hat{I}_{G^+}]$ ratio. As the nanotube length decreases, the peak

$[\hat{I}_{G^-} / \hat{I}_{G^+}]$ ratio increases, while the $(FWHM)_{G^-}$ decreases. These effects cancel, resulting in a constant integrated $[I_{G^-} / I_{G^+}]$ ratio with L_{tube}.

The length dependence of the integrated $[I_{G^-} / I_{G^+}]$ ratio shown here, which considers several values of E_{laser}, differs from that found for E_{laser} = 457.9 nm (2.71 eV). For E_{laser} = 457.9 nm, the integrated $[I_{G^-} / I_{G^+}]$ ratio was found to increase by 1.7 as L_{tube} decreases from 100 nm to 50 nm.

Finally, Figure 3-18(h) shows the BWF asymmetry parameter $[1/q]_{G^-}$ vs. nanotube length. A large anticorrelation coefficient of r^w = -0.632 was found between $[1/q]_{G^-}$ and nanotube length. For a tube length decrease from 100 nm to 50 nm, the fitted slope gives an increase (|1/q| decrease) of 0.10, indicating a change to a more Lorentzian lineshape. A similar result was found for E_{laser} = 457.9 nm, but the effect in that case was a bit more prominent; $[1/q]_{G^-}$ decreases by 0.13 when L_{tube} decreases by 50 nm for E_{laser} = 2.71 eV.

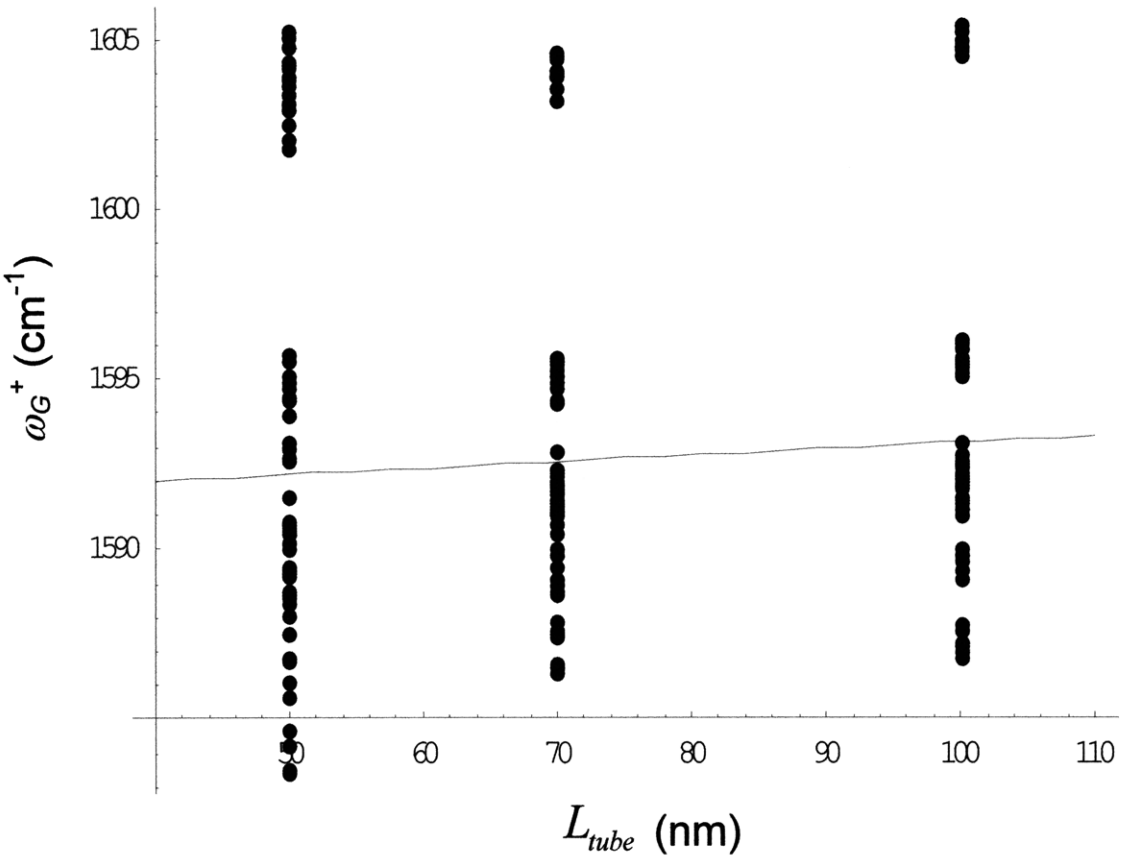

Figure 3-18(a) Scatter plot of the G^+ frequency vs. nanotube length. Each data point corresponds to a spectrum taken at a specific E_{laser}, a specific sample (nanotube length), and a specific spot on that sample. The linear fit to the data points is superimposed onto the scatter plot.

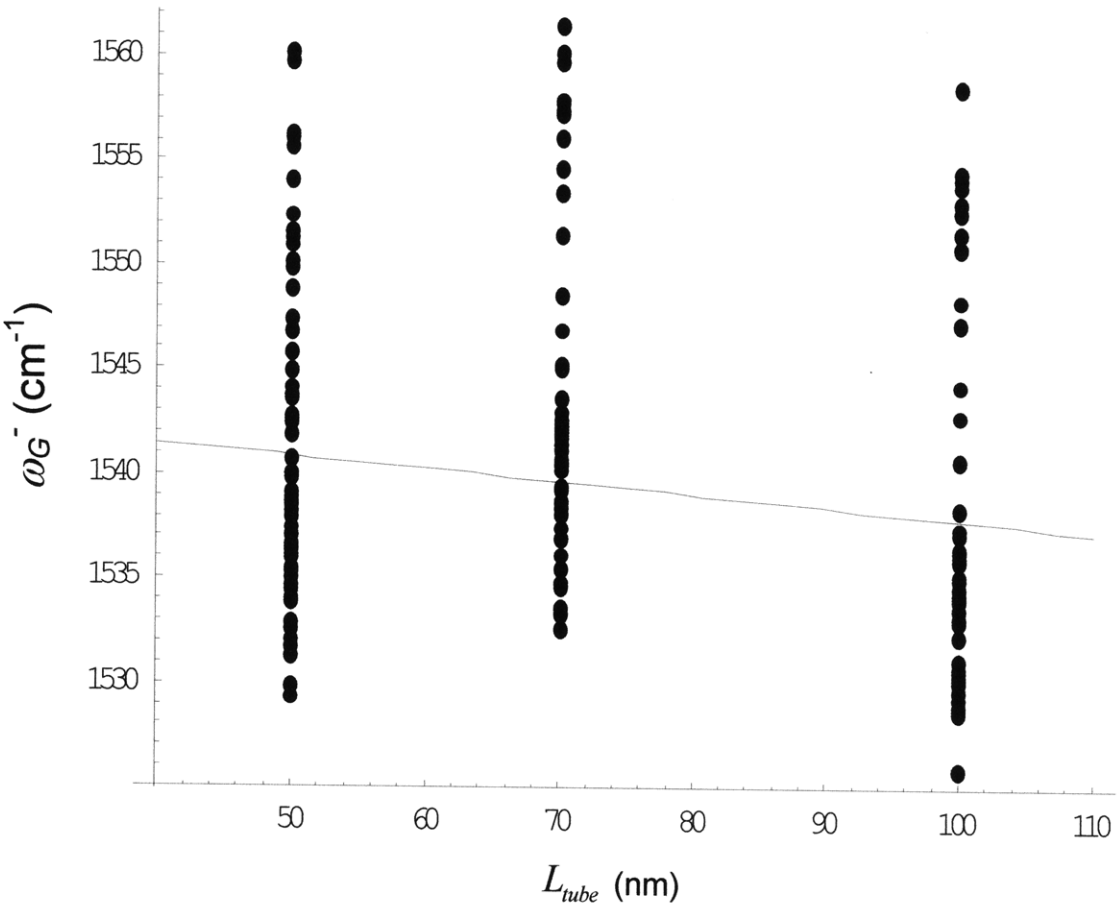

Figure 3-18(b) Same as Figure 3-18(a), but plot of G^- frequency vs nanotube length.

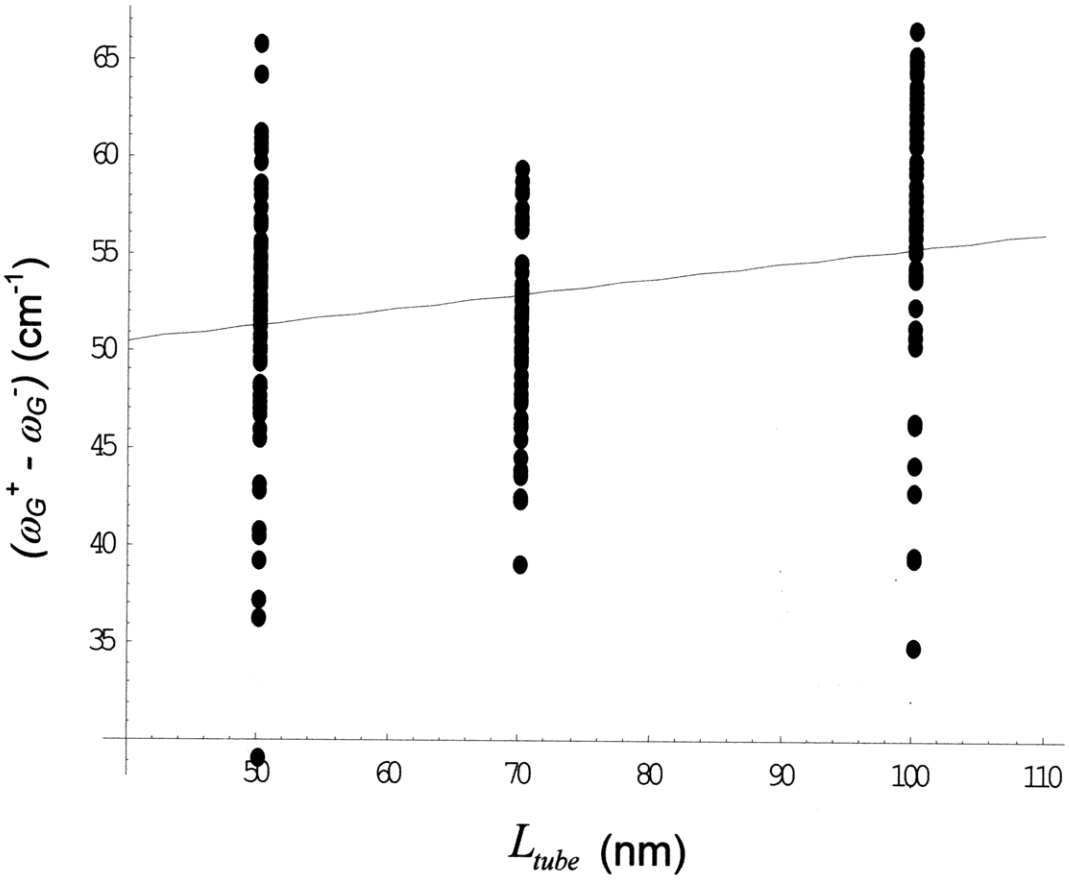

Figure 3-18(c) Same as Figure 3-18(a), but plot of the frequency difference $(\omega_{G^+} - \omega_{G^-})$ vs nanotube length.

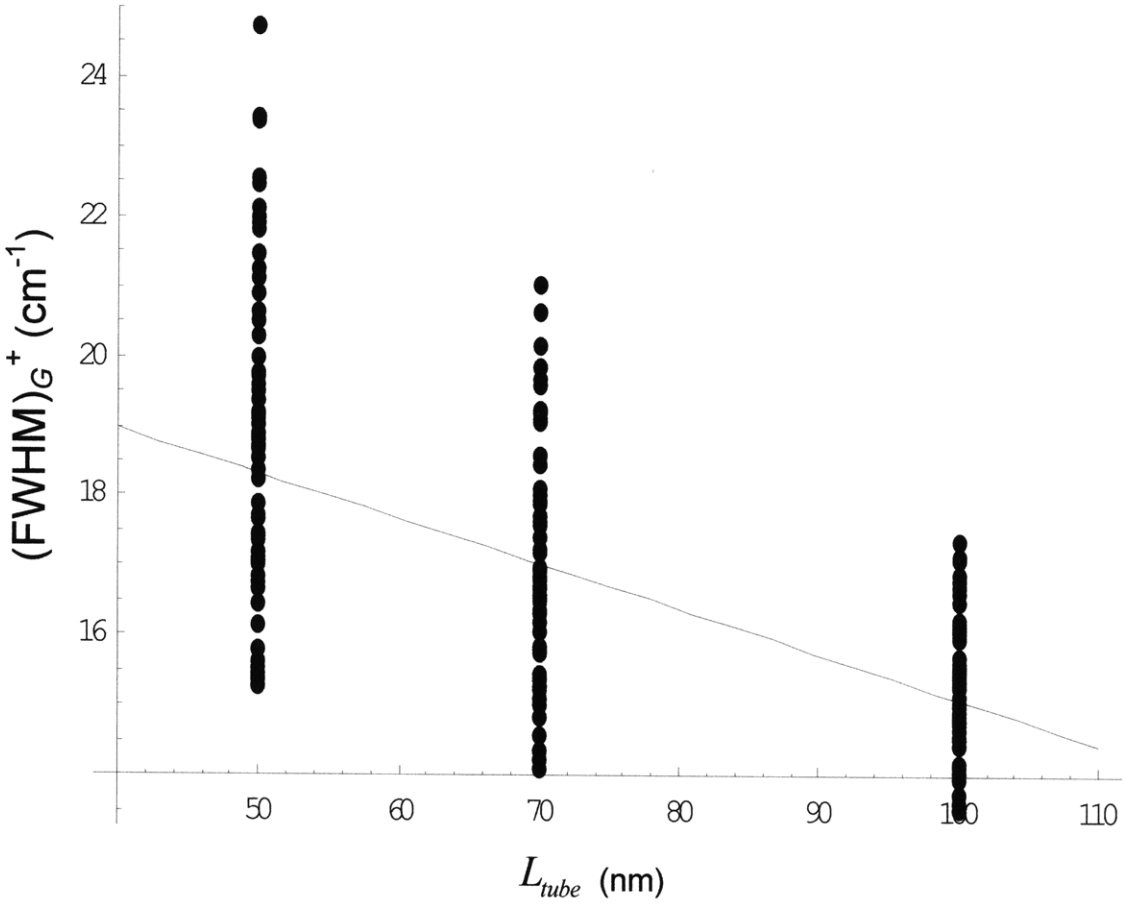

Figure 3-18(d) Same as Figure 3-18(a), but plot of the G^+ FWHM vs nanotube length.

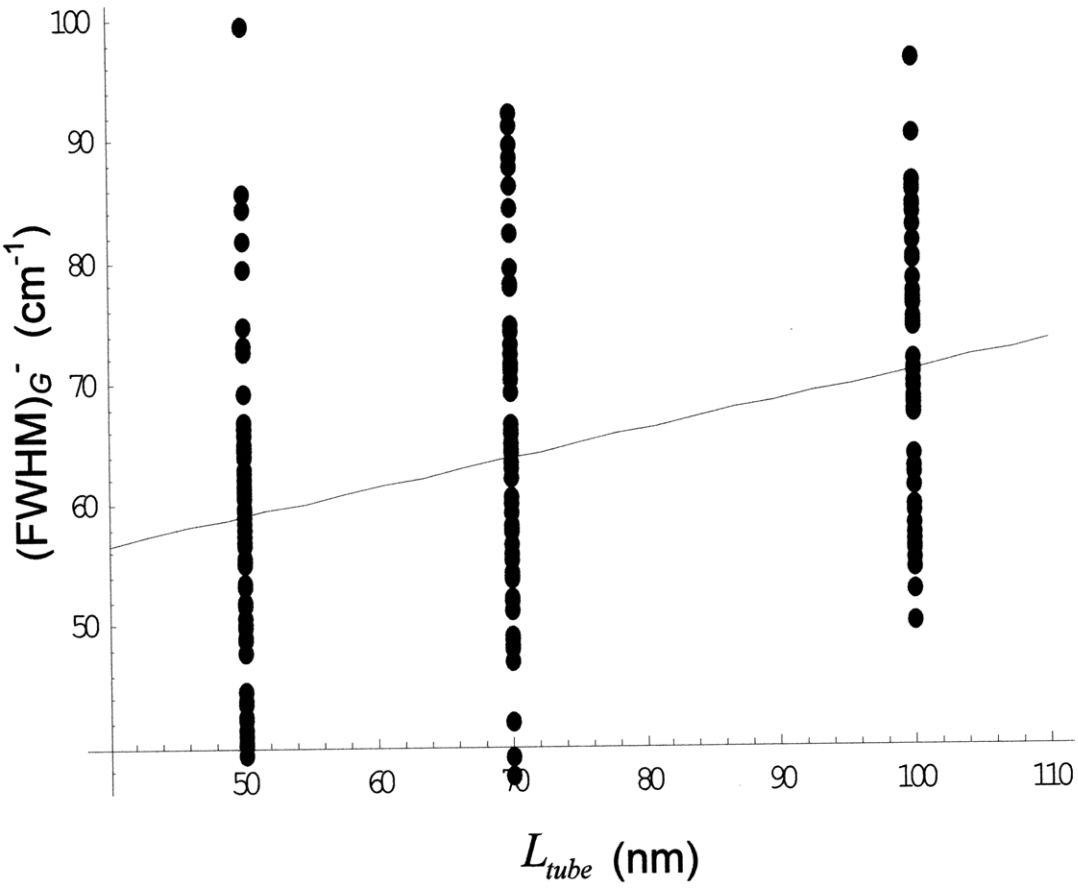

Figure 3-18(e) Same as Figure 3-18(a), but plot of the G^- FWHM vs nanotube length.

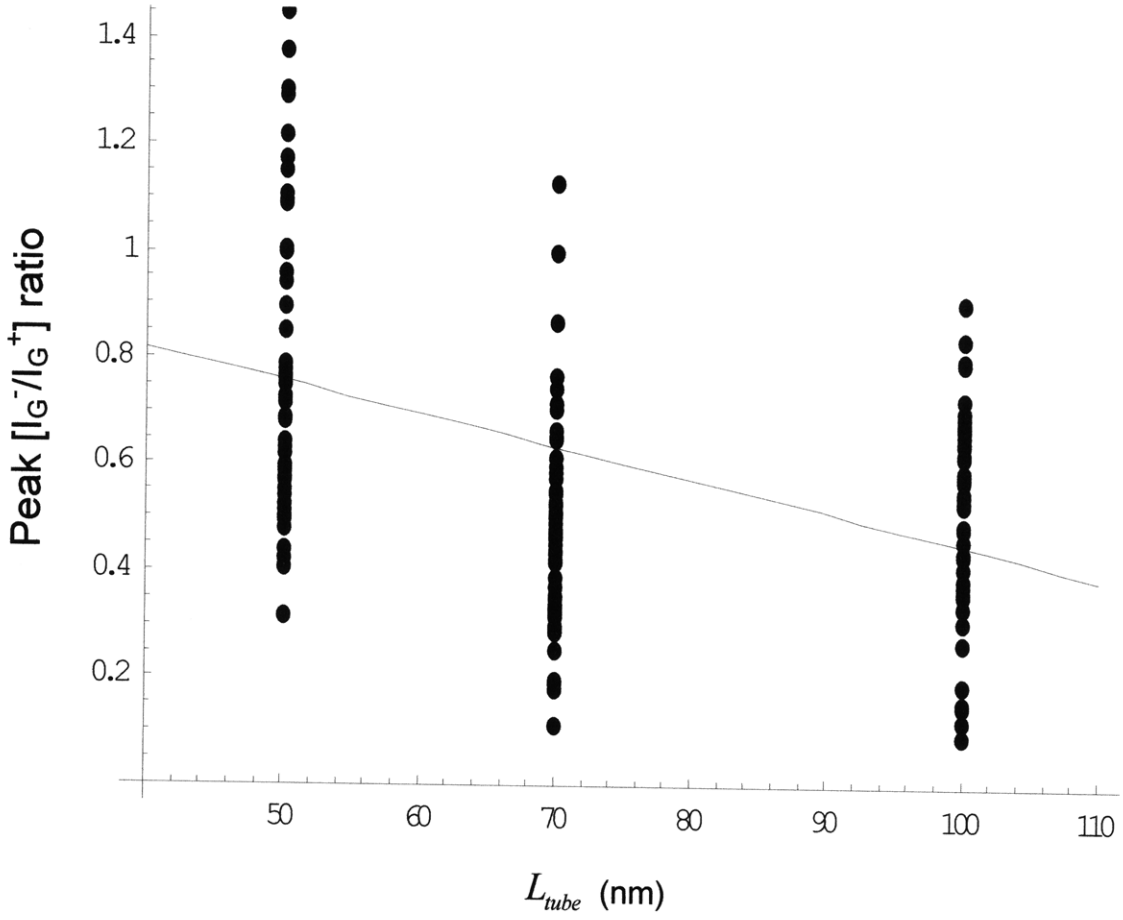

Figure 3-18(f) Same as Figure 3-18(a), but plot of the peak $[\hat{I}_{G^-} / \hat{I}_{G^+}]$ ratio vs nanotube length.

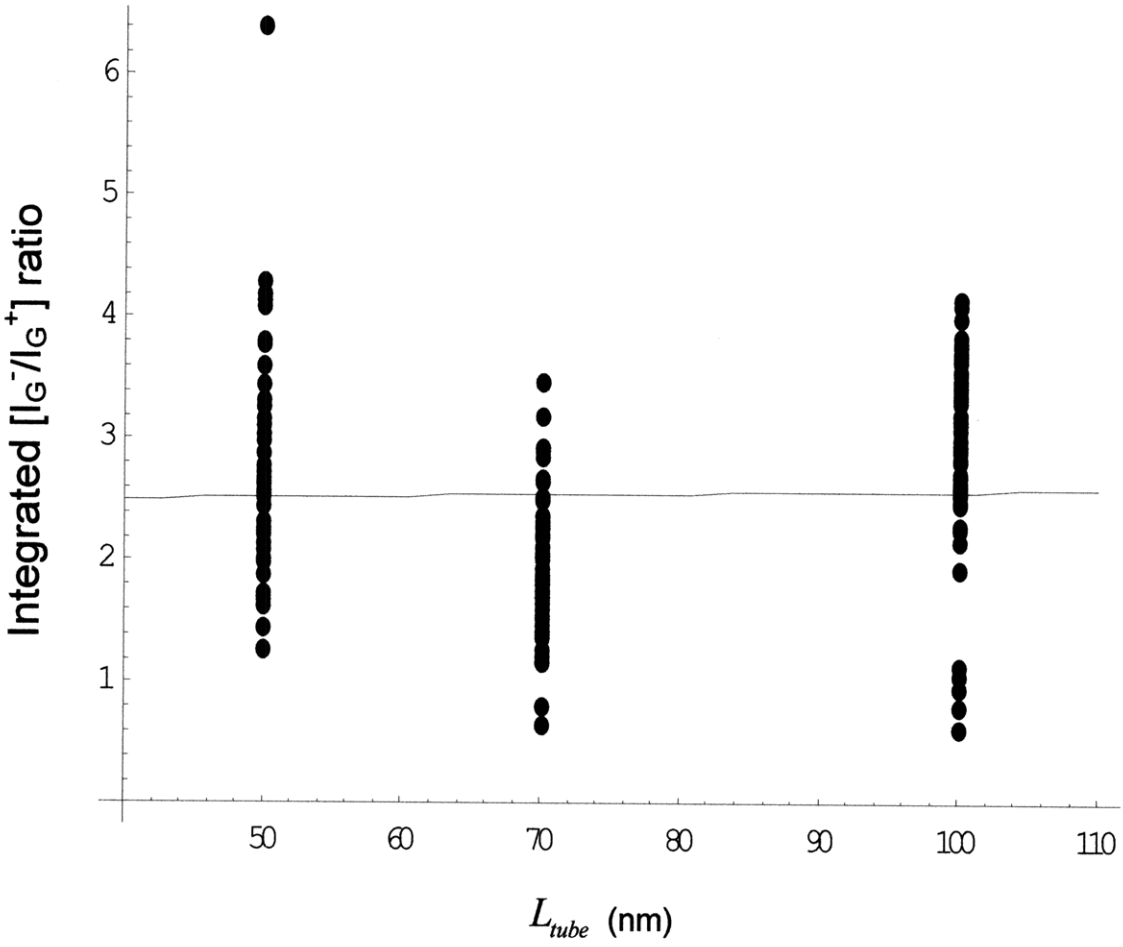

Figure 3-18(g) Same as Figure 3-18(a), but plot of the integrated $[I_{G^-} / I_{G^+}]$ ratio vs nanotube length.

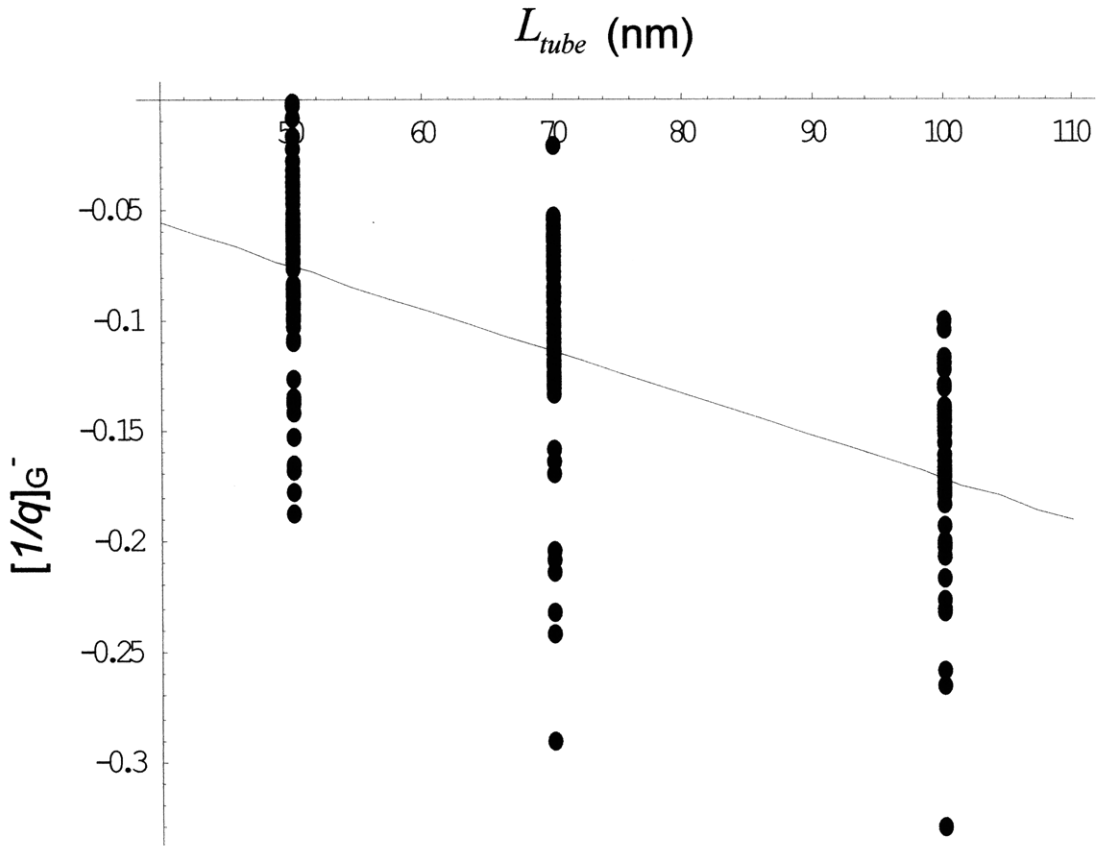

Figure 3-18(h) Same as Figure 3-18(a), but plot of the asymmetry parameter $[1/q]_{G^-}$ vs nanotube length.

G-band parameter (Y)	Linear fit of Y vs. L_{tube} (X)	Confidence interval (m_1, m_2) of slope	Confidence interval (b_1, b_2) of y-intercept
$(FWHM)_{G^-}$	0.238 X + 47.1	(0.150, 0.326)	(40.4, 53.9)
$[1/q]_{G^-}$	-0.00193 X + 0.0215	(-0.00228, -0.00158)	(-0.00527, 0.0482)
ω_{G^-}	-0.0604 X + 1544	(-0.114, -0.00724)	(1540, 1548)
$(FWHM)_{G^+}$	-0.0644 X + 21.5	(-0.0768, -0.0521)	(20.6, 22.5)
ω_{G^+}	0.0188 X + 1591	(-0.0171, 0.0548)	(1589, 1594)
$(\omega_{G^+} - \omega_{G^-})$	0.0792 X + 47.4	(0.0346, 0.124)	(44.0, 50.8)
Integrated $[I_{G^-} / I_{G^+}]$ ratio	0.00128 X + 2.45	(-0.00559, 0.00816)	(1.93, 2.98)
Peak $[\hat{I}_{G^-} / \hat{I}_{G^+}]$ ratio	-0.00611 X + 1.06	(-0.00865, -0.00357)	(0.0869, 1.26)

Table 3-4. Linear fits found for each of the (G-band parameters) Y vs. nanotube length scatter plots. The confidence intervals for the slope and y-intercepts found from each linear fit are also listed. The true values of the slopes and y-intercepts should fall within the confidence interval (between m_1 and m_2 for the slope and between b_1 and b_2 for the y-intercept) 95% of the time.

3.5 Summary of Chapter

In this chapter we examined the length dependence of the Raman G-band of carbon nanotubes. First we studied the length dependence of semiconducting nanotubes by choosing E_{laser} = 647 nm (1.92 eV), which predominantly excites the (7, 5) semiconducting nanotube. For semiconducting nanotubes, no length dependence in the frequencies ω_{G^+} and ω_{G^-} or linewidths $(FWHM)_{G^+}$ and $(FWHM)_{G^-}$ was found for both of the G-band components G^+ and G^-. Both the integrated $[I_{G^-} / I_{G^+}]$ and peak $[\hat{I}_{G^-} / \hat{I}_{G^+}]$ ratios were found to decrease by 9% and 7%, respectively, when the nanotube length L_{tube} decreases from 100 nm to 50 nm.

The Raman spectra for metallic nanotubes were found to have significant spot-to-spot variation which makes data analysis less straightforward. For metallic nanotubes, we examined the data for E_{laser} = 457.9 nm (2.71 eV). The spectra taken at this laser line have

the lowest spot-to-spot variation of all the E_{laser} used that excite metallic nanotubes. For E_{laser} = 2.71 eV, $(FWHM)_{G^+}$ increases while $(FWHM)_{G^-}$ decreases as the nanotube length gets shorter. The G^+ frequency ω_{G^+} remains the same, but the G^- frequency ω_{G^-} increases as the nanotube length decreases. The overall result is a ~15% decrease in the frequency difference $(\omega_{G^+} - \omega_{G^-})$ when the tube length decreases from 100 nm to 50 nm. Both the peak $[\hat{I}_{G^-} / \hat{I}_{G^+}]$ and integrated $[I_{G^-} / I_{G^+}]$ ratios were found to increase when L_{tube} decreases from 100 nm to 50 nm. For E_{laser} = 2.71 eV, the peak $[\hat{I}_{G^-} / \hat{I}_{G^+}]$ ratio increases from about 0.15 to 0.60, and the integrated $[I_{G^-} / I_{G^+}]$ ratio increases from about 0.98 to 2.7, as L_{tube} decreases from 100 nm to 50 nm.

Despite the significant spot-to-spot variation in the Raman spectra measured at other E_{laser}, we were able to draw general conclusions for nanotubes that exhibit the Breit-Wigner-Fano G^- feature characteristic of metallic nanotubes. We used a statistical analysis method to quantify the correlation between two variables. This technique allows us to draw meaningful conclusions even when the data are noisy. Using this correlation technique, we identified general G-band length-dependent trends when all of the E_{laser}, samples, and spots on the samples are considered. In the general case, we found that the frequency ω_{G^+} has no significant correlation with L_{tube}, and the anticorrelation of ω_{G^-} to L_{tube} is borderline significant. That is, ω_{G^-} may increase when L_{tube} decreases, but the zero slope is contained within the uncertainty of a linear fit of ω_{G^-} vs. L_{tube}. However, the frequency difference $(\omega_{G^+} - \omega_{G^-})$ has a statistically significant positive correlation with L_{tube}, meaning that when L_{tube} decreases, $(\omega_{G^+} - \omega_{G^-})$ also decreases. Since $(\omega_{G^+} - \omega_{G^-})$ corresponds to the splitting of the graphite G-band peak into LO and TO modes, the observed length dependence may be due to the lower aspect ratio for short tubes. A strong correlation was found between $(FWHM)_{G^-}$ and L_{tube}, while a strong anticorrelation was found between $(FWHM)_{G^+}$ and L_{tube}. That is, $(FWHM)_{G^-}$ decreases with decreasing L_{tube} while $(FWHM)_{G^+}$ increases as L_{tube} decreases. The BWF asymmetry parameter $[1/q]_{G^-}$ was found to have a strong negative correlation with L_{tube},

which means that the G^- lineshape becomes more Lorentzian as L_{tube} decreases. Finally, when all E_{laser} were considered, we found that the peak $[\hat{I}_{G^-} / \hat{I}_{G^+}]$ ratio increases as L_{tube} decreases while the integrated $[I_{G^-} / I_{G^+}]$ ratio has no statistically significant correlation with L_{tube}.

When the results for the specific E_{laser} = 2.71 eV are compared to the correlation analysis, which considers all spectra for all E_{laser} exciting metallic nanotubes, we find that most of the G-band parameters show the same length dependent trends. However, the strength of the length dependence differs in the two cases. The major discrepancy between E_{laser} = 2.71 eV and the general case of multiple E_{laser} lies in the length dependence of the integrated $[I_{G^-} / I_{G^+}]$. The integrated $[I_{G^-} / I_{G^+}]$ was found to increase with decreasing L_{tube} in the E_{laser} = 2.71 eV case, but $[I_{G^-} / I_{G^+}]$ shows no correlation with length in the general case.

Some of these results are reminiscent of recent experiments that probe the Kohn Anomaly in carbon nanotubes [6, 7]. In a previous work, the metallic G^- intensity increases, its linewidth decreases, and the lineshape becomes more Lorentzian as the Fermi level ε_F is tuned (by doping or applying a gate voltage) away from the Fermi point [11, 12]. The Kohn Anomaly is a manifestation of electron-phonon coupling and is expected to appear only for metallic tubes [8 – 10]. Furthermore, the width of the G^- peak is predicted to be a measure of the amount of electron-phonon coupling in the nanotube [6]. Thus the observed narrowing of the G^- peak as L_{tube} decreases is an indication of decreased electron-phonon coupling for shorter tubes. The greater length sensitivity of metallic nanotubes (as opposed to semiconducting tubes) may be because metallic G-band modes have more pronounced electron-phonon coupling than those of semiconducting tubes. Since the G^- peak corresponds to the LO phonon mode, it is not unreasonable that this peak would exhibit a strong length dependence [8, 10]. The observed increase of $(FWHM)_{G^+}$ with decreasing L_{tube} could be due to the decreased phonon lifetime that arises from scattering at the tube ends.

References

[1] M. S. Dresselhaus et al., "Raman spectroscopy of carbon nanotubes," *Physics Reports,* **409** (2005) 47.

[2] S. D. M. Brown et al., "Origin of the Breit-Wigner-Fano lineshape of the tangential G-band feature of metallic carbon nanotubes." *Physical Review B*, **63** (2001) 155414.

[3] Jorio et al., "G-band resonant Raman study of 62 isolated single-wall carbon nanotubes." *Physical Review B*, **65** (2002) 155412.

[4] P. C. Eklund et al., "Raman scattering from in-plane lattice modes in low-stage graphite-alkali-metal compounds." *Physical Review B*, **16** (1977) 3330.

[5] D. B. Wright, *First Steps in Statistics*. London: SAGE Publications Ltd (2002).

[6] K. T. Nguyen et al., "Fano Lineshape and Phonon Softening in Single Isolated Metallic Carbon Nanotubes." *Physical Review Letters*, **98** (2007) 145504.

[7] H. Farhat et al., "Phonon Softening in Individual Metallic Carbon Nanotubes due to the Kohn Anomaly." *Physical Review Letters*, **99** (2007) 145506.

[8] M. Lazzeri et al., "Phonon linewidths and electron-phonon coupling in graphite and nanotubes." *Physical Review B*, **73** (2006) 155426.

[9] Ge. G. Samsonidze et al., "Electron-phonon coupling mechanism in two-dimensional graphite and single-wall carbon nanotubes." *Physical Review B*, **75** (2007) 155420.

[10] E. Di Donato et. a.l., "Assignment of the G^+ and G^- Raman bands of metallic and semiconducting carbon based on a common valence force field," *Physical Review B,* **74** (2006) 184306.

Chapter 4 – Correlations of G-band Parameters

4.1 Introduction

In Chapter 3 we presented a statistical analysis method that allows us to quantify the correlation between nanotube length and the various G-band parameters. In addition to studying the length dependence, the techniques introduced in Chapter 3 can be used to study the general properties of the Raman spectra of carbon nanotubes and to find out which G-band parameters are correlated with each other independent of their length. To draw conclusions about carbon nanotubes in general, we separate out the length dependence by grouping the spectra by nanotube length, and performing a correlation analysis on each of the individual groups.

Recently there has been much interest in the effects of electron-phonon coupling on the Raman spectra of carbon nanotubes [1 – 5]. Such electron-phonon coupling effects typically manifest themselves in the G^- band of metallic nanotubes. Hence we will focus on metallic nanotubes in this chapter.

Table 4-1 shows the calculated weighted correlation coefficients r_{100}^w, r_{70}^w, and r_{50}^w between the various G-band parameters for 100 nm, 70 nm, and 50 nm nanotubes, respectively. Spectra taken with E_{laser} = 2.41 eV, 2.47 eV, 2.50 eV, 2.54 eV, 2.60 eV, 2.62 eV, 2.66 eV, and 2.71 eV, which excite metallic nanotubes, were considered. For the 100 nm long tubes, 54 spectra (data points) were included in the calculation. The P = 0.05 significance threshold $P_{5\%}^T$ for 54 data points is $P_{5\%}^T$ = 0.27; that is, if $|r_{100}^w| > 0.27$, then the correlation is statistically significant. For the 70 nm long tubes we have 60 data points, with a significance threshold of $P_{5\%}^T = 0.25$. There were 65 data points for the 50 nm tubes, with $P_{5\%}^T = 0.24$. Table 4-1 also lists the correlation coefficients for the full data set of 179 points, which includes all available nanotube lengths (100 nm, 70 nm, and 50 nm). For 179 data points, the significance threshold is $P_{5\%}^T = 0.15$. The table then contains 28 entries, some of which are correlated in each of the four columns, and others that are anticorrelated in each of four columns. Another category would be entries that are uncorrelated in each column. These three categories, for which length is not a factor

in the correlation, are treated in section 4.2. Finally, there are cases where a mixed message is delivered from the four columns and further investigation is needed, and the entries in this category are treated in section 4.3. In Table 4-1, the 28 entries are numbered for convenient referencing with the text.

Table 4-1. Weighted correlation coefficients $r^w(X,Y)$ between the G-band parameters X and Y.

#	X	Y	$r^w_{100}(X,Y)$ $P^T_{5\%}=0.27$	$r^w_{70}(X,Y)$ $P^T_{5\%}=0.25$	$r^w_{50}(X,Y)$ $P^T_{5\%}=0.24$	$r^w_{all}(X,Y)$ $P^T_{5\%}=0.1$
1	$(FWHM)_{G^-}$	$[1/q]_{G^-}$	0.168	0.311	0.328	-0.036
2	$(FWHM)_{G^-}$	$(\omega_{G^+}-\omega_{G^-})$	0.181	0.358	-0.173	0.180
3	$(FWHM)_{G^-}$	integrated $[I_{G^-}/I_{G^+}]$	-0.071	-0.335	-0.159	-0.117
4	$(FWHM)_{G^-}$	peak $[\hat{I}_{G^-}/\hat{I}_{G^+}]$	-0.279	-0.611	-0.553	-0.524
5	$(FWHM)_{G^-}$	ω_{G^-}	-0.22	-0.279	0.008	-0.213
6	$(FWHM)_{G^-}$	ω_{G^+}	-0.097	-0.073	-0.205	-0.087
7	$(FWHM)_{G^-}$	$(FWHM)_{G^+}$	-0.225	-0.217	-0.281	-0.397
8	$[1/q]_{G^-}$	$(\omega_{G^+}-\omega_{G^-})$	0.575	0.142	0.112	0.032
9	$[1/q]_{G^-}$	integrated $[I_{G^-}/I_{G^+}]$	0.0402	-0.246	-0.066	-0.105
10	$[1/q]_{G^-}$	peak $[\hat{I}_{G^-}/\hat{I}_{G^+}]$	0.265	-0.011	-0.930	0.279
11	$[1/q]_{G^-}$	ω_{G^-}	-0.233	0.092	0.037	0.087
12	$[1/q]_{G^-}$	ω_{G^+}	0.436	0.251	0.190	0.170
13	$[1/q]_{G^-}$	$(FWHM)_{G^+}$	0.0295	-0.076	-0.028	0.362
14	$(\omega_{G^+}-\omega_{G^-})$	integrated $[I_{G^-}/I_{G^+}]$	0.103	-0.503	-0.105	0.111
15	$(\omega_{G^+}-\omega_{G^-})$	peak $[\hat{I}_{G^-}/\hat{I}_{G^+}]$	0.028	-0.200	0.045	-0.008
16	$(\omega_{G^+}-\omega_{G^-})$	ω_{G^-}	-0.786	-0.696	-0.704	-0.750
17	$(\omega_{G^+}-\omega_{G^-})$	ω_{G^+}	-0.149	-0.089	0.302	0.170
18	$(\omega_{G^+}-\omega_{G^-})$	$(FWHM)_{G^+}$	-0.545	-0.282	0.318	0.158
19	integrated	peak	0.336	0.851	0.791	0.616

#	X	Y	$r^w_{100}(X,Y)$ $P^T_{5\%}=0.27$	$r^w_{70}(X,Y)$ $P^T_{5\%}=0.25$	$r^w_{50}(X,Y)$ $P^T_{5\%}=0.24$	$r^w_{all}(X,Y)$ $P^T_{5\%}=0.1$
	$[I_{G^-}/I_{G^+}]$	$[\hat{I}_{G^-}/\hat{I}_{G^+}]$				
20	integrated $[I_{G^-}/I_{G^+}]$	ω_{G^-}	0.153	0.0126	0.112	-0.014
21	integrated $[I_{G^-}/I_{G^+}]$	ω_{G^+}	0.389	-0.027	0.026	0.122
22	integrated $[I_{G^-}/I_{G^+}]$	$(FWHM)_{G^+}$	0.545	0.186	-0.159	0.096
23*	ω_{G^-}	peak $[\hat{I}_{G^-}/\hat{I}_{G^+}]$	0.278	0.255	0.192	0.173
24	ω_{G^+}	peak $[\hat{I}_{G^-}/\hat{I}_{G^+}]$	0.613	0.179	0.315	0.241
25	$(FWHM)_{G^+}$	peak $[\hat{I}_{G^-}/\hat{I}_{G^+}]$	0.696	0.376	0.306	0.559
26	ω_{G^-}	ω_{G^+}	0.494	0.778	0.465	0.534
27	ω_{G^-}	$(FWHM)_{G^+}$	0.514	0.583	0.030	0.292
28	ω_{G^+}	$(FWHM)_{G^+}$	0.448	0.562	0.437	0.305

Table 4-1. Weighted correlation coefficients $r^w(X,Y)$ between the G-band parameters X and Y. The weighted correlation coefficients r^w_{100}, r^w_{70}, r^w_{50}, and r^w_{all} for 100 nm, 70 nm, 50 nm tubes, and the entire dataset of mixed lengths, respectively, are listed. Values for the P = 0.05 significance threshold $P^T_{5\%}$ for each of the groups of data points are also listed in the column header. Each row is numbered for easy referencing of every correlation pair from the text.

4.2 Intrinsic G-band Behavior

We first use the results summarized in Table 4-1 to determine the correlations that are intrinsic to carbon nanotubes, rather than those that are related to one another through their length dependence. We divide the entries in Table 4-1 into four categories. The first category consists of entries for which X and Y are consistently uncorrelated; that is, all

four correlation coefficients r_{100}^{w}, r_{70}^{w}, r_{50}^{w}, and r_{all}^{w} between X and Y are below their respective P = 0.05% significance thresholds $P_{5\%}^{T}$. Similarly, the second category consists of entries for which X and Y are correlated. The third category is just like the second category, except that the negative correlation coefficients indicate anticorrelation. Finally, the fourth category ("Other") consists of X-Y pairs for which r_{100}^{w}, r_{70}^{w}, r_{50}^{w} and r_{all}^{w} do not agree with each other in terms of the sign and magnitude of the correlation coefficient. For some entries in the fourth category, the existing data are not complete enough to draw conclusions. However, other entries in the fourth category give insights into nanotube physics and will be discussed in section 4.3. Table 4-2 shows the entries in Table 4-1 grouped into the four categories mentioned above. The uncorrelated, correlated, and anticorrelated X-Y pairs will be discussed in this section.

Table 4-2. G-band parameters that are "Uncorrelated," "Correlated," "Anticorrelated," and "Other."

Uncorrelated		Correlated		Anticorrelated		Other	
#6	$(FWHM)_{G^-}$ vs. ω_{G^+}	#19	integrated $[I_{G^-}/I_{G^+}]$ vs. peak $[\hat{I}_{G^-}/\hat{I}_{G^+}]$	#4	$(FWHM)_{G^-}$ vs. peak $[\hat{I}_{G^-}/\hat{I}_{G^+}]$	#1	$(FWHM)_{G^-}$ vs. $[1/q]_{G^-}$
#9	$[1/q]_{G^-}$ vs. integrated $[I_{G^-}/I_{G^+}]$	#23*	peak $[\hat{I}_{G^-}/\hat{I}_{G^+}]$ vs. ω_{G^-}	#16	$(\omega_{G^+}-\omega_{G^-})$ vs. ω_{G^-}	#2	$(FWHM)_{G^-}$ vs. $(\omega_{G^+}-\omega_{G^-})$
#11	$[1/q]_{G^-}$ vs. ω_{G^-}	#24	peak $[\hat{I}_{G^-}/\hat{I}_{G^+}]$ vs. ω_{G^+}			#3	$(FWHM)_{G^-}$ vs. integrated $[I_{G^-}/I_{G^+}]$
#15	$(\omega_{G^+}-\omega_{G^-})$ vs. peak $[\hat{I}_{G^-}/\hat{I}_{G^+}]$	#25	peak $[\hat{I}_{G^-}/\hat{I}_{G^+}]$ vs. $(FWHM)_{G^+}$			#5	$(FWHM)_{G^-}$ vs. ω_{G^-}
#20	integrated $[I_{G^-}/I_{G^+}]$ vs. ω_{G^-}	#26	ω_{G^-} vs. ω_{G^+}			#7	$(FWHM)_{G^-}$ vs. $(FWHM)_{G^+}$
		#28	ω_{G^+} vs. $(FWHM)_{G^+}$			#8	$[1/q]_{G^-}$ vs. $(\omega_{G^+}-\omega_{G^-})$
						#10	$[1/q]_{G^-}$ vs. peak $[\hat{I}_{G^-}/\hat{I}_{G^+}]$

Uncorrelated		Correlated		Anticorrelated		Other	
						#12	$[1/q]_{G^-}$ vs. ω_{G^+}
						#13	$[1/q]_{G^-}$ vs. $(FWHM)_{G^+}$
						#14	$(\omega_{G^+} - \omega_{G^-})$ vs. integrated $[I_{G^-} / I_{G^+}]$
						#17	$(\omega_{G^+} - \omega_{G^-})$ vs. ω_{G^+}
						#18	$(\omega_{G^+} - \omega_{G^-})$ vs. $(FWHM)_{G^+}$
						#21	integrated $[I_{G^-} / I_{G^+}]$ vs. ω_{G^+}
						#22	integrated $[I_{G^-} / I_{G^+}]$ vs. $(FWHM)_{G^+}$
						#27	ω_{G^-} vs. $(FWHM)_{G^+}$

Table 4-2. The entries from Table 4-1, sorted into four categories: "Uncorrelated," "Correlated," "Anticorrelated," and "Other." The numbers after the # symbol refer to the row numbers in Table 4-1. The "Uncorrelated," "Correlated," and "Anticorrelated" categories refer to the *X-Y* pairs for which length is not a factor in the correlation (or lack thereof). A star (*) next to the corresponding number refers to a case where not all the r^w are consistent, but borderline values for r^w and physical arguments lead to the assignment of that case to a category other than "Other." The "Other" category refers to the cases where r^w_{100}, r^w_{70}, r^w_{50}, and r^w_{all} are inconsistent with each other.

The correlation coefficients r^w_{100}, r^w_{70}, r^w_{50}, and r^w_{all} between $(FWHM)_{G^-}$ and ω_{G^+}. [#6 in Tables 4-1 and 4-2] are all below their respective P = 0.05% significance thresholds $P^T_{5\%}$. Therefore, regardless of length, $(FWHM)_{G^-}$ and ω_{G^+} are uncorrelated.

This is not surprising because the two quantities are properties of the separate G-band features G^- and G^+.

Significant anticorrelation coefficients were found between the $(FWHM)_{G^-}$ and peak $[\hat{I}_{G^-}/\hat{I}_{G^+}]$ ratio [#4], for the different lengths of tubes taken individually or combined. This means that when the G^- linewidth broadens, the peak $[\hat{I}_{G^-}/\hat{I}_{G^+}]$ ratio decreases. This is an indication that the amount of electron-phonon coupling, which is related to the G^- linewidth [6], is tied to the peak $[\hat{I}_{G^-}/\hat{I}_{G^+}]$ ratio.

The frequency shift $(\omega_{G^+}-\omega_{G^-})$ and peak $[\hat{I}_{G^-}/\hat{I}_{G^+}]$ [#15] ratio are uncorrelated, since all four coefficients r^w_{100}, r^w_{70}, r^w_{50}, and r^w_{all} fall below the significance threshold $P^T_{5\%}$. The lack of correlation may be an indication of two different effects taking place. The frequency shift $(\omega_{G^+}-\omega_{G^-})$ is a geometric effect that comes from the splitting of the graphite G-band into LO (carbon atom vibrations along the nanotube axis) and TO (vibrations along the circumference) phonon modes [7, 8]. On the other hand, as discussed above, the peak $[\hat{I}_{G^-}/\hat{I}_{G^+}]$ ratio could be related to electron-phonon coupling.

The integrated $[I_{G^-}/I_{G^+}]$ ratio and ω_{G^-} are uncorrelated [#20], since all the r^w are below threshold. Similarly, the integrated $[I_{G^-}/I_{G^+}]$ ratio and $[1/q]_{G^-}$ [#9] are also uncorrelated.

The integrated $[I_{G^-}/I_{G^+}]$ ratio and peak $[\hat{I}_{G^-}/\hat{I}_{G^+}]$ ratio [#19] are correlated for each of the tube lengths and also are correlated overall.

The peak $[\hat{I}_{G^-}/\hat{I}_{G^+}]$ ratio and $(FWHM)_{G^+}$ [#25] are correlated for all the tube lengths and for the entire dataset. That is, as $(FWHM)_{G^+}$ increases, $[\hat{I}_{G^-}/\hat{I}_{G^+}]$ also increases. It is possible that a broadening in the G^+ lineshape is accompanied by a decrease in the G^+ peak intensity, which causes the peak $[\hat{I}_{G^-}/\hat{I}_{G^+}]$ ratio to increase. Figure 4-1 shows a scatter plot of the peak $[\hat{I}_{G^-}/\hat{I}_{G^+}]$ ratio vs. $(FWHM)_{G^+}$, along with linear fits to the data points.

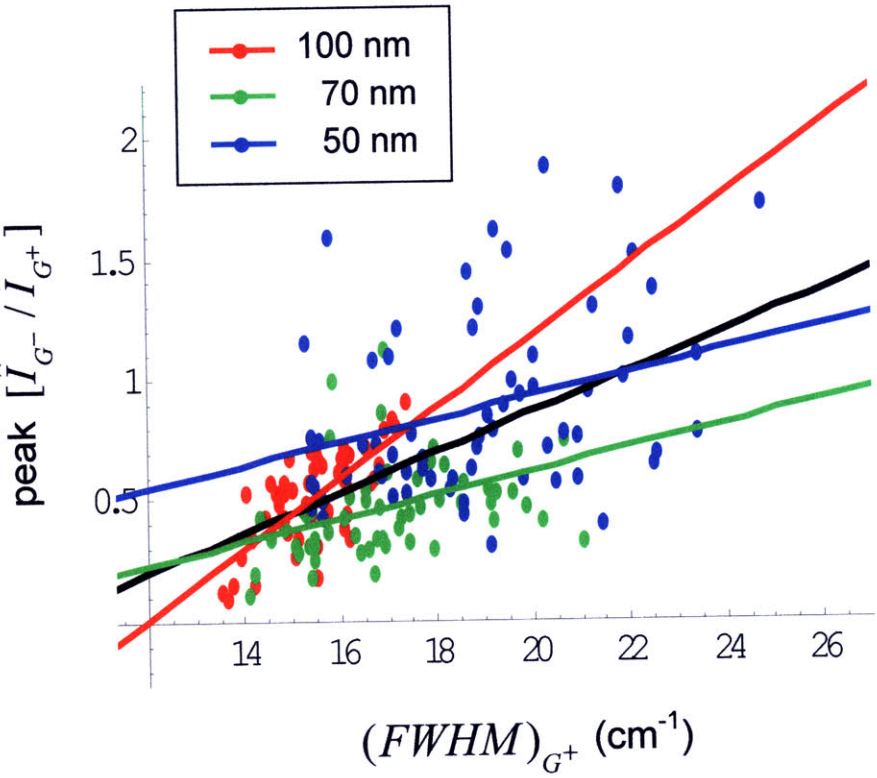

Figure 4-1. Scatter plot of the peak $[\hat{I}_{G^-} / \hat{I}_{G^+}]$ ratio vs. $(FWHM)_{G^+}$. The red, green, and blue points correspond to 100 nm, 70 nm, and 50 nm tubes, respectively. The red, green, and blue lines are linear fits to the 100 nm, 70 nm, and 50 nm data. The black line is the linear fit to all data points. The linear fit to all data points is shown in Table 4-3.

The frequencies ω_{G^-} and ω_{G^+} [#26] are correlated for each of the nanotube lengths and for the entire dataset. This means that if the G^+ peak shifts in frequency, the G^- peak accompanies the shift. Figure 4-2 plots ω_{G^-} vs. ω_{G^+}. From the plot we see that the data points fall roughly into two groups: one group with ω_{G^+} around 1605 cm^{-1} and ω_{G^-} around 1555 cm^{-1}, and a second group with ω_{G^+} around 1590 cm^{-1} with ω_{G^-} around 1535 cm^{-1}. The spectra for which ω_{G^+} is around 1605 cm^{-1} are those which were taken with E_{laser} = 501.7 nm (2.47 eV). At this laser line, a mixture of semiconducting and metallic nanotubes were excited (Table 2-1). However, spectra taken with the other laser lines also excite a mixture of semiconducting and metallic tubes, yet show a G^+ frequency of around 1590 cm^{-1}.

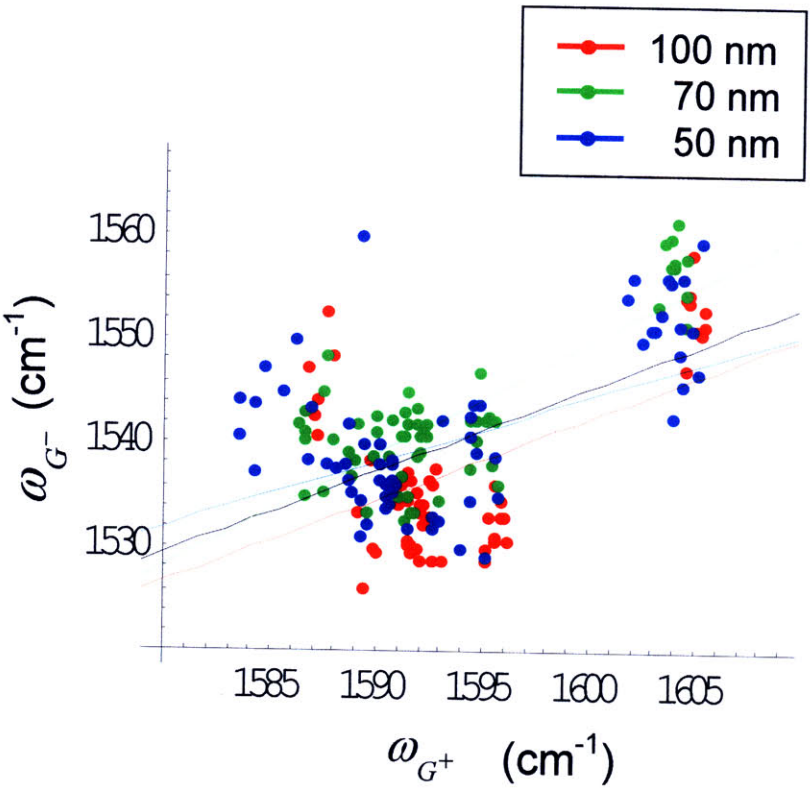

Figure 4-2. Scatter plot of ω_{G^-} vs. ω_{G^+}. The red, green, and blue points correspond to 100 nm, 70 nm, and 50 nm tubes, respectively. The red, green, and blue lines are linear fits to the 100 nm, 70 nm, and 50 nm data. The black line is the linear fit to all data points. The linear fit to all data points is shown in Table 4-3.

The G^+ peak properties, ω_{G^+} and $(FWHM)_{G^+}$ [#28], are correlated for all nanotube lengths and for the entire dataset. Figure 4-3 shows the scatter plot of $(FWHM)_{G^+}$ vs. ω_{G^+}.

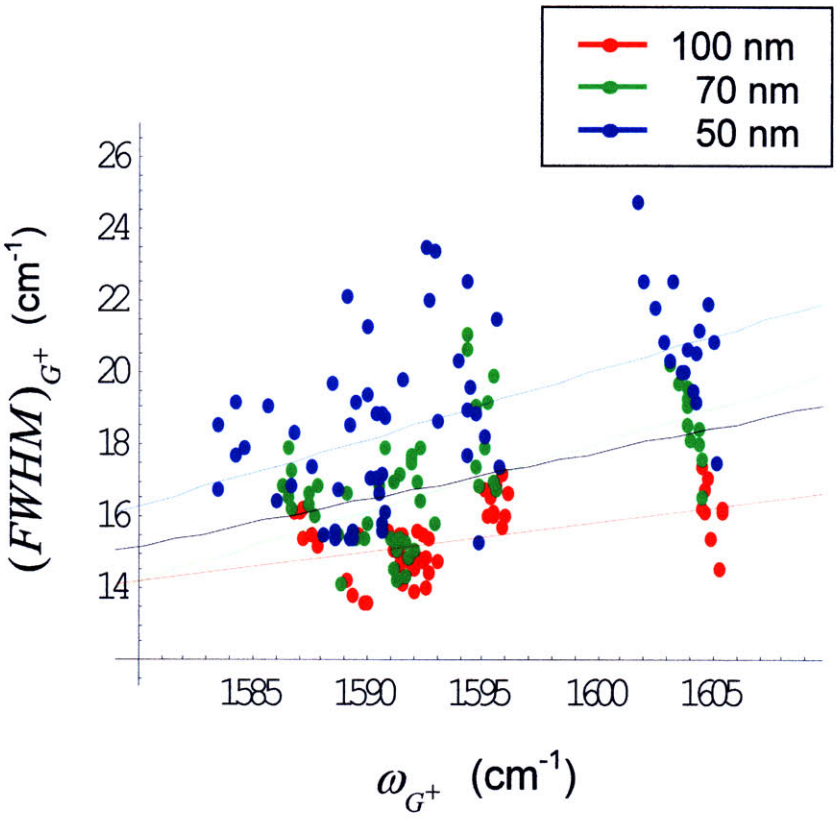

Figure 4-3. Scatter plot of $(FWHM)_{G^+}$ vs. ω_{G^+}. The red, green, and blue points correspond to 100 nm, 70 nm, and 50 nm tubes, respectively. The red, green, and blue lines are linear fits to the 100 nm, 70 nm, and 50 nm data. The black line is the linear fit to all data points. The linear fit to all data points is shown in Table 4-3.

$(\omega_{G^+} - \omega_{G^-})$ and ω_{G^+} [#16] are anticorrelated for each of the nanotube lengths and overall. This is expected and says that as ω_{G^-} decreases, the frequency difference $(\omega_{G^+} - \omega_{G^-})$ increases.

The scatter plot of the peak $[\hat{I}_{G^-} / \hat{I}_{G^+}]$ ratio vs. ω_{G^-} [#23] is shown in Figure 4-4. The calculated correlation coefficients for this pair are not entirely consistent, since $r^w_{100}(X,Y) = 0.309$, $r^w_{70} = 0.255$ and $r^w_{all} = 0.203$ are all above their respective P = 0.05 significance thresholds, but $r^w_{50} = 0.192$ is not. Yet we include this pair in the "Correlated" category for physical reasons. When ω_{G^-} decreases, its area becomes more

spread out, and so the peak $[\hat{I}_{G^-}/\hat{I}_{G^+}]$ ratio decreases. For similar reasons, the peak $[\hat{I}_{G^-}/\hat{I}_{G^+}]$ ratio vs. ω_{G+} pair [#24] are correlated (Figure 4-5).

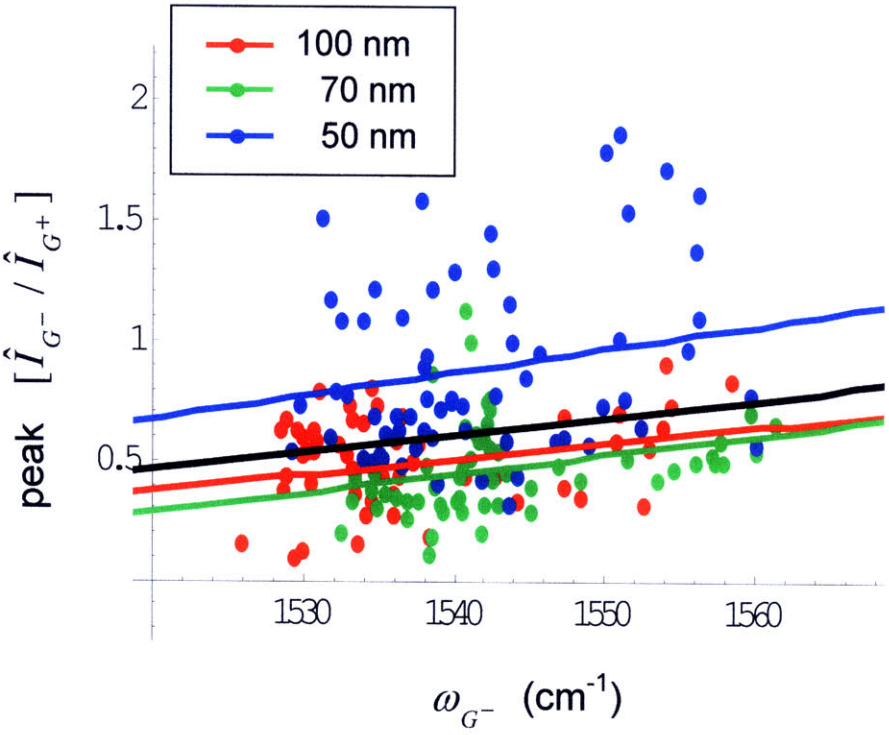

Figure 4-4. Scatter plot of peak $[\hat{I}_{G^-}/\hat{I}_{G^+}]$ ratio vs. ω_{G^-}. The red, green, and blue points correspond to 100 nm, 70 nm, and 50 nm tubes, respectively. The red, green, and blue lines are linear fits to the 100 nm, 70 nm, and 50 nm data. The black line is the linear fit to all data points. The linear fit to all data points is shown in Table 4-3.

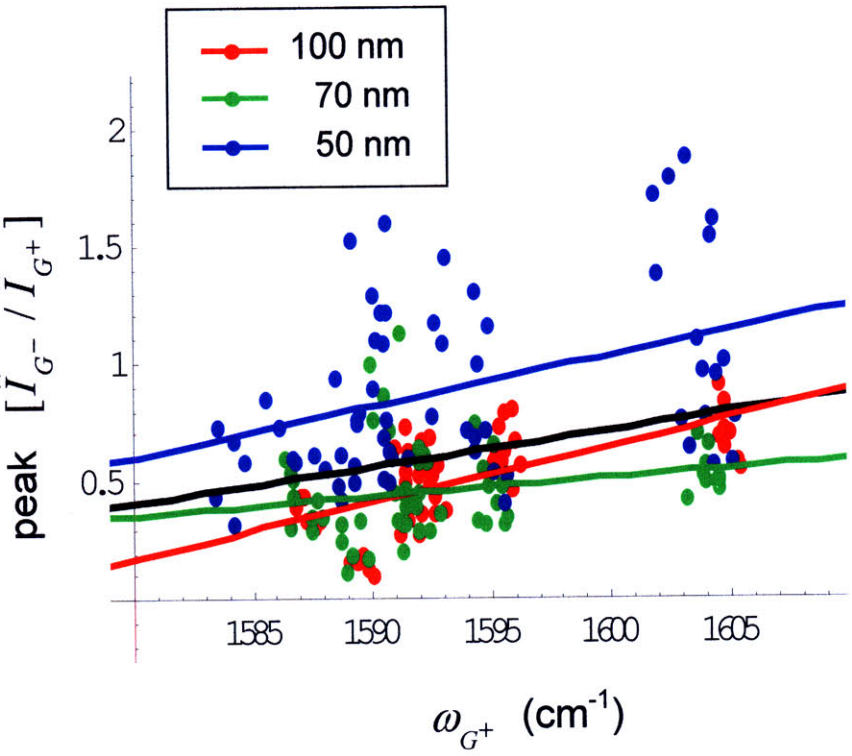

Figure 4-5. Scatter plot of peak $[\hat{I}_{G^-} / \hat{I}_{G^+}]$ ratio vs. ω_{G^+}. The red, green, and blue points correspond to 100 nm, 70 nm, and 50 nm tubes, respectively. The red, green, and blue lines are linear fits to the 100 nm, 70 nm, and 50 nm data. The black line is the linear fit to all data points. The linear fit to all data points is shown in Table 4-3.

Table 4-3 lists the pairs of G-band parameters for which we can conclude a correlation or lack of, regardless of nanotube length. For the parameters that are correlated, the linear fit to the entire dataset and confidence intervals are shown.

#	X	Y	Correlated, anti-correlated, or un-correlated?	Linear fit of Y vs. X	Confidence interval (m_1, m_2) of slope	Confidence interval (b_1, b_2) of y-intercept
#4	$(FWHM)_{G^-}$	peak $[\hat{I}_{G^-}/\hat{I}_{G^+}]$	Anti-correlated	Y = -0.013 X + 1.42	(-0.016, -0.010)	(1.22, 1.63)
#6	ω_{G^+}	$(FWHM)_{G^-}$	Un-correlated	-	-	-
	$[1/q]_{G^-}$	$(FWHM)_{G^+}$	correlated	Y = 12.5 X + 18.3	(7.70, 17.2)	(17.7, 19.0)
#15	$(\omega_{G^+}-\omega_{G^-})$	peak $[\hat{I}_{G^-}/\hat{I}_{G^+}]$	Un-correlated	-	-	-
#16	ω_{G^-}	$(\omega_{G^+}-\omega_{G^-})$	Anti-correlated	Y = -0.642 X + 1040	(-0.726, -0.558)	(913, 1170)
#19	peak $[\hat{I}_{G^-}/\hat{I}_{G^+}]$	integrated $[I_{G^-}/I_{G^+}]$	correlated	Y = 1.57 X + 1.58	(1.27, 1.87)	(1.37, 1.80)
#20	integrated $[I_{G^-}/I_{G^+}]$	ω_{G^-}	Un-correlated	-	-	-
#23*	ω_{G^-}	peak $[\hat{I}_{G^-}/\hat{I}_{G^+}]$	correlated	Y = 0.007 X − 10.8	(0.001, 0.014)	(-20.4, -1.12)
#24	ω_{G^+}	peak $[\hat{I}_{G^-}/\hat{I}_{G^+}]$	correlated	Y = 0.015 X − 24.0	(0.006, 0.025)	(-38.7, -9.24)
#25	$(FWHM)_{G^+}$	peak $[\hat{I}_{G^-}/\hat{I}_{G^+}]$	correlated	Y = -0.083 X − 0.790	(0.065, 0.101)	(-1.10, -0.481)
#26	ω_{G^+}	ω_{G^-}	correlated	Y = 0.798 X + 268	(0.611, 0.985)	(-29.9, 567)
#28	ω_{G^+}	$(FWHM)_{G^+}$	correlated	Y = 0.132 X − 193	(0.071, 0.193)	(-290, -95.9)

Table 4-3. The pairs of G-band parameters that have a clear correlation, anticorrelation, or no correlation, regardless of nanotube length. For the parameters that are correlated (or anticorrelated), the linear fit to the entire dataset (179 points) and confidence intervals are shown.

4.3 Correlations for Which Length is a Factor

In Table 4-2 there are some X-Y pairs whose correlation coefficients are inconsistent for different lengths of nanotubes. An example is the relation between $[1/q]_{G^-}$ and $(\omega_{G^+}-\omega_{G^-})$ [#8]. The 70 nm and 50 nm tubes show no correlation between

$[1/q]_{G^-}$ and $(\omega_{G^+} - \omega_{G^-})$, since r_{70}^{w} = 0.142 and r_{50}^{w} = 0.112, which are both below threshold. However, for the longest tubes there is a correlation: r_{100}^{w} = 0.575. Figure 4-6 shows a scatter plot of $(\omega_{G^+} - \omega_{G^-})$ vs. $[1/q]_{G^-}$, along with the linear fits for the different lengths of tubes. The slope for the 100 nm tubes is clearly greater than those of the 70 nm and 50 nm tubes. Also, the length dependence for the $[1/q]_{G^-}$ parameter can be seen. The red dots (100 nm tubes) tend to cluster towards more negative $[1/q]_{G^-}$, indicative of a more Breit-Wigner-Fano lineshape. The blue dots (50 nm tubes) tend to cluster near the $(\omega_{G^+} - \omega_{G^-})$ axis, indicating a more Lorentzian lineshape, and the green dots (70 nm tubes) are in between the red and blue. This length dependence of $[1/q]_{G^-}$ was discussed in Chapter 3.

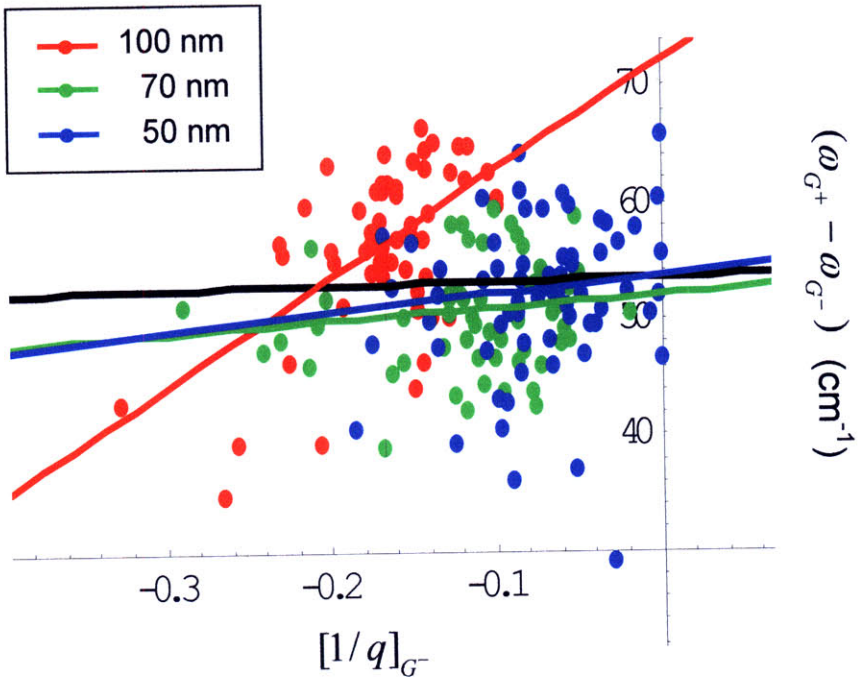

Figure 4-6. Scatter plot of $(\omega_{G^+} - \omega_{G^-})$ vs. $[1/q]_{G^-}$ [#8]. The red, green, and blue points correspond to 100 nm, 70 nm, and 50 nm tubes, respectively. The red, green, and blue lines are linear fits to the 100 nm, 70 nm, and 50 nm data. The black line is the linear fit to all data points.

The inconsistencies in the correlation coefficients for different lengths of nanotubes may be related to the different lineshapes observed for longer vs. shorter tubes. Figure 4-7(a) shows the spectra for 50 nm tubes measured with E_{laser} = 488 nm (2.54 eV). For some spots, (spots 1, 3, 4, 5, 6 and 8), the G^- peak intensity becomes quite high, surpassing the G^+ peak intensity in some cases. In Figure 4-7(b), the spectra for 100 nm tubes measured with E_{laser} = 488 nm (2.54 eV) are shown. In this case, the spectra have the broad Breit-Wigner-Fano (BWF) feature for the G^- peak, but none of the spectra have the high G^- peak intensity seen in the 50 nm tubes. The 100 nm tubes can be associated with more "BWF-type" spectra, while the 50 nm tubes can be associated with "high G^- intensity -type" spectra. The two different types of spectra could have different correlation properties among the G-band parameters. The spectra for 70 nm tubes measured with E_{laser} = 2.54 eV are also shown in Figure 4-7(c).

In the discussion to follow we will address two types of correlations: correlations that appear for the longer tubes (and possibly describe BWF-type spectra), and correlations that appear for the shorter tubes (and possibly describe high G^- intensity -type spectra).

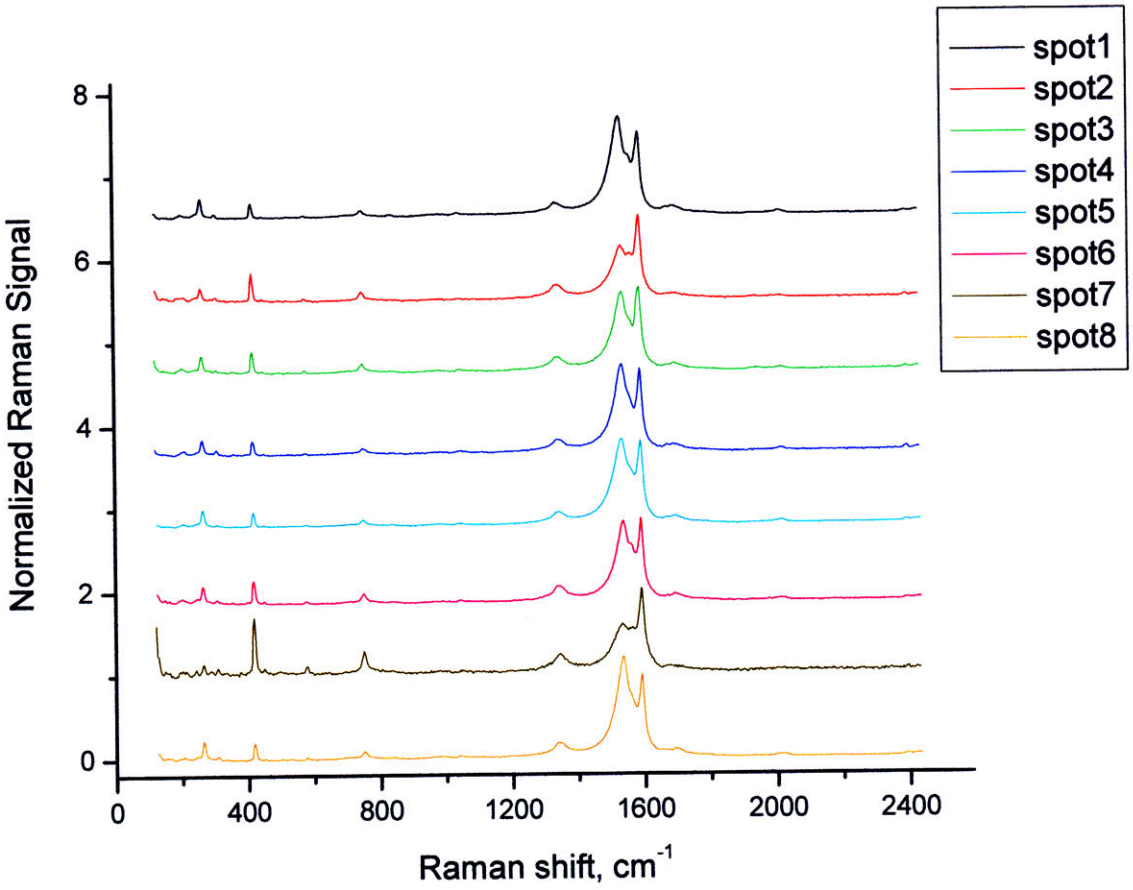

Figure 4-7(a) Raman spectra for different spots on a sample. The laser excitation energy is 488 nm (2.54 eV) and the average nanotube length is 50 nm. After a baseline was subtracted, the spectra were normalized to the G^+ peak and offset from each other.

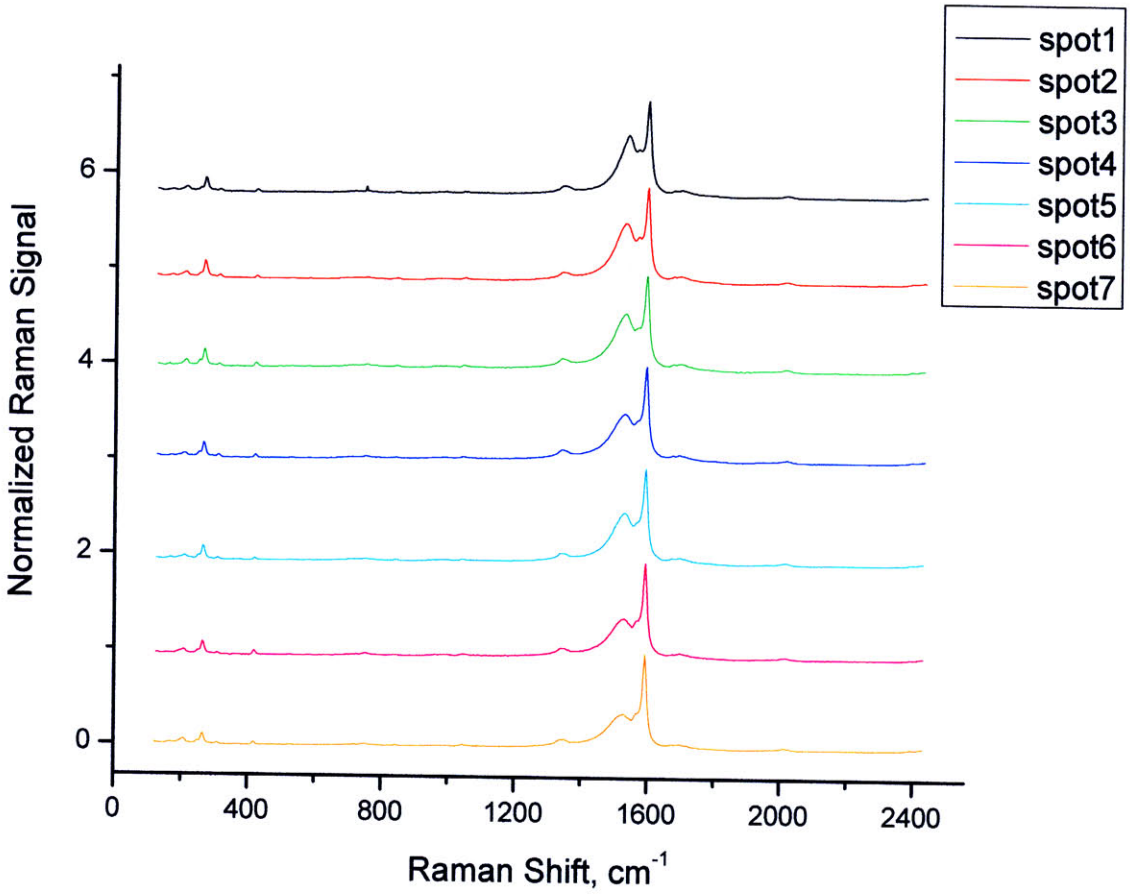

Figure 4-7(b). Raman spectra for different spots on a sample. The laser excitation energy is 488 nm (2.54 eV) and the average nanotube length is 100 nm. After a baseline was subtracted, the spectra were normalized to the G^+ peak and offset from each other.

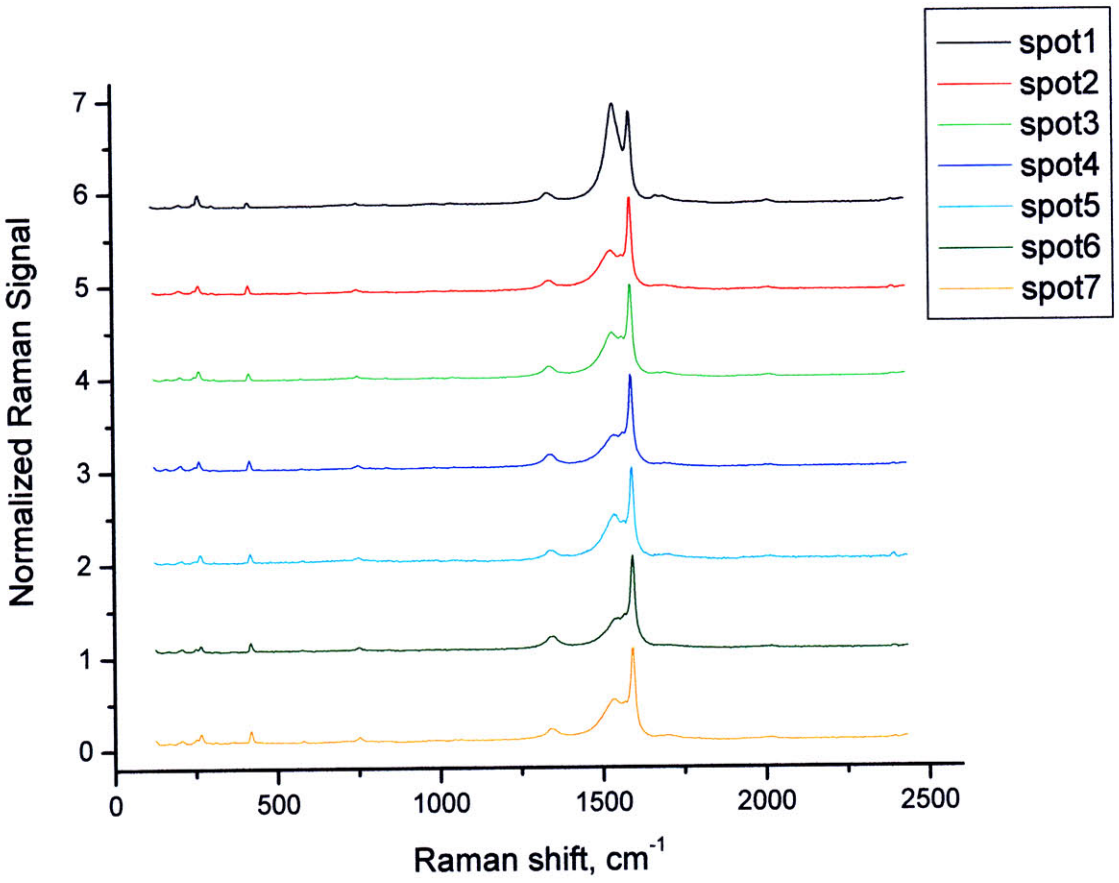

Figure 4-7(c). Raman spectra for different spots on a sample. The laser excitation energy is 488 nm (2.54 eV) and the average nanotube length is 70 nm. After a baseline was subtracted, the spectra were normalized to the G^+ peak and offset from each other.

4.3.1 Correlations that Appear for Longer Nanotubes

In this section we discuss the correlations that appear for the longer nanotubes (100 nm and sometimes 70 nm length), which likely describe the properties of the BWF lineshape for metallic carbon nanotubes.

We had discussed above the relation between $[1/q]_{G^-}$ and $(\omega_{G^+} - \omega_{G^-})$ [#8]. The scatter plot is shown in Figure 4-7. For 100 nm long tubes, there is a correlation between $[1/q]_{G^-}$ and $(\omega_{G^+} - \omega_{G^-})$. The correlations tell us that as the lineshape becomes more Lorentzian, the frequency shift increases. The linear fit is $(\omega_{G^+} - \omega_{G^-}) = 93.6\ [1/q]_{G^-} + 72.3$ with confidence intervals of (56.6, 130.6) cm^{-1} for the slope and (65.7, 78.9) cm^{-1} for

the intercept. The $[1/q]_{G^-}$ for 100 nm long tubes span a range of about -0.331 to -0.094. Within this $[1/q]_{G^-}$ range, $(\omega_{G^+} - \omega_{G^-})$ increases from about 42 cm^{-1} to 64 cm^{-1} as the lineshape becomes more Lorentzian, according to the linear fit.

The G^- frequency ω_{G^-} and $(FWHM)_{G^+}$ [#27] are correlated for the 100 nm and the 70 nm tubes, but not for the 50 nm tubes. Hence for the longer nanotubes, as the G^- frequency increases, the G^+ lineshape broadens. The linear fit for 100 nm tubes is $(FWHM)_{G^+} = 0.058\ \omega_{G^-} - 74.6$, with confidence intervals of (0.031, 0.086) for the slope and (-116, -32.9) cm^{-1} for the intercept. Figure 4-8 shows the plot of $(FWHM)_{G^+}$ vs. ω_{G^-}. Over the range of ω_{G^-} measured for 100 nm tubes, the linear fit gives an increase of $(FWHM)_{G^+}$ from only about 15 cm^{-1} to 17 cm^{-1}, and thus the effect is small.

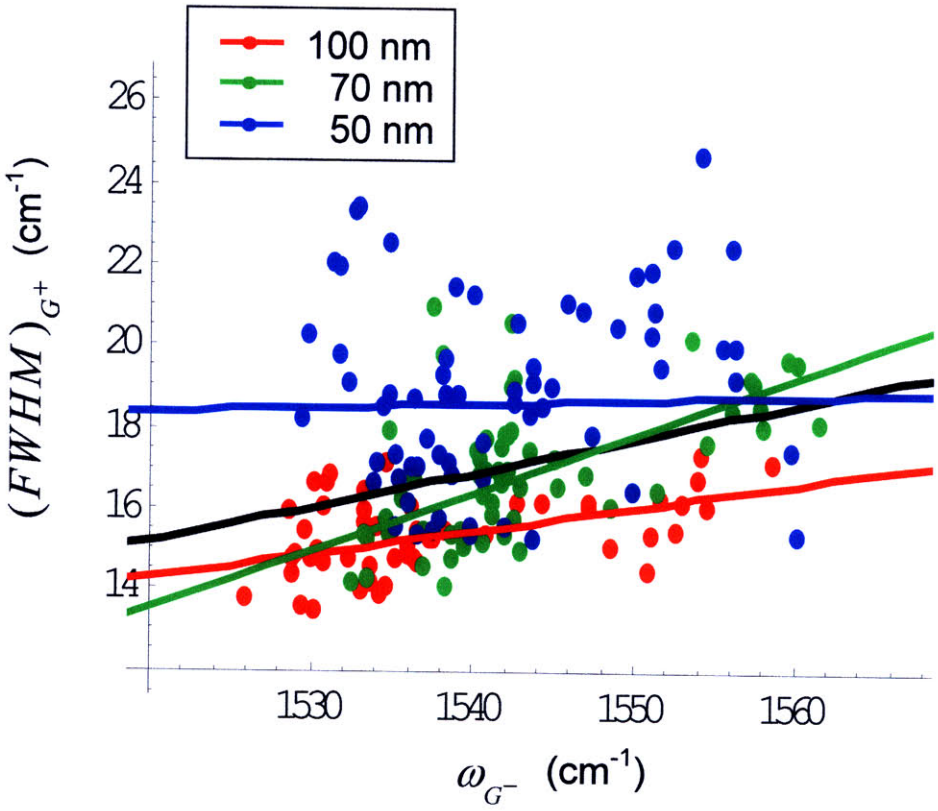

Figure 4-8. Scatter plot of $(FWHM)_{G^+}$ vs. ω_{G^-} [#27]. The red, green, and blue points correspond to 100 nm, 70 nm, and 50 nm tubes, respectively. The red, green, and blue lines are linear fits to the 100 nm, 70 nm, and 50 nm data. The black line is the linear fit to all data points.

The G^+ frequency ω_{G^+} and $[1/q]_{G^-}$ [#12] are correlated for 100 nm long tubes, correlated but at the P = 0.05 threshold for 70 nm tubes, and uncorrelated for 50 nm long tubes. Figure 4-9 shows the scatter plot of ω_{G^+} vs. $[1/q]_{G^-}$. The slope of the linear fit for 100 nm long tubes is greater than the slopes of the linear fit for 70 nm and 50 nm tubes and all lengths combined. For 100 nm long tubes, as the lineshape becomes more Lorentzian, the G^+ frequency increases. The linear fit for 100 nm long tubes is ω_{G^+} = 50.5 $[1/q]_{G^-}$ + 1602 cm^{-1}, with confidence intervals of (21.5, 79.4) cm^{-1} for the slope and (1597, 1607) cm^{-1} for the intercept. Over the $[1/q]_{G^-}$ range covered by 100 nm long tubes, the linear fit gives a ω_{G^+} change from about 1588 cm^{-1} to 1597 cm^{-1}.

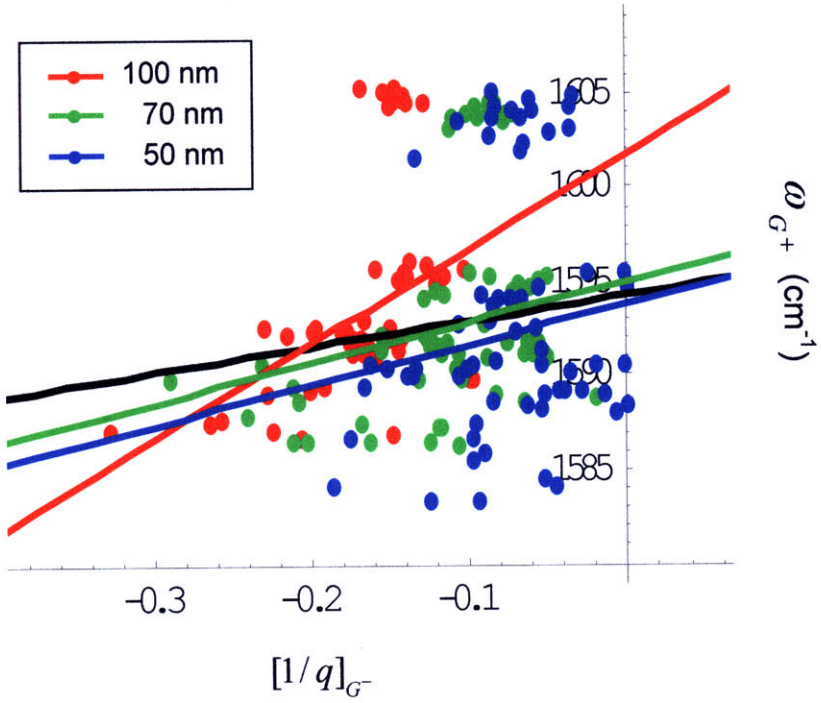

Figure 4-9. Scatter plot of ω_{G^+} vs. $[1/q]_{G^-}$ [#12]. The red, green, and blue points correspond to 100 nm, 70 nm, and 50 nm tubes, respectively. The red, green, and blue lines are linear fits to the 100 nm, 70 nm, and 50 nm data. The black line is the linear fit to all data points.

Figure 4-10 shows the frequency shift $(\omega_{G^+} - \omega_{G^-})$ vs. the G^+ linewidth $(FWHM)_{G^+}$ [#18]. The two parameters are anticorrelated for 100 nm and 70 nm long tubes. The broader the G^+ linewidth, the less the frequency shift. An opposite slope occurs for the 50 nm tubes. The linear fit for 100 nm tubes is $(\omega_{G^+} - \omega_{G^-})$ = -2.06 $(FWHM)_{G^+}$ + 87.5 with confidence intervals of (-4.13, 0.017) for the slope and (55.8, 119) cm^{-1} for the intercept. Over the $(FWHM)_{G^+}$ range covered by 100 nm long tubes, the linear fit gives a $(\omega_{G^+} - \omega_{G^-})$ change from about 60 cm^{-1} to 52 cm^{-1}.

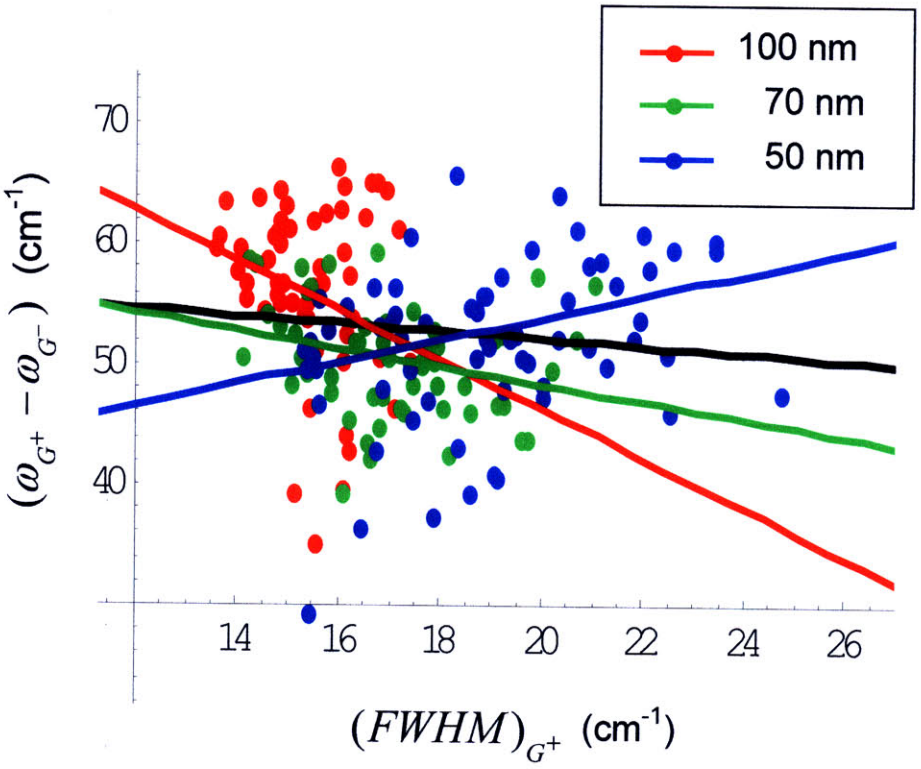

Figure 4-10. Scatter plot of $(\omega_{G^+} - \omega_{G^-})$ vs. $(FWHM)_{G^+}$ [#18]. The red, green, and blue points correspond to 100 nm, 70 nm, and 50 nm tubes, respectively. The red, green, and blue lines are linear fits to the 100 nm, 70 nm, and 50 nm data. The black line is the linear fit to all data points.

For the 100 nm tubes, there is a positive correlation between ω_{G^+} and the integrated $[I_{G^-} / I_{G^+}]$ ratio [#21]. As the G^+ frequency increases, the integrated $[I_{G^-} / I_{G^+}]$ ratio increases as well. The linear fit is $[I_{G^-} / I_{G^+}]$ = 0.069 ω_{G^+} - 107 with confidence intervals of (0.024, 0.115) cm for the slope and (-180, -34.7) for the intercept.

Figure 4-11 shows the scatter plot of integrated $[I_{G^-} / I_{G^+}]$ vs ω_{G^+}. Over the ω_{G^+} range covered by 100 nm long tubes, the linear fit gives an integrated $[I_{G^-} / I_{G^+}]$ change from about 2.5 to 3.7.

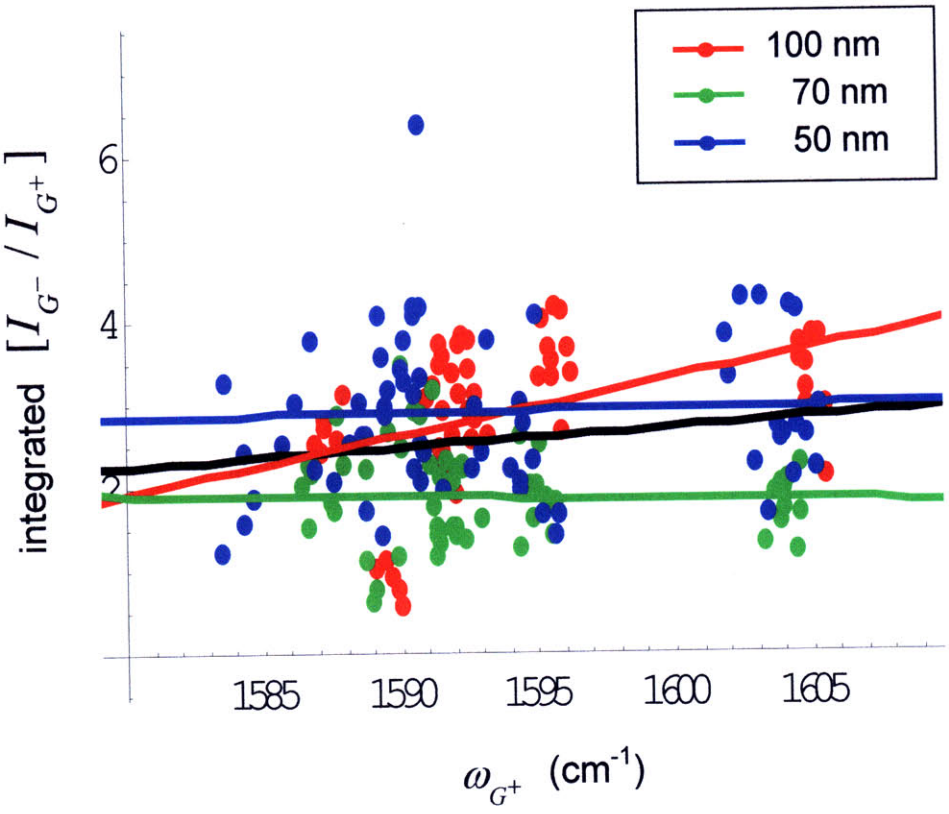

Figure 4-11. Scatter plot of integrated $[I_{G^-} / I_{G^+}]$ vs. ω_{G^+} [#21]. The red, green, and blue points correspond to 100 nm, 70 nm, and 50 nm tubes, respectively. The red, green, and blue lines are linear fits to the 100 nm, 70 nm, and 50 nm data. The black line is the linear fit to all data points.

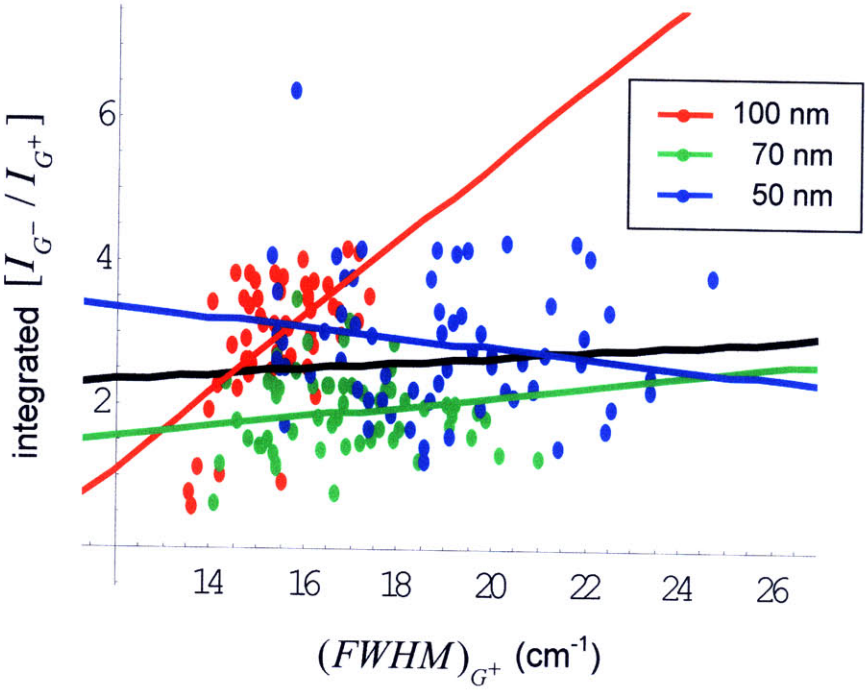

Figure 4-12. Same as Figure 4-12, but plot of integrated $[I_{G^-} / I_{G^+}]$ vs. $(FWHM)_{G^+}$ [#22].

There is also a positive correlation between $(FWHM)_{G^+}$ and the integrated $[I_{G^-} / I_{G^+}]$ ratio [#22] for the 100 nm tubes only. As $(FWHM)_{G^+}$ increases, the integrated $[I_{G^-} / I_{G^+}]$ ratio also increases, consistent with correlation #21. The linear fit is integrated $[I_{G^-} / I_{G^+}] = 0.532\ (FWHM)_{G^+}$ - 5.27 with confidence intervals of (0.304, 0.760) cm for the slope and (-8.76, -1.79) for the intercept. Figure 4-12 shows the scatter plot of integrated $[I_{G^-} / I_{G^+}]$ vs $(FWHM)_{G^+}$. Over the $(FWHM)_{G^+}$ range covered by 100 nm long tubes, the linear fit gives an integrated $[I_{G^-} / I_{G^+}]$ change from about 2 to 4.

Table 4-4 summarizes the *X-Y* pairs for which correlation occurs at longer nanotube lengths, as well as the linear fits and confidence intervals for the 100 nm tubes.

#	X	Y	Linear fit of Y vs. X for 100 nm tubes	Confidence interval (m_1, m_2) of slope	Confidence interval (b_1, b_2) of y-intercept
#8	$[1/q]_{G^-}$	$(\omega_{G^+} - \omega_{G^-})$	$Y = 93.6\,X + 72.3$	(56.6, 130.6) cm^{-1}	(65.7, 78.9) cm^{-1}
#27	ω_{G^-}	$(FWHM)_{G^+}$	$Y = 0.058\,X - 74.6$	(0.031, 0.086)	(-116, -32.9) cm^{-1}
#12	$[1/q]_{G^-}$	ω_{G^+}	$Y = 50.5\,X + 1602$	(21.5, 79.4) cm^{-1}	(1597, 1607) cm^{-1}
#18	$(FWHM)_{G^+}$	$(\omega_{G^+} - \omega_{G^-})$	$Y = -2.06\,X + 87.5$	(-4.13, 0.017)	(55.8, 119) cm^{-1}
#21	ω_{G^+}	integrated $[I_{G^-} / I_{G^+}]$	$Y = 0.069\,X - 107$	(0.024, 0.115) cm	(-180, -34.7)
#22	$(FWHM)_{G^+}$	integrated $[I_{G^-} / I_{G^+}]$	$Y = 0.532\,X - 5.27$	(0.304, 0.760) cm	(-8.76, -1.79)

Table 4-4. The pairs of G-band parameters for which the correlation appears for longer (100 nm) tubes. For the parameters that are correlated (or anticorrelated), the linear fit to the points corresponding to 100 nm tubes and confidence intervals are given in the table.

4.3.2 Correlations that Appear for Shorter Nanotubes

We also observe correlations that appear for the shorter nanotubes (50 nm and maybe 70 nm long) but not for the 100 nm long nanotubes. We associate these correlations with a high G^- intensity rather than the BWF feature.

Figure 4-13 shows the scatter plot of $[1/q]_{G^-}$ vs. $(FWHM)_{G^-}$ [#1]. For 70 nm and 50 nm long tubes, $(FWHM)_{G^-}$ and $[1/q]_{G^-}$ were found to be correlated. Thus, as the G^- peak becomes more symmetric, its lineshape broadens. The linear fit for 50 nm long tubes is $[1/q]_{G^-} = 0.001\,(FWHM)_{G^-} - 0.149$ with confidence intervals of (0.0003, 0.002) cm for the slope and (-0.202, -0.095) for the intercept. The range of $(FWHM)_{G^-}$ for 50 nm long tubes is about 40 – 100 cm^{-1}. The linear fit gives a $[1/q]_{G^-}$ change from -0.1 (for 40 cm^{-1} $(FWHM)_{G^-}$) to -0.03 (for 100 cm^{-1} $(FWHM)_{G^-}$). This trend is unexpected, considering that in Chapter 3 it was found that as nanotubes get shorter, the G^- peak

becomes more Lorentzian and $(FWHM)_{G^-}$ decreases. However, the overall result for all the lengths is that $[1/q]_{G^-}$ and $(FWHM)_{G^-}$ are uncorrelated.

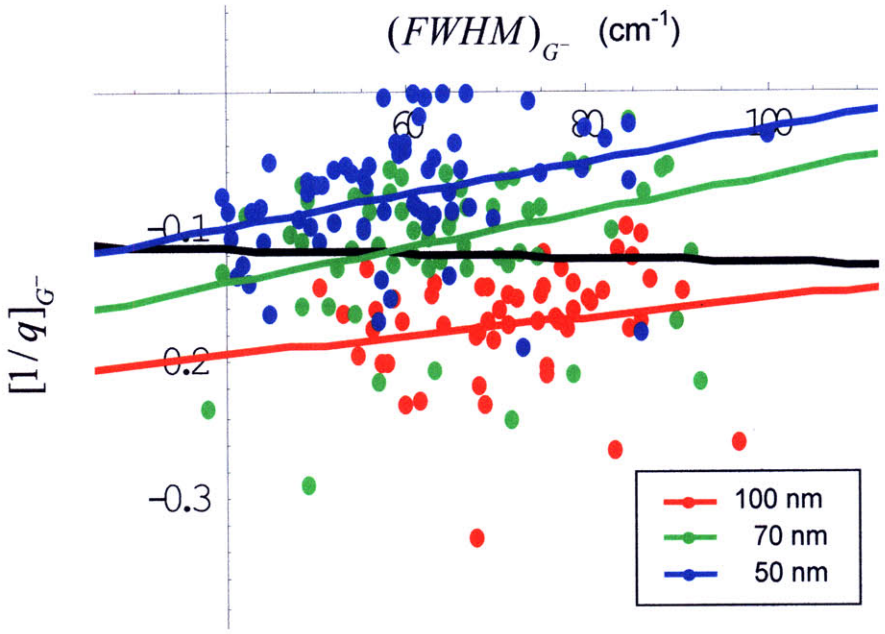

Figure 4-13. Scatter plot of $[1/q]_{G^-}$ vs. $(FWHM)_{G^-}$ [#1]. The red, green, and blue points correspond to 100 nm, 70 nm, and 50 nm tubes, respectively. The red, green, and blue lines are linear fits to the 100 nm, 70 nm, and 50 nm data. The black line is the linear fit to all data points.

Figure 4-14 shows a scatter plot of $(FWHM)_{G^+}$ vs. $(FWHM)_{G^-}$ [#7]. There is an anticorrelation for the shortest (50 nm long) nanotubes, and an overall anticorrelation for all lengths of tubes combined. Thus, when the G^- lineshape narrows, the G^+ lineshape broadens. This is similar to the results from Chapter 3, where it was found that as nanotube length decreases, the G- peak gets narrower while the G^+ lineshape broadens. The length dependence can be seen in Figure 4-14, in which the red points (100 nm tubes) cluster around the lower right, where the G^- lineshape is broad and G^+ is narrow. The blue points (50 nm tubes) cluster around the upper left, where G^- is narrower in its range and G^+ is broader in its range. The linear fit is $(FWHM)_{G^+}$ = -0.051 $(FWHM)_{G^-}$ + 21.6 with confidence intervals of (-0.094, -0.007) for the slope and (18.9, 24.2) cm^{-1} for the intercept. Figure 4-13 shows the scatter plot of integrated $(FWHM)_{G^+}$ vs $(FWHM)_{G^-}$.

Over the $(FWHM)_{G^-}$ range covered by 50 nm long tubes, the linear fit gives a $(FWHM)_{G^+}$ change from about 20 cm^{-1} to 17 cm^{-1}.

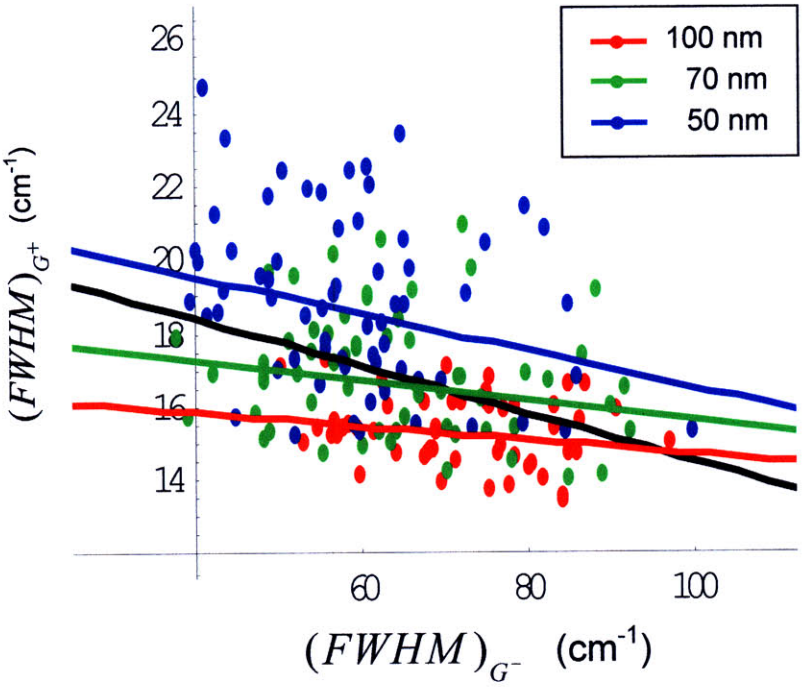

Figure 4-14. Scatter plot of $(FWHM)_{G^+}$ vs. $(FWHM)_{G^-}$ [#7]. The red, green, and blue points correspond to 100 nm, 70 nm, and 50 nm tubes, respectively. The red, green, and blue lines are linear fits to the 100 nm, 70 nm, and 50 nm data. The black line is the linear fit to all data points.

As mentioned in Section 4.3.1, the frequency shift $(\omega_{G^+} - \omega_{G^-})$ and the G^+ linewidth $(FWHM)_{G^+}$ [#18] are anticorrelated for 100 nm and 70 nm long tubes. However, for the 50 nm tubes, the slope is opposite (Figure 4-10): for this case $(\omega_{G^+} - \omega_{G^-})$ and $(FWHM)_{G^+}$ are positively correlated for the shortest tubes. For 50 nm tubes, the broader the G^+ peak, the greater the frequency shift $(\omega_{G^+} - \omega_{G^-})$. The linear fit is $(\omega_{G^+} - \omega_{G^-})$ = 0.913 $(FWHM)_{G^+}$ + 35.6 with confidence intervals of (0.228, 1.60) for the slope and (22.8, 48.4) cm^{-1} for the intercept. Over the $(FWHM)_{G^+}$ range covered by 50 nm long tubes, the linear fit gives a $(\omega_{G^+} - \omega_{G^-})$ change from about 50 cm^{-1} to 58 cm^{-1}.

For 50 nm tubes, $[1/q]_{G^-}$ and the peak $[\hat{I}_{G^-}/\hat{I}_{G^+}]$ ratio [#10] have a large anticorrelation coefficient, although this pair is uncorrelated for 70 nm tubes and borderline for 100 nm tubes. When all tube lengths are considered together, $[1/q]_{G^-}$ and the peak $[\hat{I}_{G^-}/\hat{I}_{G^+}]$ ratio are correlated. For 50 nm long tubes, the linear fit is $[\hat{I}_{G^-}/\hat{I}_{G^+}]$ = -0.708 $[1/q]_{G^-}$ + 0.810, with confidence intervals of (-2.62, 1.20) for the slope and (0.639, 0.980) for the intercept. The scatter plot of peak $[\hat{I}_{G^-}/\hat{I}_{G^+}]$ vs. $[1/q]_{G^-}$ is shown in Figure 4-15. Within the $[1/q]_{G^-}$ range covered by 50 nm tubes, the peak $[\hat{I}_{G^-}/\hat{I}_{G^+}]$ ratio only changes by about 0.15; thus it is not a strong dependence.

Table 4-5 summarizes the *X*-*Y* pairs for which correlation occurs at shorter nanotube lengths, as well as the linear fits and confidence intervals for the 50 nm long tubes.

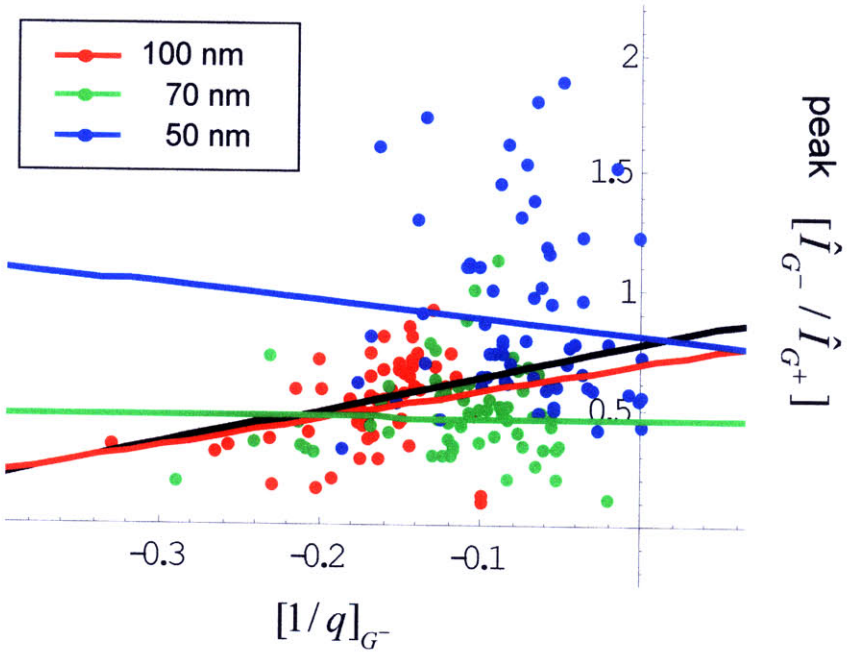

Figure 4-15. Scatter plot of peak $[\hat{I}_{G^-}/\hat{I}_{G^+}]$ vs. $[1/q]_{G^-}$ [#10]. The red, green, and blue points correspond to 100 nm, 70 nm, and 50 nm tubes, respectively. The red, green, and blue lines are linear fits to the 100 nm, 70 nm, and 50 nm data. The black line is the linear fit to all data points.

#	X	Y	**Linear fit of Y vs. X for 50 nm tubes**	**Confidence interval (m_1, m_2) of slope**	**Confidence interval (b_1, b_2) of y-intercept**
#1	$(FWHM)_{G^-}$	$[1/q]_{G^-}$	$Y = 0.001\,X - 0.149$	(0.0003, 0.002) cm	(-0.202, -0.095)
#7	$(FWHM)_{G^-}$	$(FWHM)_{G^+}$	$Y = -0.051\,X + 21.6$	(-0.094, -0.007)	(18.9, 24.2) cm^{-1}
#10	$[1/q]_{G^-}$	peak $[\hat{I}_{G^-} / \hat{I}_{G^+}]$ ratio	$Y = -0.708\,X + 0.810$	(-2.62, 1.20)	(0.639, 0.980)
#18	$(FWHM)_{G^+}$	$(\omega_{G^+} - \omega_{G^-})$	$Y = 0.913\,X + 35.6$	(0.228, 1.60)	(22.8, 48.4) cm^{-1}

Table 4-5. The pairs of G-band parameters for which the correlation appears for shorter (50 nm) tubes. For the parameters that are correlated (or anticorrelated), the linear fit to the points corresponding to 50 nm tubes and confidence intervals are shown.

4.3.3 Other/Inconclusive Correlations

There are a number of X-Y pairs that are not consistently correlated, anticorrelated or uncorrelated (as covered in Section 4.2), nor are the correlations neatly classified by length (Section 4.3.1 and 4.3.2). An example is the correlation between $[1/q]_{G^-}$ and $(FWHM)_{G^+}$ [#13]. The correlation coefficients for the length groups, r^w_{100}, r^w_{70}, and r^w_{50}, are all less than the $P^T_{5\%}$ threshold. However, the coefficient for the entire dataset has a value r^w_{all} = 0.362, which is greater than threshold and indicates a positive correlation. Figure 4-16 shows a scatter plot of $(FWHM)_{G^+}$ vs. $[1/q]_{G^-}$. From the figure we see that the data points span a range of about 14 – 24 cm^{-1} for $(FWHM)_{G^+}$, and between 0 and -0.3 for $[1/q]_{G^-}$. These data show a visual dependence on length. It can be seen from Figure 4-1 that the shorter tubes are more Lorentzian. For the shorter tubes, the increase

of the G^+ linewidth may be due to scattering at the nanotube ends. Therefore, the overall positive correlation between $[1/q]_{G^-}$ and $(FWHM)_{G^+}$ could come from the different lengths of tubes available. Since each sample (L_{tube} = 50, 70 100 nm) has a low length variation of 10% [9], each individual length group would show uncorrelated $[1/q]_{G^-}$ and $(FWHM)_{G^+}$. However, when the different lengths of tubes are examined together, a correlation between $[1/q]_{G^-}$ and $(FWHM)_{G^+}$ can be seen.

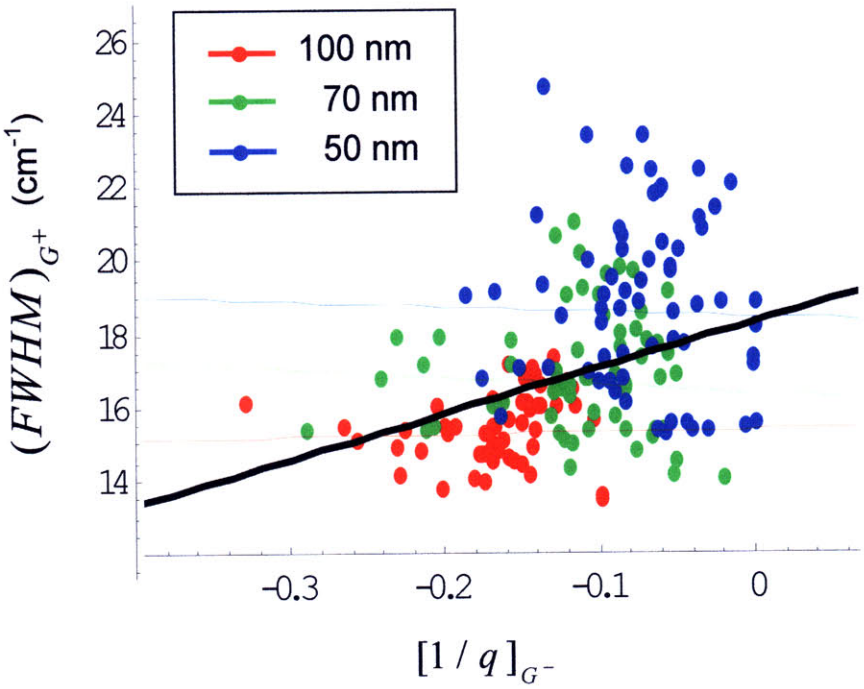

Figure 4-16. Scatter plot of $(FWHM)_{G^+}$ vs. $[1/q]_{G^-}$. The red, green, and blue points correspond to 100 nm, 70 nm, and 50 nm tubes, respectively. The red, green, and blue lines are linear fits to the 100 nm, 70 nm, and 50 nm data. The black line is the linear fit to all data points. The linear fit to all data points is shown in Table 4-3.

In addition, there are some cases for which the intermediate length tubes (70 nm) have a significant correlation coefficient, but the 100 nm and 50 nm tubes show no significant correlation. In these cases, there is simply not enough data from which draw conclusions. The cases which fall in this category are [#2], [#3], [#5] and [#14]. Future

work needs to be done with a greater number of samples to fully understand the G-band correlations.

4.4 High G^- Intensity Spectra

The Raman spectra for different spots on the same sample, measured using E_{laser} = 488 nm (2.54 eV), are shown in Figures 4-7(a) and (b). From these figures it is clear that the spectra can vary widely for a given sample and laser excitation energy. We can loosely separate these spectra into two groups: "Type 1" spectra, which have peak G^- intensities that are as high or higher than their respective G^+ intensities, and "Type 0" spectra, which have lower G^- peak intensities. Examples of Type 1 spectra are spots 1, 3, 4, 5, 6, and 8 in Figure 4-7(a). All of the spectra in Figure 4-7(b) are classified as Type 0.

For the 100 nm long tubes sample, none of the spectra are Type 1. Of the 60 spectra available for the 70 nm long tubes sample, only 5 were Type 1. The 50 nm length tubes had by far the greatest occurrence of high G^- intensity spectra: out of 65 spectra, 29 were Type 1. Type 1 spectra occurred for all E_{laser} exciting metallic nanotubes except for 2.71 eV. Of all the E_{laser} considered, E_{laser} = 2.47 eV was found to have the greatest probability of Type 1 spectra occurring, with 10 out of 16 spectra for the 50 nm long nanotubes sample being Type 1.

First we consider the general G-band properties of Type 0 and Type 1 spectra. Table 4-6 lists the average and standard deviation values of the various G-band parameters, for the Type 0 and Type 1 spectra. By definition, the peak $[\hat{I}_{G^-} / \hat{I}_{G^+}]$ ratio (and by extension, the integrated $[I_{G^-} / I_{G^+}]$ ratio) is significantly higher for the Type 1 spectra than Type 0 spectra. It is not surprising that the average G^- linewidth, $(FWHM)_{G^-}$, is smaller for the Type 1 spectra. The G^+ linewidth is about the same for the two types of spectra. The frequencies ω_{G^-} and ω_{G^+}, as well as the frequency shift $(\omega_{G^+} - \omega_{G^-})$, are about the same for the two groups of spectra. The G^- peak asymmetry parameter $[1/q]_{G^-}$ is also very similar for Type 0 and Type 1 spectra. Thus, despite the lower $[\hat{I}_{G^-} / \hat{I}_{G^+}]$ ratio, Type 0 lineshapes are not more Fano-like than Type 1 lineshapes.

G-band Parameter	Type 0 Mean	Type 0 Standard Deviation	Type 1 Mean	Type 1 Standard Deviation
peak $[\hat{I}_{G^-} / \hat{I}_{G^+}]$	0.615	0.126	1.20	0.330
integrated $[I_{G^-} / I_{G^+}]$	2.27	0.545	3.52	0.860
$(\omega_{G^+} - \omega_{G^-})$	52.7 cm^{-1}	7.18 cm^{-1}	51.9 cm^{-1}	5.74 cm^{-1}
ω_{G^-}	1540 cm^{-1}	7.00 cm^{-1}	1543 cm^{-1}	8.40 cm^{-1}
$(FWHM)_{G^-}$	64.6 cm^{-1}	9.44 cm^{-1}	51.8 cm^{-1}	10.1 cm^{-1}
$[1/q]_{G^-}$	-0.0698	0.0507	-0.0844	0.0408
ω_{G^+}	1593 cm^{-1}	6.82 cm^{-1}	1595 cm^{-1}	6.55 cm^{-1}
$(FWHM)_{G^+}$	18.8 cm^{-1}	2.14 cm^{-1}	19.6 cm^{-1}	2.33 cm^{-1}

Table 4-6. The average and standard deviation values of the various G-band parameters for Type 0 and Type 1 spectra.

The weighted correlation coefficients between the various G-band parameters were calculated for Type 1 and Type 0 spectra, in order to examine the differences between the two groups. We only consider the 50 nm length tubes because that sample had sizable numbers of Type 1 and Type 0 spectra. This approach has the further advantage of separating out length dependent effects. Also, spectra taken using the E_{laser} = 2.71 eV laser line were excluded from the correlation calculations because no Type 1 spectra were found for this laser line. This avoids division-by-zero errors and ensures that meaningful weights are assigned to the rest of the data set. Frequently, the calculated correlation coefficients were below the P = 0.05 significance threshold. However, in these cases, unless the correlation coefficients are significantly below threshold, differences between Type 0 and Type 1 spectra can still be identified by comparing the slopes between the two G-band parameters being considered.

Table 4-7 lists the weighted correlation coefficients r^w and slopes between the various G-band parameters for Type 0 and Type 1 spectra. In some cases, both the full data set (29 points per group) and a truncated data set with outliers removed were considered. Also included in Table 4-7 is the P significance value corresponding to the calculated r^w and the number of data points considered. For example, if r^w = 0.325 and

P = 0.09, then if the true correlation is zero, a correlation coefficient of 0.325 will be observed 9 percent of the time.

Table 4-7. The weighted correlation coefficients, P significance value, and slopes for the various G-band parameters after the data has been grouped according to Type 0 or Type 1.

#	*X*	*Y*	**Type 0** r^w **(P)**	**Type 1** r^w **(P)**	**Type 0 slope**	**Type 1 slope**	**Comment**
1	$(FWHM)_{G^-}$	$[1/q]_{G^-}$	0.325 (0.09)	0.454 (0.02)	0.002	0.002	No difference between Type 0 and 1.
2	$(FWHM)_{G^-}$	$(\omega_{G^+} - \omega_{G^-})$	-0.063 (0.75)	-0.218 (0.26)	N/A (uncor-related)	N/A (uncor-related)	Both types are have r^w significantly below P = 0.05 threshold.
3	$(FWHM)_{G^-}$	integrated $[I_{G^-} / I_{G^+}]$	0.334 (0.08)	0.294 (0.14)	0.019	0.024	No difference between Type 0 and 1.
4	$(FWHM)_{G^-}$	peak $[\hat{I}_{G^-} / \hat{I}_{G^+}]$	-0.066 (0.734)	0.452 (0.01)	N/A (uncor-related)	-0.013	Anticorrelation occurs for Type 1 but not Type 0.
5	$(FWHM)_{G^-}$	ω_{G^-}	0.070 (0.723)	-0.077 (0.71)	N/A (uncor-related)	N/A (uncor-related)	Both types are have r^w significantly below P = 0.05 threshold.
6	$(FWHM)_{G^-}$	ω_{G^+}	0.099 (0.61)	-0.369 (0.06)	N/A (uncor-related)	-0.246	Anticorrelation suggested for Type 1.
7	$(FWHM)_{G^-}$	$(FWHM)_{G^+}$	0.050 (0.80)	-0.360 (0.07)	N/A (uncor-related)	-0.101	Anticorrelation suggested for Type 1.
8	$[1/q]_{G^-}$	$(\omega_{G^+} - \omega_{G^-})$	0.246 (0.20)	0.200 (0.30)	29.4	29.8	No difference between Type 0 and Type 1.
9	$[1/q]_{G^-}$	integrated $[I_{G^-} / I_{G^+}]$	-0.313 (0.10)	-0.179 (0.35)	-3.32	-3.84	When outlier is removed from Type 1 data, the slope changes sign. Thus the Type 1 behavior is inconclusive.
10	$[1/q]_{G^-}$	peak $[\hat{I}_{G^-} / \hat{I}_{G^+}]$	-0.151 (0.434)	0.209 (0.277)	N/A (uncor-related)	N/A (uncor-related)	No difference between Type 0 and Type 1.
11	$[1/q]_{G^-}$	ω_{G^-}	0.033 (0.87)	0.010 (0.96)	N/A (uncor-related)	N/A (uncor-related)	No difference between Type 0 and Type 1.

Table 4-7. The weighted correlation coefficients, P significance value, and slopes for the various G-band parameters after the data has been grouped according to Type 0 or Type 1.

#	*X*	*Y*	**Type 0** r^w **(P)**	**Type 1** r^w **(P)**	**Type 0 slope**	**Type 1 slope**	**Comment**
12	$[1/q]_{G^-}$	ω_{G^+}	0.302 (0.11)	0.256 (0.18)	33.6	31.5	No difference between Type 0 and Type 1.
13	$[1/q]_{G^-}$	$(FWHM)_{G^+}$	0.011 (0.95)	0.212 (0.27)	N/A (uncor-related)	N/A (uncor-related)	No difference between Type 0 and Type 1.
14	$(\omega_{G^+} - \omega_{G^-})$	integrated $[I_{G^-} / I_{G^+}]$	-0.082 (0.67)	-0.002 (0.99)	N/A (uncor-related)	N/A (uncor-related)	No difference between Type 0 and Type 1.
15	$(\omega_{G^+} - \omega_{G^-})$	peak $[\hat{I}_{G^-} / \hat{I}_{G^+}]$	0.080 (0.68)	0.167 (0.39)	N/A (uncor-related)	N/A (uncor-related)	No difference between Type 0 and Type 1.
16	$(\omega_{G^+} - \omega_{G^-})$	ω_{G^-}	-0.597 (0.001)	-0.712 (1.5E-5)	-0.638	-0.816	No significant difference between Type 0 and Type 1.
17	$(\omega_{G^+} - \omega_{G^-})$	ω_{G^+}	0.389 (0.04)	0.223 (0.24)	0.362	0.184	Correlated for Type 0 but not Type 1
18	$(\omega_{G^+} - \omega_{G^-})$	$(FWHM)_{G^+}$	0.234 (0.22)	0.340 (0.07)	0.078	0.126	No significant difference between Type 0 and Type 1.
19	integrated $[I_{G^-} / I_{G^+}]$	peak $[\hat{I}_{G^-} / \hat{I}_{G^+}]$	0.704 (2.0E-5)	0.589 (7.8E-4)	0.149	0.194	No difference between Type 0 and Type 1.
20	integrated $[I_{G^-} / I_{G^+}]$	ω_{G^-}	-0.015 (0.94)	-0.045 (0.82)	N/A (uncor-related)	N/A (uncor-related)	No difference between Type 0 and Type 1.
21	integrated $[I_{G^-} / I_{G^+}]$	ω_{G^+}	-0.105 (0.59)	-0.065 (0.74)	N/A (uncor-related)	N/A (uncor-related)	No difference between Type 0 and Type 1.
22	integrated $[I_{G^-} / I_{G^+}]$	$(FWHM)_{G^+}$	-0.221 (0.25)	-0.505 (0.005)	-0.825	-1.31	Anticorrelation occurs for Type 1 but not for Type 0.
23	peak $[\hat{I}_{G^-} / \hat{I}_{G^+}]$	ω_{G^-}	0.107 (0.58)	0.177 (0.36)	N/A (uncor-related)	N/A (uncor-related)	No difference between Type 0 and Type 1.
24	peak $[\hat{I}_{G^-} / \hat{I}_{G^+}]$	ω_{G^+}	0.209 (0.28)	0.448 (0.01)	N/A (uncor-related)	7.82	Correlation occurs for Type 1 but not for Type 0.
25	peak $[\hat{I}_{G^-} / \hat{I}_{G^+}]$	$(FWHM)_{G^+}$	0.295 (0.12)	0.213 (0.27)	N/A (uncor-related)	N/A (uncor-related)	No difference between Type 0 and Type 1.

#	X	Y	Type 0 r^w (P)	Type 1 r^w (P)	Type 0 slope	Type 1 slope	Comment
26	ω_{G^-}	ω_{G^+}	0.507 (0.005)	0.526 (0.003)	0.442	0.379	No difference between Type 0 and Type 1.
27	ω_{G^-}	$(FWHM)_{G^+}$	0.150 (0.44)	-0.009 (0.96)	N/A (uncor-related)	N/A (uncor-related)	No difference between Type 0 and Type 1.
28	ω_{G^+}	$(FWHM)_{G^+}$	0.424 (0.02)	0.398 (0.03)	0.151	0.180	No significant difference between Type 0 and Type 1.

Table 4-7. The weighted correlation coefficients, P significance value, and slopes for the various G-band parameters after the data has been grouped according to Type 0 or Type 1.

4.4.1 Correlations Associated with Type 0 Spectra

In this section we will discuss the correlations between the G-band parameters that occur for Type 0 spectra but not for Type 1 spectra. According to Table 4-7, only entry [#17], ω_{G^+} vs. $(\omega_{G^+} - \omega_{G^-})$, fit in this category. The scatter plot of ω_{G^+} vs. $(\omega_{G^+} - \omega_{G^-})$ for Type 0 spectra is shown in Figure 4-17(a). From the linear fit shown in Figure 17(a), we see that ω_{G^+} changes from about 1585 cm^{-1} to about 1595 cm^{-1} when $(\omega_{G^+} - \omega_{G^-})$ changes from 40 cm^{-1} to 60 cm^{-1}. For Type 0 tubes, the linear fit is $\omega_{G^+} = 0.362(\omega_{G^+} - \omega_{G^-}) + 1573$, with confidence intervals of (0.023, 0.791) for the slope and (1555, 1592) cm^{-1} for the intercept. From Table 4-7, we find that the G^- frequency ω_{G^-} and $(\omega_{G^+} - \omega_{G^-})$ [#16] are anticorrelated for both Type 1 and Type 0 tubes. Hence for Type 0 tubes the frequency shift arises from both a G^- downshift and a G^+ upshift. In Figure 4-17(b) the plot of ω_{G^-} vs. $(\omega_{G^+} - \omega_{G^-})$ is shown for Type 0 spectra.

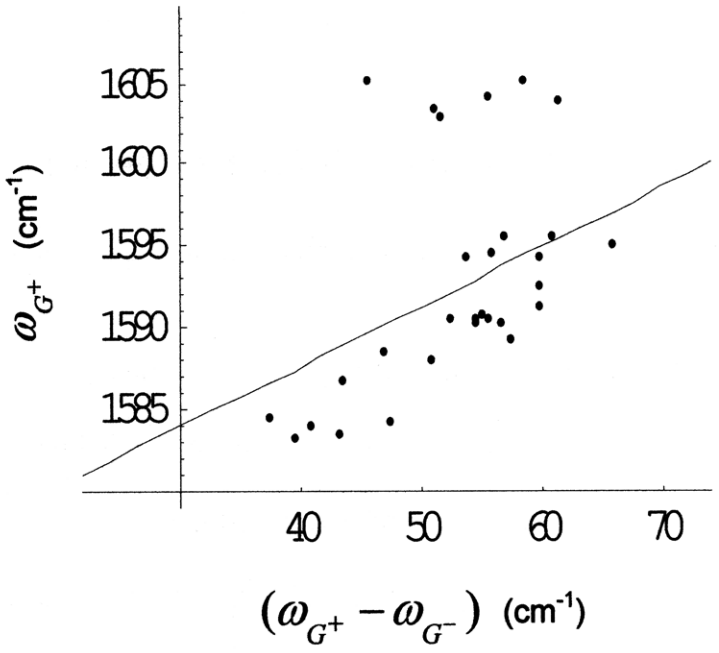

Figure 4-17(a). Scatter plot of ω_{G^+} vs. $(\omega_{G^+} - \omega_{G^-})$ for Type 0 spectra, with the linear fit superimposed. The linear fit is ω_{G^+} = $0.362(\omega_{G^+} - \omega_{G^-})$ + 1573, with confidence intervals of (0.023, 0.791) for the slope and (1555, 1592) cm^{-1} for the intercept.

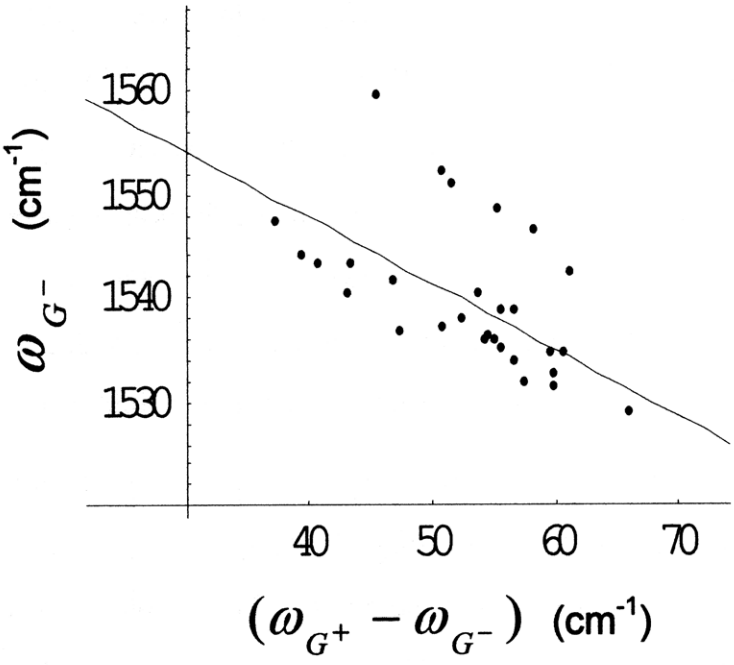

Figure 4-17(b). Scatter plot of ω_{G^-} vs. $(\omega_{G^+} - \omega_{G^-})$ for Type 0 spectra, with the linear fit superimposed. The linear fit is ω_{G^-} = $-0.638(\omega_{G^+} - \omega_{G^-})$ + 1573, with confidence intervals of (-

0.977, -0.299) for the slope and (1555, 1592) cm^{-1} for the intercept.

4.4.2 Correlations Associated with Type 1 Spectra

This section will cover the G-band correlations that occur for Type 1 spectra but not for Type 0 spectra.

In Figures 4-18(a) and (b), the peak $[\hat{I}_{G^-} / \hat{I}_{G^+}]$ ratio vs. $(FWHM)_{G^-}$ [#4] are plotted for Type 1 and Type 0 spectra. For Type 1 spectra, the G^- linewidth, $(FWHM)_{G^-}$, and the peak $[\hat{I}_{G^-} / \hat{I}_{G^+}]$ ratio are anticorrelated. In Type 0 spectra, the peak $[\hat{I}_{G^-} / \hat{I}_{G^+}]$ ratio appears approximately constant with $(FWHM)_{G^-}$, even though $(FWHM)_{G^-}$ has a range of over 20 cm^{-1}. Although outliers are seen in Figures 4-18(a) and (b), removal of these outliers did not significantly affect the results. The linear fit for Type 1 spectra is $[\hat{I}_{G^-} / \hat{I}_{G^+}]$ = -0.0126 $(FWHM)_{G^-}$ + 1.80, with confidence intervals of (-0.022, -0.003) cm for the slope and (1.27, 2.32) for the intercept.

One of the main differences between Type 0 and Type 1 spectra is the linewidth of the G^- peak. The $(FWHM)_{G^-}$ ranges from 55 cm^{-1} – 85 cm^{-1} for Type 0 spectra, while $(FWHM)_{G^-}$ for Type 1 spectra remains mostly below 60 cm^{-1}. According to Ref. 32, electron-phonon coupling is the major source of the G^- peak broadening for metallic carbon nanotubes, and $(FWHM)_{G^-}$ is a measure of the amount of electron-phonon coupling. Thus, Type 1 spectra would be expected to have reduced electron-phonon coupling when compared to Type 0 spectra. The anticorrelation of the $(FWHM)_{G^-}$ and the peak $[\hat{I}_{G^-} / \hat{I}_{G^+}]$ ratio for Type 1 spectra is an indication that a high $[\hat{I}_{G^-} / \hat{I}_{G^+}]$ ratio is related to reduced electron-phonon coupling. Furthermore, since a significant number of Type 1 spectra were only observed in the 50 nm tubes sample, the decreased electron-phonon coupling is likely a finite length effect. This is supported by the recent assignment of the G^- peak of metallic nanotubes to the LO phonon mode [3 – 5].

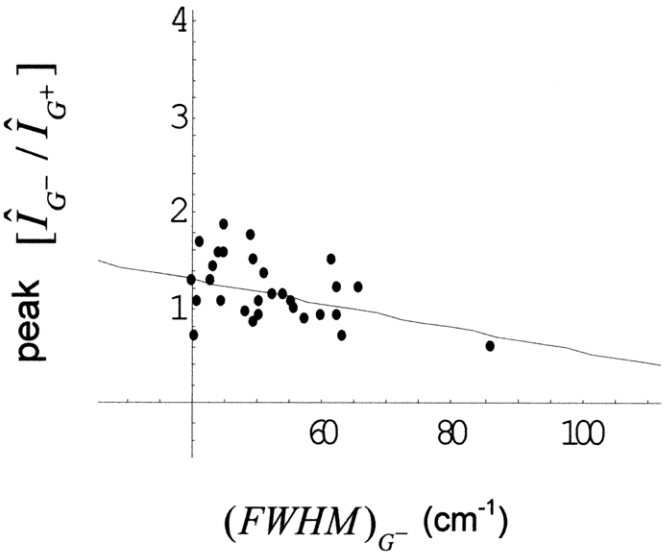

Figure 4-18(a). Scatter plot of peak $[\hat{I}_{G^-} / \hat{I}_{G^+}]$ ratio vs. $(FWHM)_{G^-}$ [#4] for Type 1 spectra. The linear fit is $[\hat{I}_{G^-} / \hat{I}_{G^+}]$ = -0.0126 $(FWHM)_{G^-}$ + 1.80, with confidence intervals of (-0.022, -0.003) cm for the slope and (1.27, 2.32) for the intercept.

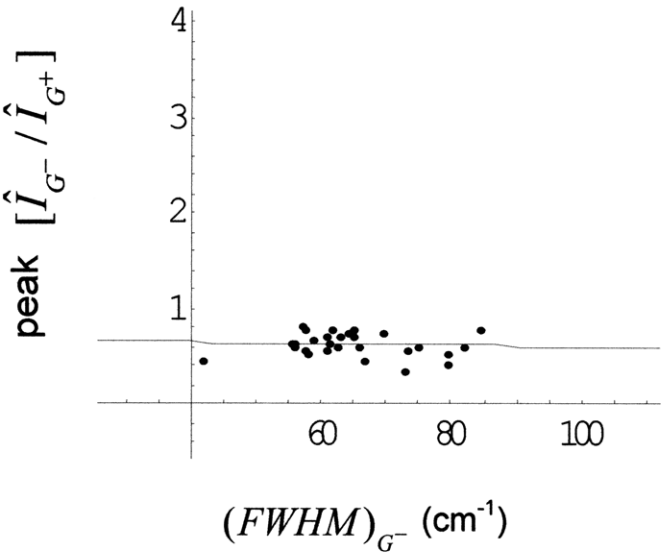

Figure 4-18(b). Scatter plot of peak $[\hat{I}_{G^-} / \hat{I}_{G^+}]$ ratio vs. $(FWHM)_{G^-}$ [#4] for Type 0 spectra. The correlation coefficient in this case was not statistically significant.

Another relation that appears for Type 1, but not Type 0, spectra is the probable anticorrelation of ω_{G^+} and $(FWHM)_{G^-}$ [#6]. The correlation coefficient of -0.369 is significant at the P = 0.06 level for the 27 data points involved. The linear fit for Type 1 spectra is ω_{G^+} = -0.246 $(FWHM)_{G^-}$ + 1605, with confidence intervals of (-0.502, 0009) for the slope and (1592, 1618) for the intercept. The scatter plot is shown in Figure 4-19.

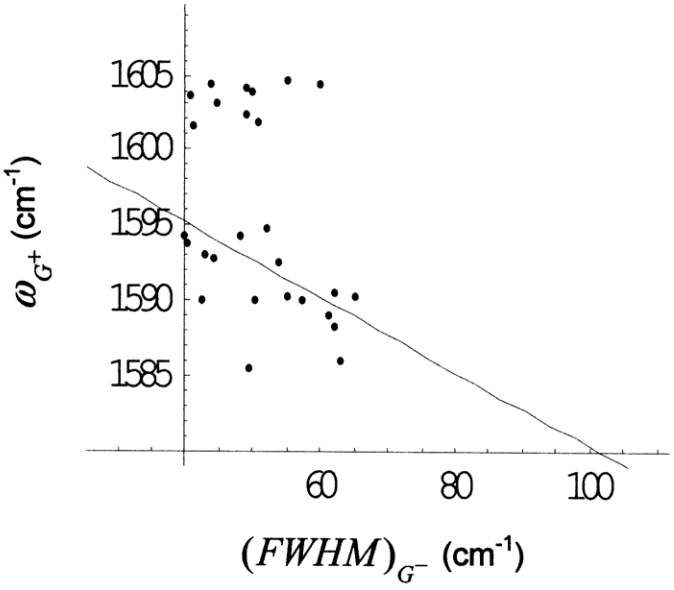

Figure 4-19. Scatter plot of ω_{G^+} vs. $(FWHM)_{G^-}$ [#6] for Type 1 spectra. The linear fit is ω_{G^+} = -0.246 $(FWHM)_{G^-}$ + 1605, with confidence intervals of (-0.502, 0009) for the slope and (1592, 1618) for the intercept.

The $(FWHM)_{G^+}$ and integrated $[I_{G^-} / I_{G^+}]$ ratio [#22] were found to be anticorrelated for Type 1 spectra only. The linear fit for Type 1 spectra is $(FWHM)_{G^+}$ = -1.31 $[I_{G^-} / I_{G^+}]$ + 23.7 with confidence intervals of (-2.19, -0.426) cm^{-1} for the slope and (20.5, 27.0) cm^{-1} for the intercept. This is plotted in Figure 4-20. As the integrated $[I_{G^-} / I_{G^+}]$ ratio increases, the G^+ linewidth decreases for Type 1 spectra.

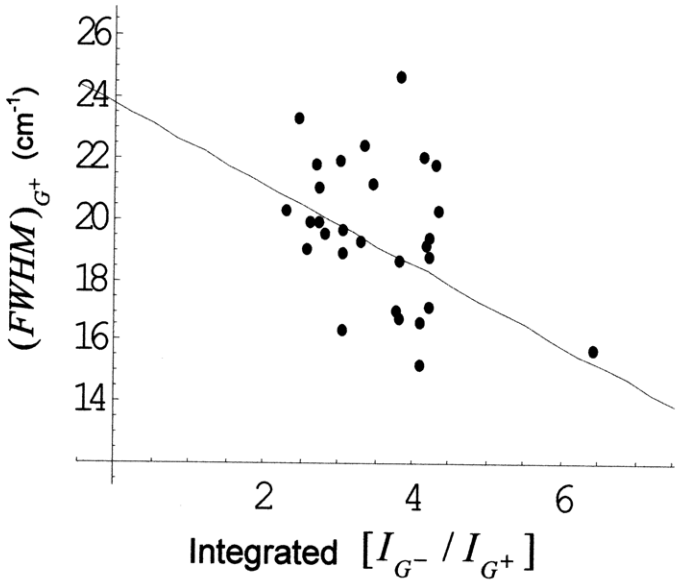

Figure 4-20. Scatter plot of $(FWHM)_{G^+}$ vs. integrated $[I_{G^-} / I_{G^+}]$ ratio [#22] for Type 1 spectra. The linear fit is $(FWHM)_{G^+}$ = -1.31 $[I_{G^-} / I_{G^+}]$ + 23.7 with confidence intervals of (-2.19, -0.426) cm^{-1} for the slope and (20.5, 27.0) cm^{-1} for the intercept.

For Type 1 spectra, the G^+ frequency and peak $[\hat{I}_{G^-} / \hat{I}_{G^+}]$ ratio [#24] were found to be correlated. An increase in peak $[\hat{I}_{G^-} / \hat{I}_{G^+}]$ ratio is accompanied by a G^+ frequency upshift. The linear fit for Type 1 spectra is ω_{G^+} = 7.82 $[\hat{I}_{G^-} / \hat{I}_{G^+}]$ + 1584, with confidence intervals of (1.65, 14.0) cm^{-1} for the slope and (1576, 1591) cm^{-1} for the intercept. The scatter plot for Type 1 spectra is shown in Figure 4-21.

The final relationship that occurs for Type 1 spectra is the anticorrelation between $(FWHM)_{G^-}$ and $(FWHM)_{G^+}$ [#7]. The correlation coefficient is -0.360, which is significant at the P = 0.07 level for the 27 data points. The linear fit for Type 1 spectra is $(FWHM)_{G^+}$ = -0.101 $(FWHM)_{G^-}$ + 24.6, with confidence intervals of (-0.209, 0.007) for the slope and (19.0, 30.2) for the intercept. The $(FWHM)_{G^+}$ vs. $(FWHM)_{G^-}$ plot for Type 1 spectra is shown in Figure 4-22(a). For comparison, the corresponding plot for Type 0 spectra, for which there is no correlation, is shown in Figure 4-22(b).

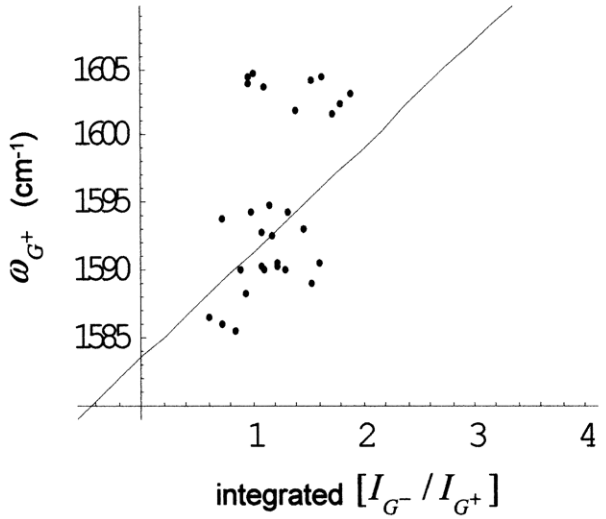

Figure 4-21. Scatter plot of ω_{G^+} vs. peak $[\hat{I}_{G^-} / \hat{I}_{G^+}]$ ratio [#24] for Type 1 spectra. The linear fit is ω_{G^+} = 7.82 $[\hat{I}_{G^-} / \hat{I}_{G^+}]$ + 1584, with confidence intervals of (1.65, 14.0) cm^{-1} for the slope and (1576, 1591) cm^{-1} for the intercept.

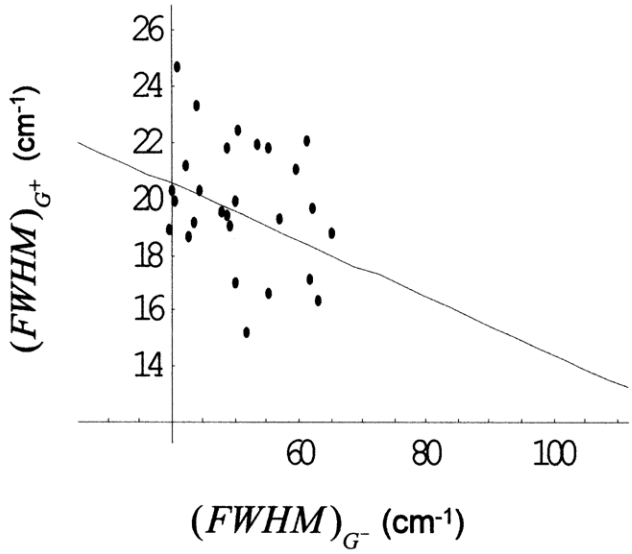

Figure 4-22(a). Scatter plot of $(FWHM)_{G^+}$ vs. $(FWHM)_{G^-}$ [#7] for Type 1 spectra. The linear fit is $(FWHM)_{G^+}$ = -0.101 $(FWHM)_{G^-}$ + 24.6, with confidence intervals of (-0.209, 0.007) for the slope and (19.0, 30.2) for the intercept.

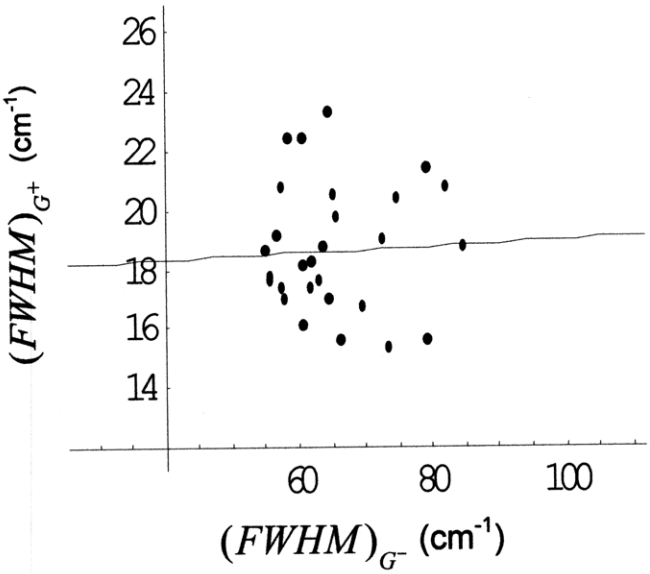

Figure 4-22(b). Scatter plot of $(FWHM)_{G^+}$ vs. $(FWHM)_{G^-}$ [#7] for Type 0 spectra. The correlation coefficient is below the P = 0.05 significance threshold in this case.

4.4.3 Summary of Correlations

The information summarized in Table 4-7 was used to determine the differences, if any exist, between Type 0 and Type 1 spectra. For example, $(FWHM)_{G^-}$ and $(FWHM)_{G^+}$ [#7] are uncorrelated for Type 0 spectra but anticorrelated for Type 1 spectra. This finding is independent of length, since only 50 nm long tubes were considered when calculating the correlation coefficients for Type 0 and Type 1 spectra. The anticorrelation between $(FWHM)_{G^-}$ and $(FWHM)_{G^+}$ also occurs for the shorter (50 nm) tubes but not for the longer (100 nm) tubes, as listed in Tables 4-5 and 4-4. Therefore this anticorrelation occurs for the shorter tubes because the 50 nm long tubes have a much higher occurrence of Type 1 spectra than the longer lengths of tubes.

As another example, we consider the relationship between $(FWHM)_{G^-}$ and $[1/q]_{G^-}$ [#1]. Type 0 spectra have r^w = 0.325, which is significant at the P = 0.09 level. Type 1 spectra have r^w = 0.454, which is significant at the P = 0.02 level. The slope of $[1/q]_{G^-}$ vs. $(FWHM)_{G^-}$ for either Type 0 and Type 1 group is 0.002. Therefore there is

not much difference between Type 0 and Type 1 spectra regarding the $(FWHM)_{G^-}$ vs. $[1/q]_{G^-}$ correlation. $(FWHM)_{G^-}$ and $[1/q]_{G^-}$ were found to be correlated for 50 nm long tubes but not for 100 nm long tubes (Tables 4-5 and 4-4). Therefore, the correlation between $(FWHM)_{G^-}$ and $[1/q]_{G^-}$ is brought about by length, and not simply because the 50 nm long nanotubes have more occurrence of Type 1 spectra.

By combining the information contained in Tables 4-1, 4-2, 4-4, 4-5 and 4-7, further grouping of the correlations between the G-band parameters can be made. There are correlations that exist in shorter (50 nm) tubes, that are caused by the increased occurrence of Type 1 spectra for shorter tubes. There are correlations that exist for shorter tubes, but are unrelated to the occurrence of Type 1 spectra. There are correlations that exist for Type 1 spectra, but not necessarily for shorter tubes (i.e., not listed in Table 4-5). There are correlations associated with Type 0 spectra but not related to longer tubes (not listed in Table 4-4). There are correlations that exist for longer nanotubes only (Table 4-4); however we cannot say whether these correlations are Type 0 related because we only considered the 50 nm length sample when classifying the spectra as Type 0 or Type 1. There are general G-band properties, where the correlations (or lack thereof) were the same for Type 0 and Type 1, and the correlations are unrelated to length (not listed in Tables 4-4 and 4-5). Finally, there were inconclusive results, where the 70 nm length sample showed significant correlation coefficients while the 50 nm and 100 nm length samples did not. For these inconclusive cases, no difference was observed between Type 0 and Type 1 spectra. These classifications are summarized in Table 4-8.

Correlations associated with Type 1 spectra, but not necessarily with shorter tubes.	**Correlations associated with Type 0 spectra, but not necessarily with longer tubes.**
[#4] $(FWHM)_{G^-}$ vs. peak $[\hat{I}_{G^-} / \hat{I}_{G^+}]$ (-) **[#6]** $(FWHM)_{G^-}$ vs. ω_{G^+} (-) **[#22]** integrated $[I_{G^-} / I_{G^+}]$ vs. $(FWHM)_{G^+}$ (-) **[#24]** peak $[\hat{I}_{G^-} / \hat{I}_{G^+}]$ vs. ω_{G^+} (+)	**[#17]** $(\omega_{G^+} - \omega_{G^-})$ vs. ω_{G^+} (+)
Shorter tubes, caused by occurrence of Type 1	**Longer tubes, caused by occurrence of Type 1**
[#7] $(FWHM)_{G^-}$ vs. $(FWHM)_{G^+}$ (-)	No conclusion can be made because only the shorter tubes were grouped into Type 0 and Type 1 spectra.
Shorter tubes, but not Type 1 related	**Longer tubes, but not necessarily Type 0 related**
[#1] $(FWHM)_{G^-}$ vs. $[1/q]_{G^-}$ (+) **[#10]** $[1/q]_{G^-}$ vs. peak $[\hat{I}_{G^-} / \hat{I}_{G^+}]$ (-) **[#17]** $(\omega_{G^+} - \omega_{G^-})$ vs. ω_{G^+} (+) **[#18]** $(\omega_{G^+} - \omega_{G^-})$ vs. $(FWHM)_{G^+}$ (+)	**[#8]** $[1/q]_{G^-}$ vs. $(\omega_{G^+} - \omega_{G^-})$ (+) **[#12]** $[1/q]_{G^-}$ vs. ω_{G^+} (+) **[#18]** $(\omega_{G^+} - \omega_{G^-})$ vs. $(FWHM)_{G^+}$ (-) **[#21]** integrated $[I_{G^-} / I_{G^+}]$ vs. ω_{G^+} (+) **[#22]** integrated $[I_{G^-} / I_{G^+}]$ vs. $(FWHM)_{G^+}$ (+) **[#27]** ω_{G^-} vs. $(FWHM)_{G^+}$ (+)
General G-band, not length or Type related	**Other/Inconclusive results**
[#9] $[1/q]_{G^-}$ vs. integrated $[I_{G^-} / I_{G^+}]$ (U) **[#11]** $[1/q]_{G^-}$ vs. ω_{G^-} (U) **[#15]** ω_{G^-} vs. integrated $[\hat{I}_{G^-} / \hat{I}_{G^+}]$ (U) **[#16]** $(\omega_{G^+} - \omega_{G^-})$ vs. ω_{G^-} (-) **[#19]** integrated $[I_{G^-} / I_{G^+}]$ vs. peak $[\hat{I}_{G^-} / \hat{I}_{G^+}]$ (+) **[#20]** integrated $[I_{G^-} / I_{G^+}]$ vs. ω_{G^-} (U) **[#23]** peak $[\hat{I}_{G^-} / \hat{I}_{G^+}]$ vs. ω_{G^-} (+) **[#25]** peak $[\hat{I}_{G^-} / \hat{I}_{G^+}]$ vs. $(FWHM)_{G^-}$ (+) **[#26]** ω_{G^-} vs. ω_{G^+} (+) **[#28]** ω_{G^+} vs. $(FWHM)_{G^+}$ (+)	**[#2]** $(FWHM)_{G^-}$ vs. $(\omega_{G^+} - \omega_{G^-})$ **[#3]** $(FWHM)_{G^-}$ vs. integrated $[I_{G^-} / I_{G^+}]$ **[#5]** $(FWHM)_{G^-}$ vs. ω_{G^-} **[#13]** $[1/q]_{G^-}$ vs. $(FWHM)_{G^+}$ **[#14]** $(\omega_{G^+} - \omega_{G^-})$ vs. integrated $[I_{G^-} / I_{G^+}]$

Table 4-8. The relationships between the G-band parameters, classified by combining the information summarized in Tables 4-1, 4-2, 4-4, 4-5 and 4-7. Positive correlations are denoted by (+), anticorrelations by (-), and uncorrelated pairs by (U).

References

[1] K. T. Nguyen et al., "Fano Lineshape and Phonon Softening in Single Isolated Metallic Carbon Nanotubes." *Physical Review Letters*, **98** (2007) 145504.

[2] H. Farhat et al., "Phonon Softening in Individual Metallic Carbon Nanotubes due to the Kohn Anomaly." *Physical Review Letters*, **99** (2007) 145506.

[3] E. Di Donato et. a.l., "Assignment of the G^+ and G^- Raman bands of metallic and semiconducting carbon based on a common valence force field," *Physical Review B,* **74** (2006) 184306.

[4] V. N. Popov and P. Lambin, "Symmetry-adapted tight-binding calculations of the totally symmetric A_1 phonons of single-walled carbon nanotubes and their resonant Raman intensity," *Physica E,* **37** (2007) 97.

[5] M. Lazzeri et al., "Phonon linewidths and electron-phonon coupling in graphite and nanotubes," *Physical Review B,* **73** (2006) 155426.

[6] M. Lazzeri et al., "Phonon linewidths and electron-phonon coupling in graphite and nanotubes." *Physical Review B*, **73** (2006) 155426.

[7] S. D. M. Brown et al., "Origin of the Breit-Wigner-Fano lineshape of the tangential G-band feature of metallic carbon nanotubes." *Physical Review B*, **63** (2001) 155414.

[8] M. S. Dresselhaus et al., "Raman spectroscopy of carbon nanotubes," *Physics Reports,* **409** (2005) 47.

[9] X. Y. Huang et al., "High-resolution length sorting and purification of DNA-wrapped carbon nanotubes by size-exclusion chromatography." *Anal. Chem,* 77 (2005) 6225-6228.

Chapter 5 – D-band

5.1 Overview of the Chapter

The Raman D-band line which occurs around 1350 cm^{-1} (for E_{laser} = 2.47 eV) occurs in graphite and is attributed to a breakdown in selection rules brought about by defects, including finite size effects [1]. In carbon nanotubes, the D-band can also be activated by their finite size or by lattice defects [2]. Hence the D-band intensity is expected to have a length dependence as well, with the D-band intensity increasing as the nanotube length decreases, and the termination portion of the tube becomes a larger fraction of the tube length.

In this chapter we first compare our results with previous work on the D-band of short nanotubes [3] and nanographite [4]. We then use the correlation analysis introduced in Chapter 3 to determine the length and laser excitation energy dependence of the D-band intensity, frequency and linewidth. We also discuss the dependence of the D-band parameters (frequency, intensity and linewidth) on whether the nanotube is semiconducting or metallic.

5.2 Comparison to Prior Works

The length dependence of the D-band for carbon nanotubes was previously studied in Ref. 3 for E_{laser} ranging from 1.83 eV to 2.33 eV. In the previous work, the focus was on semiconducting SWNTs and data at only one laser line which was in resonance with metallic tubes were examined. It was found that the D-band scattering intensity for the metallic SWNTs was much larger than for the semiconducting SWNTs [3]. The integrated intensity ratio between the D-band and G-band I_D / I_G was found to vary linearly with $1/L_{tube}$, the reciprocal of the nanotube length. In addition, for metallic nanotubes excited with E_{laser} = 2.33 eV, the dependence of I_D / I_G on nanotube length and E_{laser} was found to be similar to the behavior of nanographite, as discussed further below.

In nanographite, Raman spectroscopy is used to determine the crystallite size from the I_D / I_G ratio [4]. For nanographite, the Raman I_D / I_G ratio was found to be related to the crystallite size L_α and E_{laser} by the following equation [4]:

$$L_\alpha = \frac{560}{E_{laser}^4}\left(\frac{I_D}{I_G}\right)^{-1} . \qquad (5.1)$$

Figure 5-1 shows the results from Ref 3, where the quantity $(I_D / I_G)E_{laser}^4$ is plotted vs. the reciprocal of nanotube length $1/L_{tube}$. The lines corresponding to different values of E_{laser} are shown. Also included in Figure 5-1 is the line corresponding to Equation 5-1 for nanographite. It was found that the $(I_D / I_G)E_{laser}^4$ data for metallic nanotubes excited with E_{laser} = 2.33 eV are consistent with the nanographite line. In this chapter we report Raman scattering measurements for many laser lines where metallic tubes contribute strongly to the resonance spectra in an attempt to determine whether metallic nanotubes in general follow the L_{tube} and E_{laser} dependence found for nanographites.

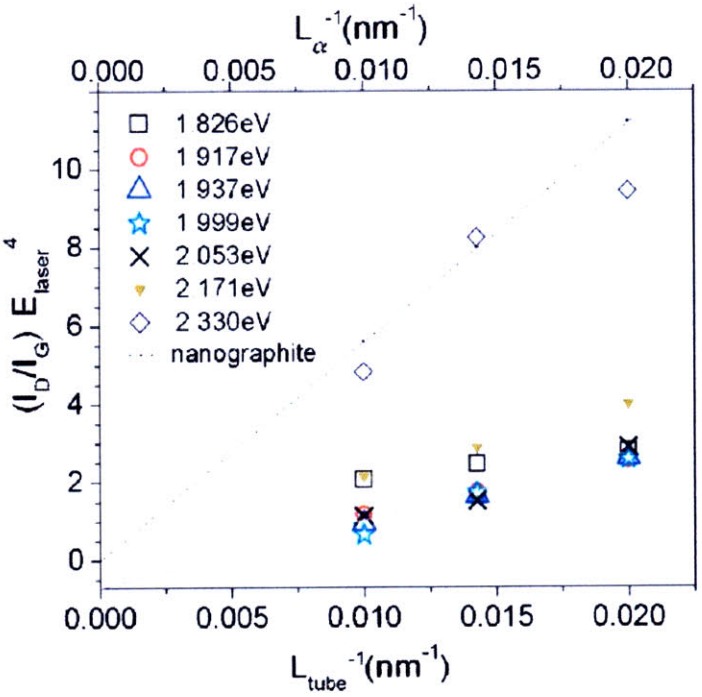

Figure 5-1. $(I_D / I_G)E_{laser}^4$ plotted vs. $1/L_{tube}$. The data corresponding to different values of E_{laser} probing carbon nanotubes, as well as the relation for nanographite (dotted line), are shown. The plot is taken from Ref 3.

In the current study, Raman spectra were taken using E_{laser} = 1.92 eV, 2.41 eV, 2.47 eV, 2.50 eV, 2.54 eV, 2.60 eV, 2.62 eV, 2.66 eV, and 2.71 eV. The laser lines used in the previous study [3] probed mostly semiconducting tubes. For the E_{laser} used here, a mixture of semiconducting and metallic tubes were resonant (Table 2-1); however, most of the spectra show a broad G-band which is characteristic of metallic nanotubes, with the exception of the spectra taken using E_{laser} = 1.92 eV. Therefore, we tentatively assume that metallic tubes contribute the most to the Raman spectra shown here. Figure 5-2 shows an example of a Raman trace for metallic tubes in the vicinity of the D- and G-bands (E_{laser} = 2.54 eV). Peak fitting was performed on the Raman spectra to separate out the D-band, as well as the individual components of the G-band.

As discussed in detail in Chapter 3 of this thesis, the G-band of metallic nanotubes is dominated by two peaks: the broad, asymmetric Breit-Wigner-Fano feature at 1530 cm^{-1} (the G^- peak, lower branch), and the sharp Lorentzian (G^+) peak at 1592 cm^{-1}. There is also a third G-band component that frequently appears around 1570 cm^{-1} (the G^- peak, upper branch). The G^+ peak was recently assigned to the LO mode of semiconducting nanotubes, the G^- upper branch was assigned to the TO mode of both semiconducting and metallic nanotubes, and the G^- lower branch corresponds to the LO mode of metallic nanotubes [5, 6].

For carbon nanotubes, we normalized the integrated intensity of the D-band to only the integrated intensity of the G^+ component. In the chapter on the G-band, it was found that the G^- lineshape and relative intensity vary significantly with nanotube length. Therefore the integrated intensity of the entire G-band, including the G^- component, would not make a suitable normalization factor. Furthermore, since the Breit-Wigner-Fano feature does not appear in nanographite, it is more appropriate to normalize the nanotube D-band to the G^+ peak in order to make an adequate comparison to the work of Cancado et al. [4]. Henceforth we will only consider the integrated intensity ratio between the D-band and the G^+ component, I_D / I_{G^+}.

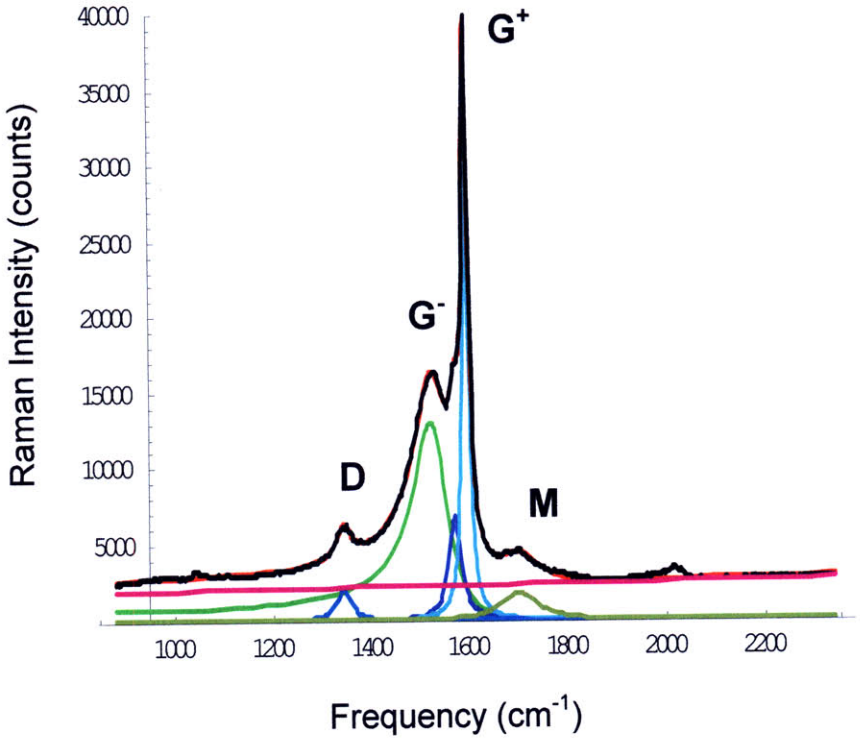

Figure 5-2. Sample peak fitting results showing the individual peaks in the vicinity of the Raman D- and G-bands. This Raman spectrum corresponds to metallic nanotubes probed with the 488 nm (2.54 eV) laser line. The black curve is the raw data. The individual peaks are shown, as well as a baseline that was determined by the peak fitting procedure. The red curve is the sum of the baseline and the peaks found from peak fitting. The average nanotube length L_{tube} in this case is 100 nm.

Figure 5-3 shows the integrated intensity ratio I_D / I_{G^+} plotted vs. $1/L_{tube}$, for several laser lines. Data for both semiconducting and metallic nanotubes are included. In this figure, data for the 1.83, 1.94, 2.00, 2.05, 2.17, and 2.33 eV laser lines were taken from Ref. 3. In general, the I_D / I_{G^+} ratio increases as $1/L_{tube}$ increases, as expected from Ref 3.

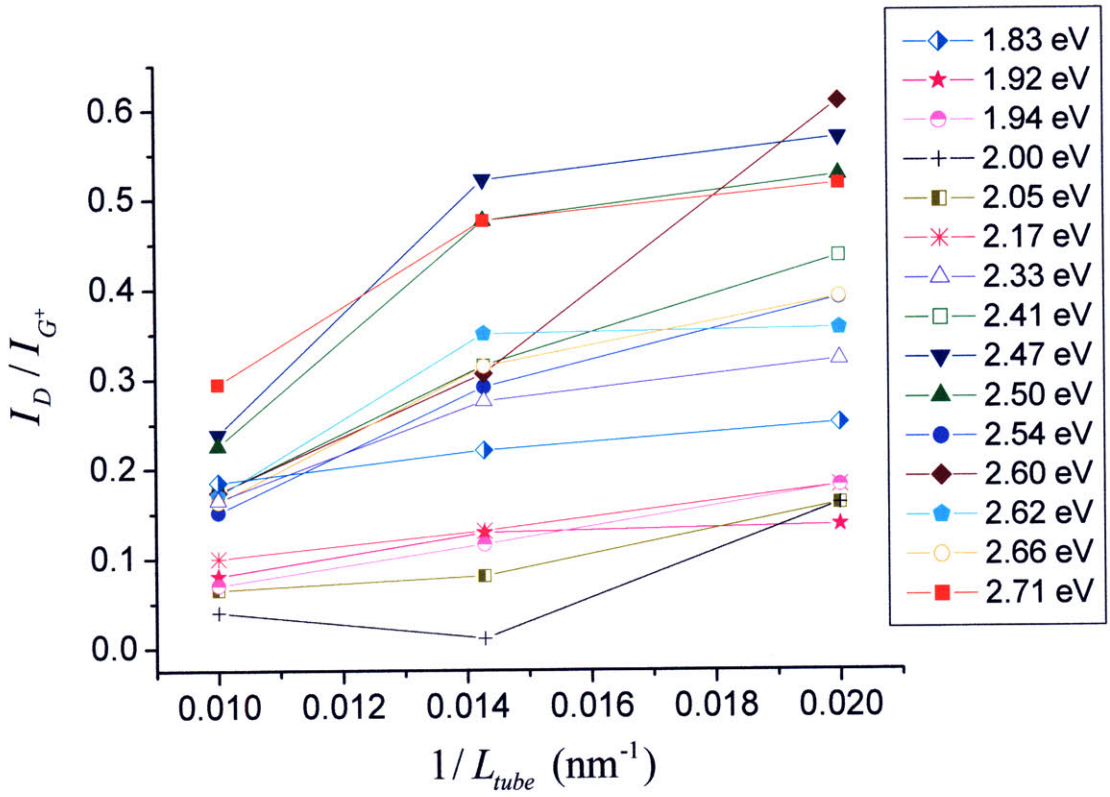

Figure 5-3. The integrated intensity ratio I_D / I_{G^+} plotted vs. $1/L_{tube}$, for different values of E_{laser}. Data for the 1.83, 1.94, 2.00, 2.05, 2.17, and 2.33 eV laser lines were taken from Ref. 3.

In Figure 5-4, $\left(I_D / I_{G^+}\right) E_{laser}^4$ vs. the reciprocal of nanotube length $1/L_{tube}$ is shown for all of the E_{laser} lines used in the current study as well as those from Ref 3. The line for nanographite is also shown. The curves corresponding to carbon nanotubes do not fall on the nanographite line, suggesting that a different equation from (5.1) is needed to relate E_{laser} and $1/L_{tube}$ to the D-band of carbon nanotubes. The $\left(I_D / I_{G^+}\right) E_{laser}^4$ curves for E_{laser} greater than 2.33 eV fall above the nanographite line, while the curves for E_{laser} less than 2.33 eV fall below the nanographite line. According to the Kataura plot (Figure 2-4), metallic nanotubes come into resonance for E_{laser} = 2.1 eV and greater. This suggests that metallic and semiconducting nanotubes may each follow a different $\left(I_D / I_{G^+}\right)$ dependence. When a model similar to Equation (5.1), but with different values for the constant and exponent was considered, a suitable fit could not be found for either semiconducting or metallic nanotubes.

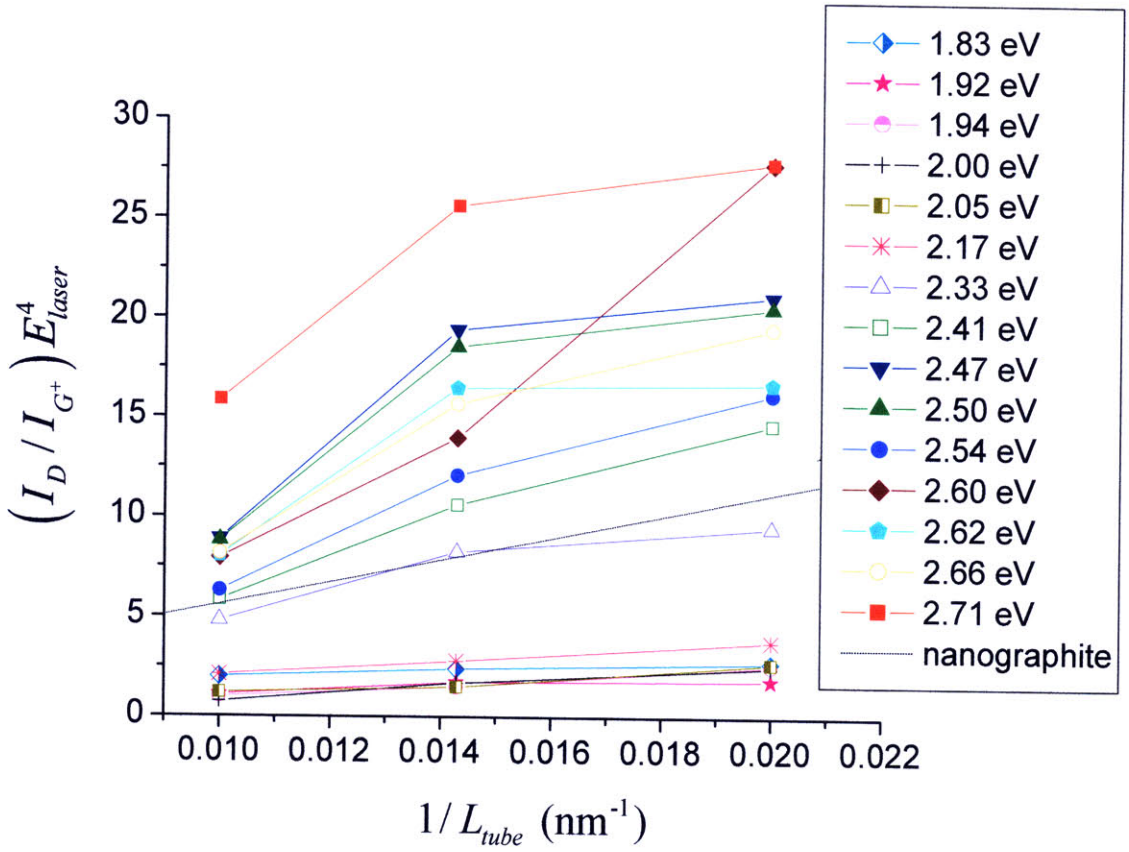

Figure 5-4. Plot of $\left(I_D / I_{G^+}\right) E^4_{laser}$ vs. the reciprocal of nanotube length $1/L_{tube}$ for several laser lines. The line corresponding to nanographite is also shown. Data for the 1.83, 1.94, 2.00, 2.05, 2.17, and 2.33 eV laser lines were taken from Ref. 3.

5.3 Correlation Analysis of the D-band

We now use the correlation analysis method introduced in Chapter 3 to examine the L_{tube} and E_{laser} dependence of the various D-band parameters (frequency, FWHM linewidth, and integrated and peak intensity). Spectra for E_{laser} = 2.71, 2.66, 2.62, 2.60, 2.54, 2.50, 2.47, 2.41, 2.16, 2.12, 2.07, 2.03, and 1.92 eV were available. This wide range of laser excitation energies allow us to study both semiconducting and metallic nanotubes. We will investigate the differences regarding the D-band behavior between semiconducting and metallic nanotubes, as well as the D-band properties common to both types of nanotubes.

Peak fitting was performed on all spectra to extract the D-band parameters and to separate the G-band components. The integrated and peak D-band intensities were normalized to the G^+ peak. Three samples with average tube lengths of 100, 70, and 50 nm were studied, and spectra were taken for multiple spots on each sample, resulting in a total of 291 spectra. These spectra could then be divided in two groups, corresponding to metallic or semiconducting nanotubes, depending on the laser excitation energy. The G-band for E_{laser} = 2.41 eV and greater exhibited the broad Breit-Wigner-Fano (BWF) G^- (lower branch) lineshape, which is a signature of metallic nanotubes. For spectra taken with E_{laser} = 2.16, 2.12, 2.07, 2.03 and 1.92 eV, the intensity of the lower branch of the G^- peak was small and could be fit by a Lorentzian, which is typical for semiconducting nanotubes. Because of the observed G-band lineshapes, and the fact that the lower E_{laser} excitation energies tend to excite semiconducting nanotubes, the spectra measured with E_{laser} = 2.16 eV and lower went into the semiconducting group, and the spectra measured with E_{laser} = 2.41 eV and greater were considered as metallic. Correlation coefficients between the D-band parameters and L_{tube} or E_{laser} were then calculated separately for the semiconducting and metallic groups, and for all the spectra combined.

For the metallic group, 178 data points (spectra) were available, which results in a P = 0.05 significance threshold of $|r| \geq 0.15$ for the correlation coefficient. The semiconducting group contains 113 data points and the P = 0.05 significance threshold is $|r| \geq 0.19$. There were 291 data points for the combined metallic + semiconducting group, for a P = 0.05 significance threshold of $|r| \geq 0.12$. The calculated weighted correlation coefficients for the D-band parameters are summarized in Table 5-1, for the three groups of data.

X-Y Pair	**Semiconducting; P = 0.05 threshold:** $\|r\| \geq 0.19$	**Metallic; P = 0.05 threshold:** $\|r\| \geq 0.15$	**Semiconducting + Metallic; P = 0.05 threshold:** $\|r\| \geq 0.12$
ω_D vs. L_{tube}	-0.159	-0.108	-0.052
$(FWHM)_D$ vs. L_{tube}	-0.180	-0.672	-0.330
Peak $\left(I_D / I_{G^+}\right)$ vs. L_{tube}	-0.328	-0.738	-0.419
Integrated $\left(I_D / I_{G^+}\right)$ vs. L_{tube}	-0.282	-0.743	-0.467
ω_D vs. E_{laser}	0.874	0.512	0.944
$(FWHM)_D$ vs. E_{laser}	-0.176	-0.040	0.237
Peak $\left(I_D / I_{G^+}\right)$ vs. E_{laser}	-0.381	-0.140	0.641
Integrated $\left(I_D / I_{G^+}\right)$ vs. E_{laser}	-0.269	-0.037	0.566

Table 5-1. The calculated weighted correlation coefficients for the various D-band parameters. The correlation coefficients for semiconducting nanotubes, metallic nanotubes, and combined semiconducting and metallic nanotubes are shown. The corresponding P = 0.05 significance threshold values for each group are listed in the first row.

5.4 General D-band Properties

In this section we address the general D-band properties. These are correlations that occur for all three groups of data: metallic spectra only, semiconducting spectra only, and both semiconducting and metallic spectra.

We find that the D-band frequency ω_D and E_{laser} are correlated for all three cases in Table 5-1. The scatter plot of ω_D vs. E_{laser} is shown in Figure 5-5, with different point colors for each tube length. The linear fit is ω_D = 54.2 E_{laser} + 1203 cm^{-1}, with confidence intervals of (52.0, 56.4) cm^{-1}/eV for the slope and (1198, 1209) cm^{-1} for the intercept. The dependence of ω_D on E_{laser} is expected, and the fitted slope agrees with the value of 53 cm^{-1}/eV reported in the literature [7]. When the metallic nanotubes are

considered separately, we find a fit of ω_D = 36.0 E_{laser} + 1250 cm^{-1}, with confidence intervals of (27.0, 45.0) cm^{-1}/eV for the slope and (1227, 1273) cm^{-1} for the intercept. For semiconducting tubes, the fit is ω_D = 58.7 E_{laser} + 1194 cm^{-1}, with confidence intervals of (52.6, 64.9) cm^{-1}/eV for the slope and (1181, 1206) cm^{-1} for the intercept. Since the confidence intervals for semiconducting and metallic tubes do not overlap for both the slope and intercept, the dispersion for semiconducting and metallic tubes should be considered independently of one another.

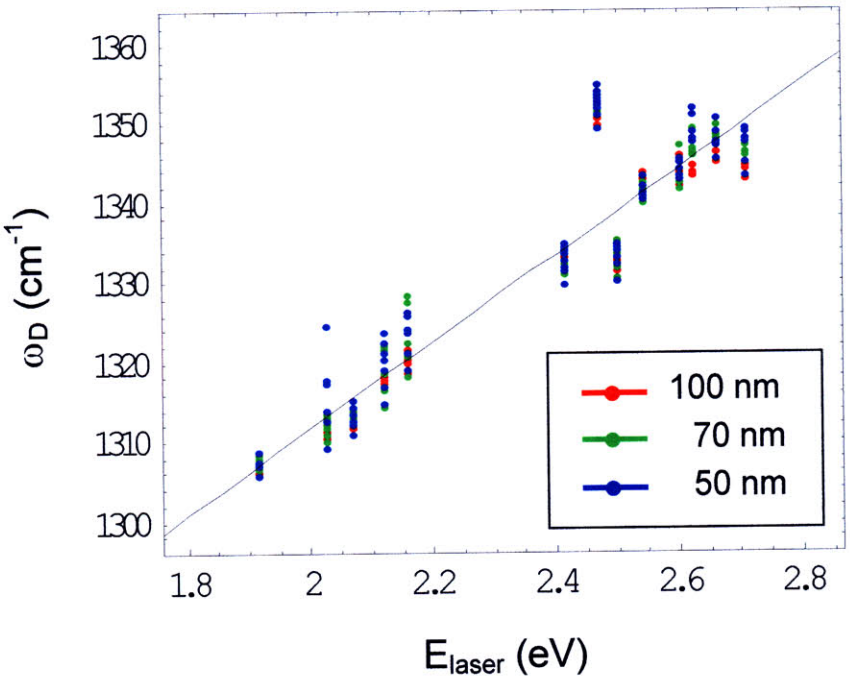

Figure 5-5. Scatter plot of ω_D vs. E_{laser}, with different point colors for each tube length. The linear fit to all the data points, ω_D = 54.2 E_{laser} + 1203 cm^{-1}, is superimposed.

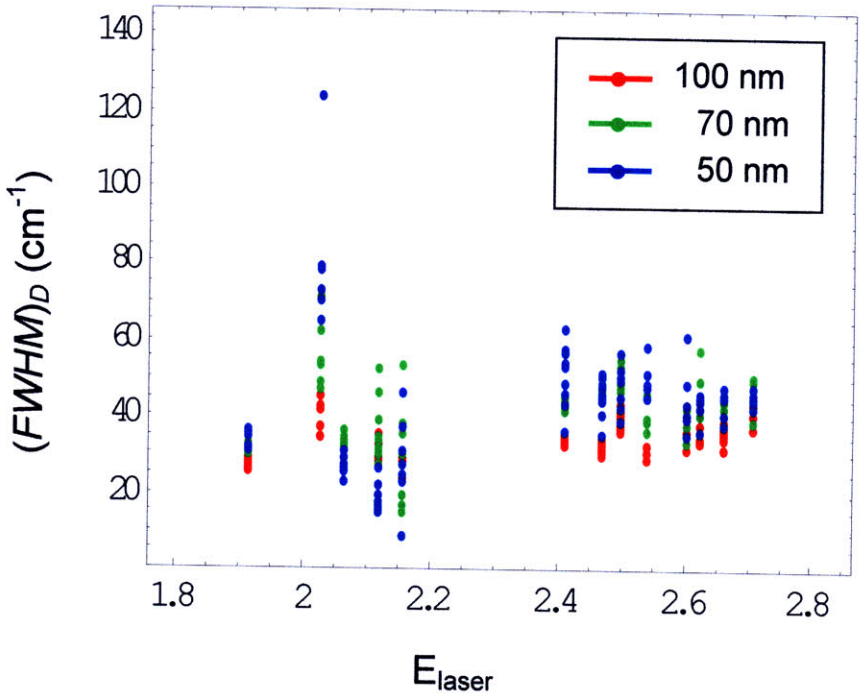

Figure 5-6. Scatter plot of $(FWHM)_D$ vs. E_{laser}, with different point colors for each tube length.

We find that ω_D does not depend on length, whether metallic or semiconducting tubes, or both, are considered. This lack of length dependence can be seen in Figure 5-5, as the different colors of points corresponding to different lengths are mostly on top of each other.

On Figure 5-6 the $(FWHM)_D$ is plotted against E_{laser}. No linear correlation was found between $(FWHM)_D$ and E_{laser} for metallic or semiconducting nanotubes (Table 5-1). When semiconducting and metallic nanotubes are taken together, there is a positive correlation between $(FWHM)_D$ and E_{laser}, but from Figure 5-6, this correlation is not convincing.

As expected, both the peak and integrated $\left(I_D / I_{G^+}\right)$ are anticorrelated with length. The linear fits and confidence intervals are listed in Table 5-2, which also includes the fits for ω_D vs. E_{laser} which are strongly correlated.

Group	Linear fit	Confidence interval of slope	Confidence interval of *y*-intercept
M+S	ω_D = 54.2 E_{laser} + 1203	(52.0, 56.4)	(1198, 1209)
M	ω_D = 36.0 E_{laser} + 1250	(27.0, 45.0)	(1227, 1273)
S	ω_D = 58.7 E_{laser} + 1194	(52.6, 64.9)	(1181, 1206)
M+S	Peak $\left(I_D / I_{G^+}\right)$ = -0.00147 L_{tube} + 0.209	(-0.00183, -0.00110)	(0.181, 0.237)
M	Peak $\left(I_D / I_{G^+}\right)$ = -0.00227 L_{tube} + 0.308	(-0.00257, -0.00195)	(0.285, 0.332)
S	Peak $\left(I_D / I_{G^+}\right)$ = -0.000195 L_{tube} + 0.0506	(-0.000301, -0.0000898)	(0.0425, 0.0586)
M+S	Integrated $\left(I_D / I_{G^+}\right)$ = -0.00413 L_{tube} + 0.570	(-0.00503, -0.00323)	(0.501, 0.639)
M	Integrated $\left(I_D / I_{G^+}\right)$ = -0.00587 L_{tube} + 0.789	(-0.00666, -0.00509)	(0.729, 0.849)
S	Integrated $\left(I_D / I_{G^+}\right)$ = -0.00134 L_{tube} + 0.221	(-0.00220, -0.000480)	(0.156, 0.287)

Table 5-2. The L_{tube} and E_{laser} dependence of the D-band parameters for which the correlation coefficients were found to be statistically significant for the three groups: metallic (M), semiconducting (S), and combined metallic and semiconducting (M+S). The linear fits and confidence intervals for each of the three groups of data are listed.

5.5 Metallic vs. Semiconducting Nanotubes

We now consider how the D-band properties differ for metallic and semiconducting nanotubes.

The correlation coefficient between the D-band linewidth, $(FWHM)_D$, and L_{tube} was found to be statistically significant for metallic nanotubes but not for semiconducting nanotubes (Table 5-1). For metallic nanotubes, $(FWHM)_D$ is anticorrelated with L_{tube}

and increases from about 38 cm^{-1} to 50 cm^{-1} as L_{tube} decreases from 100 nm to 50 nm. The linear fit for metallic nanotubes is $(FWHM)_D$ = -0.219 L_{tube} + 58.3 cm^{-1}, with confidence intervals of (-0.255, -0.183) for the slope and (55.6, 61.0) for the intercept. In nanographite, the D-band linewidth was also found to vary inversely with the crystallite size L_a [8]. For crystallite sizes smaller than the phonon mean free path, the phonon lifetime should be proportional, and hence the FWHM should be inversely proportional, to L_a [8]. The result found here may indicate that the D-band phonon mean free path is greater than 100 nm for metallic nanotubes but not for semiconducting nanotubes.

The peak and integrated $\left(I_D / I_{G^+}\right)$ were found to be anticorrelated with E_{laser} for semiconducting tubes but not for metallic tubes. For semiconducting tubes, we find that peak $\left(I_D / I_{G^+}\right)$ = -0.0559 E_{laser} + 0.151 with confidence intervals of (-0.0815, -0.0304) for the slope and (0.0987, 0.204) for the intercept. We also find for semiconducting tubes integrated $\left(I_D / I_{G^+}\right)$ = -0.315 E_{laser} + 0.772 with confidence intervals of (-0.528, -0.103) for the slope and (0.334, 1.21) for the intercept.

The anticorrelation of the peak and integrated $\left(I_D / I_{G^+}\right)$ on E_{laser} for semiconducting tubes appear to be unrelated to length-dependence effects. When the data is grouped by length, we find that semiconducting tubes of 100 nm and 50 nm length show an anticorrelation between E_{laser} and peak and integrated $\left(I_D / I_{G^+}\right)$. Semiconducting tubes of 70 nm length have uncorrelated peak and integrated $\left(I_D / I_{G^+}\right)$ vs. E_{laser}. On the other hand, for metallic tubes, E_{laser} and integrated $\left(I_D / I_{G^+}\right)$ are uncorrelated when the 100 nm, 70 nm, and 50 nm length tubes are considered separately. The peak $\left(I_D / I_{G^+}\right)$ and E_{laser} are anticorrelated for 70 nm metallic tubes but uncorrelated for 100 nm and 50 nm metallic tubes. Thus there is no systematic length effect.

Besides the aforementioned correlations, there are further differences between semiconducting and metallic nanotubes. Metallic nanotubes seem to be more sensitive to changes in length than semiconducting nanotubes. In the linear fit of peak $\left(I_D / I_{G^+}\right)$ vs. L_{tube}, metallic nanotubes have a slope that is an order of magnitude greater than

semiconducting tubes (Table 5-2). For the integrated $\left(I_D / I_{G^+}\right)$ vs. L_{tube}, metallic nanotubes have a slope that is about 6 times greater than semiconducting tubes. Furthermore, as mentioned above, the D-band FWHM is length dependent for metallic tubes but not for semiconducting tubes. The difference in length sensitivity between metallic and semiconducting nanotubes may be due to the difference in binding energy between excitons in metallic vs. semiconducting tubes [9, 10]. In metallic nanotubes, the exciton binding energy is less than 0.2 eV, while the exciton binding energy in semiconducting tubes is can be as large as 1 eV [9]. Hence for a metallic nanotube, the exciton size is large compared to that of a semiconducting nanotube. Since the exciton size for a metallic nanotube is about 10-50 nm, the increased length dependence seen here for metallic nanotubes could be a finite size effect [10].

In addition, metallic nanotubes have a greater peak and integrated $\left(I_D / I_{G^+}\right)$ than semiconducting nanotubes. This is evident in Figures 5-7 and 5-8, which plot the peak and integrated $\left(I_D / I_{G^+}\right)$ vs. E_{laser}. In the figures, a step can be seen in $\left(I_D / I_{G^+}\right)$ when E_{laser} changes from being resonant with semiconducting tubes to metallic tubes.

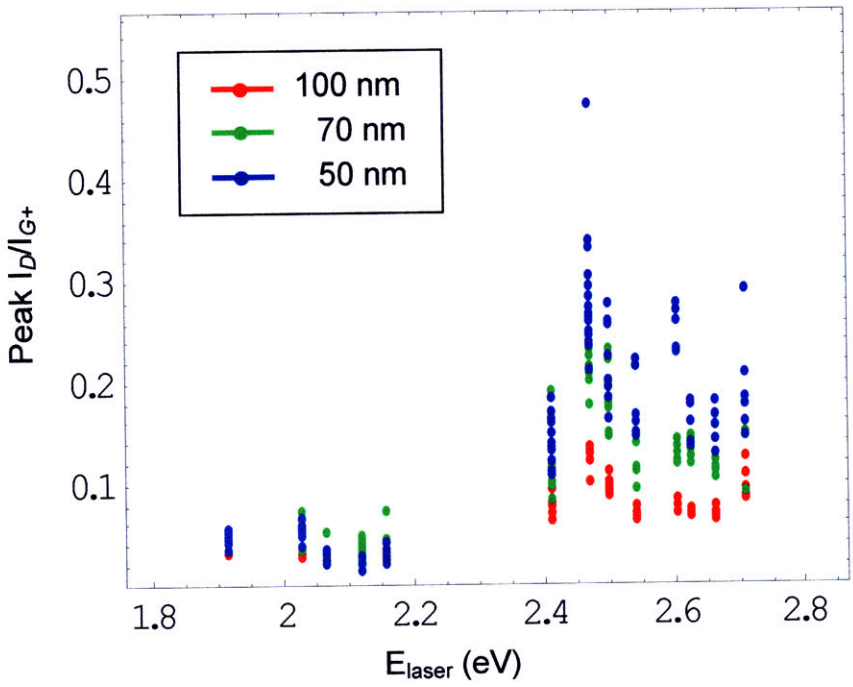

Figure 5-7. E_{laser} dependence of the peak $\left(I_D / I_{G^+}\right)$, with different point colors for each tube length.

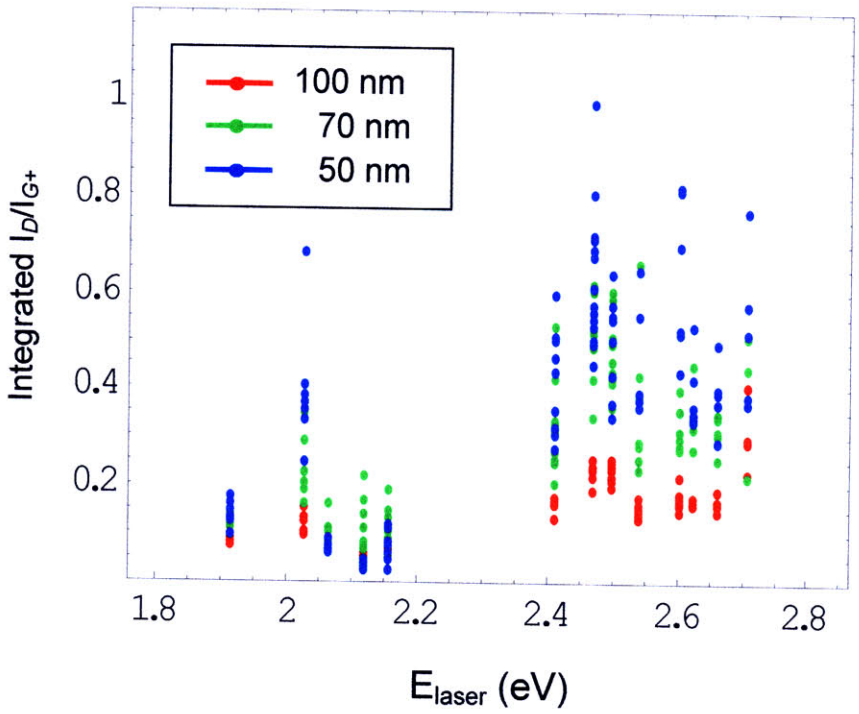

Figure 5-8. E_{laser} dependence of the integrated $\left(I_D / I_{G^+}\right)$, with different point colors for each tube length.

5.6 Summary

In this chapter we examined the length and E_{laser} dependence of the D-band, as well as the differences between semiconducting and metallic nanotubes. As a continuation of previous work [3], we attempted to determine whether the length and E_{laser} dependence of the D-band intensity for carbon nanotubes was similar to that of nanographite [4]. However, a relation between the integrated I_D / I_{G^+} ratio, E_{laser}, and L_{tube}, analogous to the nanographite formula (Equation 5-1), could not be fit from the data. Correlation analysis was used to determine the D-band dependence on L_{tube} and E_{laser}. Regardless of whether the nanotubes are semiconducting or metallic, we have found that the peak and integrated I_D / I_{G^+} ratio are inversely proportional to L_{tube}. The D-band frequency was found to linearly depend on E_{laser}, in agreement with the literature [2, 7]. However ω_D was found not to depend on L_{tube}.

A few differences were found in the D-band behavior of semiconducting vs. metallic nanotubes. For metallic nanotubes, the D-band linewidth was found to be anticorrelated with length. For semiconducting nanotubes, the peak and integrated $\left(I_D / I_{G^+}\right)$ ratio are anticorrelated with E_{laser}. Furthermore the slope of the ω_D vs. E_{laser} dependence is smaller for metallic tubes than semiconducting. Metallic nanotubes were found to have a much greater peak and integrated $\left(I_D / I_{G^+}\right)$ ratio than semiconducting nanotubes. Finally, metallic nanotubes appear to be more sensitive to changes in length, since $\left(I_D / I_{G^+}\right)$ and $(FWHM)_D$ have more length dependence for metallic nanotubes than for semiconducting tubes.

References

[1] F. Tuinstra and J. L. Koenig, "Raman Spectrum of Graphite," *Journal of Chemical Physics,* **53** (1970), 1126.

[2] M. A. Pimenta et al., "Diameter dependence of the Raman *D*-band in isolated single-wall carbon nanotubes," *Physical Review B,* **64** (2001) 041401.

[3] S. G. Chou et al., "Length characterization of DNA-wrapped carbon nanotubes using Raman spectroscopy." *Applied Physics Letters*, **90** (2007) 131109.

[4] L. G. Cancado et al., "General equation for the determination of the crystallite size L_a of nanographite by Raman spectroscopy," *Applied Physics Letters,* **88** (2006) 163106.

[5] E. Di Donato et. a.l., "Assignment of the G^+ and G^- Raman bands of metallic and semiconducting carbon based on a common valence force field," *Physical Review B,* **74** (2006) 184306.

[6] V. N. Popov and P. Lambin, "Symmetry-adapted tight-binding calculations of the totally symmetric A_1 phonons of single-walled carbon nanotubes and their resonant Raman intensity," *Physica E,* **37** (2007) 97.

[7] M. S. Dresselhaus et al., "Raman spectroscopy of carbon nanotubes," *Physics Reports,* **409** (2005) 47.

[8] L. G. Cancado, *Raman Spectroscopy of Nanographites.* PhD Thesis, Universidade Federal de Minas Gerais, 2006.

[9] J. Jiang et. a.l., "Chirality dependence of exciton effects in single-all carbon nanotubes: Tight-binding model," *Physical Review B,* **75** (2007) 035407.

[10] R. Saito (Private Communication).

Chapter 6 – G'

6.1 Introduction

The second harmonic of the D-band is the G' peak at around 2700 cm^{-1} (for E_{laser} = 2.7 eV). Whereas the D-band corresponds to a second-order process involving one elastic scattering event via a defect and one phonon scattering event, the G' band involves two phonon scattering processes [1]. Since the G' band is a double resonance process, an intense G' peak can occur in the Raman spectra of graphitic materials with no disorder or even with low disorder present [1]. Although the G' band typically appears as a single peak, double peak G' bands have also been observed for semiconducting and metallic nanotubes [2, 3]. For semiconducting tubes, the two peaks occur when the incident and scattered photons are in resonance with two different van Hove singularities (vHSs) in a single nanotube [2]. In metallic nanotubes, the two G' components appear because the trigonal warping effect splits the vHSs in the joint density of states of the nanotube [4]. The double peak G' band was frequently observed in our studies of short carbon nanotubes, for both metallic and semiconducting tubes. In this chapter, we will examine the E_{laser} and length dependence of the two peaks comprising the G' band.

The G' band was measured using E_{laser} = 457.9 nm (2.71 eV), 465.8 nm (2.66 eV), 472.7 nm (2.62 eV), 476.5 nm (2.60 eV), 600 nm (2.07 eV), 612 nm (2.03 eV), and 647 nm (1.92 eV). In most of the available spectra, the G' band was found to consist of two peaks. For these cases, the G' peak was fit using two Lorentzians (Figures 6-1). Occasionally the peak fitting procedure resulted in only one peak comprising the G' band. Single-peak G' spectra appeared in significant amounts for only E_{laser} = 612 nm (2.03 eV); in this case, all of the spectra corresponding to 50 nm long tubes had single peak G' bands, while double-peak G' bands were found for the longer tubes. The low intensity peak at 2420 cm^{-1} in Fig. 6-1 is the G* peak, which will be addressed in the following chapter.

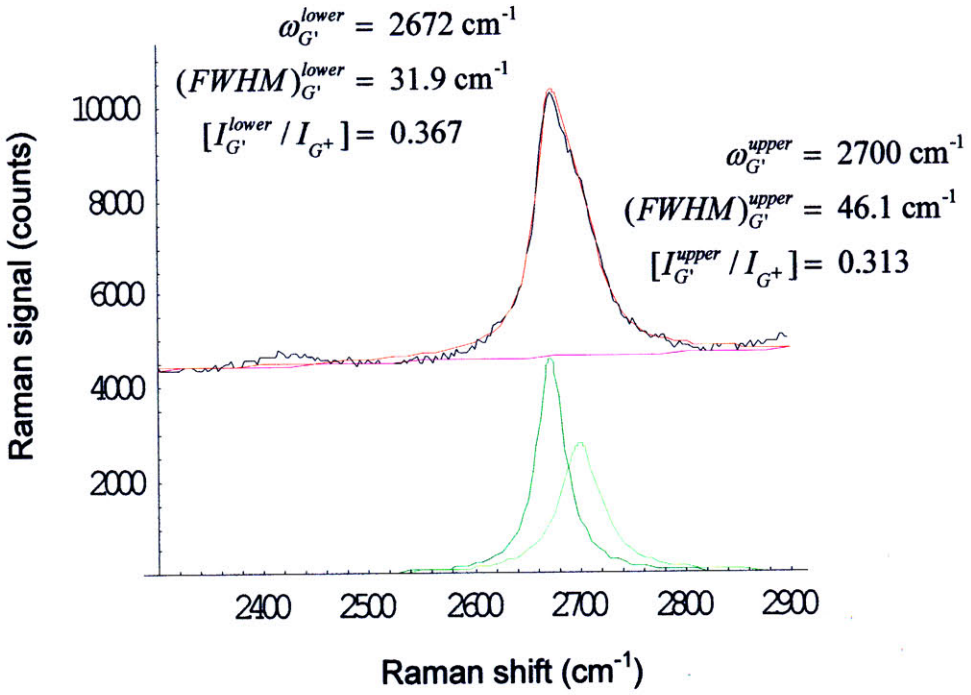

Figure 6-1(a). Lineshape fitting of the G' band. For this example, E_{laser} = 457.9 nm (2.71 eV) and L_{tube} = 100 nm. The black curve is the raw data, and the red curve is the result of the lineshape fitting. The fitting model is the sum of a baseline (magenta curve) and two Lorentzians (green curves).

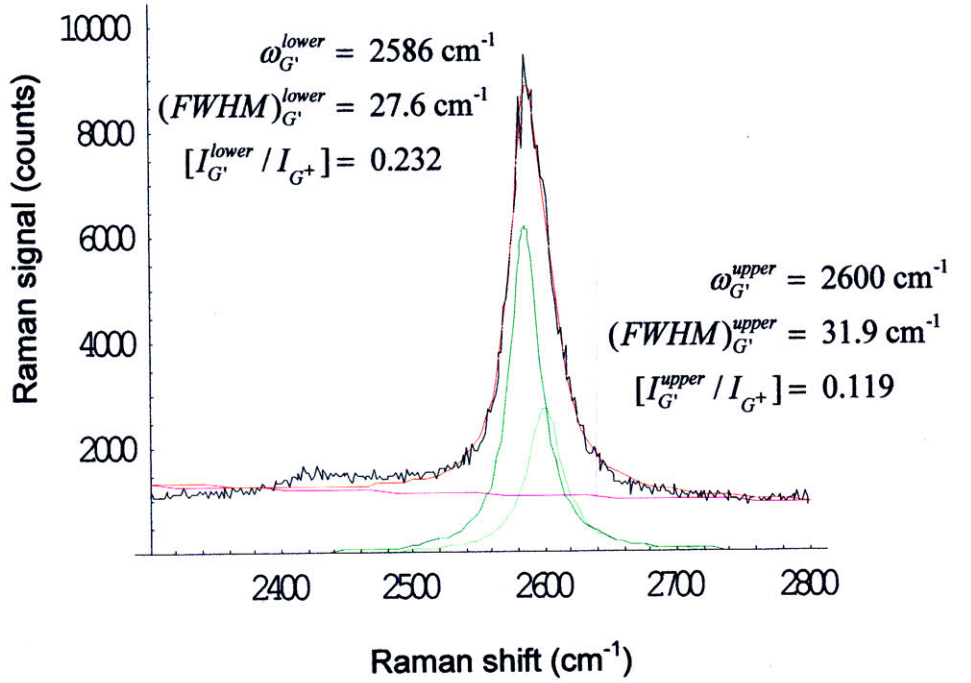

Figure 6-1(b). Same as Figure 6-1(a), but for E_{laser} = 647 nm (1.92 eV). L_{tube} = 100 nm in this figure.

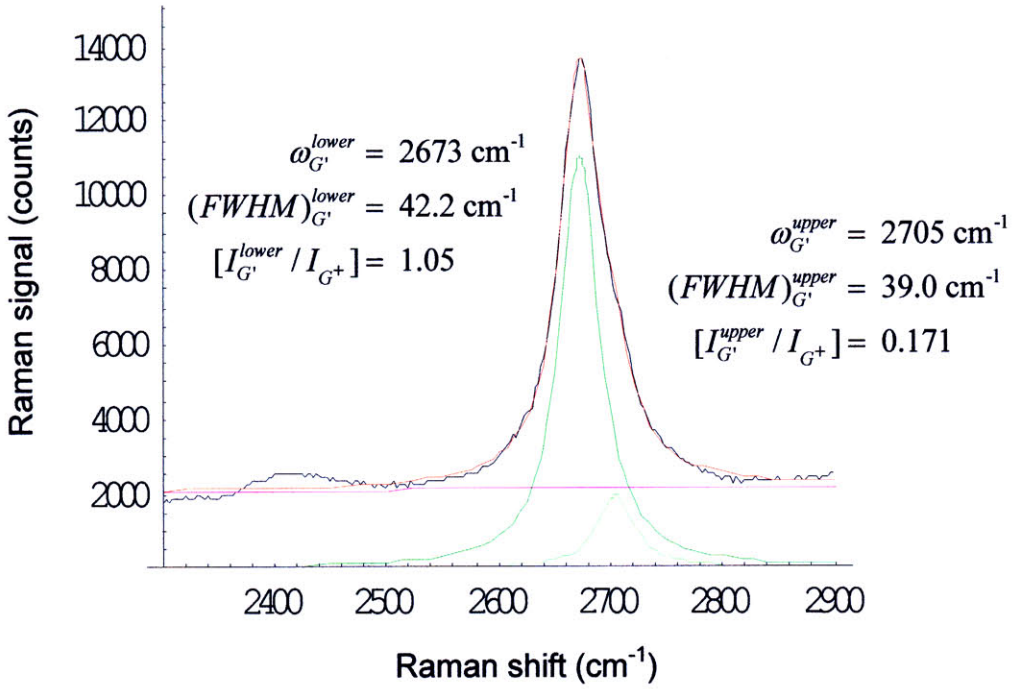

Figure 6-1(c). Same as Figure 6-1(a), but for E_{laser} = 476.5 nm (2.60 eV). L_{tube} = 100 nm in this figure.

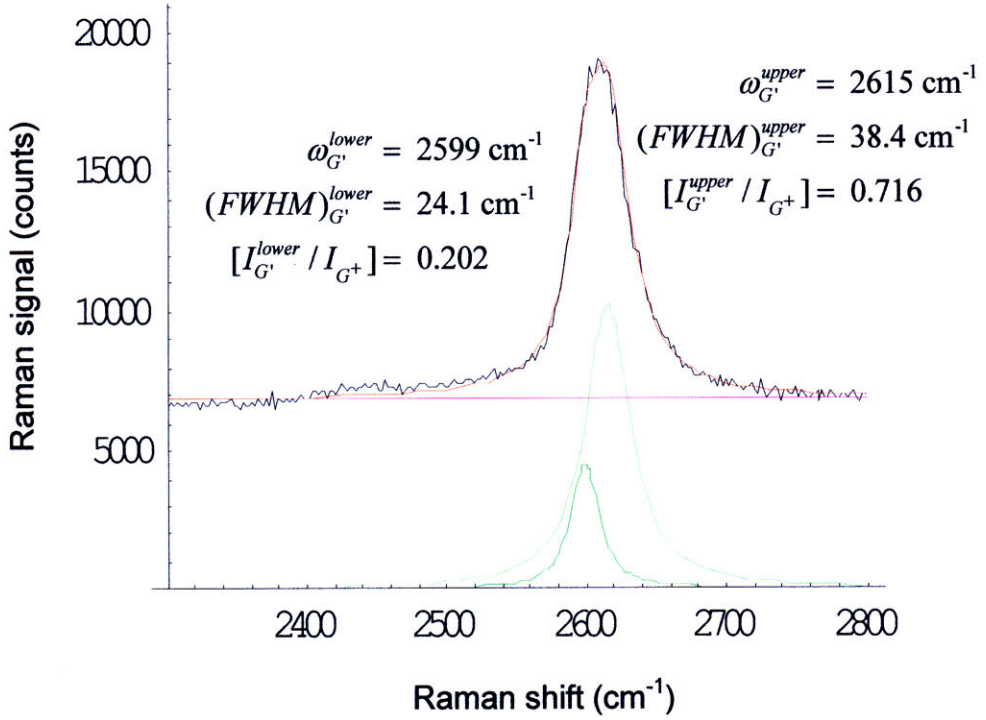

Figure 6-1(d). Same as Figure 6-1(a), but for E_{laser} = 612 nm (2.03 eV). L_{tube} = 100 nm in this figure.

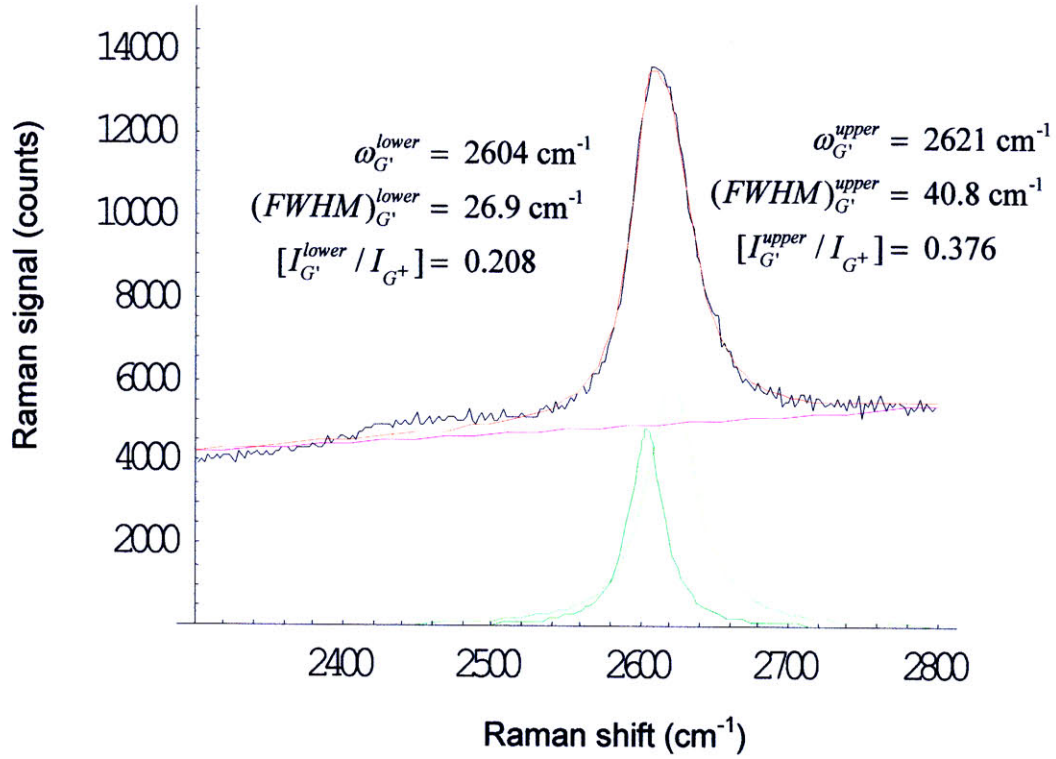

Figure 6-1(e). Same as Figure 6-1(a), but for E_{laser} = 600 nm (2.07 eV). L_{tube} = 100 nm in this figure.

6.2 The G' Frequencies and Frequency Splitting

The E_{laser} dependence of the higher frequency G' component, $\omega_{G'}^{upper}$, is shown in Figure 6-2. For the spectra available, $\omega_{G'}^{upper}$ was found to vary from about 2602 cm^{-1} to 2622 cm^{-1} for the lower E_{laser} values (E_{laser} = 1.92 – 2.07 eV), and from about 2697 cm^{-1} to 2704 cm^{-1} for the higher E_{laser} values (E_{laser} = 2.60 – 2.71 eV). The E_{laser} dependence of the lower frequency component of G', $\omega_{G'}^{lower}$, is shown in Figure 6-3. The dispersion relations of both $\omega_{G'}^{upper}$ and $\omega_{G'}^{lower}$ seem to differ according to whether E_{laser} is between 1.92 and 2.07 eV, or whether E_{laser} falls in the 2.60 – 2.71 eV range. Thus we will find the dispersion relation for these two E_{laser} ranges separately. For $1.92 \leq E_{laser} \leq 2.07$ eV, the linear fit gives the relation $\omega_{G'}^{upper} = 135E_{laser} + 2345$ cm^{-1}, with confidence intervals of (126, 144) cm^{-1}/eV for the slope and (2325, 2360) cm^{-1} for the intercept. Within the same E_{laser} range, $\omega_{G'}^{lower} = 126E_{laser} + 2344$ cm^{-1}, with confidence intervals of (121, 131)

cm^{-1}/eV for the slope and (2333, 2354) cm^{-1} for the intercept. For 2.60 ≤ E_{laser} ≤ 2.71 eV, the slope is opposite: $\omega_{G'}^{upper}$ = -62.8E_{laser} + 2867 cm^{-1}, with confidence intervals of (-78.2, -47.4) cm^{-1}/eV for the slope and (2826, 2908) cm^{-1} for the intercept. The lower frequency component has $\omega_{G'}^{lower}$ = -13.9E_{laser} + 2708 cm^{-1}, with confidence intervals of (-22.0, -5.74) cm^{-1}/eV for the slope and (2686, 2729) cm^{-1} for the intercept, for 2.60 ≤ E_{laser} ≤ 2.71 eV.

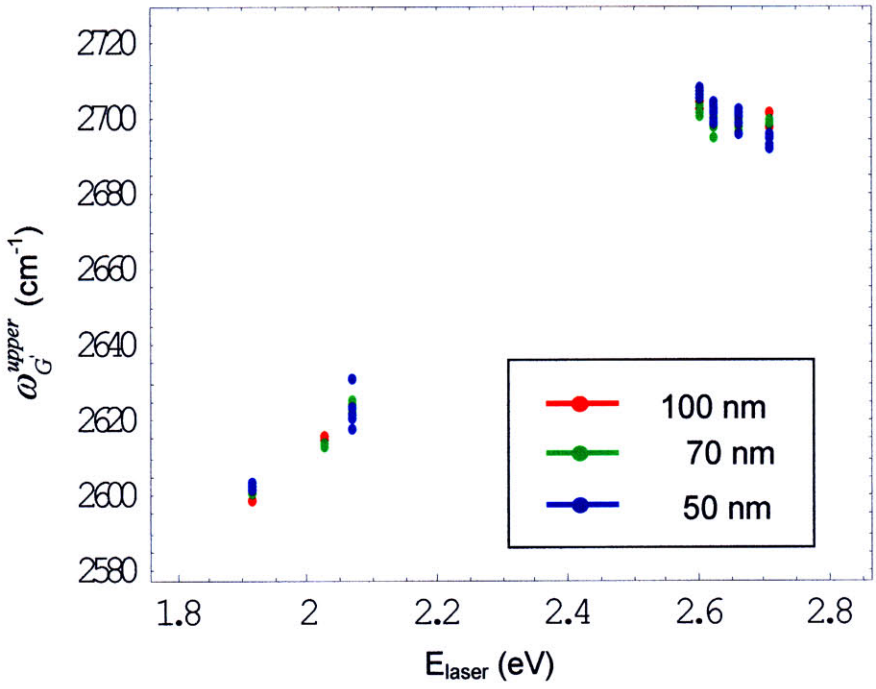

Figure 6-2. Scatter plot of the higher frequency G' component $\omega_{G'}^{upper}$ vs. E_{laser}, with different point colors for each tube length.

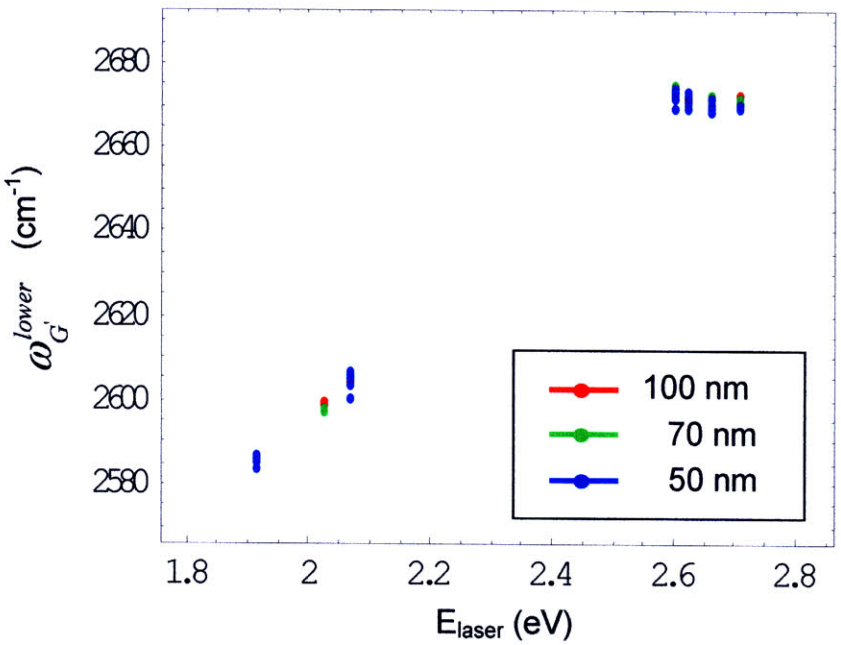

Figure 6-3. Scatter plot of the lower frequency G' component $\omega_{G'}^{lower}$ vs. E_{laser}, with different point colors for each tube length.

We also examined the G' band splitting, $\Delta\omega_{G'} \equiv \omega_{G'}^{upper} - \omega_{G'}^{lower}$. The E_{laser} dependence of $\Delta\omega_{G'}$ is shown in Figure 6-4. Like $\omega_{G'}^{upper}$ and $\omega_{G'}^{lower}$, the E_{laser} dependence of $\Delta\omega_{G'}$ differs depending on whether $1.92 \leq E_{laser} \leq 2.07$ eV or $2.60 \leq E_{laser} \leq 2.71$ eV. From Figure 6-4 it is clear that $\Delta\omega_{G'}$ is greater for points that fall within $2.60 \leq E_{laser} \leq 2.71$ eV than for points in the $1.92 \leq E_{laser} \leq 2.07$ eV range. In addition, $\Delta\omega_{G'}$ changes more rapidly with E_{laser} for $2.60 \leq E_{laser} \leq 2.71$ eV, and the slope is opposite to that of the points within $1.92 \leq E_{laser} \leq 2.07$ eV.

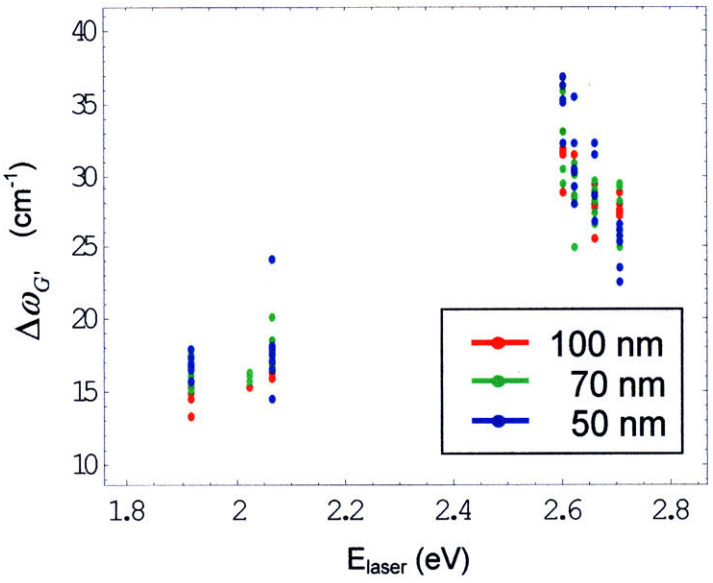

Figure 6-4. Scatter plot of the G' frequency splitting $\Delta\omega_{G'}$ vs. E_{laser}, with different point colors for each tube length.

Previous works have indicated that the double peak structure of G' arises from two energy levels being excited for a given E_{laser}, and each peak corresponds to one of the two states in resonance [36, 37]. When $\Delta\omega_{G'}$ is converted to energy ΔE, it represents the energy separation between the two resonant states. In Ref. 4, the proportionality constant between $\Delta\omega_{G'}$ and ΔE was found to be the G' frequency dispersion; i.e. $\Delta\omega_{G'} = (\partial\omega_{G'} / \partial E_{laser})\Delta E$. In our case there are two possible values for the dispersion: $(\partial\omega_{G'}^{upper} / \partial E_{laser})$ for the upper frequency component of G', and $(\partial\omega_{G'}^{lower} / \partial E_{laser})$ for the lower frequency component.

For $2.60 \leq E_{laser} \leq 2.71$ eV, $(\partial\omega_{G'}^{lower} / \partial E_{laser})$ = -13.9 cm^{-1}/eV, and the corresponding ΔE ranges from 1.91 eV (for E_{laser} = 2.71 eV) to 2.34 eV (for E_{laser} = 2.60 eV). These values for the energy separation between resonant states are unreasonably high. On the other hand, for the upper frequency component, $(\partial\omega_{G'}^{upper} / \partial E_{laser})$ = -62.8 cm^{-1}/eV for $2.60 \leq E_{laser} \leq 2.71$ eV. This corresponds to an energy separation ΔE that ranges from 0.424 eV (for E_{laser} = 2.71 eV) to 0.518 eV (for E_{laser} = 2.60 eV). This is a more reasonable ΔE which has a physical interpretation: for $2.60 \leq E_{laser} \leq 2.71$ eV, the average frequency $\omega_{G'}^{upper}$ is 2701 cm^{-1}, which gives a scattered phonon energy of 0.33 eV. Then, a ΔE range of 0.424 – 0.518 eV is about equal to the scattered phonon energy plus

a resonant window of 0.1 – 0.2 eV. Thus, for 2.60 ≤ E_{laser} ≤ 2.71 eV, the lower component of G' may arise from resonance with the scattered photon, while the upper component of G' could be due to resonance with the incident photon.

In the 1.92 ≤ E_{laser} ≤ 2.07 eV range, $(\partial\omega_{G'}^{upper}/\partial E_{laser})$ = 135 cm^{-1}/eV, and $(\partial\omega_{G'}^{lower}/\partial E_{laser})$ = 126 cm^{-1}/eV. The two dispersions are comparable to each other, but for consistency we use $(\partial\omega_{G'}^{upper}/\partial E_{laser})$ to compute ΔE. Table 6-1 lists the average $\Delta\omega_{G'}$ and corresponding ΔE for each E_{laser}. For 1.92 ≤ E_{laser} ≤ 2.07 eV, we find that ΔE is around 0.12 eV, which is very much smaller than the ΔE for higher E_{laser}. If we assume a resonant window of 0.2 eV [3], then a ΔE of 0.12 eV could arise from two closely spaced states, both within the G' resonant window, which are simultaneously excited by the incident photon.

E_{laser} (eV)	Average $\Delta\omega_{G'}$ (cm^{-1})	ΔE (eV)
2.71	26.6	0.424
2.66	28.7	0.457
2.62	29.8	0.475
2.60	32.5	0.518
2.07	17.5	0.130
2.03	15.8	0.117
1.92	15.9	0.118

Table 6-1. The measured frequency separation $\Delta\omega_{G'}$ between the two G' components, and corresponding energy separation ΔE, for each E_{laser}.

The two mechanisms discussed above for the double peak structure are further supported by the Kataura plot (Figure 6-5). We use the observed RBM (radial breathing modes) to identify the states that are resonant with a given E_{laser}; the RBMs and resonant tubes are listed in Table 6-2. For 2.60 ≤ E_{laser} ≤ 2.71 eV, the observed RBMs at 286 – 310 cm^{-1} indicate resonance with the (6, 6) and (7, 4) nanotubes. The (10, 1) and (6, 5) tubes are resonant at an energy around 0.42 eV below the (6, 6) and (7, 4) tubes, which agrees with the measured ΔE for 2.60 ≤ E_{laser} ≤ 2.71 eV. Therefore for 2.60 ≤ E_{laser} ≤ 2.71 eV, the upper component of G' could be due to incident photon resonance with the

(6, 6) and (7, 4) tubes, while the lower G' component could be caused by resonance of the scattered photon with the (10, 1) and (6, 5) tubes.

For E_{laser} = 2.07 eV and lower, the observed RBMs suggest that nanotubes from families 27, 23 and 19 are resonant. In this case, for an assumed resonant window of 0.2 eV [3], multiple states could be excited by the incident photon, resulting in a double peak structure for G'. This scenario is especially likely for the metallic nanotubes in the lower branch of family 27, which is composed of tubes that are closely spaced in energy.

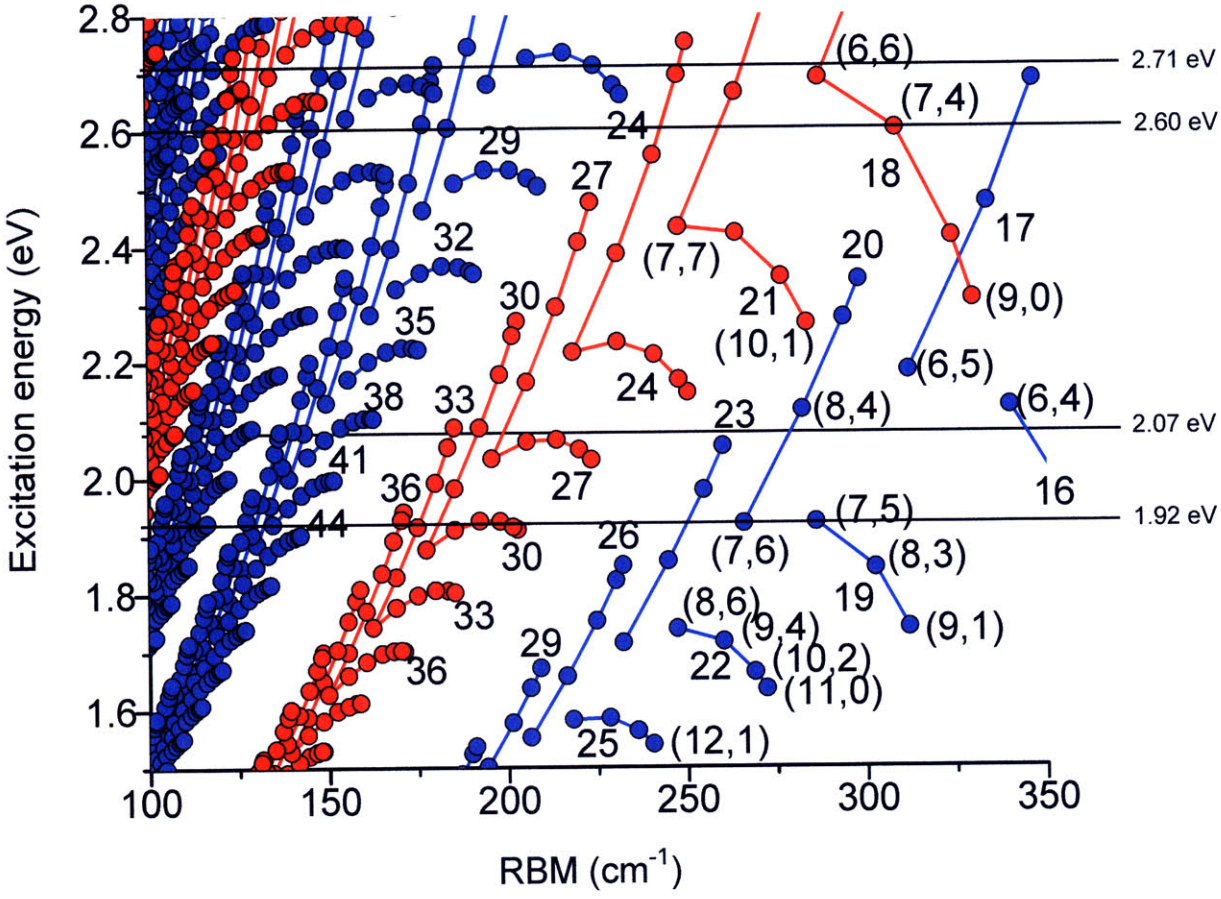

Figure 6-5. Kataura plot. The E_{laser} ranges of interest are marked by the horizontal lines.

E_{laser} (eV)	Observed RBMs (cm^{-1})	Resonant nanotubes, based on the most intense RBMs
2.71	227, 286, 302	(6, 6), possibly (7, 4)
2.66	180, 230, 291, 310	(6, 6), (7, 4)
2.62	206, 228, 262, 287, 306	(7, 4)
2.60	206, 224, 264, 286, 307	(7, 4), possibly family 29
2.07	218, 256, 281	Family 27
2.03	199, 218, 259, 285	Family 27, family 23
1.92	197, 267, 286	(7, 5)

Table 6-2. The observed RBMs for each laser excitation energy (see Chapter 8). The most intense RBMs for a given E_{laser} are underlined. The third column gives the resonant tubes, based on the underlined RBMs in the second column.

6.3 Intensities of the G' Peaks

In this section we examine the integrated intensities of the two G' peaks, which are normalized to the integrated intensity of the G^+ peak. When normalizing the G' peaks to G^+, we always use the corresponding G^+ data for each spot on the sample. Figures 6-6 and 6-7 show the E_{laser} dependences of the integrated intensity ratios $[I_{G'}^{upper} / I_{G^+}]$, for the higher frequency G' component, and $[I_{G'}^{lower} / I_{G^+}]$ for the lower frequency G' component. We have observed that the normalized peak intensities closely follow the integrated intensities. Figure 6-8 shows the integrated intensity ratio $[I_{G'}^{lower} / I_{G'}^{upper}]$ between the two G' peaks. In Table 6-3, the average values of $[I_{G'}^{lower} / I_{G^+}]$ and $[I_{G'}^{upper} / I_{G^+}]$, as well as the ratio $[I_{G'}^{lower} / I_{G'}^{upper}]$ are given for each E_{laser}.

For $2.60 \leq E_{laser} \leq 2.71$ eV, the intensity ratio $[I_{G'}^{upper} / I_{G^+}]$, which is related to resonance with the incident photon, increases with increasing E_{laser}. This trend can be explained by considering which nanotubes are excited, as indicated by the ω_{RBM} and the Kataura plot in Fig. 6-5. For E_{laser} = 2.60 and 2.62 eV, the dominant RBMs at around 306 cm^{-1} (Table 6-2) indicate a resonance with the (7, 4) tube. As E_{laser} increases, the RBMs at 286 cm^{-1} and 291 cm^{-1} become more prominent, indicating resonance with the (6, 6) tube

in addition to the (7, 4) tube. Thus, $[I_{G'}^{upper} / I_{G+}]$ increases with E_{laser} in the $2.60 \leq E_{laser} \leq 2.71$ eV range because more nanotubes are resonant at the higher laser excitation energies. In this E_{laser} range, $I_{G'}^{lower} > I_{G'}^{upper}$, even at $E_{laser} = 2.71$ eV.

For $E_{laser} = 2.03$ eV, the dominant RBMs indicate resonances with the tubes of families 23 and 27. For this E_{laser}, the high average value of $[I_{G'}^{upper} / I_{G+}]$ could be due to the multiple nanotubes in resonance with E_{laser}, especially the closely spaced states with regard to E_{laser} of family 27. For $E_{laser} = 2.07$ eV, the average $[I_{G'}^{upper} / I_{G+}]$ is less than for $E_{laser} = 2.03$ eV because only tubes from family 27 are excited, according to the observed dominant ω_{RBM} values. For $E_{laser} = 1.92$ eV, the lower frequency G' component has a larger intensity than the higher frequency G' component, according to Table 6-3. Here $[I_{G'}^{lower} / I_{G'}^{upper}]$ is opposite from that observed G' for $E_{laser} = 2.03$ eV and 2.07 eV, which both have $[I_{G'}^{lower} / I_{G'}^{upper}]$ less than 1, with the smallest value of the intensity ratio occurring at 2.03 eV.

For $E_{laser} = 1.92$ eV, there is a sharp and intense RBM centered at 286 cm^{-1}, and the (7, 5) tube falls squarely on a resonance with this specific E_{laser} and RBM combination, according to the Kataura plot in Fig. 6-5. The observed RBM at 267 cm^{-1} is a shoulder of, and has about a third of the intensity of, the 286 cm^{-1} RBM peak and $E_{laser} = 1.92$ eV could excite the (7, 6) tube. The smallest RBM peak observed for $E_{laser} = 1.92$ eV has $\omega_{RBM} = 197$ cm^{-1} and could excite the family 30 nanotubes; however this RBM intensity is about 7 times less than that of the 286 cm^{-1} peak so the resonance is weak. Therefore, in the case of $E_{laser} = 1.92$ eV, the more intense lower frequency G' component could be due to resonance with the (7, 5) tube. Then, the less intense higher frequency component would arise from resonance with the (8, 4) tube, which has an E_{ii} further away from $E_{laser} = 1.92$ eV but could still fall within the resonance window. Another possibility is that the two peaks arise from the (7, 6) tube and the family 23 tubes. In both cases, a smaller matrix element could also be the reason that the higher frequency G' component is less intense than the lower frequency peak. For $E_{laser} = 1.92$ eV, the normalized intensities of the upper and lower frequency peaks are relatively low, and this could indicate that few tubes are contributing to the spectra.

In the $2.60 \leq E_{laser} \leq 2.71$ eV range, the normalized intensity of the lower frequency component, $[I_{G'}^{lower} / I_{G^+}]$, increases with decreasing E_{laser}. As mentioned above, in this E_{laser} range, the lower frequency component is associated with resonance with the scattered phonon. As E_{laser} decreases, the incident photon energy, and therefore the scattered photon energy, becomes closer to the excitation energy for the (8, 4) tube. This can explain why $[I_{G'}^{lower} / I_{G^+}]$ increases as E_{laser} decreases, for $2.60 \leq E_{laser} \leq 2.71$ eV. This explanation is supported by considering that the energy separation between the (6, 6) and (10, 1) tube is 0.423 eV, while the energy separation between the (6, 6) and the (8, 4) tube is 0.573 eV. The observed average energy separation ΔE increases from 0.424 eV to 0.518 eV as E_{laser} decreases from 2.71 eV to 2.60 eV (Table 6-1). Thus it is possible that for the lower E_{laser} in the $2.60 \leq E_{laser} \leq 2.71$ eV range, the scattered photon comes into resonance with the (8, 4) tube in addition to the (10, 1) and (6, 5) tubes that were resonant in the case of the higher E_{laser}.

For $1.92 \leq E_{laser} \leq 2.07$ eV, $[I_{G'}^{lower} / I_{G^+}]$ is lower than those for the higher E_{laser}. A possible reason for this lies in the different origins of the secondary G' peak for the high vs. low values of E_{laser}. For $1.92 \leq E_{laser} \leq 2.07$ eV, the double peak structure in Fig. 6-1 comes from resonance with two states within the resonant window. Thus the incident photons have to be divided between the upper and lower states. In the case of $2.60 \leq E_{laser} \leq 2.71$ eV, the incident photons do not have to be split between states: first, the incident photons excite the upper frequency state, and then the resulting scattered photons excite the lower frequency state.

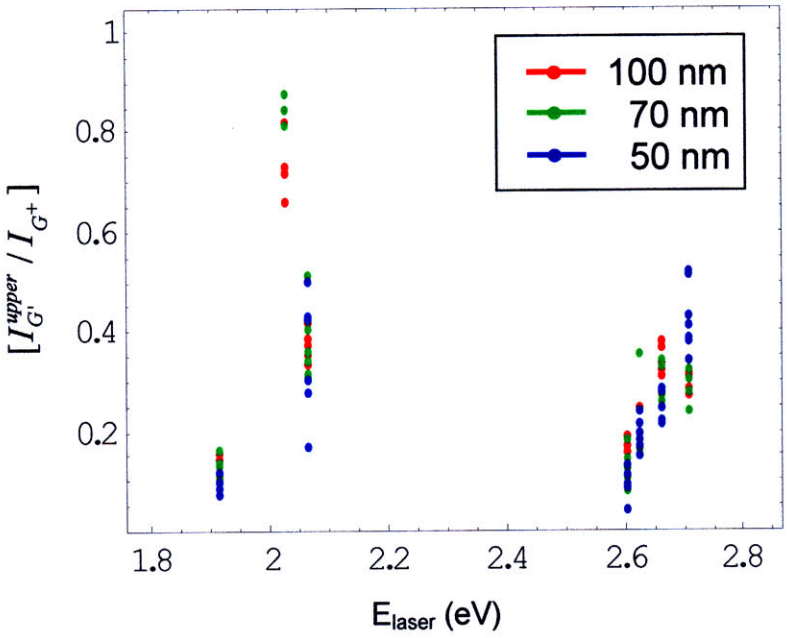

Figure 6-6. E_{laser} dependence of the integrated intensity ratio $[I_{G'}^{upper} / I_{G^+}]$ for the higher frequency component of G'. Different point colors are used for the different tube lengths.

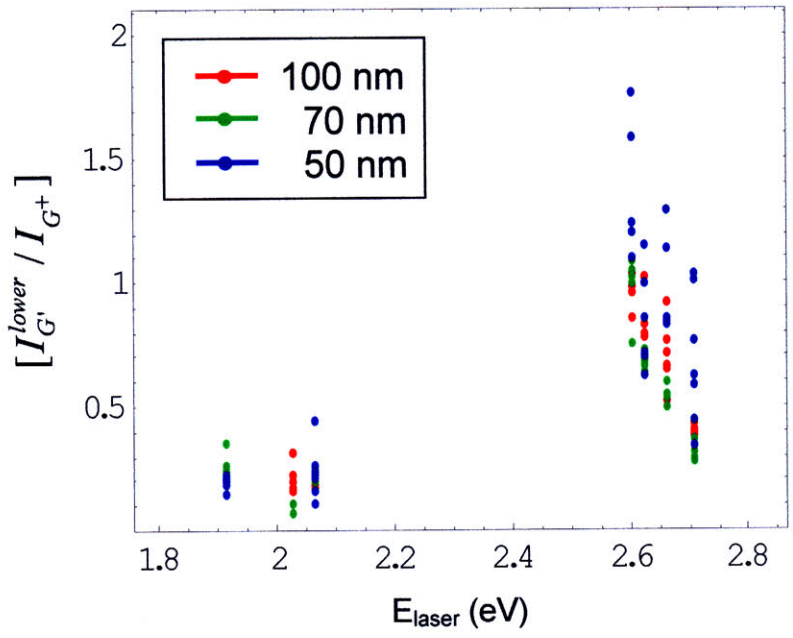

Figure 6-7. E_{laser} dependence of the integrated intensity ratio $[I_{G'}^{lower} / I_{G^+}]$ for the lower frequency component of G'. Different point colors are used for the different tube lengths.

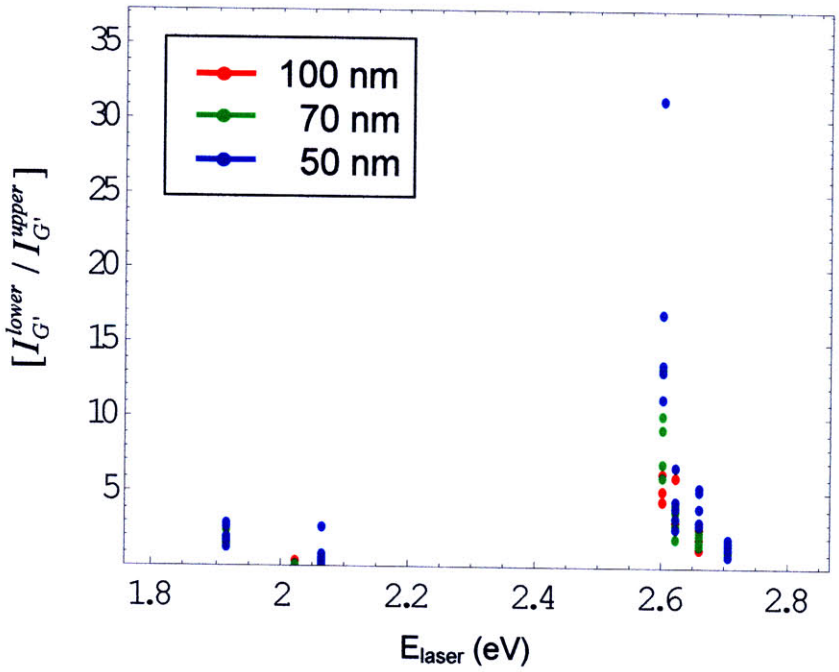

Figure 6-8. E_{laser} dependence of the integrated intensity ratio $[I_{G'}^{lower} / I_{G'}^{upper}]$ between the two frequency components of G'. Different point colors are used for the different tube lengths.

E_{laser} (eV)	Average $[I_{G'}^{lower} / I_{G^+}]$	Average $[I_{G'}^{upper} / I_{G^+}]$	Average $[I_{G'}^{lower} / I_{G'}^{upper}]$
2.71	0.502	0.351	1.38
2.66	0.747	0.294	2.68
2.62	0.770	0.206	3.96
2.60	1.11	0.131	10.15
2.07	0.221	0.356	0.696
2.03	0.174	0.774	0.230
1.92	0.221	0.117	1.95

Table 6-3. The average values of $[I_{G'}^{lower} / I_{G^+}]$ and $[I_{G'}^{upper} / I_{G^+}]$, and $[I_{G'}^{lower} / I_{G'}^{upper}]$, for each value of E_{laser}.

6.4 Linewidths of the G' Peaks

Figures 6-9 and 6-10 show the $(FWHM)_{G'}^{upper}$ and $(FWHM)_{G'}^{lower}$ linewidths of the higher and lower frequency G' components.

In Figure 6-10 we see that $(FWHM)_{G'}^{lower}$ is smaller for the lower values of E_{laser} ($1.92 \leq E_{laser} \leq 2.07$ eV) than for the higher E_{laser} values ($2.60 \leq E_{laser} \leq 2.71$ eV). This is reasonable considering that for $1.92 \leq E_{laser} \leq 2.07$ eV, both states corresponding to the double peaks must be closely spaced together in energy, in order to fall within the resonance window. For $2.60 \leq E_{laser} \leq 2.71$ eV, the (10, 1), (8, 4) and (6, 5) tubes which are excited by the scattered photon are spaced further apart. The E_{laser} behavior of $(FWHM)_{G'}^{lower}$ closely follows the E_{laser} dependence of the intensity ratio $[I_{G'}^{lower} / I_{G^+}]$ (Figure 6-7). The results show that the (normalized) intensity from the resonance with the scattered photons are greater overall, coming from more different nanotubes and therefore showing more spread in linewidth.

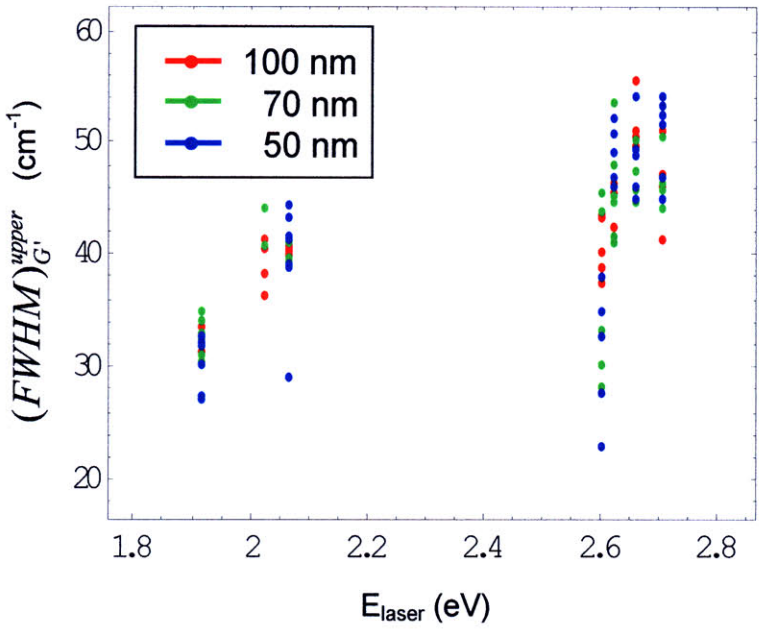

Figure 6-9. Scatter plot of the higher frequency G' component $(FWHM)_{G'}^{upper}$ vs. E_{laser}. Different point colors are used for the different tube lengths.

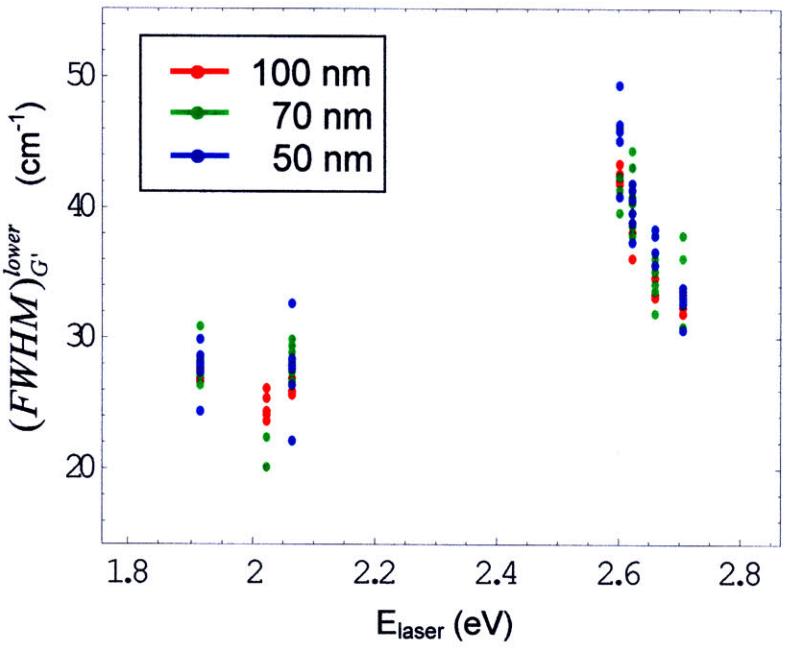

Figure 6-10. Scatter plot of the lower frequency G' component $(FWHM)_{G'}^{lower}$ vs. E_{laser}. Different point colors are used for the different tube lengths.

6.5 Length Dependence

In this section we consider the length dependence of the various G' parameters, using the linear correlation analysis introduced in Chapter 3. Since the G' behaviors are different depending on whether $1.92 \leq E_{laser} \leq 2.07$ eV or $2.60 \leq E_{laser} \leq 2.71$ eV, we consider the length dependence for these two E_{laser} ranges separately as well as together.

The G' peak frequencies, $\omega_{G'}^{upper}$ and $\omega_{G'}^{lower}$, were found to be independent of L_{tube}. In addition, The FWHM linewidth for both G' components were found to be independent of L_{tube}. As for the length dependence of the frequency splitting $\Delta\omega_{G'}$, only the tubes for which $1.92 \leq E_{laser} \leq 2.07$ eV were found to have a statistically significant correlation coefficient. For nanotubes excited by $1.92 \leq E_{laser} \leq 2.07$ eV, the linear fit is $\Delta\omega_{G'} = -0.036\, L_{tube} + 19.2$ cm^{-1}, with confidence intervals of (-0.056, -0.015) cm^{-1}/nm for the slope and (17.6, 20.9) cm^{-1} for the intercept. This slope corresponds to a modest $\Delta\omega_{G'}$ increase of 1.8 cm^{-1} as the tube length decreases by 50 nm. However, the length dependence is similar for nanotubes excited with $2.60 \leq E_{laser} \leq 2.71$ eV, despite the

below threshold correlation coefficient for these tubes. For $2.60 \leq E_{laser} \leq 2.71$ eV, the slope is similar, since the linear fit is $\Delta\omega_{G'} = -0.025\, L_{tube} + 31.4$ cm^{-1} corresponding to a 1.25 cm^{-1} increase in $\Delta\omega_{G'}$ as the tube length decreases by 50 nm. As expected, zero slope is included in the confidence interval for tubes excited by $2.60 \leq E_{laser} \leq 2.71$ eV: the confidence intervals for this E_{laser} range are (-0.060, 0.010) cm^{-1}/nm for the slope and (28.7, 34.1) cm^{-1} for the intercept.

Although there is little direct length dependence of $\Delta\omega_{G'}$, we observe that short and long tubes differ in their $\Delta\omega_{G'}$ vs. E_{laser} behavior. Figures 6-11(a) – (c) show $\Delta\omega_{G'}$ vs. E_{laser} for L_{tube} = 50, 70, and 100 nm, for nanotubes excited by $1.92 \leq E_{laser} \leq 2.07$ eV. Figures 6-12(a) – (c) show the same, but for $2.60 \leq E_{laser} \leq 2.71$ eV.

For the $1.92 \leq E_{laser} \leq 2.07$ eV range, 50 and 70 nm tubes show similar linear fits in $\Delta\omega_{G'}$ vs. E_{laser}, although zero slope is included in the confidence intervals. The linear fit for 70 nm long tubes in the $1.92 \leq E_{laser} \leq 2.07$ eV range is $\Delta\omega_{G'} = 7.39E_{laser} + 1.93$ cm^{-1} with confidence intervals of (-1.90, 16.7) cm^{-1}/eV for the slope and (-16.7, 20.6) cm^{-1} for the intercept. The linear fit for 50 nm long tubes in the $1.92 \leq E_{laser} \leq 2.07$ eV range is $\Delta\omega_{G'} = 7.74E_{laser} + 1.99$ cm^{-1} with confidence intervals of (-9.96, 25.5) cm^{-1}/eV for the slope and (-33.3, 37.3) cm^{-1} for the intercept. For $1.92 \leq E_{laser} \leq 2.07$ eV, 100 nm long tubes have a lower intercept and a greater slope that does not include zero in the confidence interval: the linear fit is $\Delta\omega_{G'} = 13.2\ E_{laser} - 10.8$ cm^{-1} with confidence intervals of (9.23, 17.1) cm^{-1}/eV for the slope and (-18.7, -2.85) cm^{-1} for the intercept.

For nanotubes excited by $2.60 \leq E_{laser} \leq 2.71$ eV, the difference in the $\Delta\omega_{G'}$ vs. E_{laser} behavior for short vs. long tubes is more striking. The linear fit for 100 nm long tubes in the $2.60 \leq E_{laser} \leq 2.71$ eV range is $\Delta\omega_{G'} = -30.2E_{laser} + 109$ cm^{-1} with confidence intervals of (-44.7, -15.8) cm^{-1}/eV for the slope and (70.9, 147) cm^{-1} for the intercept. The numbers are similar for 70 nm tubes in this E_{laser} range: in this case, $\Delta\omega_{G'} = -31.3E_{laser} + 112$ cm^{-1} with confidence intervals of (-54.6, -8.08) cm^{-1}/eV for the slope and (50.6, 174) cm^{-1} for the intercept. However, $\Delta\omega_{G'}$ for the shortest tubes in the $2.60 \leq E_{laser} \leq 2.71$ eV range have a much greater E_{laser} dependence. For the 50 nm long tubes,

$\Delta\omega_{G'}$ = -85.1E_{laser} + 256 cm^{-1} with confidence intervals of (-110, -60.4) cm^{-1}/eV for the slope and (190, 321) cm^{-1} for the intercept.

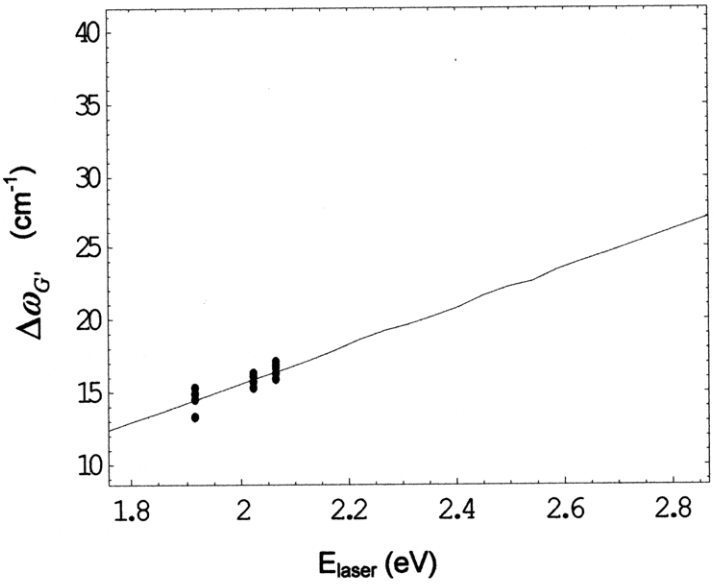

Figure 6-11(a). Scatter plot of the G' frequency splitting $\Delta\omega_{G'}$ vs. E_{laser}, for nanotubes with L_{tube} = 100 nm, in the .92 ≤ E_{laser} ≤ 2.07 eV range. The linear fit is $\Delta\omega_{G'}$ = 13.2 E_{laser} – 10.8 cm^{-1} with confidence intervals of (9.23, 17.1) cm^{-1}/eV for the slope and (-18.7, -2.85) cm^{-1} for the intercept.

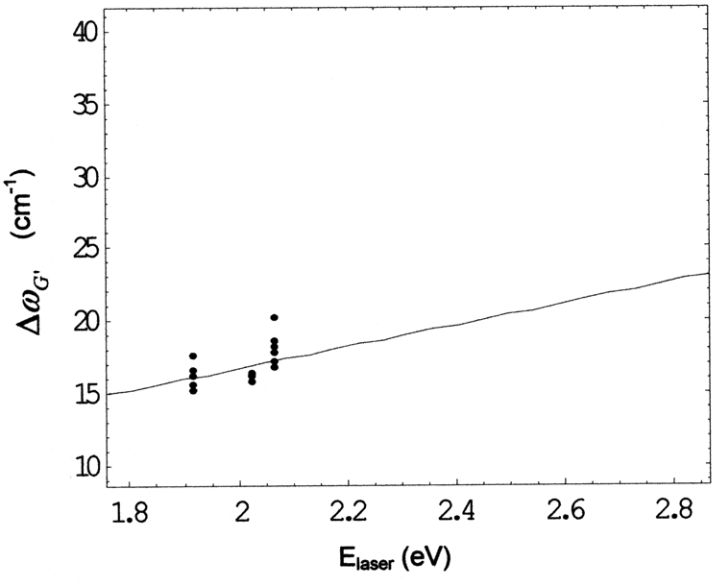

Figure 6-11(b). Same as Fig. 6-11(a), but with L_{tube} = 70 nm. The linear fit is $\Delta\omega_{G'}$ = 7.39E_{laser} + 1.93 cm^{-1} with confidence intervals of (-1.90, 16.7) cm^{-1}/eV for the slope and (-16.7, 20.6) cm^{-1} for the intercept.

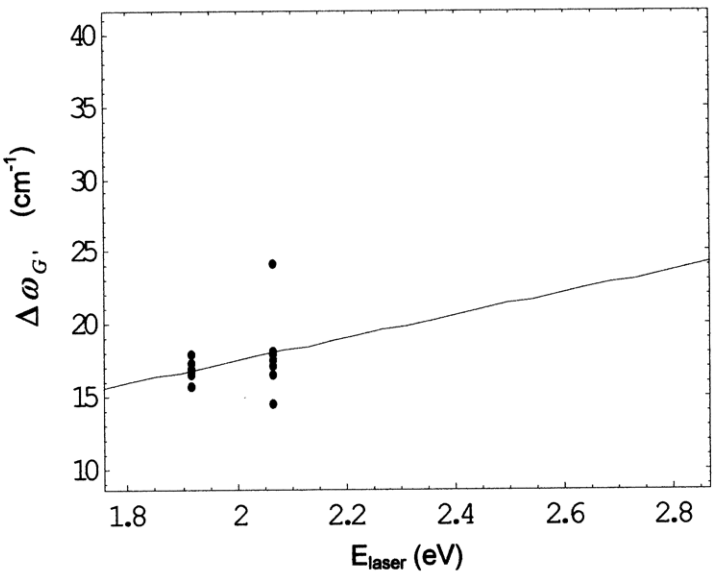

Figure 6-11(c). Same as Fig. 6-11(a), but with L_{tube} = 50 nm. The linear fit is $\Delta\omega_{G'} = 7.74E_{laser} + 1.99$ cm^{-1} with confidence intervals of (-9.96, 25.5) cm^{-1}/eV for the slope and (-33.3, 37.3) cm^{-1} for the intercept.

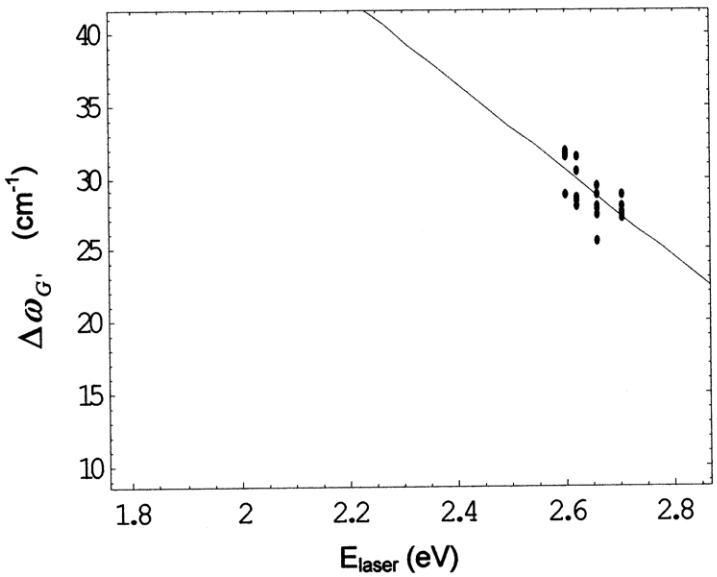

Figure 6-12(a). Scatter plot of the G' frequency splitting $\Delta\omega_{G'}$ vs. E_{laser}, for nanotubes with L_{tube} = 100 nm, in the 2.60 ≤ E_{laser} ≤ 2.71 eV range. The linear fit is $\Delta\omega_{G'} = -30.2E_{laser} + 109$ cm^{-1} with confidence intervals of (-44.7, -15.8) cm^{-1}/eV for the slope and (70.9, 147) cm^{-1} for the intercept.

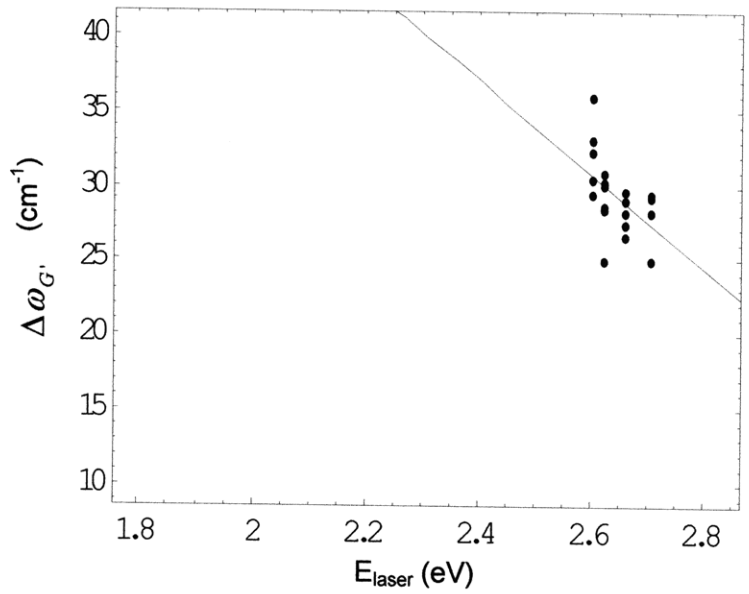

Figure 6-12(b). Same as Fig. 6-12(a), but with L_{tube} = 70 nm. The linear fit is $\Delta\omega_{G'}$ = -31.3E_{laser} + 112 cm^{-1} with confidence intervals of (-54.6, -8.08) cm^{-1}/eV for the slope and (50.6, 174) cm^{-1} for the intercept.

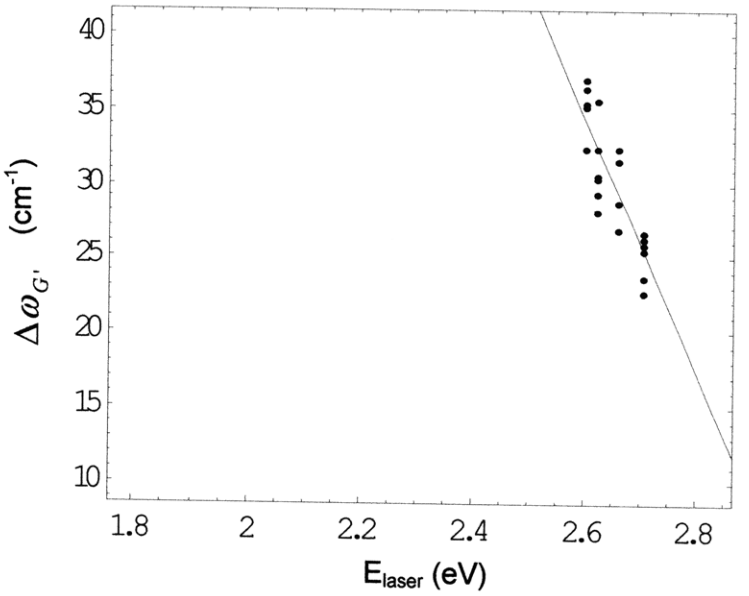

Figure 6-12(c). Same as Fig. 6-12(a), but with L_{tube} = 70 nm. The linear fit is $\Delta\omega_{G'}$ = -85.1E_{laser} + 256 cm^{-1} with confidence intervals of (-110, -60.4) cm^{-1}/eV for the slope and (190, 321) cm^{-1} for the intercept.

The integrated intensity ratio $[I_{G'}^{upper} / I_{G^+}]$ of the higher frequency G' component was found to be independent of L_{tube}. The lower frequency G' component shows a length dependence in $[I_{G'}^{lower} / I_{G^+}]$ only for tubes in the $2.60 \leq E_{laser} \leq 2.71$ eV range, for which the $[I_{G'}^{lower} / I_{G^+}]$ ratio increases as the tube gets shorter. In the $2.60 \leq E_{laser} \leq 2.71$ eV range, the linear fit is $[I_{G'}^{lower} / I_{G^+}] = -5.36E_{laser} + 15.0$ with confidence intervals of (-6.77, -3.96) eV^{-1} for the slope and (11.3, 18.7) for the intercept. Figures 6-13(a) and (b) plot the integrated intensity ratio $[I_{G'}^{lower} / I_{G^+}]$ vs. L_{tube} for the two distinct E_{laser} ranges.

The integrated intensity ratio between the two G' peaks, $[I_{G'}^{lower} / I_{G'}^{upper}]$, was also examined as a function of L_{tube}. Figures 6-14(a) and (b) show $[I_{G'}^{lower} / I_{G'}^{upper}]$ vs. L_{tube}, for the excitation energy ranges $1.92 \leq E_{laser} \leq 2.07$ eV and $2.60 \leq E_{laser} \leq 2.71$ eV. For the range $1.92 \leq E_{laser} \leq 2.07$ eV, the linear fit gives $[I_{G'}^{lower} / I_{G'}^{upper}] = -0.012\ L_{tube} + 1.94$, with confidence intervals of (-0.024, 0.00009) nm^{-1} for the slope and (1.01, 2.87) for the intercept. In this E_{laser} range, zero slope appears in the confidence interval, so there appears to be no length dependence. On the other hand, for $2.60 \leq E_{laser} \leq 2.71$ eV, $[I_{G'}^{lower} / I_{G'}^{upper}]$ increases as the nanotube gets shorter. For $2.60 \leq E_{laser} \leq 2.71$ eV, the linear fit gives $[I_{G'}^{lower} / I_{G'}^{upper}] = -0.067\ L_{tube} + 9.55$, with confidence intervals of (-0.124, -0.010) nm^{-1} for the slope and (5.22, 13.9) for the intercept.

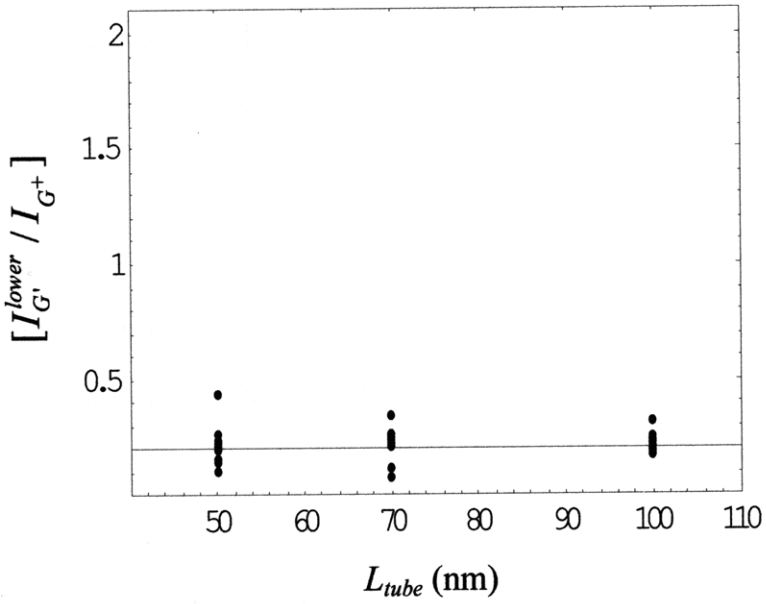

Figure 6-13(a). The length dependence of the integrated intensity ratio for the lower frequency G' component, $[I_{G'}^{lower} / I_{G^+}]$ vs. L_{tube} , for $1.92 \leq E_{laser} \leq 2.07$ eV. In this case the calculated correlation coefficient was below the P = 0.05 significance threshold.

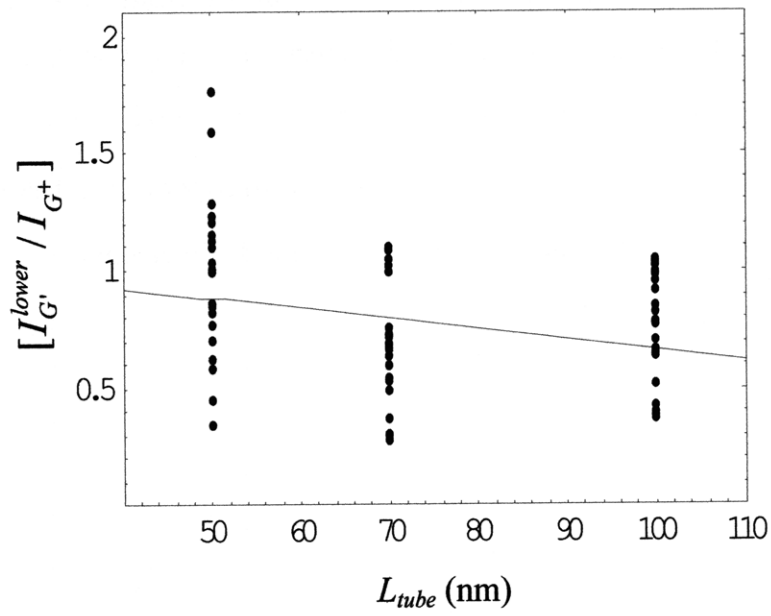

Figure 6-13(b). The length dependence of the integrated intensity ratio for the lower frequency G' component, $[I_{G'}^{lower} / I_{G^+}]$ vs. L_{tube} , for $2.60 \leq E_{laser} \leq 2.71$ eV. There is a statistically significant anticorrelation in this case. The linear fit shown here is $[I_{G'}^{lower} / I_{G^+}] = -0.0044\, L_{tube} + 1.10$.

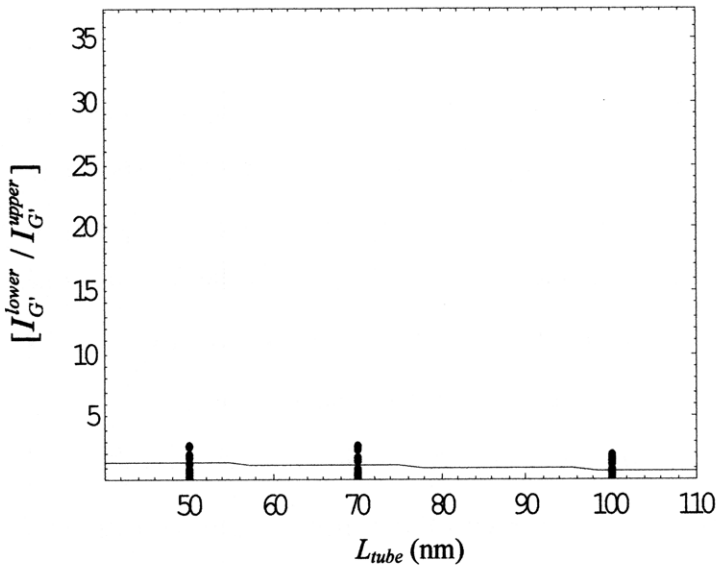

Figure 6-14(a). The length dependence of the integrated intensity ratio between the two G' components, $[I_{G'}^{lower} / I_{G'}^{upper}]$, vs. L_{tube} , for $1.92 \leq E_{laser} \leq 2.07$ eV. In this case the linear fit gives $[I_{G'}^{lower} / I_{G'}^{upper}] = -0.012\ L_{tube} + 1.94$, with confidence intervals of (-0.024, 0.00009) nm^{-1} for the slope and (1.01, 2.87) for the intercept.

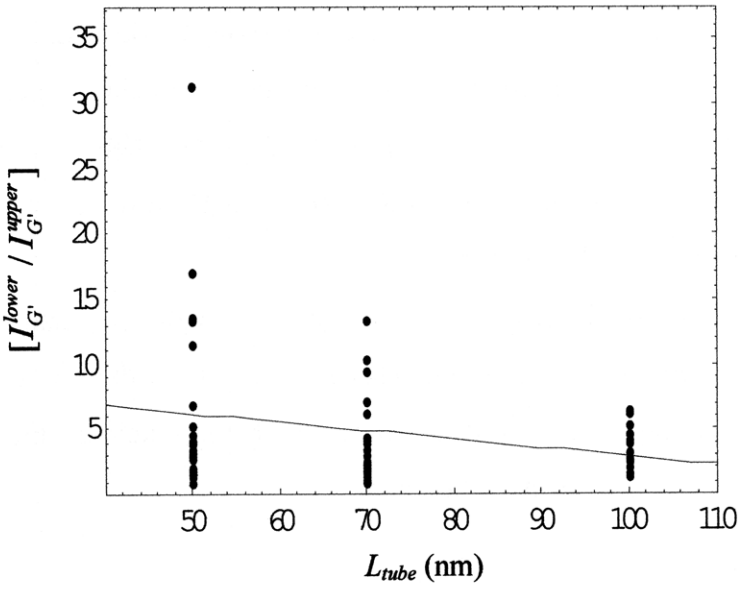

Figure 6-14(b). The length dependence of the integrated intensity ratio between the two G' components, $[I_{G'}^{lower} / I_{G'}^{upper}]$, vs. L_{tube} , for $2.60 \leq E_{laser} \leq 2.71$ eV. In this case the linear fit gives $[I_{G'}^{lower} / I_{G'}^{upper}] = -0.067\ L_{tube} + 9.55$, with confidence intervals of (-0.124, -0.010) nm^{-1} for the slope and (5.22, 13.9) for the intercept.

6.6 Summary

In this chapter, we examined the E_{laser} and length dependence of the two peaks comprising the G' band. Spectra were taken using several laser lines, which fall into two distinct ranges: $1.92 \leq E_{laser} \leq 2.07$ eV, and $2.60 \leq E_{laser} \leq 2.71$ eV. We have found that the G' band properties are quite different, depending on whether E_{laser} is in the higher or lower eV range. For example, the frequencies of both the upper and lower G' peaks, $\omega_{G'}^{upper}$ and $\omega_{G'}^{lower}$, are higher for $2.60 \leq E_{laser} \leq 2.71$ eV than for the lower eV range.

We also examined the G' band splitting, $\Delta\omega_{G'} \equiv \omega_{G'}^{upper} - \omega_{G'}^{lower}$. When $\Delta\omega_{G'}$ is converted to energy ΔE, it represents the energy separation between the two states which are simultaneously excited. We have found that $\Delta\omega_{G'}$ is greater for points that fall within $2.60 \leq E_{laser} \leq 2.71$ eV than for points in the $1.92 \leq E_{laser} \leq 2.07$ eV range. For $2.60 \leq E_{laser} \leq 2.71$ eV, the corresponding energy separation ΔE was found to range from 0.424 eV to 0.518 eV. This is about equal to the scattered phonon energy, which is 0.33 eV, plus a resonant window of 0.1 – 0.2 eV. Thus, for $2.60 \leq E_{laser} \leq 2.71$ eV, the lower component of G' may arise from resonance with the scattered photon, while the upper component of G' could be due to resonance with the incident photon. In the $1.92 \leq E_{laser} \leq 2.07$ eV range, we found that ΔE is around 0.12 eV, which is very much smaller than the ΔE for higher E_{laser}. If we assume a resonant window of 0.2 eV [3], then a ΔE of 0.12 eV could arise from two closely spaced states, both within the G' resonant window, which are simultaneously excited by the incident photon.

The intensities of the two G' components vary with E_{laser}, and are dependent on the number of (n, m) tubes which are resonant. The linewidths of the G' peaks also depend on the number of different nanotubes being excited. Finally, the length dependence of the G' band seems to be minor.

References

[1] R. Saito, A. Jorio et al., "Dispersive Raman spectra observed in graphite and single wall carbon nanotubes," *Physica B* **323** (2002) 100.

[2] M. S. Dresselhaus et al., "Raman spectroscopy of carbon nanotubes," *Physics Reports,* **409** (2005) 47.

[3] A. G. Souza Filho, A. Jorio, et al., "Anomalous two-peak G'-band Raman effect in one isolated single-wall carbon nanotube," *Physical Review B,* **65** (2002) 085417.

[4] A. G. Souza Filho, A. Jorio, et al., "Probing the electronic trigonal warping effect in individual single-wall carbon nanotubes using phonon spectra," *Chemical Physics Letters,* **354** (2002) 62.

Chapter 7 – The G* Peak

In this chapter, we examine the properties of the G* peak at 2417 cm^{-1} (for E_{laser} = 2.66 eV) were examined. The G* peak is a weak feature in the vicinity of the G' band. Studies on graphene have shown that the G* band is a combination mode involving an iTO and an LO phonon [1].

In Figures 7-1(a) and (b), representative Raman spectra in the vicinity of the G* and G' bands are shown for metallic and semiconducting nanotubes. The G* peak was resolved for E_{laser} = 457.9 nm (2.71 eV), 465.8 nm (2.66 eV), 472.7 nm (2.62 eV), 476.5 nm (2.60 eV), 600 nm (2.07 eV), and 647 nm (1.92 eV). According to the observed RBM frequencies, each of these laser lines excite a combination of metallic and semiconducting tubes, as was shown in Chapter 2. However, the Raman spectra taken with 600 nm and 647 nm laser lines show a narrow G-band lineshape that is typical of semiconducting nanotubes, while spectra taken with the other laser lines show a broad G-band characteristic of metallic tubes (Chapter 3). Thus we tentatively assume that the 600 nm (2.07 eV) and 647 nm (1.92 eV) laser lines excite predominantly semiconducting tubes, while the rest of the laser lines excite metallic tubes. In few-layer grapheme, the G* feature has a skewed lineshape, and the skewness depends on the number of graphene layers [2]. However, in our case, the data is weak and thus any skewness is difficult to study. Hence, for our study, a single Lorentzian was used to fit the G* peak.

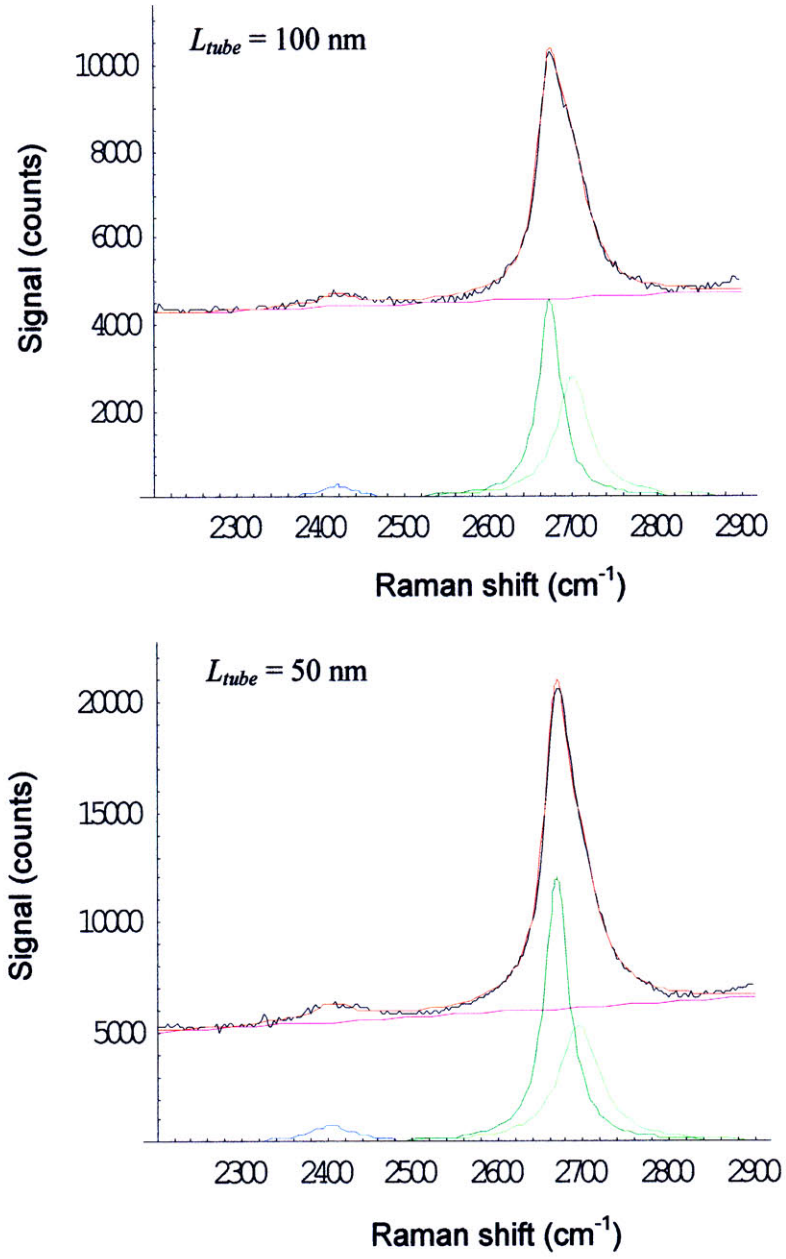

Figure 7-1(a). Raman spectra and peak fitting in the vicinity of the G' band (at 2700 cm^{-1}) and G* band (at 2400 cm^{-1}) bands. The raw data (not normalized) is shown in these figures. Spectra for L_{tube} = 100 nm (top) and L_{tube} = 50 nm (bottom) are shown. The peak fitting model consists of a baseline (magenta line) plus Lorentzians (blue and green curves). The black curve is the raw data and the red curve is the sum of the peak fitting components. The laser excitation energy is 2.71 eV, which is resonant with metallic nanotubes.

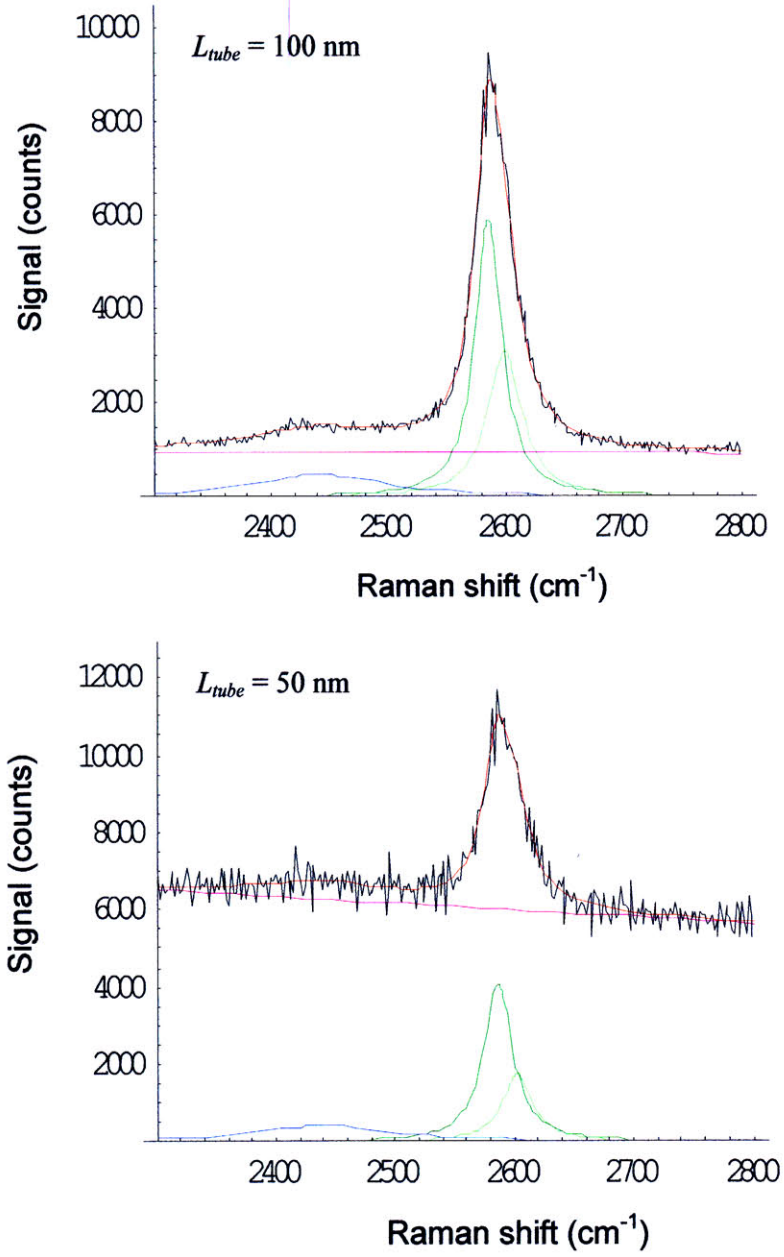

Figure 7-1(b). Same as Figure 7-1(a), but with E_{laser} = 1.92 eV, which excites semiconducting nanotubes.

The integrated $[I_{G^-} / I_{G^+}]$ and peak $[\hat{I}_{G^-} / \hat{I}_{G^+}]$ ratios are plotted against E_{laser} in Figure 7-2. For semiconducting nanotubes, the relationship between the intensity ratios and E_{laser} could not be identified because data for only two values of E_{laser} were available. For metallic nanotubes, both the integrated $[I_{G^-} / I_{G^+}]$ and peak $[\hat{I}_{G^-} / \hat{I}_{G^+}]$ ratios appear to decrease with increasing E_{laser}. We consider the metallic nanotubes only when calculating the correlation coefficient r^w. Between the integrated $[I_{G^-} / I_{G^+}]$ ratio and E_{laser},

$r^w = -0.517$ which is above the P = 0.05 threshold of $|r| \geq 0.24$ for the 66 data points available. The linear fit for metallic tubes is integrated $[I_{G^-} / I_{G^+}]$ = -0.625 E_{laser} + 1.75, with confidence intervals of (-0.883, -0.367) eV^{-1} for the slope and (1.07, 2.43) for the intercept. For the peak $[\hat{I}_{G^-} / \hat{I}_{G^+}]$ vs. E_{laser}, $r^w = -0.448$ for metallic tubes which signifies an anticorrelation. The linear fit for metallic tubes is peak $[\hat{I}_{G^-} / \hat{I}_{G^+}]$ = -0.0875 E_{laser} + 0.252, with confidence intervals of (-0.131, -0.0440) eV^{-1} for the slope and (0.137, 0.368) for the intercept.

In Figures 7-3(a) – (c), plots of the integrated vs. L_{tube} are shown for combined metallic and semiconducting tubes (Figure 7-3(a)), metallic tubes only (Figure 7-3(b)), and semiconducting tubes only (Figure 7-3(c)). For the combined semiconducting and metallic tubes, the correlation coefficient is $r^w = -0.306$ between the integrated $[I_{G^-} / I_{G^+}]$ ratio and L_{tube}. This is an anticorrelation since the corresponding P = 0.05 threshold is $|r| \geq 0.19$ for the 108 data points available. For the combined semiconducting and metallic tubes, the linear fit for the integrated intensity ratio is $[I_{G^-} / I_{G^+}]$ = -0.00170 L_{tube} + 0.235, with confidence intervals of (-0.00272, -0.000681) nm^{-1} for the slope and (0.158, 0.313) for the intercept. When semiconducting nanotubes are considered separately, $r^w = -0.381$ which is above the P = 0.05 threshold of $|r| \geq 0.30$ for 42 data points. The linear fit for semiconducting tubes for the integrated intensity ratio is $[I_{G^-} / I_{G^+}]$ = -0.00335 L_{tube} + 0.391, with confidence intervals of (-0.00595, -0.000751) nm^{-1} for the slope and (0.193, 0.589) for the intercept. We find that the length dependence is considerably smaller for metallic nanotubes. For metallic tubes, $r^w = -0.370$ which is an anticorrelation, since the P = 0.05 threshold is $|r| \geq 0.24$ for the 66 data points. The linear fit for metallic tubes for the integrated intensity ratio is $[I_{G^-} / I_{G^+}]$ = -0.000877 L_{tube} + 0.158, with confidence intervals of (-0.00143, -0.000328) nm^{-1} for the slope and (0.116, 0.199) for the intercept. Thus the slope of the integrated intensity ratio $[I_{G^-} / I_{G^+}]$ vs. L_{tube} is much smaller for metallic tubes than for semiconducting tubes.

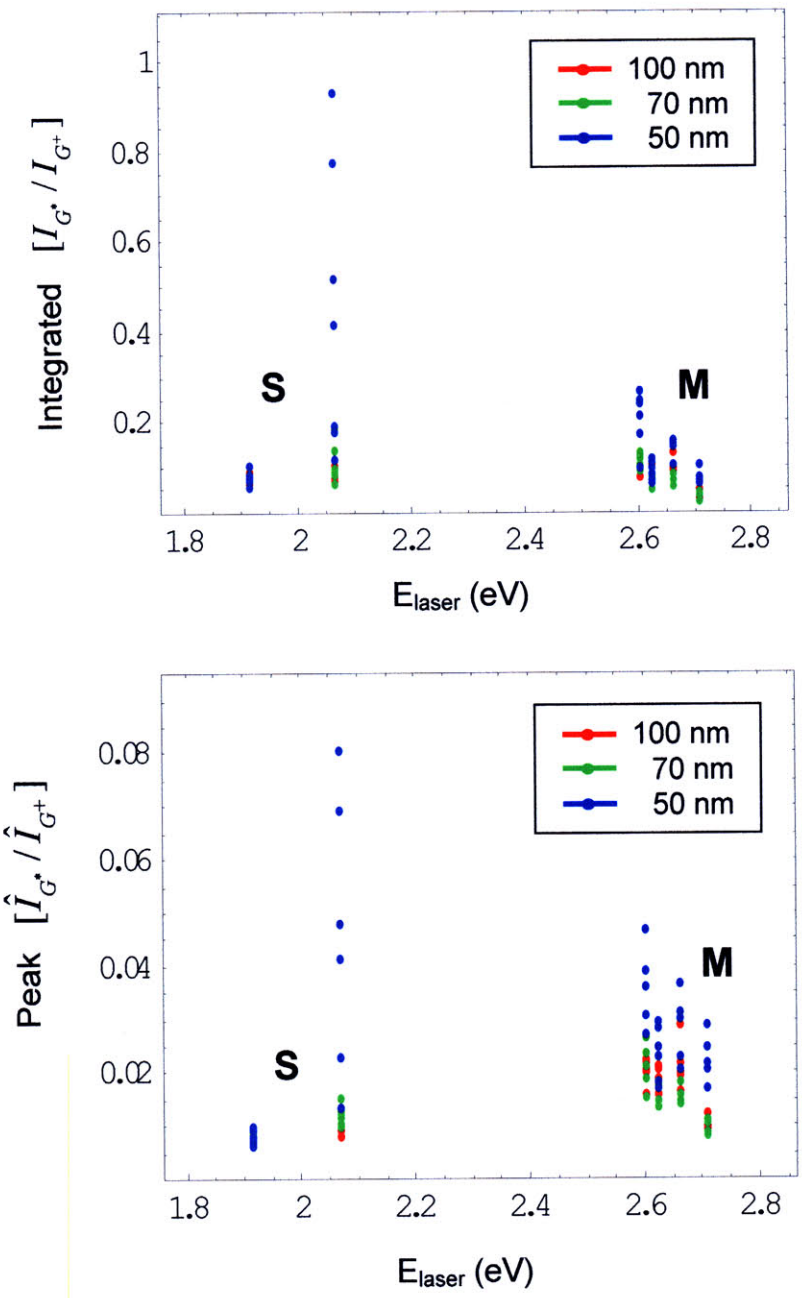

Figure 7-2. The integrated $[I_{G^-} / I_{G^+}]$ (top) and peak $[\hat{I}_{G^-} / \hat{I}_{G^+}]$ (bottom) ratios plotted against E_{laser}. Semiconducting (S) and metallic (M) tubes are shown in this figure. The different point colors signify different values of L_{tube}. It can be seen from the plots that the spread in the intensity ratios is unusually large for $E_{laser} = 2.07$ eV.

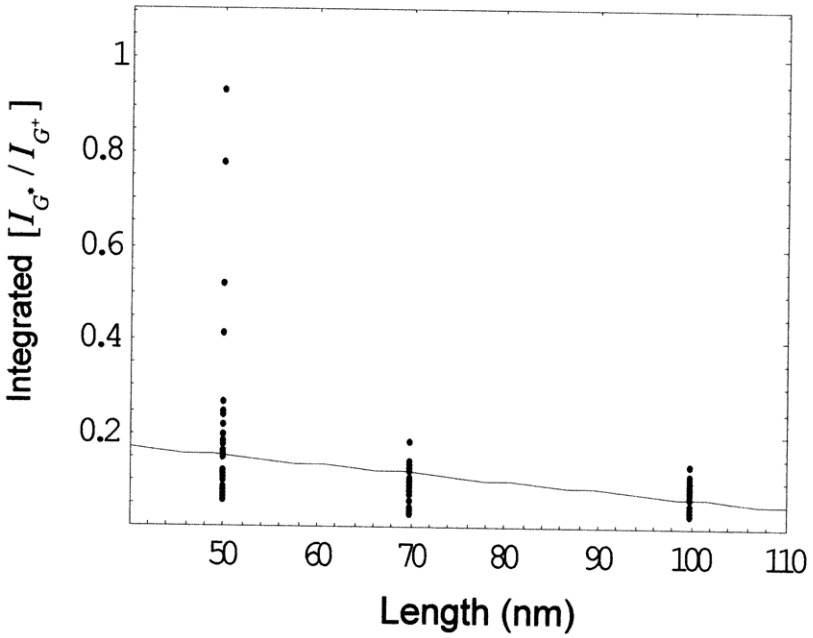

Figure 7-3(a). Integrated $[I_{G^*} / I_{G^+}]$ vs. L_{tube} for semiconducting and metallic nanotubes. The linear fit is $[I_{G^*} / I_{G^+}] = -0.00170\, L_{tube} + 0.235$. The spread for 50 nm tubes is much larger than for the other lengths.

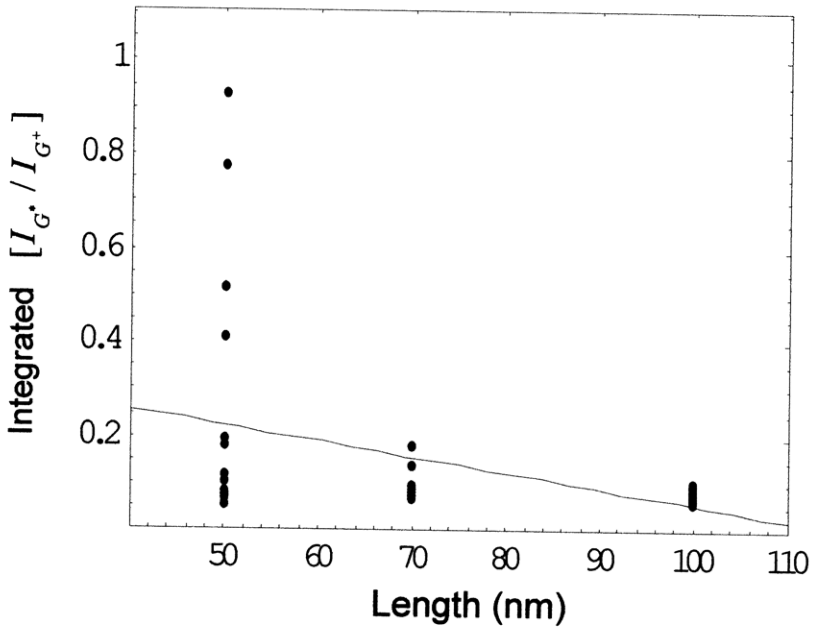

Figure 7-3(b). Integrated $[I_{G^*} / I_{G^+}]$ vs. L_{tube} for semiconducting nanotubes only. The linear fit is $[I_{G^*} / I_{G^+}] = -0.00335\, L_{tube} + 0.391$. The spread for 50 nm tubes is much larger than for the other lengths.

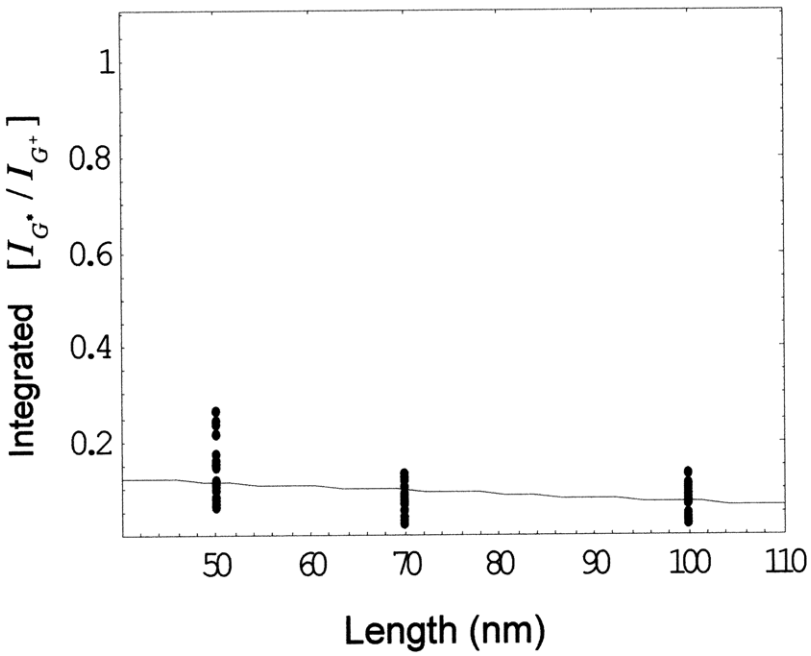

Figure 7-3(c). Integrated $[I_{G^*} / I_{G^+}]$ vs. L_{tube} for metallic nanotubes only. The linear fit is $[I_{G^*} / I_{G^+}]$ = -0.000877 L_{tube} + 0.158. The spread for 50 nm tubes is much larger than for the other lengths.

The difference between metallic and semiconducting tubes is much less pronounced when the length dependence of the peak $[\hat{I}_{G^*} / \hat{I}_{G^+}]$ ratio, instead of the integrated intensity ratio, is considered. For metallic tubes, $r^w = -0.470$ between peak $[\hat{I}_{G^*} / \hat{I}_{G^+}]$ and L_{tube}, and for semiconducting tubes, $r^w = -0.401$; there is an anticorrelation in both cases. Metallic tubes show a linear fit of the peak intensity ratio $[\hat{I}_{G^*} / \hat{I}_{G^+}]$ = -0.000180 L_{tube} + 0.0337 with confidence intervals of (-0.000264, -0.0000954) nm^{-1} for the slope and (0.0272, 0.0401) for the intercept. For semiconducting tubes, peak $[\hat{I}_{G^*} / \hat{I}_{G^+}]$ = -0.000310 L_{tube} + 0.0376 with confidence intervals of (-0.000537, -0.0000842) nm^{-1} for the slope and (0.0204, 0.0548) for the intercept. When metallic and semiconducting tubes are considered together, $r^w = -0.399$ (anticorrelated) and the linear fit for the peak intensity ratio is $[\hat{I}_{G^*} / \hat{I}_{G^+}]$ = -0.000223 L_{tube} + 0.0350 with confidence intervals of (-0.000322, -0.000124) nm^{-1} for the slope and (0.0274, 0.0425) for the intercept. The peak $[\hat{I}_{G^*} / \hat{I}_{G^+}]$ ratio vs. L_{tube} plots are shown in Figures 7-4(a) – (c).

In Figures 7-2 through 7-4, outliers with high normalized G* intensities can be seen. These outliers occur for spectra with L_{tube} = 50 nm, and measured with E_{laser} = 2.07 eV. Spectra for the outliers, along with more normal spectra, are shown in Figure 7-5. The main difference between the outliers and normal spectra is that the data is noisier for the outliers. Despite this, it can be seen from Figure 7-5 that the G* peak is a real effect.

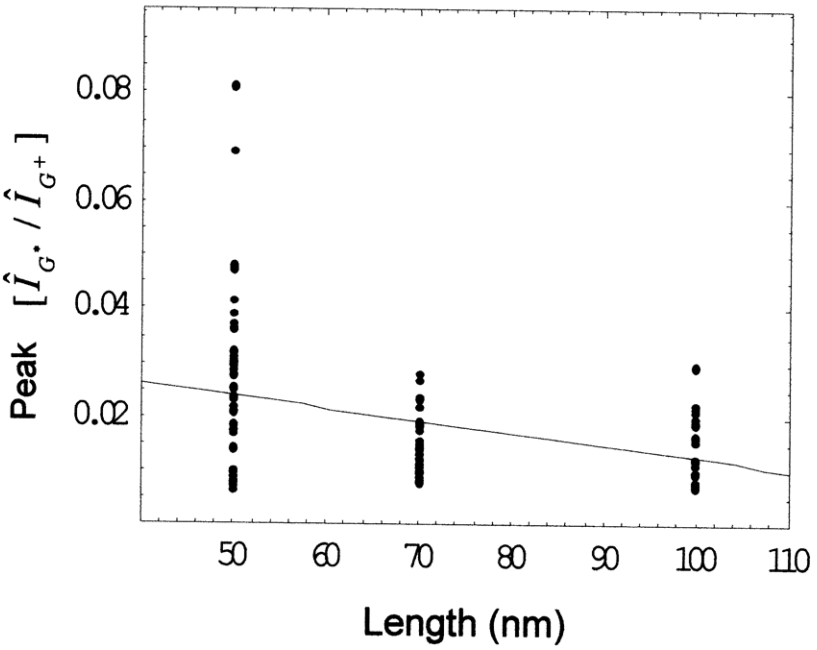

Figure 7-4(a). Peak $[\hat{I}_{G^*} / \hat{I}_{G^+}]$ vs. L_{tube} for semiconducting and metallic nanotubes. The linear fit is $[\hat{I}_{G^*} / \hat{I}_{G^+}]$ = -0.000223 L_{tube} + 0.0350.

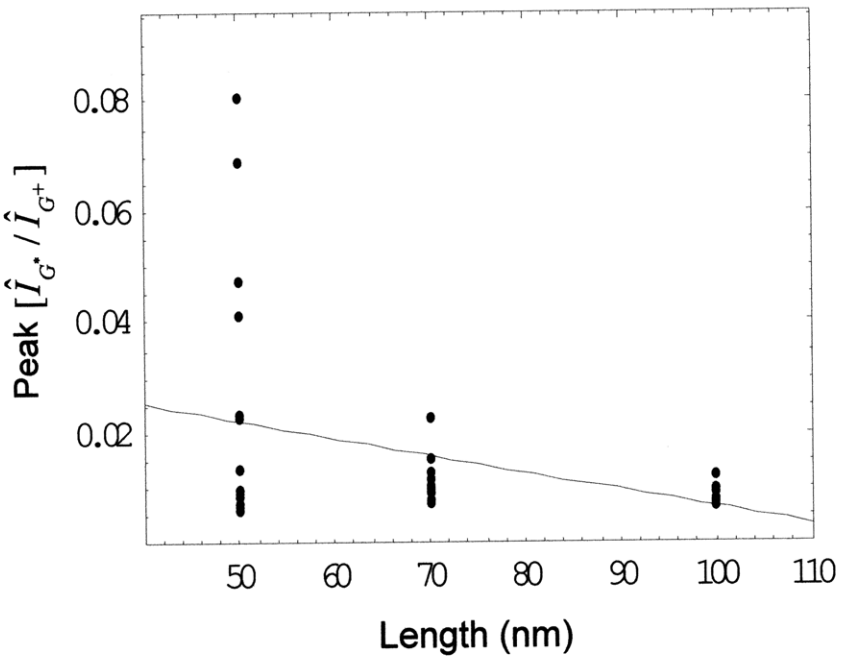

Figure 7-4(b). Peak $[\hat{I}_{G^-} / \hat{I}_{G^+}]$ vs. L_{tube} for semiconducting nanotubes only. The linear fit is $[\hat{I}_{G^-} / \hat{I}_{G^+}]$ = -0.000310 L_{tube} + 0.0376.

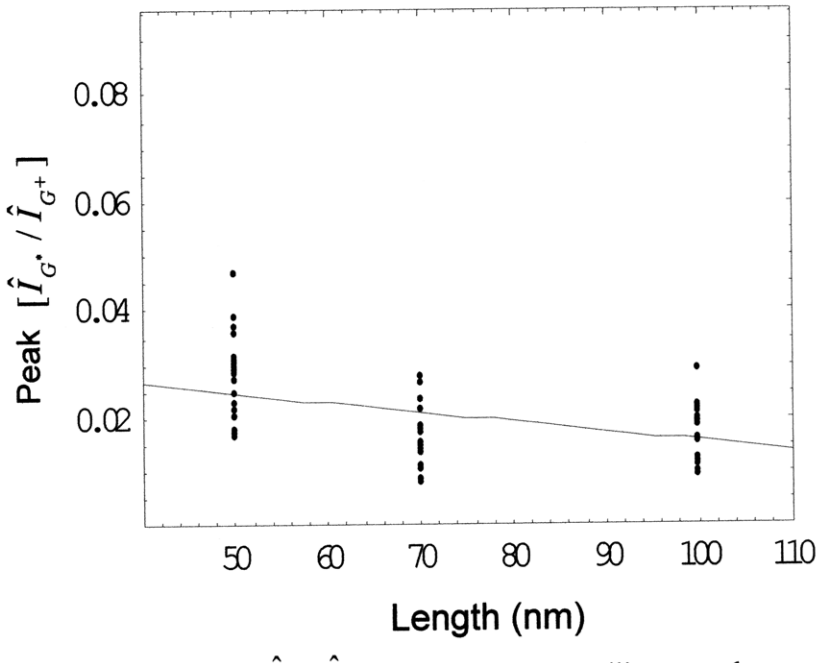

Figure 7-4(c). Peak $[\hat{I}_{G^-} / \hat{I}_{G^+}]$ vs. L_{tube} for metallic nanotubes only. The linear fit is $[\hat{I}_{G^-} / \hat{I}_{G^+}]$ = -0.000180 L_{tube} + 0.0337.

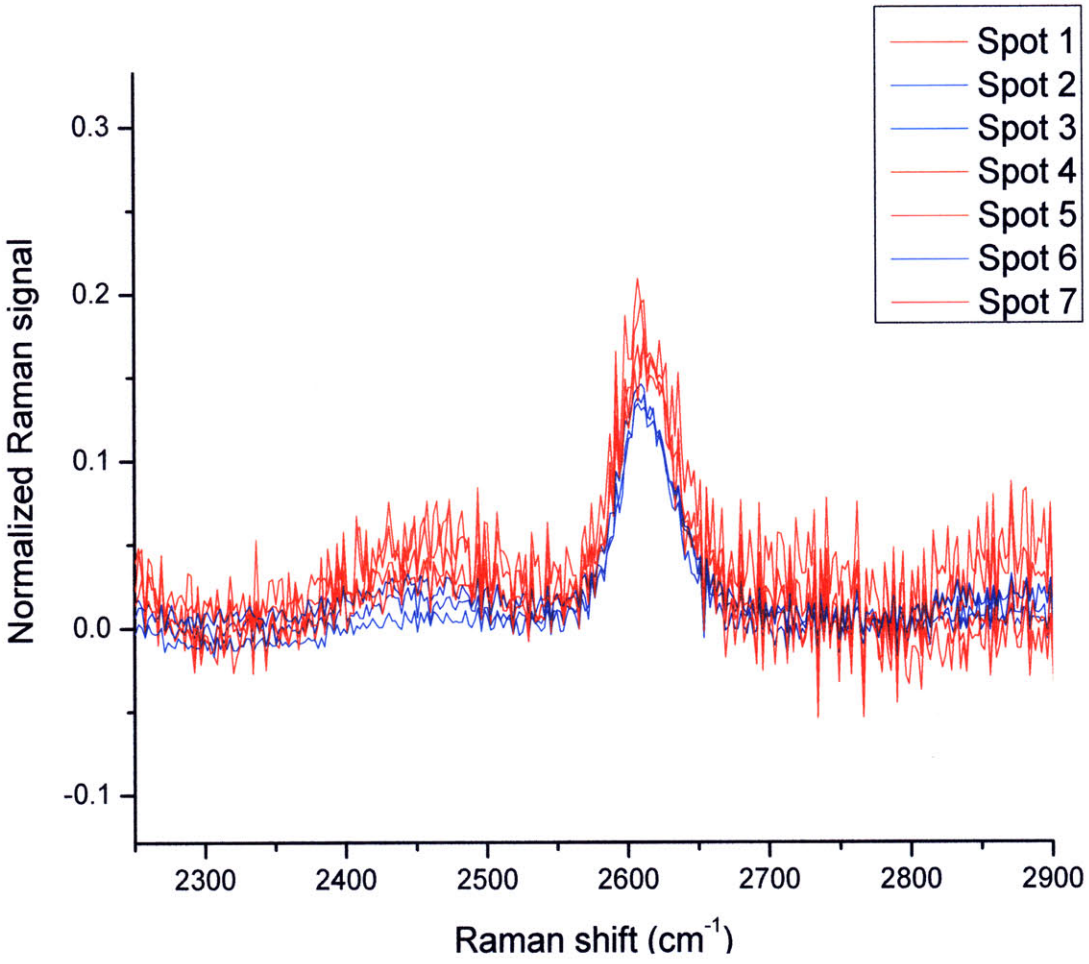

Figure 7-5. Raman spectra in the vicinity of the G' (at 2600 cm^{-1}) and G* (at 2450 cm^{-1}) features. For this figure, E_{laser} = 2.07 eV, L_{tube} = 50 nm, and spectra are shown for different spots on the sample. The red curves correspond to the outliers for the normalized G* intensity, and the blue curves correspond to the normal points.

The plot of the G* FWHM vs. E_{laser} is shown in Figure 7-6. The FWHM appears to decrease as E_{laser} increases, and the corresponding correlation coefficient is $r^w = -0.801$, which is an anticorrelation. The linear fit is $(FWHM)_{G^*}$ = -77.2 E_{laser} + 279 cm^{-1}, with confidence intervals of (-88.3, -66.0) cm^{-1}/eV for the slope and (252, 306) cm^{-1} for the intercept.

The length dependence of $(FWHM)_{G^*}$ was also examined. For the combined semiconducting and metallic tubes, $r^w = -0.156$ between $(FWHM)_{G^*}$ and L_{tube}, which is

below threshold. When semiconducting tubes are considered separately, $r^w = -0.076$ which is also below threshold. However, $(FWHM)_{G^*}$ and L_{tube} are anticorrelated for metallic tubes, since $r^w = -0.328$ which is above threshold. The linear fit for metallic tubes is $(FWHM)_{G^*}$ = -0.303 L_{tube} + 98.1 cm^{-1}, with confidence intervals of (-0.520, -0.085) cm^{-1}/nm for the slope and (81.5, 115) cm^{-1} for the intercept. Plots of $(FWHM)_{G^*}$ vs. L_{tube} for semiconducting and metallic tubes are shown in Figures 7-7(a) and (b).

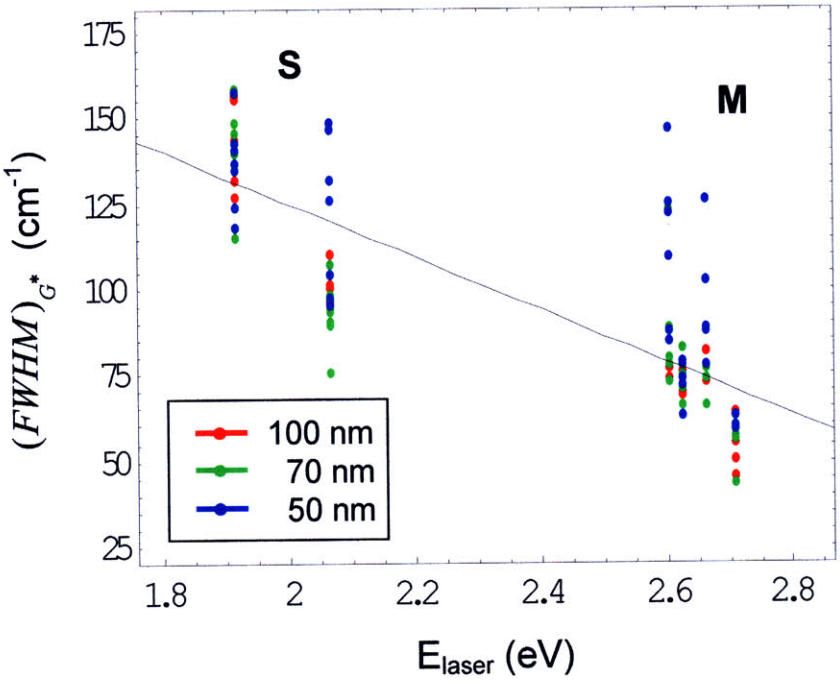

Figure 7-6. $(FWHM)_{G^*}$ vs. E_{laser} for semiconducting (S) and metallic (M) nanotubes. Different point colors are used for different L_{tube}. The linear fit is $(FWHM)_{G^*}$ = -77.2 E_{laser} + 279 cm^{-1}.

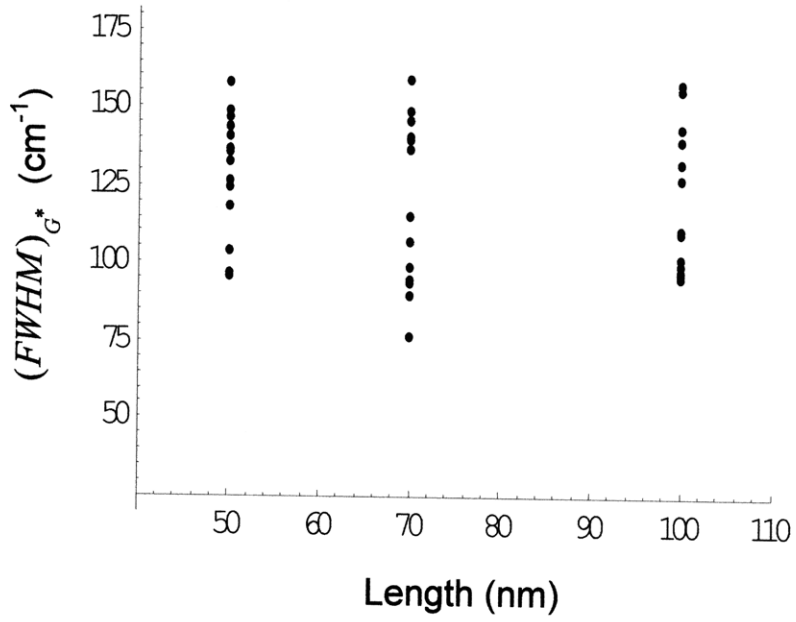

Figure 7-7(a). $(FWHM)_{G^*}$ vs. L_{tube} for semiconducting tubes. In this case, $(FWHM)_{G^*}$ and L_{tube} are uncorrelated.

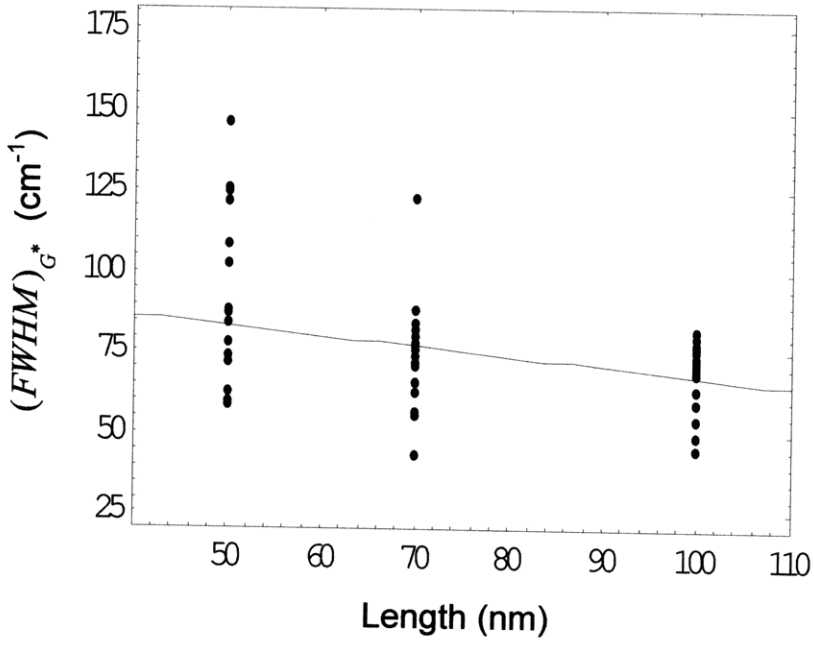

Figure 7-7(b). $(FWHM)_{G^*}$ vs. L_{tube} for metallic tubes. In this case, $(FWHM)_{G^*}$ and L_{tube} are anticorrelated, and the linear fit is $(FWHM)_{G^*} = -0.303\, L_{tube} + 98.1$ cm^{-1}.

The dispersive behavior of the G* frequency, ω_{G^*}, is shown in Figure 7-8. ω_{G^*} decreases with increasing E_{laser}, and the corresponding correlation coefficient is $r^w = -0.857$. The linear fit is ω_{G^*} = -41.1 E_{laser} + 2526 cm^{-1}, with confidence intervals of (-45.8, -36.3) cm^{-1}/eV for the slope and (2514, 2537) cm^{-1} for the intercept. This differs from an earlier work that reports almost no dispersion for single-wall and double-wall nanotubes, as well as for highly oriented pyrolytic graphite [1]. However, measurements of G* in few-layer graphene also report a negative dispersion, with magnitude of about -26 cm^{-1}/eV [2]. When metallic tubes are considered separately, $r^w = -0.342$ (anticorrelated) and the linear fit is ω_{G^*} = -61.6 E_{laser} + 2580 cm^{-1}, with confidence intervals of (-104, -19.4) cm^{-1}/eV for the slope and (2468, 2692) cm^{-1} for the intercept. The ω_{G^*} vs. E_{laser} behavior for just the semiconducting nanotubes were not considered, because data for only two values of E_{laser} were available. As for the length dependence, ω_{G^*} and L_{tube} were found to be uncorrelated, whether metallic ($r^w = 0.139$), semiconducting ($r^w = 0.091$), or combined metallic and semiconducting tubes ($r^w = 0.031$) were considered.

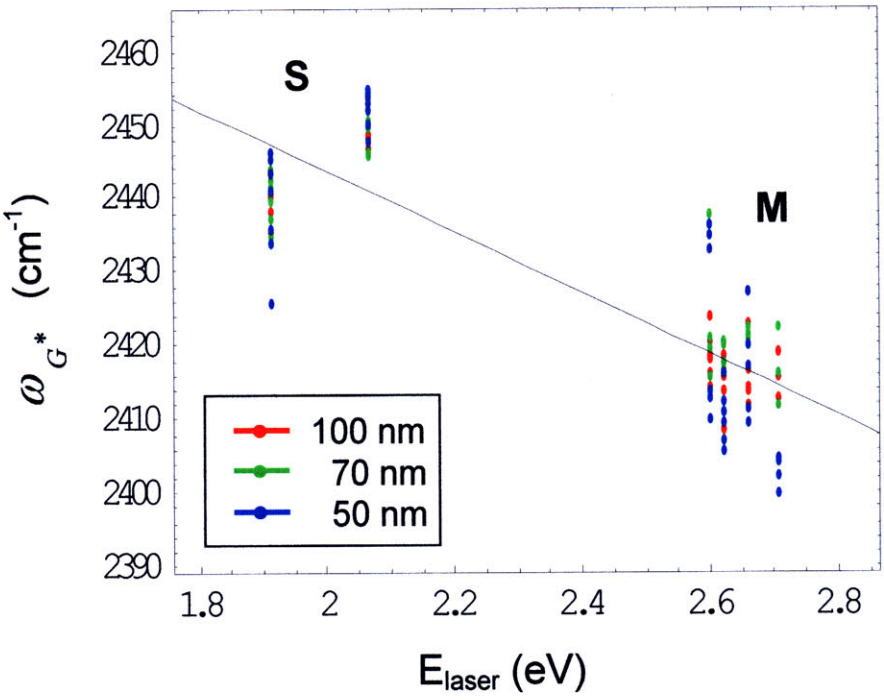

Figure 7-8. ω_{G^*} vs. E_{laser} for semiconducting (S) and metallic (M) nanotubes. Different point colors are used for different L_{tube}. The linear fit is ω_{G^*} = -41.1 E_{laser} + 2526 cm^{-1}. If only the tubes in the range 2.60 – 2.71 eV are considered, then the linear fit is ω_{G^*} = -61.6 E_{laser} + 2580 cm^{-1}.

Summary

In this chapter, the properties of the G* peak at 2417 cm^{-1} (for E_{laser} = 2.66 eV) were examined. We found that the G* feature is very weak and noisy in our spectra. A few effects were found that are above the noise level. For metallic and semiconducting nanotubes, the integrated $[I_{G^*} / I_{G^+}]$ intensity ratio was found to increase as L_{tube} decreases, and the effect seems to be more pronounced for semiconducting tubes. The peak $[\hat{I}_{G^*} / \hat{I}_{G^+}]$ ratio also increases with decreasing L_{tube}, but the difference between metallic and semiconducting tubes is less evident. The G* FWHM linewidth decreases with increasing E_{laser}, and for metallic tubes, increases with decreasing L_{tube}. The G* frequency ω_{G^*} was found to be independent of L_{tube}. The measured frequency dispersion is ω_{G^*} = -41.1 E_{laser} + 2526 cm^{-1}, which differs from an earlier work that reports almost

no dispersion [3]. However, measurements of G* in few-layer graphene also report a negative dispersion, with magnitude of about -26 cm^{-1}/eV [2].

References

[1] D. L. Mafra et al., "Determination of LA and TO phonon dispersion relations of grapheme near the Dirac point by double resonance Raman scattering," *Physical Review B* **76** (2007) 233407.

[2] A. Reina (Private Communication).

[3] T. Shimada et al., "Origin of the 2450 cm^{-1} Raman bands in HOPG, single-wall and double-wall carbon nanotubes," *Carbon,* **43** (2005) 1049.

Chapter 8 – Length Dependence of the RBM Peak

8.1 Introduction

The peaks between 120 – 350 cm^{-1} in the Raman spectra of carbon nanotubes correspond to the radial breathing mode (RBM). The RBM is a first order Raman feature that originates from vibrations along the radial direction of the nanotube; thus, unlike the G-band, RBM peaks do not appear in the Raman spectra of other graphitic materials. The measured RBM frequency ω_{RBM} can be used to estimate the nanotube diameter, since ω_{RBM} is inversely proportional to the diameter [1]. In addition, the measured ω_{RBM} in conjunction with the Kataura plot can be used to tentatively determine the (n, m) indices of the nanotubes in a sample, as was done in Chapter 2.

In this chapter we will examine the length dependence of the RBM peak. It is important to check whether size-exclusion chromatography inadvertently sorts the nanotubes according to diameter, in addition to length. This question can be answered by determining the length dependence of the RBM frequency.

8.2 The RBM Spectra

Representative Raman spectra are shown in Figures 8-1(a), (b) and (c) for three different values of E_{laser}. The RBM regions are shown in the insets. In Figure 8-1(a), E_{laser} = 647 nm (1.92 eV), and the RBM region is dominated by a sharp peak at 287 cm^{-1}. In Figure 8-1(b), E_{laser} = 465.8 nm (2.66 eV), and there are several small RBM peaks. In examining the length dependence of the RBM, we will first restrict the analysis to two E_{laser} excitation energies for which a strong RBM peak is found. These laser excitation energies are E_{laser} = 647 nm (1.92 eV), for which the RBM around 287 cm^{-1} indicates resonance with the (7, 5) semiconducting nanotube, and E_{laser} = 496.5 nm (2.50 eV), for which the sharp RBM at 267 cm^{-1} indicates resonance with the (8, 5) metallic nanotube. Figure 8-1(c) shows a Raman spectrum measured using E_{laser} = 496.5 nm (2.50 eV). In Figures 8-2(a) and (b), the normalized RBM spectrum for different spots on the L_{tube} =

100 nm sample, for two values of E_{laser}. According to Figures 8-2(a) and (b), not much spot-to-spot variation can be found in the RBM peak positions.

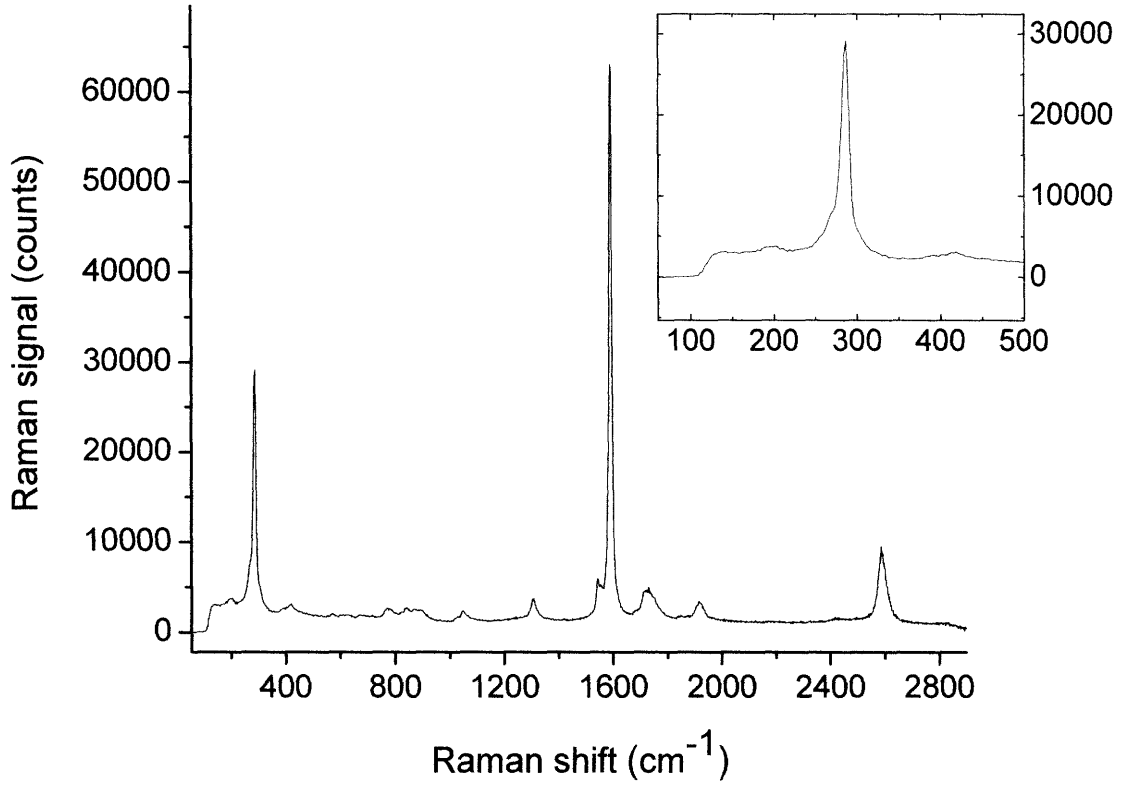

Figure 8-1(a) Raman spectrum for the sample with L_{tube} = 100 nm. The laser excitation energy is E_{laser} = 647 nm (1.92 eV). The inset shows the RBM region.

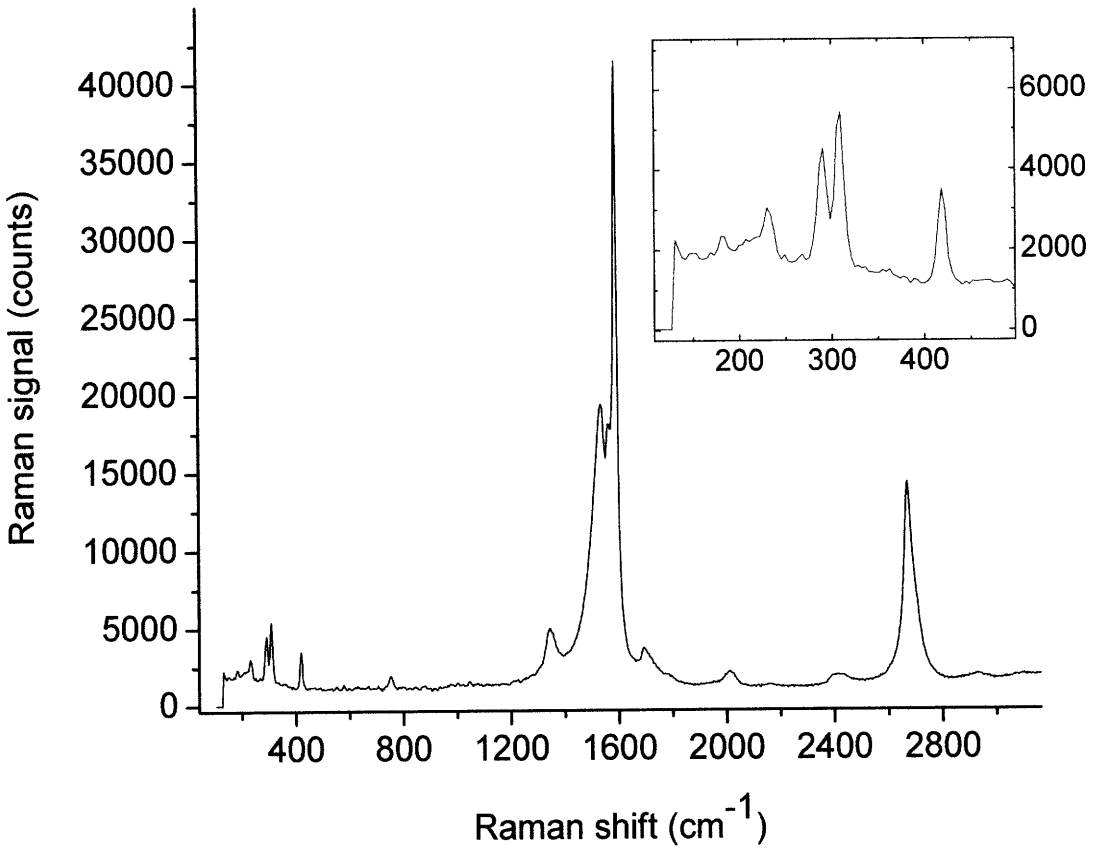

Figure 8-1(b). Same as Figure 8-1(a), but with E_{laser} = 465.8 nm (2.66 eV) and L_{tube} = 100 nm.

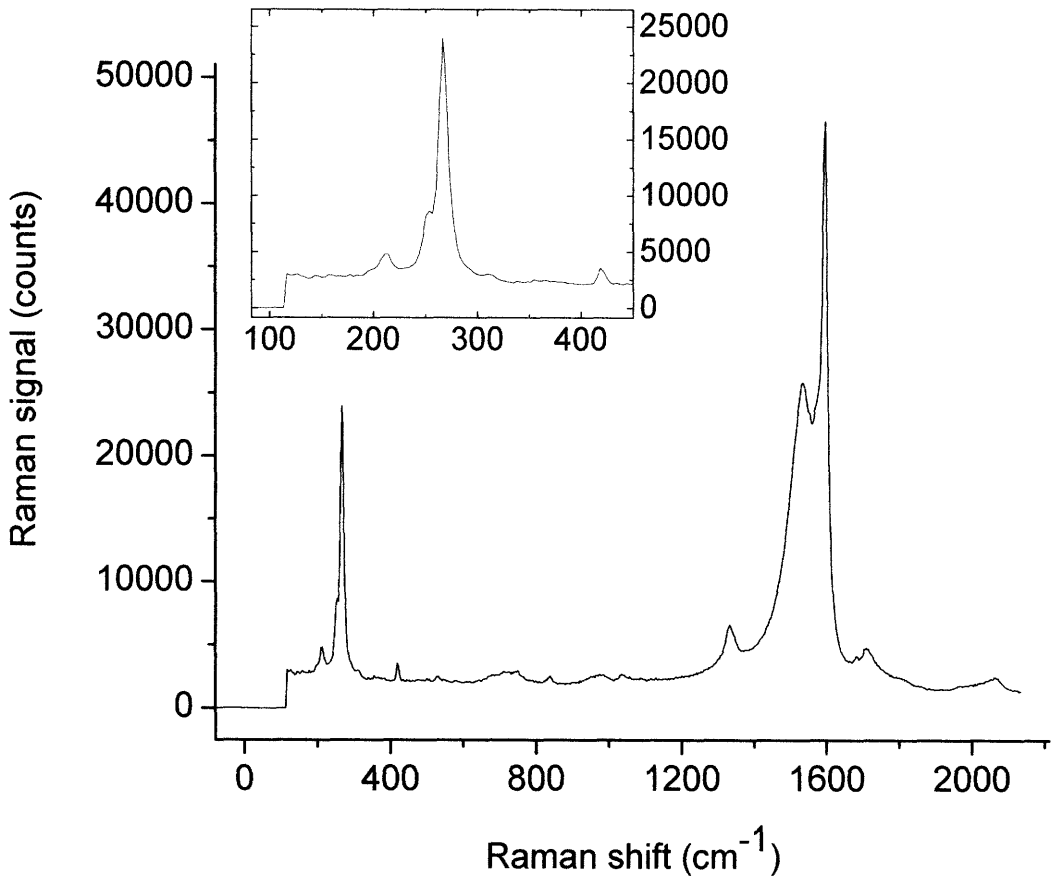

Figure 8-1(c). Same as Figure 8-1(a), but with E_{laser} = 496.5 nm (2.50 eV) and L_{tube} = 100 nm.

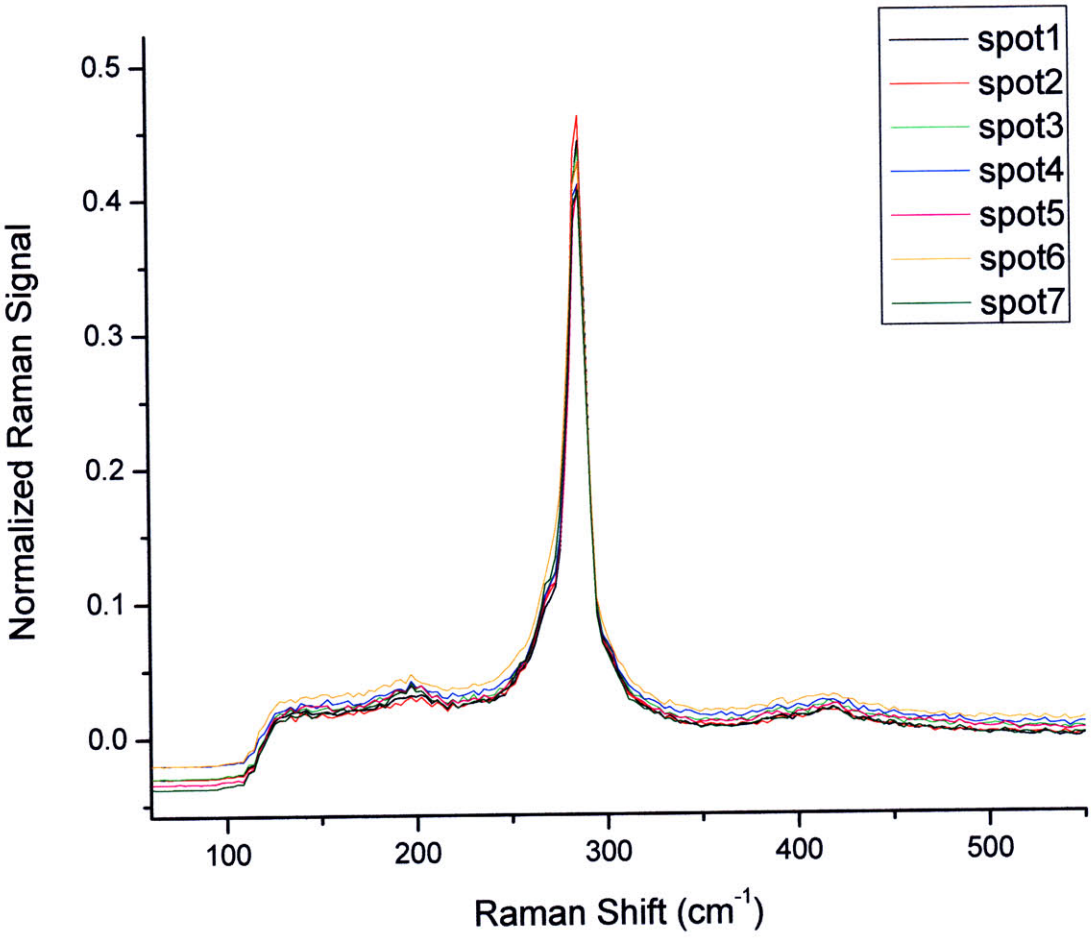

Figure 8-2(a). Raman spectra for different spots on the L_{tube} = 100 nm sample. The laser excitation energy is 647 nm (1.92 eV), and the spectra have been normalized to the G^+ peak after a baseline was subtracted. For this E_{laser}, very little variation in the RBM spectra is seen from one spot to another on the sample.

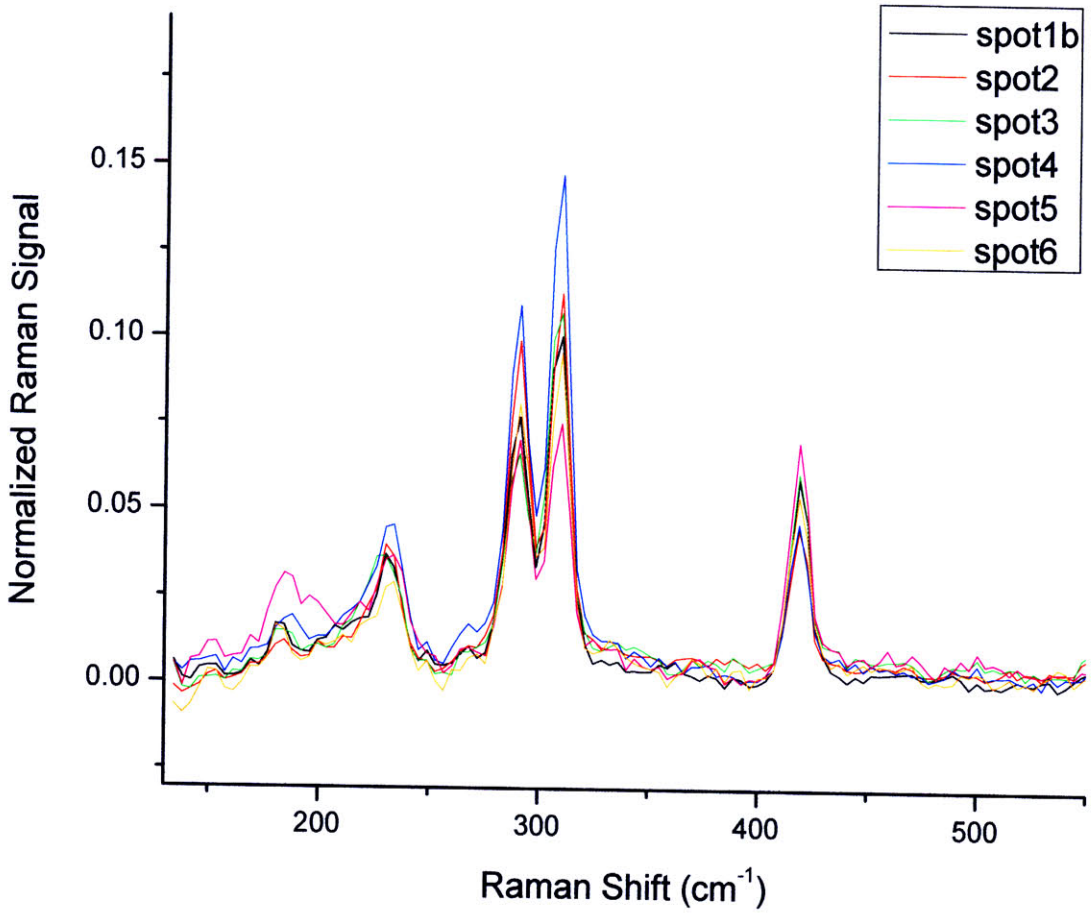

Figure 8-2(b). Same as Figure 8-2(a), but with E_{laser} = 465.8 nm (2.66 eV). L_{tube} = 100 nm for this figure. The spectra have been normalized to the G+ peak after a baseline was subtracted. For this E_{laser}, more variation in the RBM spectra is seen from one spot to another than for Figure 8-2(a).

Peak fitting was performed in the vicinity of the RBM feature in order to extract the frequencies, linewidths and intensities of the RBM peaks. Sample peak fitting curves are shown in Figures 8-3(a) and (b) for the two E_{laser} being considered. Although smaller peaks were found in addition to the sharpest RBM feature in a given spectrum, we focus only on the strongest individual peak here to determine the length dependence of the RBM peak frequencies, linewidths and intensities.

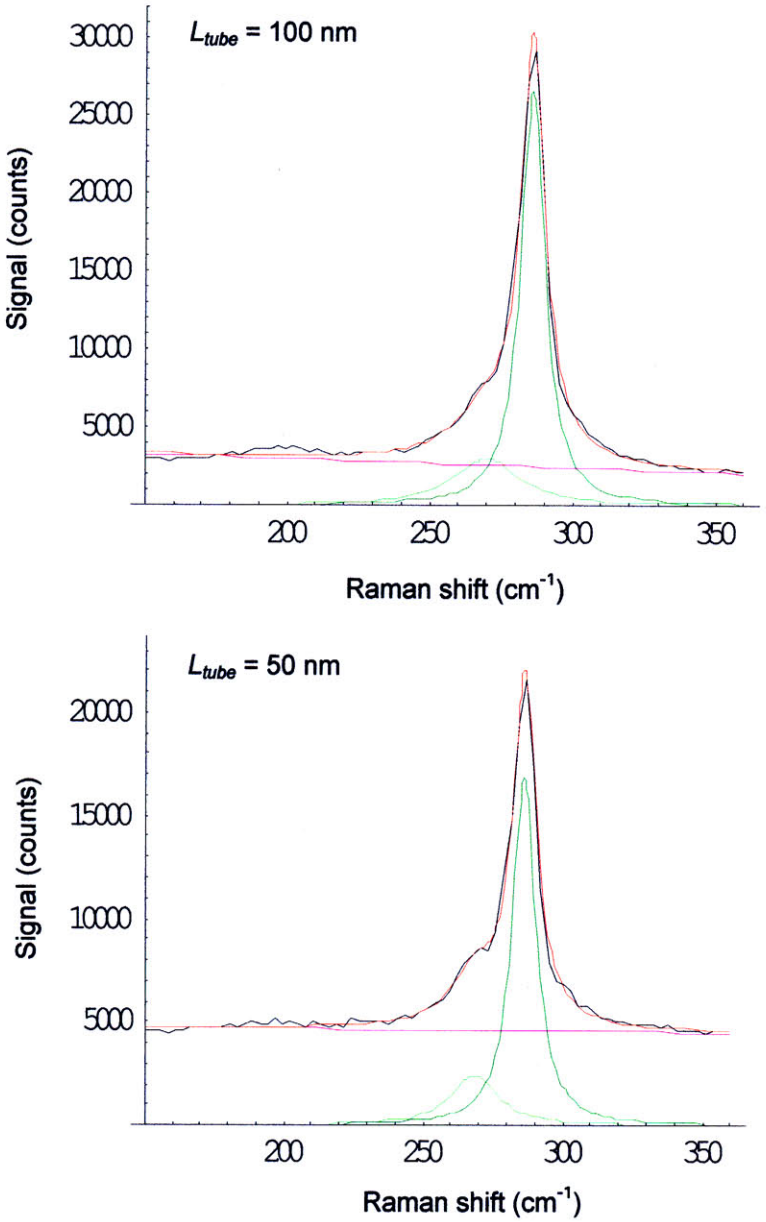

Figure 8-3(a). Peak fitting 12345 results for the RBM region, for E_{laser} = 647 nm (1.92 eV). Spectra for L_{tube} = 100 nm (top) and L_{tube} = 50 nm (bottom) are shown. The peak fitting model consists of a baseline (magenta line) plus two Lorentzians (green curves). The black curve is the raw data and the red curve is the sum of the peak fitting components.

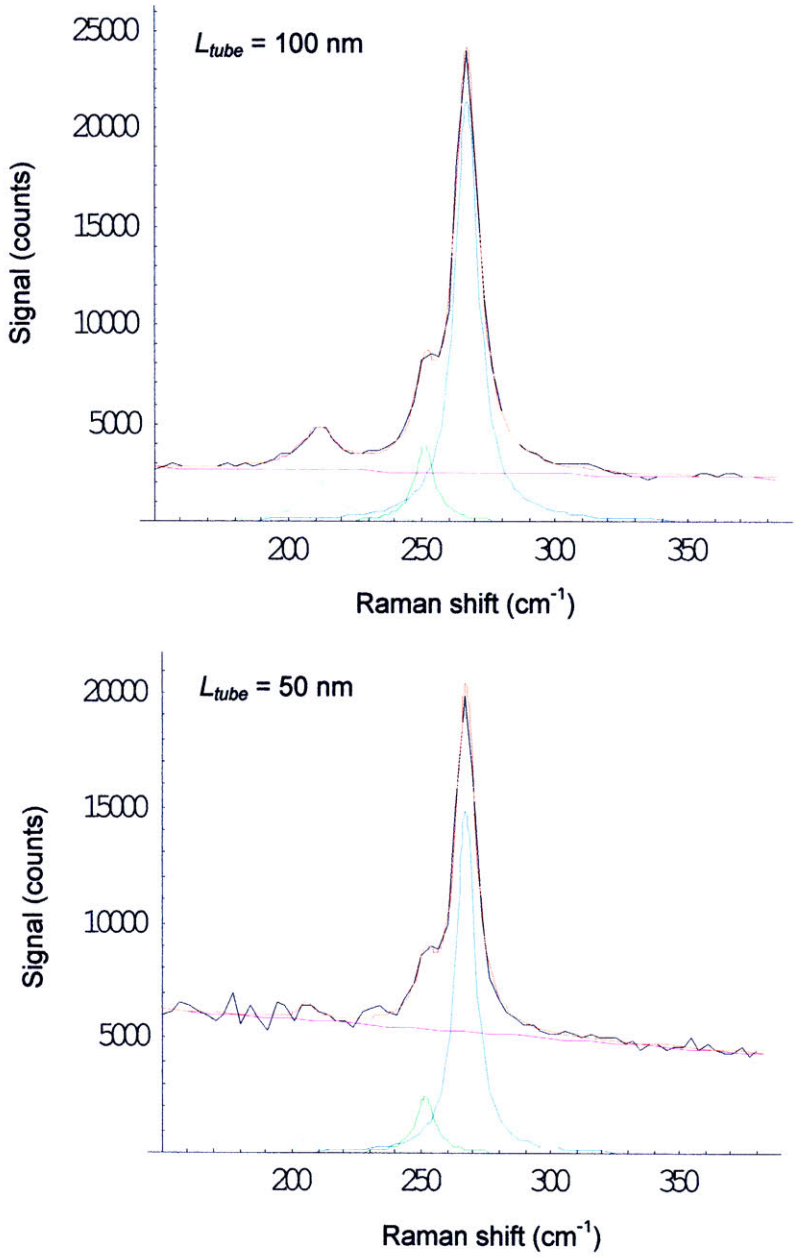

Figure 8-3(b). Peak fitting results for the RBM region, for E_{laser} = 496.5 nm (2.50 eV). Spectra for L_{tube} = 100 nm (top) and L_{tube} = 50 nm (bottom) are shown. The peak fitting model consists of a baseline (magenta line) plus three Lorentzians (green and blue curves). The black curve is the raw data and the red curve is the sum of the peak fitting components.

8.3 Length Dependence of a Single RBM Peak

In this section we will use linear correlation analysis to examine the length dependence of the RBM for semiconducting and metallic nanotubes. As discussed above, we restrict the analysis to the E_{laser} = 647 nm (1.92 eV) and E_{laser} = 496.5 nm (2.50 eV) laser lines, since spectra taken with these E_{laser} show a single strong RBM peak. Using the procedure described in Chapter 3, the correlation coefficients between the RBM peak parameters and the length were calculated, and general trends were identified. For the semiconducting nanotubes (E_{laser} = 1.92 eV), there were 21 data points, which require a correlation coefficient of $|r| \geq 0.43$ in order to reach the P = 0.05 significance threshold. There were 27 data points for the metallic tubes (E_{laser} = 2.50 eV), which require $|r| \geq 0.38$ for a correlation to be statistically significant at the P = 0.05 level.

The correlation between the integrated $[I_{RBM} / I_{G^+}]$ ratio and L_{tube}, as well as the correlation between the peak $[\hat{I}_{RBM} / \hat{I}_{G^+}]$ ratio and L_{tube}, were examined. For semiconducting nanotubes, the weighted correlation coefficient r^w = 0.213 between the peak $[\hat{I}_{RBM} / \hat{I}_{G^+}]$ ratio and L_{tube} which is below threshold. Similarly, r^w = 0.403 and is below threshold for correlations between the integrated $[I_{RBM} / I_{G^+}]$ ratio and L_{tube} for semiconducting nanotubes. Therefore, for semiconducting nanotubes, no length dependence of the normalized RBM intensity was found.

On the other hand, metallic nanotubes have a length dependence in the normalized RBM intensity. For metallic nanotubes, both the integrated $[I_{RBM} / I_{G^+}]$ and L_{tube} (r^w = 0.577), as well as the peak $[\hat{I}_{RBM} / \hat{I}_{G^+}]$ and L_{tube} (r^w = 0.410), are correlated. The linear fits are: integrated $[I_{RBM} / I_{G^+}] = 0.00356\, L_{tube} + 0.0319$, with confidence intervals of (0.00149, 0.00564) nm^{-1} for the slope and (-0.126, 0.190) for the intercept; and the peak $[\hat{I}_{RBM} / \hat{I}_{G^+}] = 0.00419\, L_{tube} + 0.190$, with confidence intervals of (0.000353, 0.00802) nm^{-1} for the slope and (-0.102, 0.482) for the intercept. Figures 8-4(a) and (b) show the integrated $[I_{RBM} / I_{G^+}]$ vs. L_{tube} and peak $[\hat{I}_{RBM} / \hat{I}_{G^+}]$ vs. L_{tube} plots for semiconducting and metallic nanotubes. According to Figures 8-4(a) and (b), the

normalized RBM intensity decreases as L_{tube} decreases from 100 nm to 70 nm. However, from 70 nm to 50 nm, the normalized RBM intensity appears to increase. These two opposite length behaviors may be due to the exciton properties in carbon nanotubes. The increased length sensitivity of metallic nanotubes may be due to the fact that the exciton size in metallic nanotubes is relatively large at 10 – 50 nm. Thus the transition from L_{tube} = 100 nm to L_{tube} = 70 nm may show different behaviors than the transition from L_{tube} = 70 nm to L_{tube} = 50 nm, because in the latter, the nanotube length approaches the exciton size. However, the overall effect for metallic tube is a positive correlation between the normalized intensity ratios and L_{tube}.

For both metallic and semiconducting nanotubes, the RBM full-width half-maximum linewidth and length are uncorrelated (r^w = 0.414 for E_{laser} = 1.92 eV and r^w = -0.315 for E_{laser} = 2.50 eV). Thus, the RBM linewidth does not depend on length. The plots of FWHM vs. L_{tube} are shown in Figure 8-5. The FWHM values for metallic and semiconducting nanotubes are similar: for the metallic tubes, the average FWHM is 11.1 cm^{-1}, while semiconducting tubes have average FWHM of 9.65 cm^{-1}.

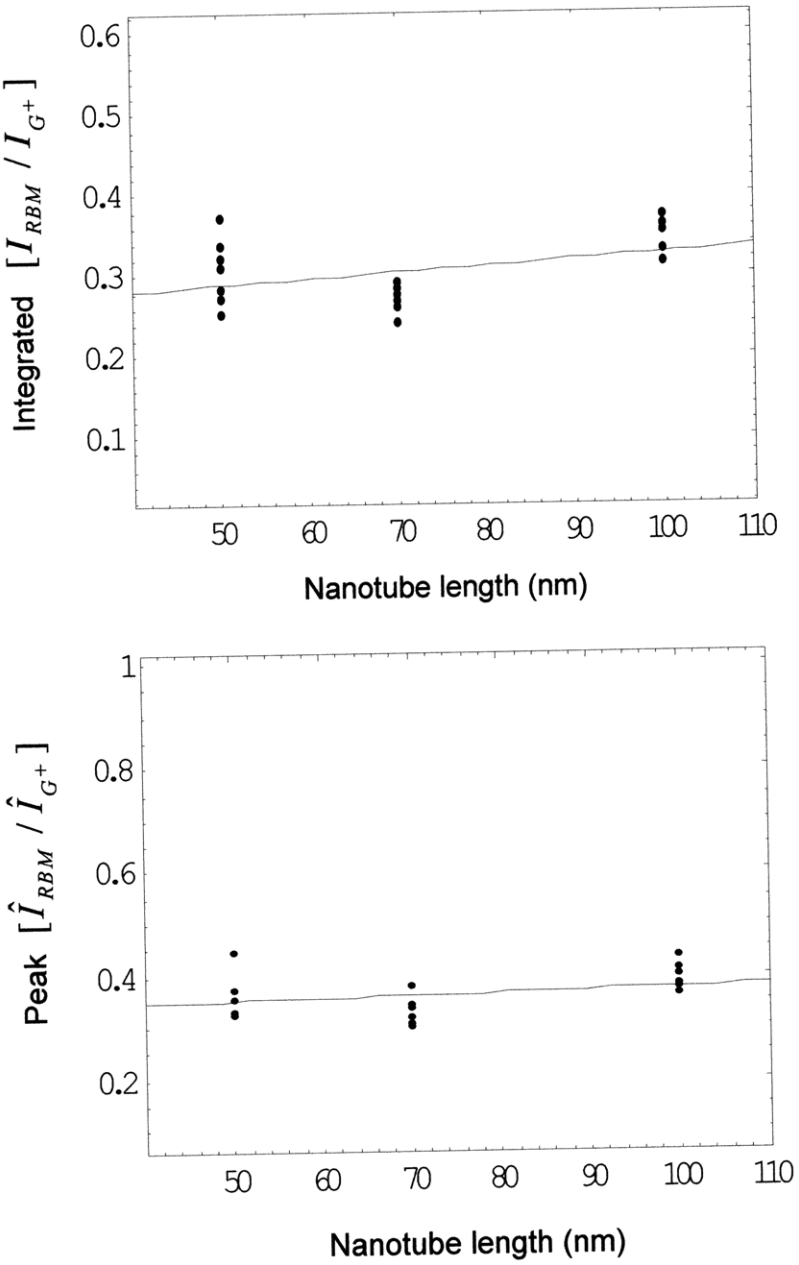

Figure 8-4(a). Scatter plots of the integrated $[I_{G^-} / I_{G^+}]$ ratio vs. L_{tube} (top) and peak $[\hat{I}_{G^-} / \hat{I}_{G^+}]$ ratio vs. L_{tube} (bottom). The laser excitation energy is 1.92 eV which excites semiconducting nanotubes. No statistically significant correlation was found for either of the plots in this figure.

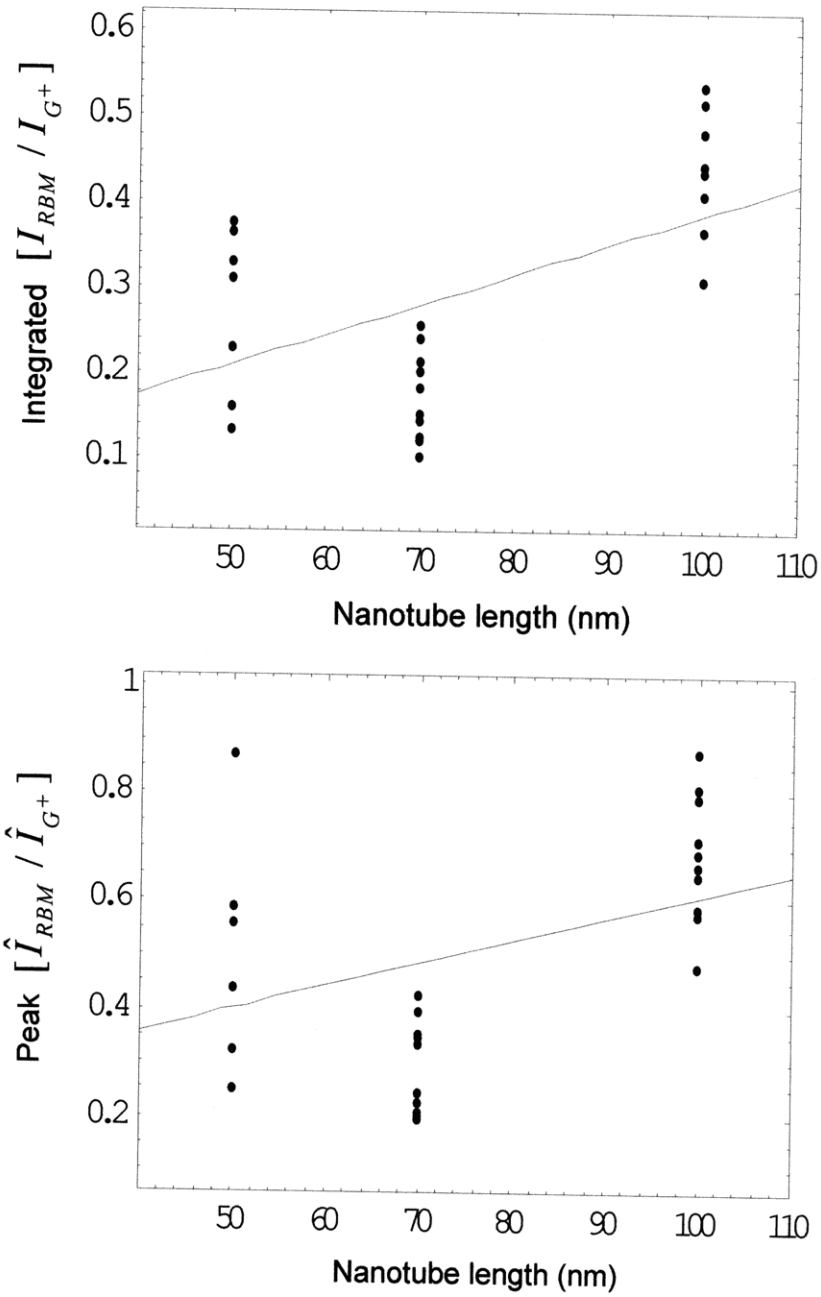

Figure 8-4(b). Same as Figure 8-4(a), but for metallic nanotubes (E_{laser} = 2.50 eV). The correlations are statistically significant in these cases. The linear fits are integrated $[I_{RBM} / I_{G^+}] = 0.00356\, L_{tube} + 0.0319$ and peak $[\hat{I}_{RBM} / \hat{I}_{G^+}] = 0.00419\, L_{tube} + 0.190$.

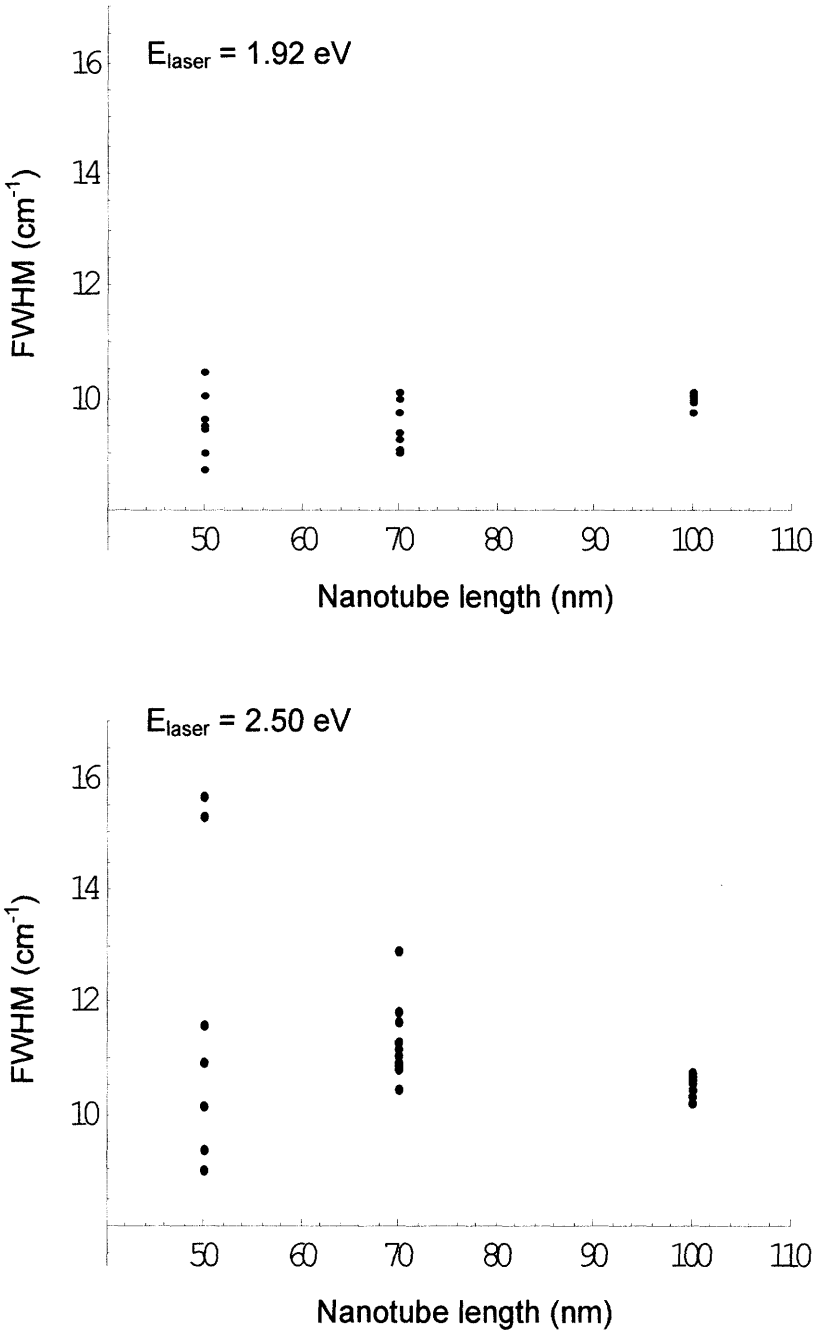

Figure 8-5. FWHM vs. L_{tube} for both E_{laser}.

For semiconducting nanotubes, the correlation coefficient between the RBM frequency ω_{RBM} and L_{tube} is -0.628. For metallic nanotubes, r^w = -0.449. Therefore ω_{RBM} and L_{tube} are anticorrelated. The linear fit for semiconducting nanotubes is ω_{RBM} = -0.0167 L_{tube} + 288 cm^{-1}, with confidence intervals of (-0.0267, -0.00677) cm^{-1}/nm for the

slope and (287, 288) for the intercept. For metallic tubes, the fit is ω_{RBM} = -0.0114 L_{tube} + 268 cm^{-1}, with confidence intervals of (-0.0207, -0.00205) cm^{-1}/nm for the slope and (267, 269) for the intercept. The plots of ω_{RBM} vs. L_{tube} are shown in Figure 8-6. From Figure 8-5, it can be seen that although the anticorrelation is statistically significant, the slopes are small enough such that ω_{RBM} remains approximately constant with L_{tube} for both E_{laser}. From Figure 8-6 it can be seen that has only a slight upshift of 1 – 2 cm^{-1}, which is below the spectrometer resolution of about 5 cm^{-1}. Thus, ω_{RBM} does not change appreciably with L_{tube}.

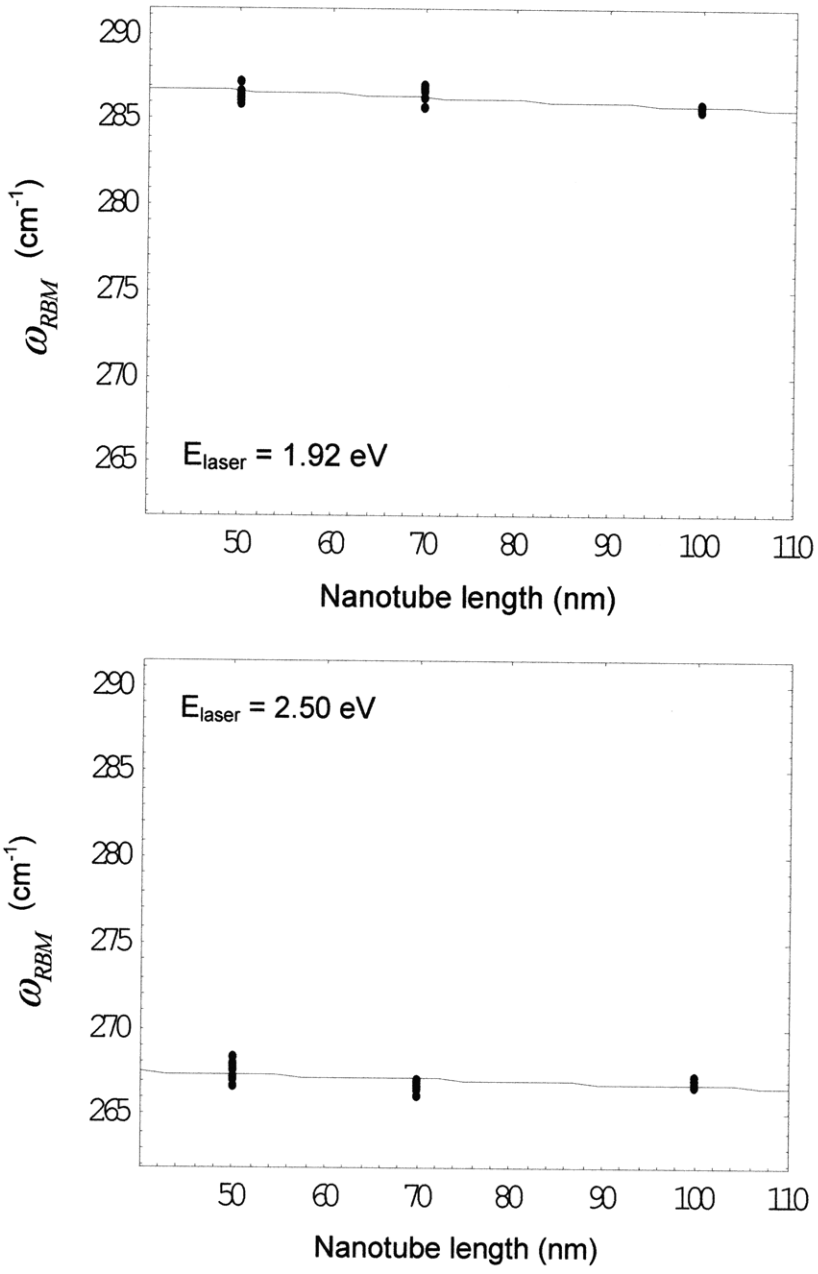

Figure 8-6. ω_{RBM} vs. L_{tube} for both E_{laser}.

8.4 Length Dependence of ω_{RBM} Across Several E_{laser}

In this section we check whether the size-exclusion chromatography process inadvertently sorts the nanotubes according to diameter. We examine the RBM frequencies for each of the different L_{tube} samples, for a succession of closely spaced values of E_{laser}. Table 8-1 shows the observed RBM frequencies in the E_{laser} range of 2.41

– 2.71 eV, for L_{tube} = 50, 70, and 100 nm. We see that in general, the same RBM are present for the different L_{tube}, at a given E_{laser}. The exceptions occur when some RBM which are present for L_{tube} = 100 nm are not visible for L_{tube} = 70 nm and L_{tube} = 50 nm. This can be attributed to the noisier spectra that are typical for the shorter length nanotubes. For the shorter tubes, the weaker RBM peaks may not be visible above the noise. The results summarized in Table 8-1 contribute to the case that the length sorting process does not also sort the nanotubes according to diameter.

E_{laser} (eV)	L_{tube} (nm)	Observed ω_{RBM} (cm^{-1})						
2.41	100	153	189	249	264	270		
	70	156	189	249	264	273		
	50		186	249	267	273		
2.47	100	228	267	280				
	70		267	280				
	50		267	283				
2.50	100	211	254	267	309			
	70		250	267				
	50		254	267				
2.54	100		163	208	249	263	287	307
	70		163	208	249	263	287	307
	50	149	163	205	246	263	287	307
2.60	100	205	226	265	286	307		
	70	206	228		286	307		
	50		224			307		
2.62	100	142	175	206	230	263	287	307
	70	143	178	207	229	263	288	305
	50	147	180		233	265	292	311
2.66	100	180	230	291	310			
	70	183	230	290	309			
	50	184	230	290	310			
2.71	100	227	286	305				
	70	223	286	305				
	50	223	286	305				

Table 8-1. The observed RBM frequencies in the E_{laser} range of 2.41 – 2.71 eV, for L_{tube} = 50, 70, and 100 nm.

8.5 Summary

In this chapter we checked the length dependence of the RBM peak. We first focused on a single RBM peak for semiconducting nanotubes as well as a corresponding RBM peak for metallic tubes. When the RBM intensity was normalized to the G^+ peak, no length dependence was found for semiconducting tubes. However, the normalized RBM intensity for metallic tubes was found to decrease overall as the tube length decreases. For metallic tubes, after a decrease in normalized intensity in going from L_{tube} = 100 nm to L_{tube} = 70 nm, there is a normalized intensity increase when L_{tube} goes from 70 nm to 50 nm. It is possible that at L_{tube} around 50 nm, the exciton size for metallic nanotubes approaches the tube length, which may result in a different length dependence from more macroscopic lengths. More data need to be taken at intermediate nanotube lengths to better understand this length dependence. For both semiconducting and metallic nanotubes, the RBM full-width half-maximum linewidth was found to be independent of length. Finally, we examined the RBM frequencies for the different L_{tube} across several closely spaced values of E_{laser}. The results contribute to the case that the length sorting process does not also sort the nanotubes according to diameter.

Reference

[1] M. S. Dresselhaus et al., "Raman spectroscopy of carbon nanotubes," *Physics Reports,* **409** (2005) 47.

Chapter 9 – Summary and Future Work

9.1 Summary and Conclusions

Recent advances in post-growth processing have allowed the sorting of carbon nanotubes by length [1]. In particular, length sorted nanotube samples, with finite lengths approaching the exciton size, are now available. Hence, it is now possible to perform experiments that explore the finite size effects, as well as the length dependence, of carbon nanotubes. Although there are many experimental and theoretical studies of the diameter dependence of carbon nanotubes, only a few studies of length dependence effects in carbon nanotubes exist. In this thesis, we have examined the length dependence of the Raman spectra in carbon nanotubes.

In general, we have found that the spectra fall into two categories. One category has a broad G^- peak (around 1540 cm^{-1}) that is commonly seen in metallic nanotubes, and the other category has a narrow G^- peak. The broad G^- peak occurs for the higher E_{laser} (2.41 – 2.71 eV). Although for all E_{laser}, a mixture of semiconducting and metallic tubes were excited, we tentatively group the spectra taken with the higher E_{laser} range as being from metallic nanotubes, and the spectra from the lower E_{laser} range as being from semiconducting nanotubes. When the spectra are divided in this way, we have found that the properties of the various Raman peaks differ markedly between the two groups.

We have found that the Raman spectra, especially for metallic tubes, varies for different spots on the same sample. This results in noisier data, where the length-dependent trends are not very obvious. However, a statistical analysis method exists through which correlations can be identified from noisy data. Throughout this thesis, we have used this method to examine the length and E_{laser} dependence of the Raman spectra. The details of this method were explained in Chapter 3.

The length dependence of the Raman G-band was examined in Chapter 3. The length dependence was examined in terms of the two major components of the G-band: the sharp G^+ peak at 1590 cm^{-1}, and the lower frequency G^- peak around 1540 cm^{-1}. The length dependence of metallic nanotubes were studied in greater detail, since the G-band for metallic nanotubes is more complicated than for semiconducting tubes. Metallic nanotubes appear to have a more pronounced length dependence than semiconducting

tubes. For semiconducting nanotubes, the frequencies and linewidths of the G^+ and G^- peaks were found to be independent of length. The peak intensity ratio $[\hat{I}_{G^-} / \hat{I}_{G^+}]$ was found to decrease by 7% when L_{tube} decreases from 100 nm to 50 nm.

For metallic nanotubes, we found that when L_{tube} decreases, the frequency difference $(\omega_{G^+} - \omega_{G^-})$ also decreases. Since $(\omega_{G^+} - \omega_{G^-})$ corresponds to the splitting of the graphite G-band peak into LO and TO modes, the observed length dependence may be due to the lower aspect ratio for short tubes. In addition, $(FWHM)_{G^-}$ decreases with decreasing L_{tube}, while $(FWHM)_{G^+}$ increases as L_{tube} decreases. Also, the asymmetric Breit-Wigner-Fano lineshape of the G^- peak becomes more Lorentzian as L_{tube} decreases. Finally, the peak $[\hat{I}_{G^-} / \hat{I}_{G^+}]$ ratio increases as L_{tube} decreases while the integrated $[I_{G^-} / I_{G^+}]$ ratio remains the same. Some of these results are reminiscent of recent experiments that probe the Kohn Anomaly in carbon nanotubes [2, 3]. In a previous work, the metallic G^- intensity increases, its linewidth decreases, and the lineshape becomes more Lorentzian as the Fermi level ε_F is tuned (by doping or applying a gate voltage) away from the Fermi point [2, 3]. The Kohn Anomaly is a manifestation of electron-phonon coupling and is expected to appear only for metallic tubes [4 – 6]. Furthermore, the width of the G^- peak is predicted to be a measure of the amount of electron-phonon coupling in the nanotube [4]. Thus the observed narrowing of the G^- peak as L_{tube} decreases is an indication of decreased electron-phonon coupling for shorter tubes. The greater length sensitivity of metallic nanotubes (as opposed to semiconducting tubes) may be because metallic G-band modes have more pronounced electron-phonon coupling than those of semiconducting tubes. Since the G^- peak corresponds to the LO phonon mode, it is not unreasonable that this peak would exhibit a strong length dependence [4, 6]. The observed increase of $(FWHM)_{G^+}$ with decreasing L_{tube} could be due to the decreased phonon lifetime that arises from scattering at the tube ends.

Chapter 3 focused on the length dependence of the carbon nanotube G-band. In Chapter 4, we extended our G-band studies and examined the correlations between the different G-band parameters (frequency, linewidth, relative intensity, and asymmetry) for

carbon nanotubes in general, irrespective of length. We investigated whether certain relationships existed, such as whether the G^- lineshape asymmetry is correlated with the linewidth. Because the G-band of metallic nanotubes is more complex than that of semiconducting tubes, with the asymmetric lineshape (due to coupling to an electronic continuum) and electron-phonon coupling effects, we focused our attention on metallic nanotubes in Chapter 4. We have found that the Raman spectra, each taken at different spots on the samples, could be loosely grouped into two types depending on the observed G-bands. "Type 1" spectra have peak G^- intensities that are as high or higher than their respective G^+ intensities, and "Type 0" spectra have lower G^- peak intensities. In our study, many spectra were found to be of the high G^- intensity type, occurring mostly for the shortest (L_{tube} = 50 nm) tubes. Out of 65 spectra for L_{tube} = 50 nm, 29 spectra were Type 1. In this chapter, the Type 0 and Type 1 spectra were examined independently to check whether the correlations between the G-band parameters are different for the two groups. We also investigated whether the length-dependent effects discussed in Chapter 3 were due to the high occurrence of Type 1 spectra for the shortest nanotubes. An example of a relationship that occurs for Type 1 but not for Type 0 spectra is the anticorrelation of $(FWHM)_{G^-}$ and the peak $[\hat{I}_{G^-} / \hat{I}_{G^+}]$ ratio (as the normalized G^- peak intensity increases, the G^- linewidth narrows). The correlations among the various G-band parameters are summarized in Table 4-8.

In Chapter 5 we examined the length dependence of the Raman D-band, which is activated by finite size or lattice defects [7]. We first compared our results with previous work on the D-band of short nanotubes [8] and nanographite [9]. In nanographite, an application of Raman spectroscopy is to estimate crystallite size, L_α, from the measured I_D / I_G intensity ratio, according to the formula $L_\alpha = \frac{560}{E_{laser}^4}\left(\frac{I_D}{I_G}\right)^{-1}$. It was our aim to determine whether a similar relation applies for carbon nanotubes. However, a relation between the integrated I_D / I_{G^+} ratio, E_{laser}, and L_{tube}, analogous to the nanographite formula, could not be fit from the data. Correlation analysis was used to determine the D-band dependence on L_{tube} and E_{laser}. Regardless of whether the nanotubes are

semiconducting or metallic, we have found that the peak and the integrated I_D / I_{G^+} ratio are inversely proportional to L_{tube}. This was expected because the D-band arises from a breakdown in selection rules brought about by finite size effects [10]. The D-band frequency, ω_D, was found to depend linearly on E_{laser}, in agreement with the literature [11, 7]. However ω_D was found not to depend on L_{tube}.

A few differences were found in the D-band behavior of semiconducting vs. metallic nanotubes. For metallic nanotubes, the D-band linewidth was found to be anticorrelated with length. For semiconducting nanotubes, the peak and integrated $\left(I_D / I_{G^+}\right)$ ratio are anticorrelated with E_{laser}. Furthermore the slope of the ω_D vs. E_{laser} dependence is smaller for metallic tubes than for semiconducting tubes. Metallic nanotubes were found to have a greater peak and integrated $\left(I_D / I_{G^+}\right)$ ratio than semiconducting nanotubes. Finally, metallic nanotubes appear to be more sensitive to changes in length, since $\left(I_D / I_{G^+}\right)$ and $(FWHM)_D$ have more length dependence for metallic nanotubes than for semiconducting tubes. The difference in length sensitivity between metallic and semiconducting nanotubes may be due to the difference in binding energy between excitons in metallic vs. semiconducting tubes [12, 13]. In metallic nanotubes, the exciton binding energy is less than 0.2 eV, while the exciton binding energy in semiconducting tubes is can be as large as 1 eV [12]. Hence for a metallic nanotube, the exciton size is large compared to that of a semiconducting nanotube. Since the exciton size for a metallic nanotube is about 10-50 nm, the increased length dependence seen here for metallic nanotubes could be a finite size effect [13].

In Chapter 6 we studied the G' peak, which is the second harmonic of the D-band. Although the G' band typically appears as a single peak, double peak G' bands have also been observed for semiconducting and metallic nanotubes [11, 14]. Previous works have indicated that the double peak structure of G' arises from two energy levels being excited for a given E_{laser}, and each peak corresponds to one of the two states in resonance [14, 15]. The double peak G' band was frequently observed in our studies of short carbon nanotubes, for both metallic and semiconducting tubes. In this chapter, we examined the E_{laser} and length dependence of the two peaks comprising the G' band. Spectra were taken

using several laser lines, which fall into two distinct ranges: $1.92 \leq E_{laser} \leq 2.07$ eV, and $2.60 \leq E_{laser} \leq 2.71$ eV. We have found that the G' band properties are quite different, depending on whether E_{laser} is in the higher or lower eV range. For example, the frequencies of both the upper and lower G' peaks, $\omega_{G'}^{upper}$ and $\omega_{G'}^{lower}$, are higher for $2.60 \leq E_{laser} \leq 2.71$ eV than for the lower eV range.

We also examined the G' band splitting, $\Delta\omega_{G'} \equiv \omega_{G'}^{upper} - \omega_{G'}^{lower}$. When $\Delta\omega_{G'}$ is converted to energy ΔE, it represents the energy separation between the two states which are simultaneously excited. We have found that $\Delta\omega_{G'}$ is greater for points that fall within $2.60 \leq E_{laser} \leq 2.71$ eV than for points in the $1.92 \leq E_{laser} \leq 2.07$ eV range. For $2.60 \leq E_{laser} \leq 2.71$ eV, the corresponding energy separation ΔE was found to range from 0.424 eV to 0.518 eV. This is about equal to the scattered phonon energy, which is 0.33 eV, plus a resonant window of 0.1 – 0.2 eV. Thus, for $2.60 \leq E_{laser} \leq 2.71$ eV, the lower component of G' may arise from resonance with the scattered photon, while the upper component of G' could be due to resonance with the incident photon. In the $1.92 \leq E_{laser} \leq 2.07$ eV range, we found that ΔE is around 0.12 eV, which is very much smaller than the ΔE for higher E_{laser}. If we assume a resonant window of 0.2 eV [14], then a ΔE of 0.12 eV could arise from two closely spaced states, both within the G' resonant window, which are simultaneously excited by the incident photon.

The intensities of the two G' components vary with E_{laser}, and are dependent on the number of (n, m) tubes which are resonant. The linewidths of the G' peaks also depend on the number of different nanotubes being excited. Finally, the length dependence of the G' band seems to be minor.

In Chapter 7, the properties of the G* peak at 2417 cm^{-1} (for E_{laser} = 2.66 eV) were examined. The G* peak in carbon nanotubes is attributed to an overtone mode of the LO phonon [16]. In our spectra, the G* feature is very weak and noisy. A few effects were found that are above the noise level. For metallic and semiconducting nanotubes, the integrated $[I_{G^*} / I_{G^+}]$ intensity ratio was found to increase as L_{tube} decreases, and the effect seems to be more pronounced for semiconducting tubes. The peak $[\hat{I}_{G^*} / \hat{I}_{G^+}]$ ratio also increases with decreasing L_{tube}, but the difference between metallic and semiconducting tubes is less evident. The G* FWHM linewidth decreases with increasing

E_{laser}, and for metallic tubes, increases with decreasing L_{tube}. The G* frequency ω_{G^*} was found to be independent of L_{tube}. The measured frequency dispersion is ω_{G^*} = -41.1 E_{laser} + 2526 cm^{-1}, which differs from an earlier work that reports almost no dispersion [16]. However, measurements of G* in few-layer graphene also report a negative dispersion, with magnitude of about -26 cm^{-1}/eV [17].

Finally, Chapter 8 addressed the length dependence of the radial breathing mode (RBM) peaks, which occur between 120 – 350 cm^{-1} and originate from vibration along the radial direction of the nanotube. The measured RBM frequency ω_{RBM} can be used to estimate the nanotube diameter, since ω_{RBM} is inversely proportional to the diameter [11]. In addition, the measured ω_{RBM} in conjunction with the Kataura plot can be used to tentatively determine the (*n, m*) indices of the nanotubes in a sample. To determine the length dependence, we focused on a single RBM peak for semiconducting nanotubes as well as a corresponding RBM peak for metallic tubes. When the RBM intensity was normalized to the G^+ peak, no length dependence was found for semiconducting tubes. However, the normalized RBM intensity for metallic tubes was found to decrease overall as the tube length decreases. For metallic tubes, after a decrease in normalized intensity in going from L_{tube} = 100 nm to L_{tube} = 70 nm, there is a normalized intensity increase when L_{tube} goes from 70 nm to 50 nm. It is possible that at L_{tube} around 50 nm, the exciton size for metallic nanotubes approaches the tube length, which may result in a different length dependence from more macroscopic lengths. More data need to be taken at intermediate nanotube lengths to better understand this length dependence. For both semiconducting and metallic nanotubes, the RBM full-width half-maximum linewidth was found to be independent of length. Finally, we examined the RBM frequencies for the different L_{tube} across several closely spaced values of E_{laser}. The results contribute to the case that the length sorting process does not also sort the nanotubes according to diameter.

9.2 Future Work

In this section, we will discuss new research directions suggested by this work. One possibility is the study of doping effects on length-sorted carbon nanotube samples. Throughout this thesis, we have found that metallic tubes show a greater sensitivity to length than semiconducting tubes. Hence, it would be interesting to see whether nanotubes of different carrier concentrations, tuned by doping, would exhibit different sensitivities to nanotube length.

A direct extension of the work presented in this thesis would be the detailed study of the Raman spectra of a wider variety of length-sorted nanotubes. In this thesis, only three different tube lengths were studied: L_{tube} = 50, 70, and 100 nm. This is only a small subset of possible lengths, as length-sorted samples with average lengths less than 20 nm, and as long as several hundreds of nm, are available [18]. Thus, the length dependence of longer (and not just finite-sized) tubes can be examined. One effect that is frequently seen in our data is a different trend occurring when going from L_{tube} = 100 nm to L_{tube} = 70 nm, versus the L_{tube} = 70 nm to L_{tube} = 50 nm transition. An example is shown in Figure 3-11, which is reproduced below. In Figure 3-11(d), we see that the peak $[\hat{I}_{G^-} / \hat{I}_{G^+}]$ intensity ratio decreases when L_{tube} decreases from 100 nm to 70 nm, but increases when L_{tube} transitions from 70 nm to 50 nm. While this effect could be noise, it is also possible that different physics is involved in either side of the L_{tube} = 70 nm transition. Since the exciton size for a metallic nanotube is about 10 – 50 nm, the effects seen in the sub-100 nm length range could signify the transition from macroscopic length to finite size. Besides the finite size nanotubes, it would be of interest to study the length dependence of longer (greater than L_{tube} = 100 nm) tubes, since the longer tubes are more commonly available and widely used. Hence a study using a greater range of L_{tube} would give a clearer picture of the length dependence of carbon nanotubes.

In this study, we have observed a significant spot-to-spot variation in the Raman spectra for each sample. The inhomogeneity in the Raman spectra could arise because multiple (n, m) nanotubes are excited by the same laser line. To better understand the spot-to-spot variation, it would be interesting to study the Raman spectra of length-sorted

nanotubes at the single nanotube level. A clearer understanding of the underlying physics would then be possible, since the exact (*n, m*) indices for the resonant tube would be known. Isolated nanotubes can be studied by using a very dilute sample, such that the probability of finding more than one resonant nanotube in a given light spot is very small [19].

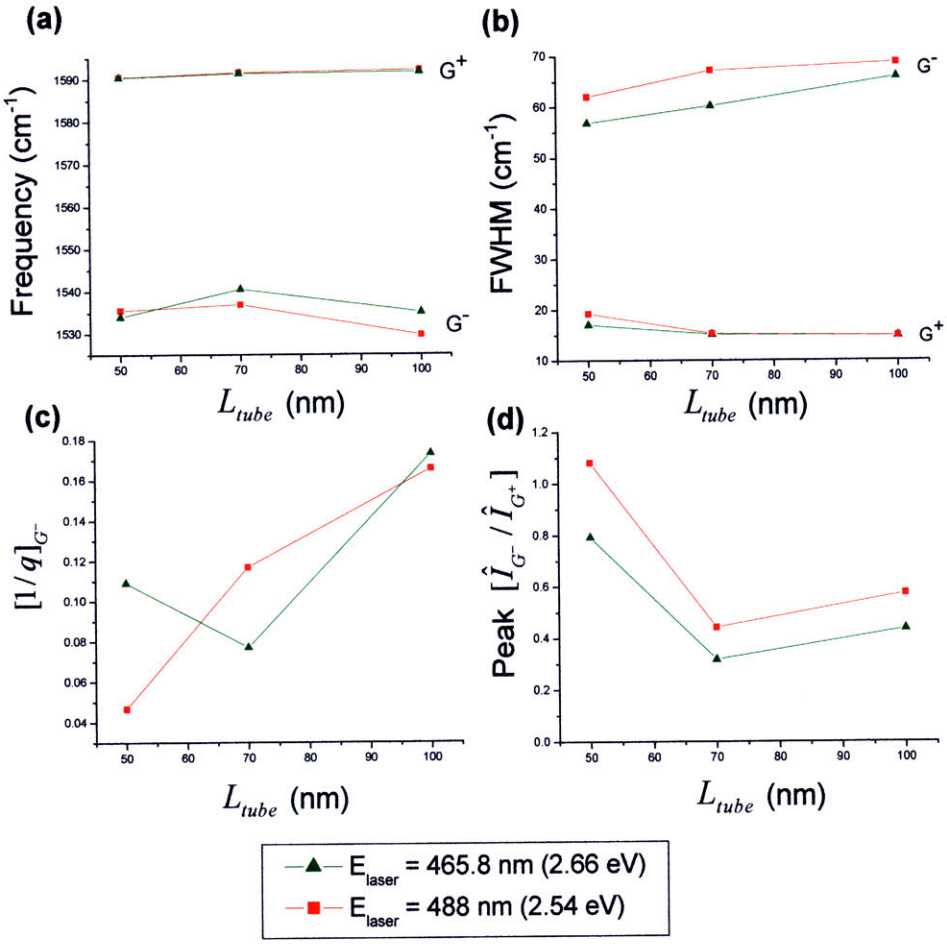

Figure 3-11. The G-band length dependence for two laser lines that excite metallic nanotubes. The red curves correspond to nanotubes excited with the 488 nm (2.54 eV) laser line, and the green curves correspond to nanotubes excited at 465.8 nm (2.66 eV). Each point represents the median value taken over several spots on a sample. The **(a)** frequency, **(b)** the FWHM linewidth, **(c)** the magnitude of the asymmetry parameter $[1/q]_{G^-}$, and **(d)** the peak $[\hat{I}_{G^-} / \hat{I}_{G^+}]$ ratio are shown vs. L_{tube}.

A length dependence Raman study using polarized light would also be interesting. An "antenna effect" has been observed in carbon nanotubes, by which the Raman features have maximum intensity for light polarized parallel to the nanotube axis, and minimized for light polarized perpendicular to the axis [20 – 22]. The integrated $[I_{G^-} / I_{G^+}]$ intensity ratio in particular seems especially sensitive to polarization. In a previous work, $[I_{G^-} / I_{G^+}]$ was found to be strongly dependent on the polarization angle, with $[I_{G^-} / I_{G^+}]$ being maximized for light polarized parallel to the tube axis, and minimized for light polarized perpendicular to the axis [19]. In this thesis, we have shown that spectra with high $[I_{G^-} / I_{G^+}]$ ratios tend to appear for the shortest nanotubes. A Raman study using polarized light may lead to a clearer understanding of the origin of the high $[I_{G^-} / I_{G^+}]$ intensity ratios that we have observed. In general, it would be interesting to see whether the reduced anisotropy for short tubes would result in the antenna effect being less pronounced for finite length tubes.

References

[1] X. Y. Huang et al., "High-resolution length sorting and purification of DNA-wrapped carbon nanotubes by size-exclusion chromatography." *Anal. Chem,* **77** (2005) 6225-6228.

[2] K. T. Nguyen et al., "Fano Lineshape and Phonon Softening in Single Isolated Metallic Carbon Nanotubes." *Physical Review Letters*, **98** (2007) 145504.

[3] H. Farhat et al., "Phonon Softening in Individual Metallic Carbon Nanotubes due to the Kohn Anomaly." *Physical Review Letters*, **99** (2007) 145506.

[4] M. Lazzeri et al., "Phonon linewidths and electron-phonon coupling in graphite and nanotubes." *Physical Review B*, **73** (2006) 155426.

[5] Ge. G. Samsonidze et al., "Electron-phonon coupling mechanism in two-dimensional graphite and single-wall carbon nanotubes." *Physical Review B*, **75** (2007) 155420.

[6] E. Di Donato et. a.l., "Assignment of the G^+ and G^- Raman bands of metallic and semiconducting carbon based on a common valence force field," *Physical Review B,* **74** (2006) 184306.

[7] M. A. Pimenta et al., "Diameter dependence of the Raman *D*-band in isolated single-wall carbon nanotubes," *Physical Review B,* **64** (2001) 041401.

[8] S. G. Chou et al., "Length characterization of DNA-wrapped carbon nanotubes using Raman spectroscopy." *Applied Physics Letters*, **90** (2007) 131109.

[9] L. G. Cancado et al., "General equation for the determination of the crystallite size L_a of nanographite by Raman spectroscopy," *Applied Physics Letters,* **88** (2006) 163106.

[10] F. Tuinstra and J. L. Koenig, "Raman Spectrum of Graphite," *Journal of Chemical Physics,* **53** (1970), 1126.

[11] M. S. Dresselhaus et al., "Raman spectroscopy of carbon nanotubes," *Physics Reports,* **409** (2005) 47.

[12] J. Jiang et. a.l., "Chirality dependence of exciton effects in single-all carbon nanotubes: Tight-binding model," *Physical Review B,* **75** (2007) 035407.

[13] R. Saito (Private Communication).

[14] A. G. Souza Filho, A. Jorio, et al., "Anomalous two-peak G'-band Raman effect in one isolated single-wall carbon nanotube," *Physical Review B,* **65** (2002) 085417.

[15] A. G. Souza Filho, A. Jorio, et al., "Probing the electronic trigonal warping effect in individual single-wall carbon nanotubes using phonon spectra," *Chemical Physics Letters,* **354** (2002) 62.

[16] T. Shimada et al., "Origin of the 2450 cm^{-1} Raman bands in HOPG, single-wall and double-wall carbon nanotubes," *Carbon,* **43** (2005) 1049.

[17] A. Reina (Private Communication).

[18] J. A. Fagan et al., "Length-Dependent Optical Effects in Single-Wall Carbon Nanotubes." *J. A. Chem. Soc*, **129** (2007) 10607-10612.

[19] Jorio et al., "G-band resonant Raman study of 62 isolated single-wall carbon nanotubes." *Physical Review B*, **65** (2002) 155412.

[20] G. S. Duesberg et al., "Polarized Raman Spectroscopy on Isolated Single-Wall Carbon Nanotubes," *Physical Review Letters,* **85** (2000) 5436.

[21] Z. Yu and L. Brus, "Rayleigh and Raman Scattering from Individual Carbon Nanotube Bundles," *Journal of Physical Chemistry B,* **105** (2001) 1123.

[22] J. Hwang et al., "Polarized spectroscopy of aligned single-wall carbon nanotubes," *Physical Review B,* **62** (2000) R13 310.